THÈSE

En vue de l'obtention du

DOCTORAT DE L'UNIVERSITÉ DE TOULOUSE

Délivré par :

Institut National Polytechnique de Toulouse (Toulouse INP)

Discipline ou spécialité :

Photonique et système optoélectronique

Présentée et soutenue par :

M. CLEMENT DELEAU

le vendredi 6 mai 2022

Titre :

Integrated long period waveguide gratings for refractometric and gas sensing applications

---

Ecole doctorale :

Génie Electrique, Electronique, Télécommunications (GEETS)

Unité de recherche :

Laboratoire d'Analyse et d'Architecture des Systèmes (LAAS)

Directeurs de Thèse :

M. OLIVIER BERNAL

M. HAN CHENG SEAT

Rapporteurs :

M. JOEL CHARRIER, UNIVERSITE RENNES 1

M. NICOLAS LE THOMAS, GHENT UNIVERSITY

Membres du jury :

M. WILFRIED UHRING, UNIVERSITE DE STRASBOURG, Président

M. FREDERIC SURRE, UNIVERSITY OF GLASGOW, Invité

M. HAN CHENG SEAT, TOULOUSE INP, Membre

MME HÉLÈNE TAP, TOULOUSE INP, Invitée

MME MARIA-PILAR BERNAL, UNIVERSITE DE FRANCHE COMTE, Membre

MME VALÉRIE CHAVAGNAC, CNRS TOULOUSE, Membre

M. OLIVIER BERNAL, TOULOUSE INP, Membre

M. QUENTIN WILMART, CEA GRENOBLE, Membre

INTEGRATED LONG PERIOD WAVEGUIDE GRATINGS FOR REFRACTOMETRIC AND GAS SENSING APPLICATIONS

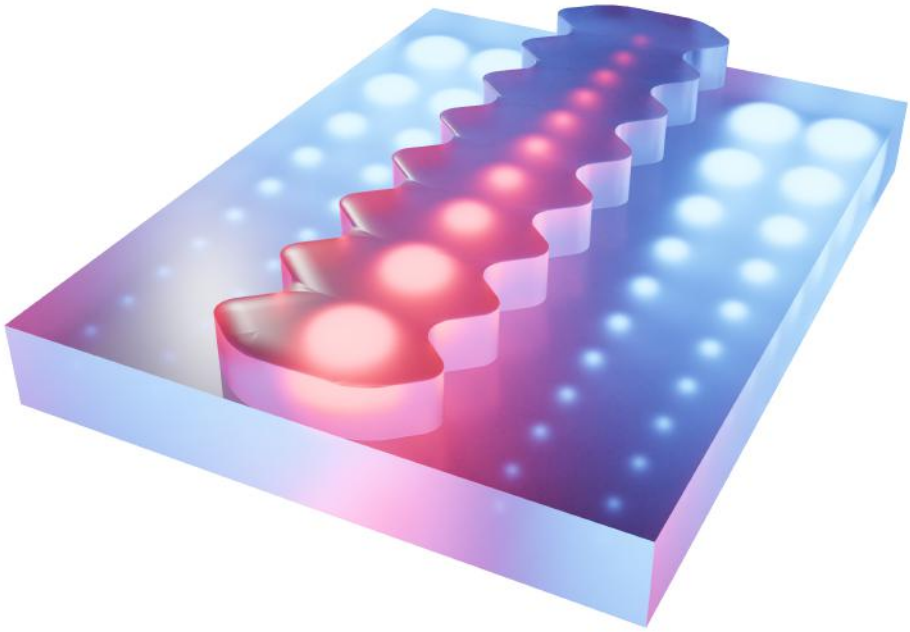

Keywords:

Long Period Grating, Integrated Photonics, Refractometry, Gas sensing, Silicon Nitride, Coupled Mode Theory, Sensor Analysis, Optical-Chemical Sensors.

Abstract :

Over the past two decades, integrated photonics have become a domain of intense research for the development of high-performance embedded sensors. Integrated chemical sensor structures, and especially those dedicated to gas monitoring, are inexorably being under acute investigation for healthcare concerns as well as industrial applications. A major issue arising from the large variety of sensor architectures that have been developed to date is : how to accurately analyze these sensing systems and compare them?

Firstly, this PhD dissertation proposes a classification framework for optical-chemical sensors, followed by a review of integrated optical gas sensing architectures. Secondly, this thesis details the models, designs and experimental work that have been carried out in the realization of integrated refractometric sensors. In particular, a specific type of refractometric structure is shown to stand out from the presented analytical framework, and was subsequently subject to more in-depth development more in-depth: the Long Period Waveguide Grating (LPWG).

A comprehensive model of LPWG mode coupling mechanisms is subsequently detailed, based on Coupled-Mode-Theory, for which a perturbation approach was used to analyze the sensing properties of these structures. By using the proposed model, several versions of the structure were then designed, simulated and optimized to present adequate spectral shape and sensitivities by using field superposition enhancement and chromatic dispersion tailoring techniques, before being eventually fabricated in the laboratory's clean-room facility using a silicon nitride photonic integrated circuit technology that was also developed in this PhD thesis.

The fabricated LPWG structures were next tested on a dedicated photonic characterization optical probe station, demonstrating exceptionally high refractometric sensitivities reaching a stable value of 11,500 nm/RIU over a wide spectral range of at least 100 nm, with a temperature cross-talk as low as 0.15 nm/°C. Additionally, based on the proposed model, a novel LPWG design is numerically developed to demonstrate the possibility of implementing LPWGs with sensitivities higher than 300,000 nm/RIU, by also taking into account and discussing the manufacturing and experimental limits of the proposed structures. Ultimately, a fabricated LPWG was employed for CO_2 gas sensing by using a polyhexamethylene biguanide porous polymer coating, thereby illustrating a practical application of the LPWG.

While the huge potential of LPWGs for sensing applications is revealed in the proposed models and reported results, we further believe that the work detailed in this PhD thesis could also be utilized for the realization of even more powerful sensors, and possibly unlock new sensing applications.

Résumé :

Depuis plus d'une vingtaine d'année, la photonique intégrée est devenu un domaine de recherche très actif pour le développement de capteurs intégrés à hautes performances. Les capteurs chimiques intégrés, et en particulier ceux dédiés à la détection de gaz, font inexorablement l'objet d'une investigation poussée pour des raisons de santé publique ainsi que pour un grand nombre d'applications industrielles. Un problème majeur lié à la grande diversité des systèmes de capteurs proposés par la communauté scientifique survient toutefois: comment analyser les différentes architectures de façon précise et ainsi pouvoir les comparer?

Dans un premier temps, cette thèse propose un modèle de classification pour les capteurs chimiques optiques, suivi d'une revue des architectures de photonique intégrée dédiées à la détection de gaz. Ensuite sont détaillés les modèles théoriques, la conception et le travail expérimental qui ont été effectués dans cette thèse pour la réalisation de capteurs réfractométriques intégrés sur silicium. En particulier, un type spécifique de structure réfractométrique semble être mis en avant par ce travail d'analyse de l'état de l'art, et a par conséquent été développé de façon plus approfondi; il s'agit des réseaux intégrés à longue période.

Un modèle détaillé du mécanisme de couplage optique mis en jeux par les réseaux à longue période est par la suite développé. Ce modèle est basé sur la théorie des modes couplés pour laquelle une approche perturbatoire est employée pour analyser les propriétés réfractométriques de ces structures. En utilisant le modèle proposé, plusieurs versions de réseaux à longue période intégrés sont conçus, simulés, puis optimisés. C'est en contrôlant les superpositions de champs optiques au niveau des guides d'ondes ainsi que les propriétés dispersives des modes optiques qu'il est possible d'obtenir de hautes sensibilités de détection ainsi que des réponses spectrales adéquates.

Ces réseaux intégrés à longue période ont ensuite été fabriqués à partir d'un procédé technologique de nitrure de silicium spécialement développé dans la salle blanche du LAAS. Puis ils ont été testés sur une station de charactérisation optique conçue dans cette thèse. Des sensibilités réfractométriques aussi hautes que 11,500 nm/RIU ont été expérimentalement obtenues et sont stables sur une large bande spectrale de 100 nm centrée sur 1550 nm, le tout avec une faible diaphonie en température de 0.15 nm/°C. De plus, en s'appuyant sur le modèle proposé, d'autres versions de réseaux à longue période intégrés démontrent via simulation la possibilité d'atteindre des sensibilités d'au moins 300,000 nm/RIU, sensiblités pour lesquelles les limites liées à la fabrications et à l'expérimentation sont abordées. Finalement, une structure de réseaux intégrés à longue période est employée pour la détection de CO2 en utilisant un film en polymère poreux: le PolyHexaMethylene Biguanide.

En plus du très fort potentiel des réseaux intégrés à longue période qui a été démontré dans cette thèse avec les modèles proposés et à travers les résultats obtenus, nous pensons également que le travail détaillé ici pourrait également servir à la réalisation de capteurs encore plus performants, et potentiellement permettre l'émergence de nouvelles applications.

Acknowledgments :

Un des quatre grands objectifs de ma vie. Dés l'âge de neuf ans, je m'imaginais déjà devenir un inventeur, un chercheur, un créateur, en regardant le dessin animé du petit génie « Dexter » ou en lisant les aventures de « Géo Trouvetout ». Pour m'avoir permis de réaliser ce rêve d'enfant pendant ces quelques dernières années qui sont allées si vite, j'aimerais remercier tous ceux qui ont construit la passerelle entre moi et mon doctorat.

Je tiens premièrement à exprimer ma plus profonde gratitude aux deux fabuleux personnages qui ont dirigé mes recherches: Olivier BERNAL, professeur à l'ENSEEIHT, pour son appui, sa sagesse et pour avoir réussi à canaliser mon esprit débordant, ainsi que Han Cheng SEAT, professeur à l'ENSEEIHT, aux compétences techniques aussi considérables que son humanité. Merci d'avoir laissé autant que possible ma créativité s'exprimer, et surtout bravo pour avoir réussi à me supporter aussi longtemps.

Je tiens également à exprimer toute ma reconnaissance à Franck CARCENAC du LAAS-CNRS, tant pour son dévouement professionnel que pour les profondes discussions que nous avons pu avoir. J'espère pouvoir vivre une carrière aussi exemplaire et pleine de vie pour avoir autant de belles histoires à raconter.

Je tiens également à remercier Frederic SURRE professeur à la James Watt School of Engineering of Glasgow, pour m'avoir poussé à aller toujours plus loin et à comprendre l'intérêt d'une rigueur exemplaire pour un résultat complet.

Je remercie les membres du jury pour leurs critiques constructives et leurs encouragements qui m'ont beaucoup touché, et particulièrement les deux rapporteurs qui m'ont fait l'honneur de lire mon manuscrit, fruit de trois années de travaux : Joël CHARRIER et Nicolas LE THOMAS. J'espère sincèrement pouvoir les recroiser et profiter plus amplement de telles sources de connaissance.

Je remercie l'ENSEEIHT et l'INP Toulouse pour m'avoir procuré un cadre de choix pour travailler sur le plus beau sujet de thèse que j'aurais pu espérer, ainsi que pour m'avoir permis d'obtenir une première expérience d'enseignement hautement enrichissante que j'ai grandement appréciée.

Je remercie également le LAAS-CNRS de m'avoir ouvert ses portes et permis d'évoluer dans un milieu scientifique de première catégorie, et particulièrement l'équipe TEAM pour avoir si bien supporté le développement technologique pendant mon doctorat ainsi que ma formation; Aurélie LECESTRE, Franck CARCENAC, Pierre-François CALMON, Laurent MAZENQ, Jean-Baptiste DOUCET, Pascal DUBREUIL ainsi que chacun des autres membres de l'équipe avec qui j'ai eu la

chance de pouvoir échanger. Je remercie aussi le réseau RENATECH pour avoir mis à ma disposition les ressources en salle blanche nécessaires à mon doctorat pour la partie de nanofabrication.

Je remercie grandement tous mes collègues de l'équipe OASIS du LAAS pour leurs supports techniques et logistiques qui ont largement facilité mes recherches; Francis JAYAT, Clément TRONCHE, Emmanuelle TRONCHE, Françoise LIZION, Hélène TAP ainsi que tout le reste de l'équipe qui a pu d'une manière ou d'une autre rendre ces dernières années encore plus appréciables.

Je souhaite également remercier toutes les personnes extérieures au domaine universitaire, qui m'ont, à leur façon, apporté leur support.

Merci premièrement à mes parents qui depuis aussi longtemps que je me souvienne, m'ont toujours poussé à aller plus loin et n'ont jamais cessés de croire en moi. Je remercie particulièrement la meilleure maman du monde pour le soutien indéfectible dont elle a pu faire preuve, ainsi que pour les magnifiques illustrations qu'elle a pu produire à ma demande pour améliorer mon manuscrit.

Merci à mes attardés de frères pour avoir permis tant que possible la décompression par les jeux vidéos pendant ces nombreux week-ends. Je ne veux pas oublier non plus tous mes amis, qui font tous aujourd'hui partie intégrante de ma vie ; Jason, Yoann, Théo, Gilles, Léna, Olivier, Julien, Marine, Luc, Rémi, ainsi que les deux Matthieux !

Et bien sur, j'aimerais remercier la meilleure copine du monde, ma petite Sara, qui a su me supporter (dans les deux sens du terme), pendant ces dernières quatre merveilleuses années. Merci de rendre ma vie encore plus parfaite.

Enfin, à toutes et à tous ceux que j'aurais eu le malheur d'oublier;

Merci à vous.

Disclaimer :

I hereby declare that this dissertation is my own original work and has not been submitted as such before to any institution. I also acknowledge all sources used and have cited these in the reference section, including my own work that have been previously published in scientific journals. Any unreferenced illustrations are the results of personal creation or commissions from relatives and are consequently self-owned.

Contents

List of Figures

List of Tables

Glossary

BBS BroadBand lightSource , page 47

BG Bragg Grating , page 65

CLMT Coupled Local-Mode Theory , page 81

CMT Coupled Mode Theory , page 71

EBL Electron Beam Lithography , page 42

EFR Evanescent Field Ratio , page 53

EI Effective index , page 34

EM Electro-Magnetic , page 9

EME EigenMode Expansion , page 79

EW Evanescent Wave , page 53

FBMS Field Beam Moving Stage , page 31

FDE Finite Difference Eigenmode (solver) , page 34

FDTD Finite-Difference Time-Domain (solver) , page 35

FOM Figure Of Merit , page 55

FSR Free Spectral Range , page 55

FWHM Full-Width (at) Half-Maximum , page 55

GI Group index , page 56

HSQ Hydrogen Silesquioxane , page 98

IR Infrared , page 8

LPCVD Low-Pressure Chemical Vapor Deposition , page 41

LPFG Long Period Fiber Grating , page 79

LPG Long Period Grating , page 66

LPWG Long Period Waveguide Grating , page 69

MRR Micro-Ring Resonator , page 59

MZI Mach-Zehnder Interferometer , page 56

NIR Near Infrared , page 19

OM Optical Microscope , page 46

OPD Optical Path Difference , page 56

OSA Optical Spectrum Analyzer , page 47

PECVD Plasma-Enhanced Chemical Vapor Deposition , page 41

PhC Photonic Crystal , page 66

PHMB PolyHexaMethylene Biguanide , page 119

PIC Photonic Integrated Circuit , page 17

PMTP Phase-Matching Turning Point, page 89

RI Refractive index , page 9

RIE Reactive Ion Etching , page 41

RIU Refractive Index Unit , page 27

SAN Styrene Acrylo-Nitrile , page 96

SD Standard Deviation , page 107

SEM Scanning Electron Microscope , page 44

SiN Silicon Nitride , page 32

SiO_2 Silicon Oxide , page 34

SOI Silicon On Insulator , page 32

SPR Surface Plasmon Resonance , page 28

TEC Thermo-Electric Cooler, page 48

VOC Volatile Organic Compound , page 85

Introduction

Motivation

By the year 2025, marketing research estimates that over a trillion sensors will be deployed through more than 100 billion devices connected within the internet of things [18], potentially doubling the sensor market for environmental monitoring. New technologies in device connectivity and artificial intelligence are driving an industrial revolution for the sensor economy that is already effectively transforming our societies in every major domain: manufacturing, transportation, healthcare, etc. Currently, over 2 billion people possess a smartphone; it is thus easy to imagine the future implementation of integrated sensing systems that can empower multi-purpose environmental monitoring. A growing need for embedded sensors with high performance that can be easily deployed can thus be envisioned.

Integrated sensors, usually compatible with CMOS process platforms, appear as the most promising candidate for cost-effective miniaturized sensors that can be mass-produced. Further, their high degree of design flexibility can potentially enable a multitude of complex architectures to be implemented within a single integrated system for multi-parameter sensing. Such systems are highly suitable for environmental monitoring requiring dense sensor network(s).

Atmospheric pollution directly affects both climate change as well as population health and is emerging as a major global concern [19]. Providing suitable sensors for *in situ* gas detection and monitoring is thus a major challenge. Integrated gas sensors could typically fulfill this role by assessing both indoor and outdoor air quality, thereby allowing relevant data to be collected for environmental analysis and mitigation. Integrated sensors could also facilitate gas monitoring in the industry, for which a distributed sensor network is often used or a requisite, for example for manufacturing process control and gas distribution.

Although historically based on electronic sensing schemes [20], integrated chemical and gas sensors are rapidly migrating towards optical schemes [21] due to the recent technological developments in integrated photonics (e.g. integrated light sources, photoreceptors [22], optical signal processing circuits, etc). The immunity of integrated photonic devices to electromagnetic and radiofrequency interferences [23] as well as their intrinsic high sensitivity potential also make them very attractive for *in situ* measurements and monitoring in harsh environments [24]. Further, being potentially able to incorporate the wide range of operating principles available in optical systems and their associated analytical methods, integrated optical chemical sensors can be designed with the highest degree of originality for current and future environmental sensing needs. This PhD, through an initial study of

the current state of the art in integrated photonic gas sensors, aims to design, develop and fabricate a novel integrated photonic architecture to achieve high sensing performances. For this purpose, an integrated version of the widely used optical fiber-based Long Period Grating sensor has been studied, realized and applied to refractometry and CO_2 sensing. The potential of this architecture is theoretically analyzed and experimentally demonstrated, achieving high sensitivities while also offering intrinsic features such as low temperature crosstalk. The experimental results obtained with these Long Period Waveguide Gratings are detailed and found to exhibit performances comparable to the current state of the art.

Dissertation Outline

This dissertation consists in: a review of the integrated optical gas sensor systems and methods, introductory chapters on integrated photonic design and experiments with a particular focus on Long Period Waveguide Grating refractometers followed by their application targeting gas sensing for CO_2, and a conclusion. Current outputs from this thesis include a conference paper (I2MTC 2020) [25] focused on the modeling of LPWGs as well as two peer-reviewed articles (IEEE Journal of Lightwave Technology and OSA Photonics Research) [14, 26] offering design guidelines completed by experimental results from the fabricated LPWG versions. A third paper is currently being submitted for consideration to a peer-reviewed journal.

Chapter 1 provides a thorough analysis of optical chemical sensors. A classification system is firstly proposed, not only for comparison of diverse sensor types but also to determine the most significant key parameters to consider during sensor design. The state of the art in integrated optical gas sensors is reviewed using this classification. From this analysis, measuring the refractive index (RI) change of a sensing film or layer functionalized to a specific gas species appears to be one of the most promising approaches for gas sensing using photonic integrated circuits (PICs).

The emphasis in **Chapter 2** is on PIC design, fabrication and characterization. This chapter proposes a set of design guidelines that has been adopted in this work. The key parameters involved in PIC design are described through the simulation and design package, followed by the detailed photonic chip fabrication processes that have been developed in this thesis. An optical characterization testbench is subsequently presented and the experimental results obtained from fundamental circuit components such as grating couplers and waveguides are discussed.

After the PIC overview, integrated refractometers are discussed in **Chapter 3**, with particular focus on the sensitivity and figures of merits. This chapter also compares refractometers exploiting different sensing mechanisms and concludes with a summary of the state of the art in integrated refractometry. In addition, experimental results obtained with fundamental refractometric structures such as Mach-Zehnder interferometers or micro-ring resonators that have been designed and

fabricated in this thesis, are also provided.

Chapter 4 attempts to provide the reader with a sound understanding of the long period grating by laying out the fundamental theoretical background in Coupled-Mode Theory. In particular, optical gratings and their operating principles are discussed through the development of grating equations derived from first principles, i.e. from Maxwell's equations for electromagnetic wave propagation in dielectric media. Based on the proposed model, the simulation of the response from a Long Period Grating is compared to results from a commercial software. The subsequent results obtained are discussed and demonstrate the proposed model to be consistent. They also allow a much greater insight on the LPWG's operating principles to be provided and analyzed. Analytical solutions for the refractometric figures of merit are then derived from the model and highlight multiple potential optimization patterns that are described.

Chapter 5 describes the three versions of LPWGs that have been developed in this thesis. The different structures are laid out, each following a specific optimization pattern or technique. The models and fabrication processes are then detailed, followed by the analysis and comparison of both simulated and experimental refractometric results. Temperature cross-sensitivity is also assessed. A discussion on the manufacturing and experimental limits of the proposed structures is also included in this chapter.

Finally, **Chapter 6** presents the experimental setup and the subsequent results obtained for an application in CO_2 gas sensing by exploiting polyhexamethylene biguanide as the sensitive permeable cladding layer for the LPWG sensor. Preliminary results based on the first LPWG topology demonstrate the potential of the structure to achieve an equivalent sensitivity of 6.8 fm/ppm.

Chapter 1

Integrated Optical Gas Sensors

Contents

As evidenced by the broad range of optical chemical sensor systems reported in multiple reviews over the past years [22, 27, 28, 29, 30], it seems almost impossible to define a comprehensive optical chemical sensor system analysis model that encompasses all the optical chemical sensing schemes while taking into account the wide ranging system configurations in the various sensor architectures. The main goal here is to identify the specific characteristics of existing sensor systems and to classify them based on a common set of system definitions. This chapter will thus attempt to first break down the overall optical chemical sensor systems into their individual components for analysis, in order to develop a **functional generalized model**, as schematically described in figure 1.1. This analysis is undertaken as a short essay that attempts to include the points of view of the previously published review papers, for which certain optical chemical sensors could not be deconstructed and analyzed according to the proposed former models.

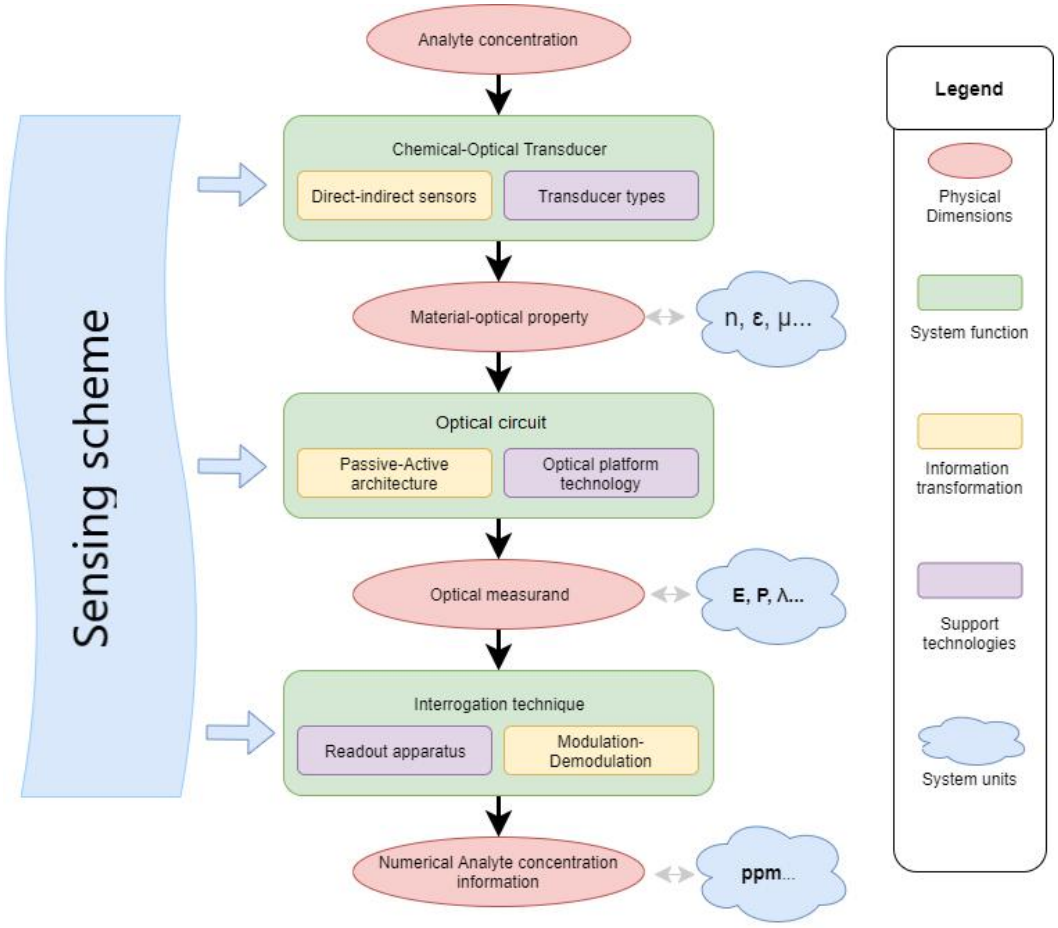

Figure 1.1: Review structure

Optical chemical sensors can be functionally defined as follows: the system perturbation first begins by a change of the chemical analyte's concentration in the sensor's surroundings, that next induces a modification of a material-optical property of the **Chemical-Optical transducer**. The latter component is simultaneously interacting with a light-wave from which optical properties are then subsequently perturbed. The **Optical circuit** comprises the different passive components and functions that enable transport and/or physical demodulation of the perturbed light-wave into a readable optical measurand. The optical measurement, in turn, can eventually be performed through various **interrogation techniques** to process the measured signal and retrieve the desired information on the analyte's concentration.

The general **physical sensing schemes** are first described in Section 1 with a brief introduction to absorption and luminescence spectroscopy, and refractometry. The optical-chemical sensing functional model is then detailed in Section 2 where each system components is described along two axes: **information physical**

transformation and **support technology**. Section 3 includes a brief introduction on integrated photonics, waveguide theory as well as on the general photonic integrated circuits technology. Section 4 will conclude this chapter by describing the state of the art of sensing systems of a particular category: integrated photonic gas sensors analyzed through Section 2's system analysis perspective.

1.1 Chemical-Optical Sensing Schemes

1.1.1 Absorption Spectroscopy

Optical absorption-based sensing techniques rely principally on **spectroscopic** mechanisms. Each chemical species possesses a particular spectral absorption signature based on its intrinsic vibrational modes [31]. Their presence can thus be studied through the spectral measurement of a light beam interacting with the analyte, which may exhibit unique absorption features that are easily readable at infrared (IR) wavelengths.

The determination of the analyte's concentration in most sensing architectures is generally inferred using Beer-Lambert law which relates the attenuation of the probing beam intensity transiting a specific medium to the degree of optical-chemical interaction at signature wavelengths. The simplest versions of absorption spectroscopic devices are known as nondispersive infrared sensors [32] and are typically used as gas detectors. In addition to direct IR absorption which is commonly used in chemical analysis, UV absorption [33] or Raman Scattering [34] are alternative techniques that can be used to detect gaseous traces.

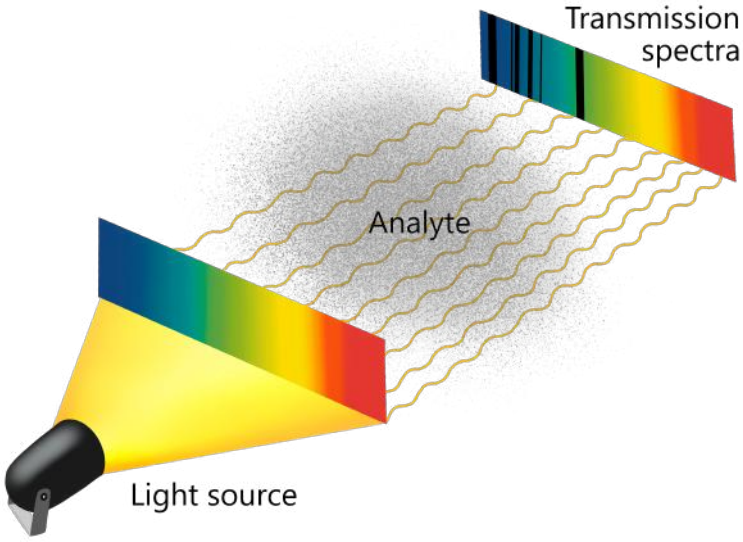

Figure 1.2: Illustration of spectrometric absorption chemical sensing

1.1.2 Luminescence spectroscopy

Luminescence spectroscopy is based on the probing and analysis of the photo-emission of a particular chemical species. **Fluorescence**, a type of photo-luminescence, is defined as the emission of light induced by photo-excitation of electrons of an atom or a molecule, resulting in spontaneous radiation emission. It is caused by the specific relaxation nature of a chemical species which has been previously excited: rather than releasing absorbed energy non-radiatively such as by heat dissipation, photons are instead emitted at characteristic wavelengths.

Sensor architectures based on luminescence schemes typically address the detection of biochemicals, nano-particles and gaseous molecules by using labelled indicators, for which chemical affinities and spectroscopic properties have largely been documented [35, 36]. However, these sensors might also encounter difficulty in labeling particular species due to the lack of chemical dye indicators. Various sensing architectures have been designed to probe different luminescent mechanisms, exploiting fluorescence properties [37] such as intensity, decay time, phase or even anisotropy of the emitted light to convert the presence of an analyte into a measurable property of the light.

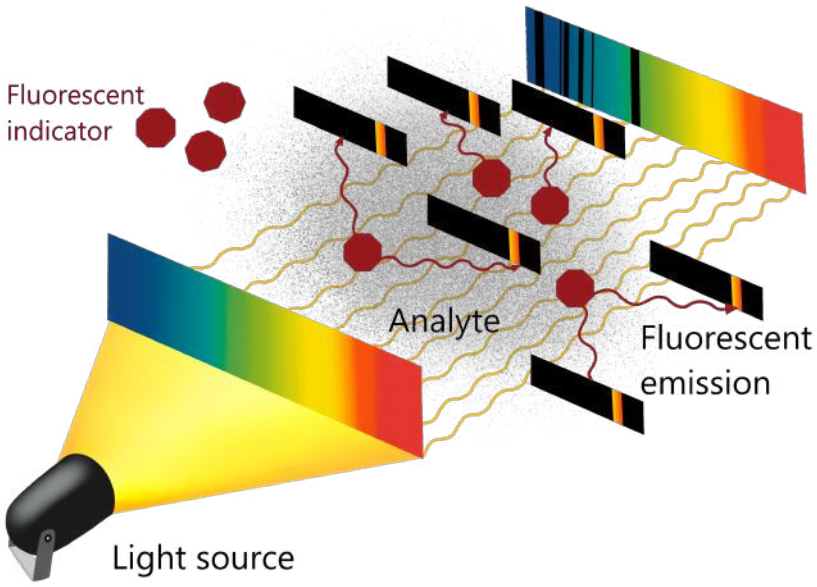

Figure 1.3: Illustration of fluorescence-based spectrometric chemical sensing

1.1.3 Refractometry

The **refractive index (RI)** of a material is defined as the ratio between the phase velocity of an electromagnetic (EM) wave in vacuum to that in a given material medium. This parameter is equal to $\sqrt{\varepsilon_r \mu_r}$ where ε_r and μ_r are respectively the relative permittivity and relative permeability of the medium. RI is a material prop-

erty that is employed in multiple sensing schemes, including temperature, strain, displacement and chemical sensing [38, 39, 40].

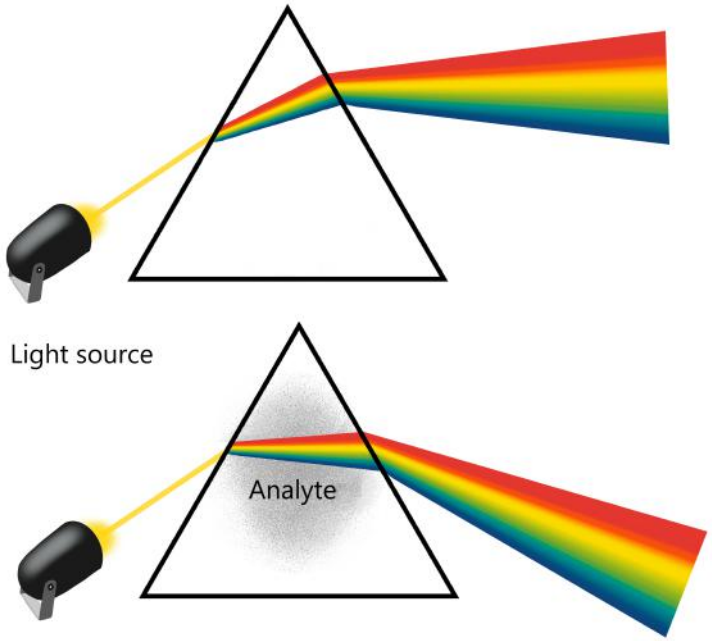

Figure 1.4: Illustration of refractometric chemical sensing principle

Modifications of the RI in a material induce phase delay variations in the electromagnetic wave, which can greatly alter the wave's spatial distribution in regions of anisotropic RI profiles. Moreover, RI is related to multiple properties (birefringence, spectral dispersion, Kerr coefficient, etc) that can produce very particular effects on light to be exploited for sensing purposes.

Measuring RI properties however requires a specific set of optical structures to allow the desired information to be properly converted into a measurable optical property such as light intensity. Many high precision systems have been developed, exploiting refractometry. The large variety of optical functions that can be implemented in optical circuits and the numerous possibilities in wavelength-scaled RI structurization of materials have led refractometers to have the widest design diversity among optical sensors. Nevertheless, since the RI of materials is broadly related to their chemical composition as well as their density, most refractometric chemical sensors are poorly selective and display important cross sensitivity to other chemical species. To counterbalance this, such sensors require the engineering of specific optical chemical transducers, as will be detailed in the next section.

1.2 Functional Analysis of the Optical Chemical Sensor System

1.2.1 Chemical-Optical Transducer

The chemical-optical transducer [22] is the physical component that enables the conversion of the concentration of a chemical analyte into a change in the **material's optical property** of the transducer. The studied material optical properties are intensive (i.e. physical property of an object that is independent of its size), such as dielectric properties, absorption coefficients, emissivity, etc. This sub-section describes the characteristics of these transducers that are typically engineered to achieve both high chemical affinity and selectivity of the transducer material to the analyte, and important optical interaction via the transducer's structure. Quantitative comparison between transducer designs is nonetheless further complicated by the multiplicity of physico-chemical affinities that are permitted for each individual analyte species.

1.2.1.1 Transducer Chemistry: Direct and Indirect sensors

Chemical sensors can be divided into two categories: direct and reagent-mediated sensors. In the first category, the sensors that rely on the measurement of the analyte's intrinsic material optical property when available, are referred to as direct sensors [22]. As shown in figure (1.1), a chemical transducer material is thus not always necessary (but might be used for efficiency or selectivity enhancement) and the conversion of the analyte's chemical concentration into a measurable optical property is ensured by the nature of the analyte uniquely. The perfect example of such sensors is the direct absorption spectroscopic sensor for which absorbance of a chemical-specific optical ray, typically in the IR region, is non-null and used to determine the analyte's concentration.

When the intrinsic optical properties of the analyte are not readily available for direct and selective detection of certain chemical species on a given sensing platform, the target analyte can subsequently be investigated through the use of an **intermediate reagent** species whose optical properties can be measured more easily. Such architectures are known as indirect reagent-mediated sensors [22], where the analyte concentration is determined through the analysis of the intermediate chemical indicator whose material optical properties depend on the level of contact with the analyte [36, 30, 28]. Certain chemico-luminescent dyes are commonly used for chemical sensing as their reaction with the analyte can lead to electromagnetic wave (EMW) emission or absorption under certain conditions. For instance, fluorescence-based gas sensors are generally based on pH modification of the material (e.g. due to oxygenation), which drives the fluorescent intensity of an indicator, such as Bromocresol purple [41] or NileRed [42] dyes. Similarly, in certain absorption-based sensors, several chemicals whose absorbance varies with the analyte's presence can serve as indicators [22]. In those cases, the analyte concentration

is indirectly inferred from the label chemical response.

Note however that the sensing architecture of direct sensors can also be chemically functionalized in order to ensure selectivity or increase sensitivity to a specific analyte. Hence, in RI measurement techniques which can potentially also be sensitive to other present species, specific chemical compound(s) can be used to induce chemically reversible bonding of a surface or volume with the analyte species of interest [43, 36]. This can thus reduce or eliminate cross sensitivity to unwanted species while increasing the analyte's concentration in the sensed region.

1.2.1.2 Transducer Material: Chemical Interaction Enhancement

The chemical-optical interaction is a mechanism that should always be optimized to achieve maximum sensitivity during the design of a chemical sensor. The transducer is the sensor's principal element that physically binds the analyte's presence to the optical system.

Chemical bonding with a chemical species can be engineered with either surface treatment or by functionalizing a liquid- or solid-state material [22]. In the case of gas sensing, in either direct or indirect sensing schemes, optical interaction with the analyte can be enhanced by using solid porous media, or surface coating within which **chemical binders** could be incorporated. This particular material is referred as an **immobilization matrix** [22, 28, 36]. This material is generally deposited as a thin film onto the surface of the sensor, thus forming together with the incorporated molecular selective compounds, the functionalized opto-chemical transducer. Opto-chemical sensitivity, selectivity, reversibility, response time and stability are the most important properties to be taken into account to design the most efficient sensitized layer.

1.2.2 Optical System

For the large majority of optical chemical sensors, the optical system consists of an optical source, an optical circuit and a photoreceptor. The optical circuit can be described by the system that converts the transducer's optical material property into a readable optical measurand. This includes both light transportation and possibly an optical modulation system that shapes the perturbed optical signal to be measured.

1.2.2.1 Passive-Active Optical Circuits

Optical sensors can generally be classified into two types. On one hand, passive [22] (or extrinsic [28]) optical sensors are defined as sensing systems whose optical circuit's sole purpose is to transport the optical signal as well as serve as the contact mean with the analyte. In these cases, the sensor performance does not depend strongly on the complexity of the optical circuitry, but instead on the associated optical technology quality (light source, photodetector, propagation loss...), the chemical-optical transducer, and the analyte's level of interaction with the optical

wave. For instance, the simplest absorption-based spectroscopic fiber sensors are used in passive configurations as the fiber's optical properties are not perturbed by the presence of the analyte.

On the other hand, in active [22] (or intrinsic [28]) optical sensors, the optical circuit itself plays a major role in the sensing process where optical structures are introduced to shape the perturbed light-wave into measurable components. It is thus an integral part of the sensing element. The aim here is to actively exploit certain characteristics of the optical measurand to enable information transfer from the transducer to the photo-receptor. Active sensors do not directly measure the analyte's presence in the transducer region but instead measure the response of an optical circuit whose sensing region (the optical chemical transducer) is perturbed. Optical mechanisms such as interference, diffraction, resonance leading to dynamic optical filtering and shaping are typically used in optical systems for sensing purposes. Certain sensors have also been reported to superpose several optical functions to enhance sensitivity. An obvious example is the Vernier sensor which superpose interference patterns to increase performance [44].

1.2.2.2 Optical Platform

For an optical sensor, the employed platform is of utmost importance. It is firstly determined by the nature or character of the sensing application such as commercial usage, cost, size, ease of integration and fabrication, performance expectations, etc. Nevertheless, the physical sensing scheme often influences the choice or design of the optical platform to be exploited.

Three platforms are utilized for developing optical chemical sensors, namely: **free-space optics, fiber optics and integrated optics**. Free-space optics [45] are based on the optical propagation of light in air or in vacuum, and generally requires the use of optical components such as lenses, mirrors, optical modulators (filters, polarizers), etc. Such systems are generally oriented towards *ex situ* measurements because of the typically cumbersome setup, dimension and susceptibility to misalignment. They generally offer relatively high sensitivity for chemical detection because the optical beam can interact fully with the analyte. Fiber and integrated optic techniques, on the other hand, are waveguide-based domains that require engineered media for lightwave propagation. Fiber optics rely on transmission of light via glass or plastic fibers while integrated optics rely on optical transit via waveguiding structures that are imprinted on solid substrates, usually using lithographic techniques. Propagation in a dielectric waveguide can enable a continuously guided lightwave to interact locally with the external environment in the vicinity of the waveguide's surface [29], contrary to free-space optics. Sensors based on this phenomenon are widely known as **evanescent wave sensors** and rely on perturbations to the modal characteristics of the propagating lightwave when the external surrounding of the waveguide is modified. While relatively complex to design and fabricate, there are several unmatched advantages in the use of guided wave optical sensing systems. Guided-wave optics offer packaging advantages that

enable *in situ* measurements while guaranteeing intrinsic resistance to mechanical and thermal perturbations. The implementation of original optical systems can also be facilitated by wavelength-scale structuring of the guiding media. In these cases, interference, diffraction and coupling patterns are much easier to control since they depend on the strict guide-specific propagation parameters. This implies that the optical effect on the resulting optical signals has an intrinsically higher stability and reproductibility.

1.2.3 Interrogation Techniques

The interrogation technique in an optical chemical sensor can be defined by the procedure that is performed to transform raw data obtained from the measurement apparatus into information on an analyte's concentration. The measurement apparatus can also typically be characterized by the parameters employed in the **opto-electronic conversion system** and the different devices that can be used to facilitate or reference these measurements. The information transduction process encompasses the **analog** signal modulation and demodulation that can be introduced to enhance detection, followed by the analysis and **logical** processing method that are necessary to decipher the measured data and subsequently display the desired information in the readout.

1.2.3.1 Measurement Apparatus

The desired chemical information can be retrieved from a photonic signal by studying a full range of optical properties, namely intensity, wavelength, polarization state, temporal components and their subsequent relationships. While these optical dimensions are initially dependent on the properties of the injected light source, they are encoded by the modulations that occur during interaction in the optical circuit and transformed into electrically-readable information. **Photoreceptors, spectrometers or imaging systems** are essential for that matter as they allow the conversion of the optical signal into an electrical signal that can be used for further processing and/or computation. The emission/detection bandwidth, dynamic range, resolution, coherence, and stability, in addition to various other parameters of opto-electronic devices have to be carefully chosen to optimize the performance of these chemical detectors.

Optical interrogation can also permit **multiplexing** several optical signals along the same optical path(s) or sensing structure with relatively little (cross) interference. This implies that the readout apparatus can further be designed to incorporate optical structures that can later be used for signal processing using different techniques. For example, reference structures and channels, which do not interact with the chemical analyte, can be used as a reference baseline at a later stage (for post-processing data analysis) to eliminate unwanted external influences to the measurement system [28] (e.g. common noises such as optical power variation, vibration or temperature variations). Similarly, correlation spectroscopy [32] involves one or

multiple reference gas cells that contain gases of known spectroscopic signatures, to be compared to the measured response.

1.2.3.2 Signal Modulation and Processing

Signal modulation of some of the optical input properties may be introduced to increase the performance of certain optical chemical sensors. Such examples include frequency domain modulation techniques such as 2f/1f wavelength modulation spectroscopy [46, 32] which aims to reduce measurement noise. Frequency modulation can also be essential in certain sensing schemes such as photo acoustic spectroscopy [47, 32] of gaseous species. These techniques might require specific electronic devices such as lock-in amplifiers or different types of electrical filters.

Non-linear optical modulations, which generally require high optical intensities, have also been used to detect chemical species. Different resonator configurations used in Kerr-comb based gas spectroscopy [48] have been demonstrated.

Data Processing addresses the computational operations to be performed on the raw numerical data, generally after analog-to-digital conversion, to obtain the desired information on the analyte (e.g. concentration, volume, presence, etc) at the output of the optical chemical sensor. It typically comprises a combination of mathematical operations and algorithms.

While data processing can be narrowed down to a simple one-data reading and proportional amplitude conversion into concentration information, most processing techniques typically require more complex processes to analyze the sensor response. An example is the data analysis of wavelength-resolved architectures where spectral pattern shifts are tracked to assess the system perturbation, as will be describe in detail in Chapter 3. More complex processing schemes include Vernier-based optical chemical sensors [44], or time-based measurement schemes such as fluorescence lifetime decay which can be exploited for chemical sensing [37]. Additionally, it is very common to de-embed the measured signal from contributions and irregularities that are induced by certain optical circuit components, such as connectors, etc. As an example, grating coupling and optical source irregularities are removed from a measured spectral signal in appendix A.11.

1.2.4 Comparison by Functional Blocks

Chemical sensing architectures are typically difficult to analyze and compare, especially when they are based on different sensing schemes or target different chemical species. This is also due, in large part, to the specific chemical behavior of various analytes. In fact, various figures of merit for each functional component in the sensor have been proposed in the literature but are yet specific to the chemical sensing schemes employed. For example, on the one hand, some refractometric chemical sensing schemes are largely described by the efficiency of the transducer to change its RI due to the presence of analytes, in terms of RIU/ppm (refractive index unit change per parts per million of analyte), while, on the other hand, the

optical architecture performances are assessed on the basis of wavelength-spectrum shifts for varying RIs in units of nm/RIU. This perspective will be further detailed in Chapter 3.

Alternatively, absorption-based chemical sensors, which are generally much more chemical-specific, can be analyzed via their chemical absorption coefficients, optical architecture's interaction efficiency with the sensed environment, and noise-reduction efficiency of the interrogation technique employed.

To facilitate comparison, a classification of the global sensor systems proposed in this thesis has been developed to evaluate each sensor's constituent functional blocks in order to determine the advantages and limits of each system. To optimize a chemical-sensing system, each functional block should be separately studied. In this thesis, a chemical-optical transducer for gas sensing based on refractometry as well as the optical architectures that can be supported by integrated photonics will be more thoroughly developed.

1.3 What Is Integrated Photonics?

1.3.1 History of Integrated Photonics

1.3.1.1 Invention of the Laser and the Optical Fiber

In 1960, Theodore Maiman realized the world's first laser after successfully creating a light amplifier system producing a perfectly rectilinear ray [49]. This invention subsequently led to the rapid growth of optical sensors in free-space as they offer significant advantages [50, 45] over their conventional electrical counterparts: immunity to electromagnetic interference, high sensitivity and selectivity together with a large variety of mechanisms that can be exploited. Shortly afterward, between 1970 and 1972, the single-mode optical fiber was invented and while it was initially developed for telecommunications, it rapidly made inroad into the sensing domain. Thanks to the intrinsic characteristics of fibers, such as small size and weight, large bandwidth, remote sensing capability, etc, typical free-space optics issues for *in situ* measurement [45] such as vibrations, misalignment, atmospheric absorption of light, could now be addressed with fiber-based optical devices. While the most basic optical sensors had their beginnings five centuries ago [50], this field of metrology has seen the most intense progress only over the last 3 decades with the advent of the ubiquitous laser source and low loss optical fiber.

1.3.1.2 Integrated Optics..

Micro-technologies became available in the 1970s with the development of micro-electronics on semiconductors, which would later revolutionize our world. This was quickly followed by the first realization of integrated waveguides [51]. Over the 1970s, the most prominent tutorials on integrated guided wave optics were published by E.A. Marcatili, D. Marcuse [52], A. W. Snyder and J. D. Love [12], focusing on waveguide propagation theory and predicting the micro-structurization

impact on optical systems. Systems based on integrated dielectric waveguides were demonstrated as a possibly better solution for optical circuitry than the equivalent fiber platform, due to their compact integration, reduced stress, mass-fabrication potential, vibration and temperature resilience. Furthermore, integrated optical circuits can facilitate the integration of electronic control and processing devices [51] on the same platform. For example, these functions have been directly connected to electrical circuits on a monolithic wafer, via micro-heaters.

1.3.1.3 ..to Integrated Photonics

It was only toward the end of the 1990s that integrated optics started to follow in the footsteps of integrated electronics that has been exerting an enormous impact on our society. Integrated optics rapidly expanded during the revolution of the telecommunications industry driven by the global outreach of the internet exploiting fiber-based communication systems which necessitate on-chip optical mux/demux [53]. Integrated optics research leading up to this period had been focused on microstructuring waveguides with wavelength and sub-wavelength features as a powerful tool to empower original waveguide designs to achieve higher performances and to target various application domains [50]. Subsequently, photonic crystals (1987) [54], diffraction gratings [55], cavity resonators, interferometers and frequency combs (2007) [56] were quickly developed on the integrated platform to perform optical signal processing such as optical filtering or modulation. This field has since mainly focused on hybridization with other micro-technology domains to produce integrated opto-mechanical or opto-electronic systems.

In the last two decades, following the expansion of the telecommunications sector, fabrication platforms have evolved with sufficient sophistication to allow a higher level of integration of optical devices and functions into micro-chips, giving birth to Photonic Integrated Circuits (PICs). To cope with the loss in the copper wire that increases with data rate and interconnect lengths, optical communication was rapidly developed on a large-scale, typically employing PICs in data centers for processing purposes. To date, the continuous growth in this research domain closely reflects the exponential expansion of the information market.

1.3.2 Optical Waveguide Theory in Integrated Optics

Waveguiding concept first appeared in the 1890s to study sound waves and was only developed for electromagnetic (EM) waves, particularly for microwave propagation within dielectric materials in the 1920s-1930s. From the 1960s, several mode propagation theories were formulated: calculation methods were firstly proposed in early 1960 to model mode profiles at optical wavelengths in planar waveguides (Marcatili...). Secondly, the optical perturbation behavior of both optical fibers (Snyder, 1972 [57]) and waveguides (Snyder and Love, 1984 [12]) have been developed based on a coupled-mode theory model, enabling various optical applications to emerge.

An **optical** mode is a solution to Maxwell's equations applied to a dielectric waveguide. This corresponds to the possibility for waveguides to propagate EM waves under specific conditions imposed by the waveguide's refractive structure. In a waveguide, modal propagation of a wave can be described by the infinite sum of continuous interferences of a wave with itself when it is partially reflected by the sidewall interfaces as it propagates along the waveguide, thereby resulting in a set of waves with a specific field distribution and propagation properties. These shapes are intrinsic to the waveguide nature (size, pattern, material, etc) and may be exploited in the design of bespoke sensing schemes.

1.3.3 Photonic Integrated Circuits

1.3.3.1 Functions versatility

The high degree of waveguide design flexibility in integrated photonics initially originated from the concept of "waveguide wiring" architectures, producing interferometers and resonators with the aid of Y-junctions (Y-branch splitters) or waveguide loops [51]. Integrated photonics is strongly influenced by the development of fabrication technologies for the micro-electronics sector. Moore's law, which was used to predict the scaling and miniaturization pace of functions in micro-electronics, can also be applied to describe either the progression of PIC function integration but also component fabrication resolution [53, 58]. The subsequent evolution in related photonics fabrication has facilitated sub-wavelength engineering of waveguides which, in turn, led to the development of numerous techniques for tailoring the optical properties of the propagating mode(s), such as spectral bandwidth and linewidth, polarization state, mode field, etc. This inherently contributed to elevate integrated photonics as the preferred platform for the design of novel photonic components but also for the integration of complex optical systems.

1.3.3.2 Drawbacks: Monolithic Integration and Propagation Loss

The diversification of optical architectures due to the large number of potential applications has led to a variety of different integrated photonics fabrication processes. Photonic circuit development principally encounters difficulties in terms of the compatibility of materials used in the fabrication of the various necessary functions/components (such as emission, light propagation and photodetection [59, 53]) to be integrated on the same PIC. For instance, for applications in the infrared region, [51] silica-based technologies are particularly suited to signal multiplexing-demultiplexing and monolithic integration with electronic functions; while ion exchange on glass is more suitable to fabricate power-splitters, lithium niobate material to electro-optical modulation functions, and semiconductors to photo-emission/reception.

Current PICs are also suffering a serious issue: their optical performances are scaled back by the limits in fabrication technology, thus giving rise to devices with relatively high loss coefficients in the dB/cm order. Yet, particular technologies have

reached propagation losses in the dB/m order [60]. PICs are typically operated in NIR to ensure compatibility with the telecommunication wavelengths at 1550 nm and 1310 nm for which the optical fiber has a minimum loss of approximately 0.25 dB/km and 0.4 dB/km, respectively. The high losses in integrated waveguides typically limit optical propagation to a few centimeters and can mainly be attributed to the material's intrinsic absorption properties in the near infrared (NIR) (e.g. from N-H bonds in the case of silicon nitride substrate) and scattering of light induced by the roughness at the waveguide sidewalls either due to the lithography or etching processes used [23].

Integrated photonics is increasingly exploited in an expanding list of applications with high economic and societal impacts [51]. And given the rapidity at which the different related technologies are being developed, the loss barrier is expected to be progressively lifted [60], potentially enabling optics and photonics to be the dominant trend in the future integrated sensor market.

1.4 Integrated Photonics for Gas Sensing

Gas sensors have recently benefited from the rise of the Internet of Things, coupled to the expansion in the nanotechnology market and the constant development of lab-on-chip integration tools. Applications [61] in air quality monitoring, portable or wearable health monitoring, disease diagnosing, industrial chemical detection and pharmaceutical production, food testing, animal and plant breeding, hazard monitoring or even fire warning, which have previously been overlooked due to technology unavailability, are rapidly revolutionizing the industrial world in terms of both economic and societal impacts. The market growth in gas sensors is forecast to reach 6.25 % per year [1], with optical systems currently making up only $\sim$ 15 % of the total share. With the ongoing development in the domain, there is thus potential for optical gas sensors to capture a more significant share of the global market. Nevertheless, the integrated chemical sensor market currently remains oriented toward micro-electrical sensing schemes based on conductivity [20], due in large part to the difficulty in integrating both the photonic light source and photodetector because of material incompatibility.

1.4.1 Gas Optical Transducer

As previously explained, certain optical chemical sensing schemes require a chemo-optical transducer. In the case of gas sensing, the transducer medium is generally chosen for its gas-permeability and chemical affinity to the gaseous analyte(s) under investigation as well as for its optical properties and ability to be deposited using different techniques [62].

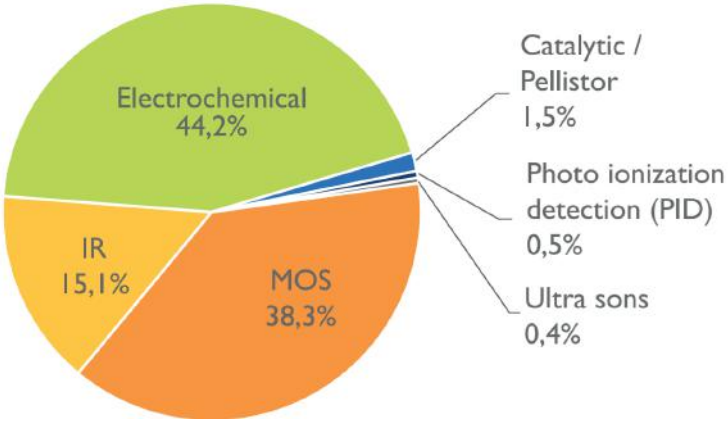

Figure 1.5: 2017 Market share in gas sensing technologies [1]

1.4.1.1 Overview

The most widely reported means for fabricating these gas permeable layers for optical sensors is through the use of nano-composite materials [36]. The most common materials that have been incorporated into integrated photonic sensing structures include porous metal-oxides [63, 64] or semiconductors such as porous silicon [65], and polymers [36] in the form of thin films [66, 67]. Other uncommon materials that have been reported in integrated photonic gas sensing include silane-based surfaces [68] or graphene-based porous materials [69]. However, as described by Korotcenkov [36], the surface-to-volume ratio is a key parameter for reagent-based gas sensing. Surface materials typically have insufficient surface-to-volume ratio, thereby greatly reducing the chemo-optical transducing capacity for gas sensing. Other multiple gas sensing schemes based on the swelling (volume change) of polymer materials in the presence of gases have also been reported [62]. The chemical engineering of both the structural and mechanical properties of porous polymers for gas sensing is further described in Chapter 6.

While some materials present natural affinities to specific gaseous analytes, certain gases however require the presence of intermediate chemicals to facilitate or enable chemical selectivity. In this case, porous polymers possess the advantage of being able to immobilize certain chemical indicators or selectors into a porous solid matrix with relative ease, while additionally increasing the contact surface with gas significantly to enhance indicator-gas reactions. These indicators comprise either dyes [70, 71, 36] that react in contact with the analyte, supramolecular compounds called cavitands [43] that can encapsulate specific chemical species such as gaseous methane [72], or nano-particles [73, 64] which exhibit bonding affinities to a particular gaseous species.

1.4.1.2 Mechanical and Chemical Characteristics in a Porous Medium

This subsection attempts to summarize Korotcenkov's description of the importance of the transducer's material structure for gas sensing when a porous medium is utilized [74]. Typically, to assess gas concentration inside a porous material, the principal parameter is the material permeability to a specific gas [75, 36]. This parameter depends on both the fluid's diffusion property and chemical solubility as follows:

$$P_{erm} = D \cdot S \tag{1.1}$$

where P_{erm}, D and S are respectively the permeability, diffusion coefficient and solubility. Here, S can be defined as the linear empirical relationship between the concentration of a particular gaseous species in a medium and its partial pressure. This parameter is expressed by Henry's law:

$$C_{max} = k_H \cdot P_{partial} \qquad \text{with } k_H = S \tag{1.2}$$

where C_{max} is the maximum permissible gas concentration (assuming steady-state), $P_{partial}$ is the partial pressure of the gas that is applied outside of the solvent, and k_H is Henry's constant or solubility coefficient S. As solubility usually makes reference to liquid mixtures, this formula can also be applied in the case of solid porous medias, for which solubility coefficients are usually different from those of their liquid counterparts [36]. A porous medium's solubility to a particular species can be enhanced by using chemical dopants, [43, 36, 76]. The diffusion parameter determines the gas concentration dynamics. The porousness of the porous matrix, which relates more to the material micro-structure rather than its chemical properties, can usually be evaluated by studying the material pore diameters and the effective surface area per volume of the material [77]. These parameters can be modified through micro-structure and chemical engineering to increase the sensitivity, selectivity and reactivity of the chemo-optical transducer [77].

1.4.1.3 Integrated Gas Optical Transducers in the Literature

Table 1.4.1.3 summarizes the different kinds of chemo-optical transducers that have been employed in integrated optical gas sensors.

The following sections discuss the different integrated optical gas sensing systems for the three main sensing schemes based on, namely, absorption, fluorescence and refractometry. It is, however, unrealistic to fairly compare the different sensor architectures since the overall limits of detection of the reported sensors mainly depend on the chemical nature of the analyte and the performance of the measurement apparatus. A non-exhaustive list of published integrated gas sensors designs and experimental results is investigated according to the proposed classification model, to outline different figures of merit and optimization patterns corresponding to each sensing scheme. The limits of integrated photonics for the implementation of these sensors are then discussed as well to show the need for compatibility between the

Ref	Year	Sensed gas species	Gas absorbent material	Gas selector	Optical scheme
[63]	2017	CO	ZnO thin films		Refractometry (SPR)
[68]	2016	Propane	Silanisation with Methoxysilane		Refractometry (Interferometry)
[69]	2016	Ammonia, Methanol, Ethylene	Graphene oxide	-	Refractometry (SPR)
[78]	2018	NH_3 Cl_2 SO_2	Polyethylene terephthalate	Methyl-red or chlorophenol-red	Fluorometry
[73]	2019	CO_2	PDMS	ZIF-8 nanoparticles	Refractometry (Interferometry)
[67]	2009	VOCS	poly(3-alkylthiophenes)	-	Absorption
[79]	1999	VOCS, Toluene	Calix-4-resorcinarene polymer network		Refractometry (SPR)
[80]	2008	Xylene	PDMS	-	Refractometry (Interferometry)
[72]	2015	Methane	PDMS -SAN	Cryptophanes	Refractometry (Interferometry)
[66]	2020	CO_2	Polyethylenimine		Refractometry (SPR)
[70]	2013	VOCS	Polyvinylpyrrolidone (PVP)	Nilered	Refractometry
[71]	2012	Toluene	PDMS	Nilered	Fluorometry
[81]	2011	CO_2	Silicon Photonic Crystal		Absorption
[82]	2017	Toluene, Acetone	polyesteramid & Poly(2-vinyl pyridine)		Refractometry (MRR)
[64]	2007	CO , NO_2 , H	InxOyNz Metal Oxide	gold nanoclusters	Refractometry (SPR)
[83]	2014	DMPP, Acetone, NB	hyperbranched carbosilane polymer HCSFA2	HFIP groups	Absorption (MRR)

Table 1.1: Examples of published matrices and chemical selectors for gaseous species in integrated photonic sensors

integrated platform properties and the gas sensing scheme.

1.4.2 Absorption-based Integrated Gas Sensors

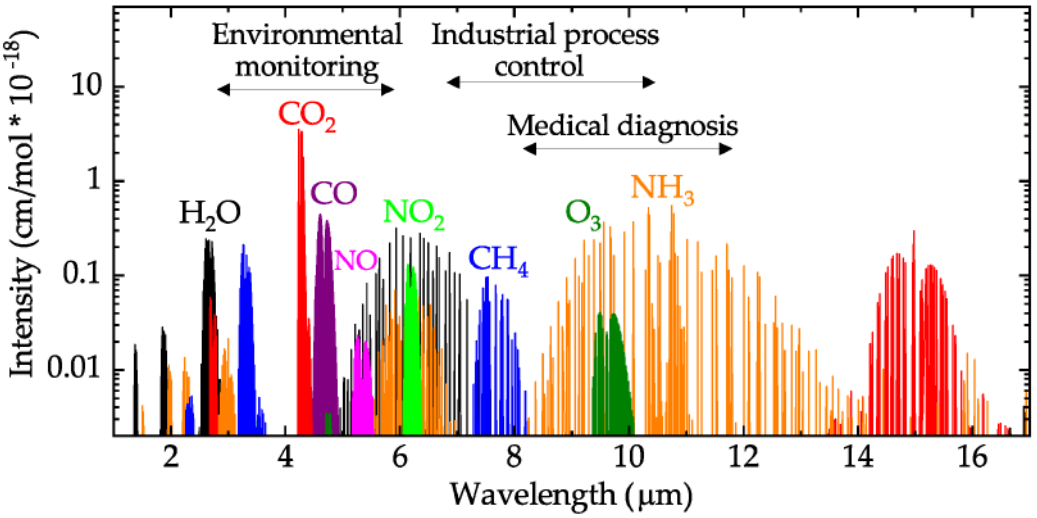

Figure 1.6: Infrared absorption spectra of various molecules from Hitran database [2, 3]

The most widely reported optical gas sensors are absorption-based devices due to their inherent simplicity. Most of them can provide information on the concentration of the analyte through interaction between the gas and the evanescent wave generated by a propagating optical mode within a specific region of a waveguide. As highlighted in the literature [84], the waveguide design is considered to be the key element for the realization of these sensors. An optimized or a "good" waveguide design generally aims at increasing the overlap of the optical propagative field and the sensed region through the optimization of two design parameters: (1) the evanescent field ratio (EFR) that denotes ratio of the evanescent field to the total power of the propagating mode, and (2) the optical path length over which the waveguide is exposed to the environment. They form the main figures of merit that are used to characterize the design potential.

Nonetheless, these sensors can encounter several technological barriers in practice. Because of their intrinsic absorption properties, most gas molecules absorb in the mid-infrared region (MIR) where the highest sensing performance is often achieved [3] as seen in figure 1.6. Gas sensors operating in this spectral region would therefore not benefit from telecommunication fabrication standards of components in NIR wavelengths (1310-1550 nm). The materials employed in integrated photonic platforms typically exhibit transparency features over a specific wavelength range as seen in [5, 59] thus strongly favoring specific optical platforms for the detection of certain gases. The high waveguide losses in integrated optics are po-

tentially also a major problem for the optimization of absorption-based sensors, as their performance proportionally depends on their optical path length. For this reason, absorption based gas-sensors require a high quality waveguides fabrication process. The propagative loss coefficient of fabricated waveguides is thus a key parameter for comparing those sensors architectures. While most research here is focused on waveguide design, other architectures have been proposed to enhance gas-optical interaction with multi-pass cells [85], resonators [83] or photonic crystals [86]. Photoacoustic gas spectroscopy has also been previously integrated on silicon for the detection of methane [87].

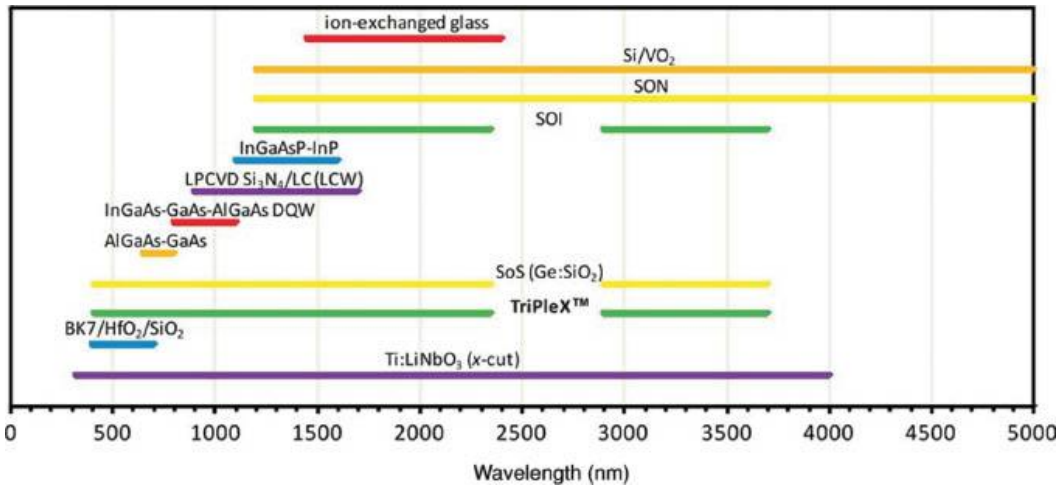

Figure 1.7: Overview of various waveguide materials employed in integrated optics and their corresponding transparency ranges [4, 5]

Table 1.4.2 summarizes the different integrated optical gas sensors and their associated performance parameters, which are EFR, optical length, and optical loss. Because the optical absorbance varies between analytes, it is observed that the limits of detection of different analytes are not entirely correlated to their figures of merit.

Ref	Year	Gas	LOD	EFR	Loss (dB/cm)	Length (mm)	Materials	λ (μm)	Optical scheme
[88]	2017	CH_4	-	47%	8.6-10.3	-	Si-SiO_2	3.39	slot wg
[84]	2017	CH_4	-	55%	2-3	-	Si-SiO_2	3.39	strip wg
[89]	2016	NH_3	5 ppm	43%	-	-	Si-SiN	3	slot wg
[90]	2017	CH_4 C_8H_{18}	-	-	-	-	-	-	plasmonic slot wg
[91]	2018	CO_2	0.5 %	19.5 %	-	10	Si-SiN	4.26	strip wg
[92]	2018	CO_2	10 %	3.3%	-	1	Si-SiN	4.27	strip wg and heater
[93]	2016	CH_4 NO	14.2-1.6 ppm	5%	2.5	17	Ge-Sb-Se	7.7	strip wg
[94]	2017	CH_4	100 ppm	25.4%	2	10	Si-SiO_2	1.65	strip wg
[95]	2019	CH_4	1%-330 ppm	12.5	8	5	Ge-Sb-Se	3.31	spiral strip wg
[96]	2020	-	-	-	-		SiN-SiO_2	2.7-3.4	strip wg
[85]	2017	CH_4 C_2H_6 C_3H_8	-	-	-	1.33	Si-SiO_2	3.2-3.4	tapered multi path cavity
[86]	2016	CO_2	20 ppm	-	-	-	Si-SiO_2	6.5	photonic crystal slab surface
[83]	2014	DMPP, Acetone, Nitrobenzene	0.002, 140, 1.5 ppm	-	6	2	SiN-SiO_2	1.423	MRR

Table 1.2: Examples of existing integrated absorption-based gas sensor parameters and their related performances

1.4.3 Fluorometric Integrated Gas Sensors

Integrated fluorescence gas sensors rely on the emission of light from a chemical indicator doped into the transducer that reacts in the presence of the gaseous species. The emitted optical intensity and/or spectral characteristics are then detected by a suitable photodetector and subsequently processed to obtain the desired information on the gas species under investigation, as illustrated in figure 1.8.

The adopted sensing scheme is generally conditioned by the chemical properties of the analyte and the available fluorescent indicators. Various gas-reagent indicators have been used for fluorescent excitation in integrated photonic schemes, as presented in Table 1.4.3. Fluorescence mainly occurs in the visible optical spectrum, thus implying the preference for silicon [97, 98, 71], organic materials [99, 42], or hybrid compositions [100] for possible integration with photo-emitters and photoreceptors able to operate in this spectral range. Typically, a porous polymer layer doped with the fluorescent dye is used as the sensing element to detect the gas species.

Fluorescent optical schemes are usually designed to maximize the optical excitation of the fluorescent dye or dopant in the porous matrix but also for optimal recovery and measurement of the emitted intensity. The optical architecture typically relies on three intrinsic fluorescence mechanisms:

1. the emitted fluorescence intensity is proportional, to a certain degree, to the optical excitation of the fluorescent dye. Several designs have been proposed to

concentrate the excitation beam onto the transducers for maximal excitation [97, 98];

2. fluorescent materials typically emit isotropically in all directions, which renders it difficult to efficiently collect the emitted fluorescence intensity. Existing solutions generally rely on circular waveguides [99] or planar photodiodes [100] to maximize photo-receptor contact with the chemical transducer and thus increase optical recovery;

3. it can be difficult to discriminate the diode-emitted intensity from the actual fluorescence intensity without a spectrometer. In this case, optical filtering can be used as an efficient solution to remove or isolate the source-emitted optical intensity before collection by the photoreceptor(s) [97].

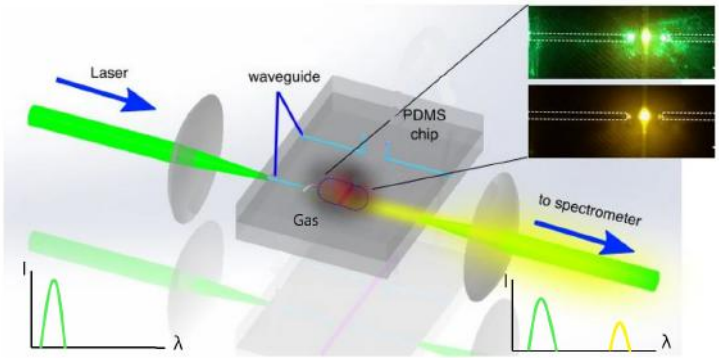

Figure 1.8: Illustration of an integrated fluorescence-based sensor for chemical sensing. Adapted from [6]

Fluorescence-based sensors are well suited for implementation in sensor arrays or networks [98] and simultaneous multi-analyte detection because of the inherent simplicity of the interrogation technique (intensity-based measurement in most cases) and the possibility to coat the sensor surface with different chemical indicator-based materials by micro-printing, for example. The similar excitation wavelengths for fluorescent dyes allow single-source optical systems to power arrays of different sensing elements, which is a major advantage for integrated planar systems.

Ref	Year	Gas	LOD	adsorber layer	Luminescence indicator	materials	λ (nm)	Optical scheme
[99]	2011	CO_2	0.5%	Polystyrene	2% Cou-marin 545T + 0.25% Macrolex Fluorescent Red	PET	460-600	circular wg
[97]	2007	O_2	0.4%	Polyurethane /PDMS	pinacyanol iodide	Silicon	590-626	polymer wg
[98]	2004	O_2	0.62%	PDMS	$Ru(dpp)_3Cl_2$	Su8 /Silicon	470	Ridge wg
[100]	2002	O_2	1%	-	ruthenium tris∼4,7-diphenyl–1, 10-phenanthroline chloride	ITO /Silicon	600	Layers coupling
[71]	2012	Toluene	-	PDMS	NileRed	Silicon	465	Silicon suspended wg
[42]	1993	Ammonia	∼ppb	PtOEPK /PS	Bromcresol Purple	B-270 glass		B-270 glass wg
[41]	2007	O_2	-	PDMS	platinum(II) octaethylporphyrin ketone	PtOEPK	590 /760	Micro patterns

Table 1.3: Examples of existing integrated fluorescence-based gas sensor parameters and performances

1.4.4 Refractometric Integrated Gas Sensors

Refractometric gas sensors are based on the measurement of the refractive index unit (RIU) change of a sensed region (e.g. top surface of a photonic chip via evanescent wave) induced by the presence or variation in concentration of a gas species [101, 76]. Gas species at atmospheric pressure and temperature have RI superior to vacuum that can be calculated by using the gas density and mean polarizability in Lorentz-Lorenz equation [102]. As a result, integrated refractometric system designs are not constrained by the use of a particular operating wavelength, and can therefore benefit from a wider range of fabrication technologies, photo-emitters and detectors [103].

The RI of a porous layer hosting different gas species can empirically be inferred from the Arago-Biot equation where:

$$n_{tot} = n_{pm} + \sum_i \frac{V_i}{V_{tot}} \cdot n_i \quad \text{with} \quad \sum_i V_i = V_{tot} \tag{1.3}$$

where n_{pm} is the RI of the porous medium without gases, V_i the volume filled by a gas i in the porous media, V_{tot} the total volume of the medium and n_i the RI of a pure gas at given pressure and concentrations [104]. Henry's law in equation (1.2) can be introduced to give:

$$n_{tot} = n_{pm} + \sum_i S_i \cdot \tilde{V}_i P_{partial,i} \cdot n_i \quad \text{with} \quad \sum_i P_{partial,i} = P_{tot} \tag{1.4}$$

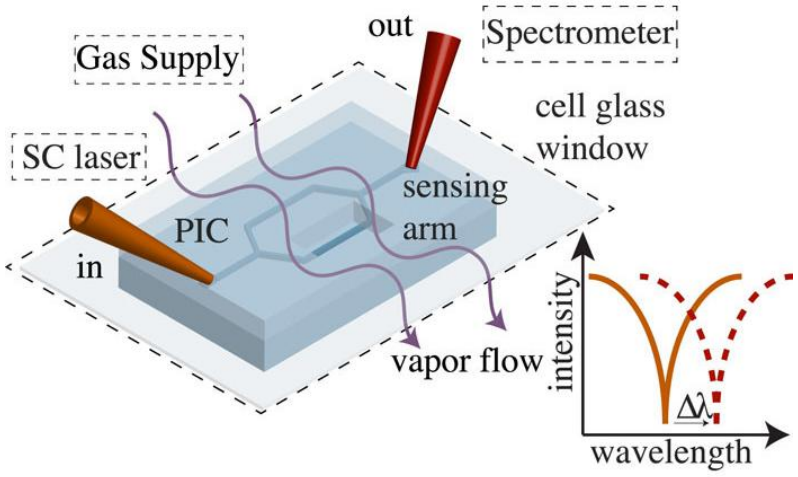

Figure 1.9: Illustration of an integrated refractometric sensor for chemical sensing based on Mach-Zehnder interferometer [7]

where $\tilde{V}_i$, S_i and $P_{partial,i}$ are respectively the gas species i's individual molar volume, solubility in the porous medium and partial pressure. Finally, Dalton's law of partial pressures can be introduced to show that the RI of a porous medium can be calculated as

$$n_{tot} = n_{pm} + \sum_i S_i \cdot \tilde{V}_i \cdot P_{tot} \cdot x_i \cdot n_i \quad \text{with} \quad \sum_i x_i = 1 \tag{1.5}$$

where x_i is the molar fraction of the gas mixture outside the medium. It can be inferred from equation (1.5) that the **refractometric sensitivity of a porous layer** depends not only on the difference in RIs of the gas constituents and their concentrations, but, more importantly, on the solubility difference of each species in the porous medium. The solubility profile therefore not only defines the gaseous sensitivity but also the selectivity of the transducer layer in refractometric sensing schemes. The transducer used in these schemes typically employs polymers [105, 106] that can be doped to enhance the sensitivity and more significantly reduce crosstalk to other gas species [72, 73].

Last, not not least, one of the most significant advantages of refractometric sensing in integrated photonics is the potential exploitation of light with **wavelength-scale structurization** [103] of waveguides. Numerous optical integrated architectures have been proposed to assess RI variations of a porous layer in the presence of an analyte, including those based on interferometers [72], resonators [105], surface plasmon resonance (SPR) [69], photonic crystals and diffraction gratings [106], which will be discussed in detail in Chapter 3. Table 1.4.4 references multiple integrated gas sensors based on refractometry that have been reported.

Ref	**Year**	**gaz**	**LOD ppm**	**Chemical transducer**	**Transducer coefficient**	**materials**	**λ (nm)**	**Optical scheme**	**Optical design sensitivity**
[105]	2016	CO_2	20	PHMB	6e-9 RIU/ppm	Silicon	1552	MRR	26000 πrad/RIU
[72]	2015	CH_4	17	SAN+ Cryptophane	2.67e-9 RIU/ppm	Si_3N_4	1550	MZI	3549 πrad/RIU
[73]	2019	CO_2	3130	PDMS+ ZIF-8	-	Silicon	660	bi-modal interf	-
[106]	2016	VOCS	-	Poly-siloxane	-	Silica on Silicon	1550	Bragg grating	449.63 nm/RIU
[69]	2016	Ethylene, Methanol, Ammonia	-	Graphene oxide	1.3e-6, 7e-6, 28e-6 RIU/ppm	Au	500-1000	SPR	-

Table 1.4: Examples of published integrated refractometric gas sensors parameters and performances

Chapter 2

Integrated Photonics Design, Fabrication and Characterization

Contents

Research in integrated photonics design has been expanding exponentially for the past decades. This is clearly demonstrated by the number of published articles which has been multiplied by nearly 50 folds over the last 25 years, as illustrated by figure (2.1). After the development of photonic building blocks such as straight and curved waveguides, micro-rings, gratings and Y-Junctions, to name a few, it has now become obvious that silicon micro-structuring could be used for designing numerous optical functions: coupling, filtering, multiplexing-demultiplexing, and modulation (e.g. geometry, RI profile), etc, resulting in a powerful tool for complex photonic applications and systems.

This chapter details the **photonic software and experimental methods** that have been employed in this thesis to design both the photonic circuits and the related components, fabricate and characterize the photonic chips, as well as perform analysis on the subsequent experimental results.

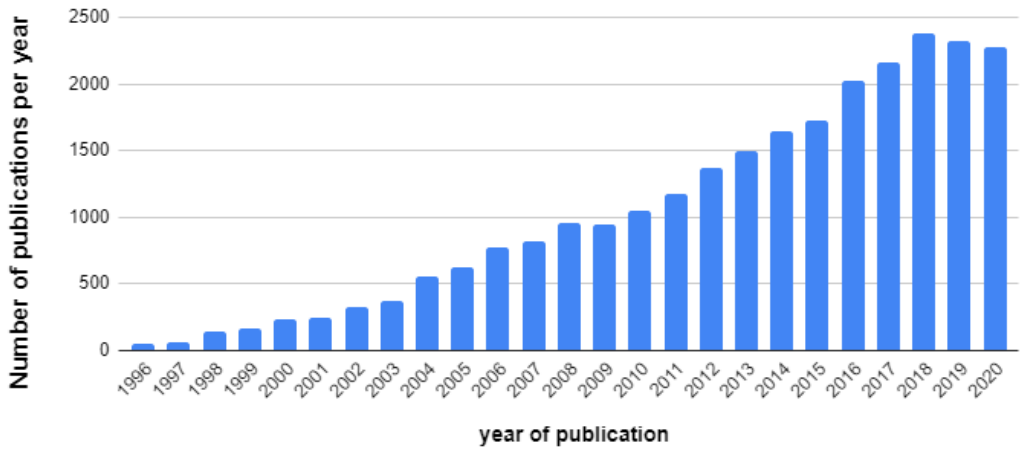

Figure 2.1: Number of 'hits' using a search of published articles on the database Web of Knowledge, with topic keywords "integrated photonics OR silicon photonics"

The first section reports the design guidelines and **computational resources** that have been used to realize photonic integrated structures and circuits. Fundamental photonic components such as waveguides and grating couplers are first designed and modeled for later applications in optical chip coupling and guidance since these fundamental functions can have a significant impact on the signal quality and, in the worst case, can hinder the targeted photonic response. Subsequently, the **fabrication process** is detailed with a discussion on the structural patterning concerns in integrated optics. In particular, a specific exposure procedure, denoted Field Beam Moving Stage (FBMS) Electron-beam lithography for waveguide fabrication is demonstrated to prevent stitching errors that usually occur during PIC patterning over large fields. Lastly, a customized probe station is developed and demonstrated to facilitate the **optical characterization** of the fabricated optical structures, paving the way for advanced photonic response tailoring [23, 107]. The grating couplers and waveguides designed in this work are then fully characterized in order to satisfy future needs in de-embedding photonic signals to extract only the optical response of the device under test.

The methodology developed for the photonic integrated circuits and/or structure development is summarized in figure 2.2.

2.1 Integrated Photonics Design and Simulation

As previously mentioned, fundamental photonic components to inject, couple and guide light are necessary to fully characterize any complex photonic devices via a dedicated testbench based on an optical probe station. After a preliminary discussion on the technical choices (technology material, process, etc) and the computational software tools employed for the design of integrated photonic structures,

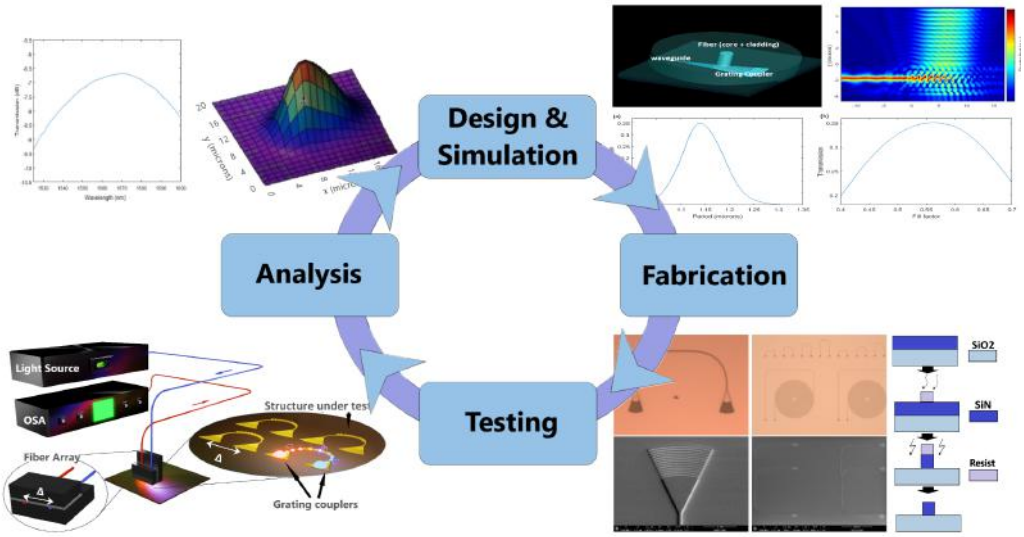

Figure 2.2: Development process for integrated photonic structures and applications

details on the optical characteristics of fundamental components such as grating couplers and waveguides, are discussed.

2.1.1 Guidelines for Photonic Chip Design

Various parameters should be taken into account when designing PICs. It is generally necessary to carefully account for the chip packaging options, experimental conditions, component requirements and application objectives. In fact, as discussed in Chapter 1, the platform material properties are fundamental for fabricating certain components to target specific applications. Additionally, a test plan should be carefully set in advance to define all the measurements that are required to not only completely characterize the photonic components but also the process. This may involve, as a result, the integration of supplementary photonics circuits.

2.1.1.1 Material Platform

In this thesis, **Silicon Nitride (SiN)** has been selected as the guiding material for the following reasons: (1) together with Silicon On Insulator (SOI) materials, they are transparent at standard telecommunications wavelengths (1260 - 1625 nm) [108], which enable possible integration with telecommunication systems; (2) the technology is CMOS compatible, thus potentially facilitating mass manufacturing of the photonic structures; (3) both the SiN-SiO2 medium-sized RI contrast and in-house fabrication processes provide high flexibility of design, especially for devices operating on RI micro-structurization; and (4) the technology is available in many foundries as well as in the LAAS cleanroom facility. SiN-based photonics is currently emerging as an alternative technology to the SOI platform [109], as it

offers interesting features that can be exploited for the development of new original architectures.

2.1.1.2 Optical Coupling

Several techniques can be employed for light coupling between a PIC chip and an optical fiber for optical characterization of structures. Butt or edge-coupling [110] is a widely used technique that relies on the alignment of a fiber tip to be in contact with the polished or cleaved side of a photonic chip bearing the cross-cut integrated waveguide. This technique is nevertheless complicated by the large difference between the fiber and integrated waveguide cross-sections and cleaving difficulty. As illustrated in figure 2.3, this difference can consequently lead to misalignment and optical leakage, which can however be partially corrected by employing waveguide tapers [111] or micro-lenses at either the PIC or fiber end to improve the coupling efficiency.

A chip-integrated grating coupler can also be employed to enable surface coupling. This can greatly facilitate photonic circuit characterization [23], but comes at the cost of a much degraded coupling efficiency, since grating couplers generally exhibit higher transmission losses (∼3-10dB) [112, 113]. Nevertheless, the impact of these losses on the photonic circuits can be partially neglected when using wavelength-resolved systems. **Bragg grating couplers** are thus employed in this thesis to enable ease of characterization of the implemented photonic structures.

2.1.2 Photonic Circuit Simulation and Design

The technological process, system packaging and the experimental specifications can strongly influence each phase of the PIC design. At the **component level**, the specific optical, material and thermal behaviors of a single structure are studied using photonic propagation modeling and optimization techniques. At the **circuit level**, light propagation is studied in terms of spectrally-distributed loss and phase delay that typically depend on the component properties. The optical contributions of the waveguides and structures to the injected signal are subsequently calculated, forming the PIC model principally constituted of operators and scattering matrices. Finally, at the **layout level**, the overall circuit pattern of the PIC must respect the fabrication and characterization requirements. These include structure locations and software format that must respectively fit into the probe station and comply to the characteristics of the lithographic equipment. Numerous tutorials for PIC designs have been proposed over the years to enable rapid introduction to the domain for novices [23].

2.1.2.1 Waveguides

The waveguide is the fundamental building block in all photonic circuits and is generally used for connecting or linking photonic components. The RI profile and dimensions of the waveguide thus have a very high impact on the circuit design as

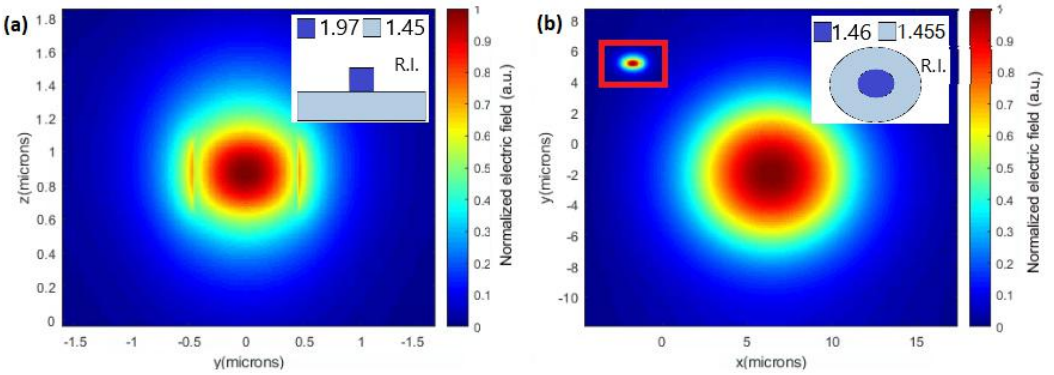

Figure 2.3: Electric field of fundamental modes of (a) 400 nm×800 nm SiN waveguide and (b) single mode fiber (SMF-28), with SiN waveguide mode for scale

they define the optical mode shape, propagation constants, minimum bending radius and evanescent field ratios, which are the most important properties to account for in guided-wave applications. However, for fabrication purposes, equal consideration should also be given in advance to other associated integrated photonic components sharing certain waveguide parameters (e.g. core thickness and width, material).

In this thesis, the optical mode calculations are principally performed with the Lumerical Inc. Software, using its *Finite Difference Eigenmode* (FDE) solver.

Here, the RIs for Silicon Nitride (SiN) n_{SiN} and Silicon Oxide (SiO_2) n_{SiO_2} are experimentally measured with an ellipsometer at $\sim$ 1.97 and $\sim$ 1.45, respectively, at 1550 nm. The waveguide cross-sectional dimensions are then set at 400 nm $\times$ 800 nm to ensure single mode propagation for cladding RIs ranging from 1 to 1.6 RIU, assuming that the cladding can be either air, SiO_2, polymers such as PDMS or SU8 with respective RIs of 1, 1.45, 1.4, and 1.58. Figure 2.3 compares the simulated electric fields and associated RI profiles of the waveguide's fundamental mode and that of a single-mode fiber (SMF-28) for 1550nm wavelength propagation. The effective index (EI) (i.e. principal propagation constant which is associated with the phase velocity of a given mode) of the waveguide's mode (figure 2.3(a)) designed with the aforementioned dimensions, is estimated to be $\sim$1.7 at 1550 nm.

Bend-induced waveguide losses that are due to coupling to radiation modes can also be estimated [114] by using the imaginary part of the calculated EIs in mode calculation models incorporating scattering boundaries that can account for waveguide curvature. Before the actual mode calculation process, the Lumerical mode solver typically adopts a conformal mapping of the RI profile [115] to simulate curvature. Figure 2.4(a) shows the simulated propagation losses due to coupling to radiation modes versus bend radius, indicating that a 50 µm bending radius is largely sufficient to limit radiation losses. Additionally, the modal mismatch between the curved and straight regions of a waveguide has been shown to possibly perturb propagation in PICs. Nevertheless, adiabatic transition can be achieved

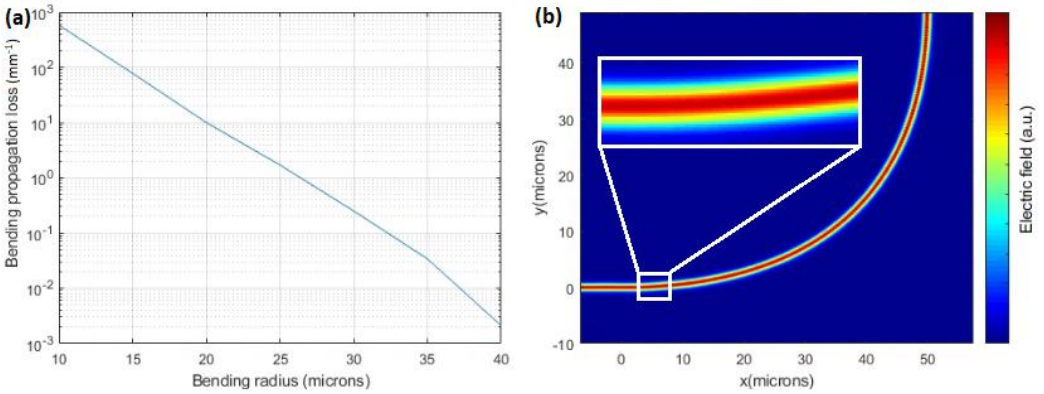

Figure 2.4: (a) Simulated propagation loss versus bend radius, simulated with FDE with conformal mapping, and (b) 2.5D FDTD simulation of Bezier-apodized waveguide curvature with 50 μm average bending radius

by using an elaborate curvature design. A widely used technique which is simple to introduce in photonic wiring circuit designs is to use curve apodization, for example, by using Bezier curves [116]. To model the behavior to curvature (or bending), the 2.5D Finite-Difference Time-Domain (FDTD) technique is a rigorous and effective method to study wave propagation. FDTD is a numerical modeling technique that is used for studying systems that rely on solving a set of time-dependent differential equations. In photonics, it is accepted as a powerful and rigorous method for simulating the propagation of electromagnetic (EM) waves through different types of wavelength-scale optical structures. The principal FDTD modeling methods are: 2D, 2.5D or 3D, which should be chosen according to the specifications of the optical structure studied. Here, 2.5D FDTD is based on a 2D model of the beam propagation in the waveguide which incorporates a global index profile in the third dimension. Figure 2.4(b) illustrates the optical field propagation in a bend region (top view) for a Bezier-apodized curved waveguide obtained using 2.5D FDTD simulation.

Note, however, that the actual propagation losses for typical optical modes in straight waveguides usually depend on the material's intrinsic optical absorption and on the rugosity of waveguide interfaces, both of which are fabrication-dependent parameters.

2.1.2.2 Grating Coupler

Modeling of grating couplers also requires important consideration at the structural level. The coupling efficiency and bandwidth of grating couplers are key parameters as they define the PIC's operating spectral range. The coupling mainly depends on the following properties: first, (1) the Bragg condition applied on a fiber-chip

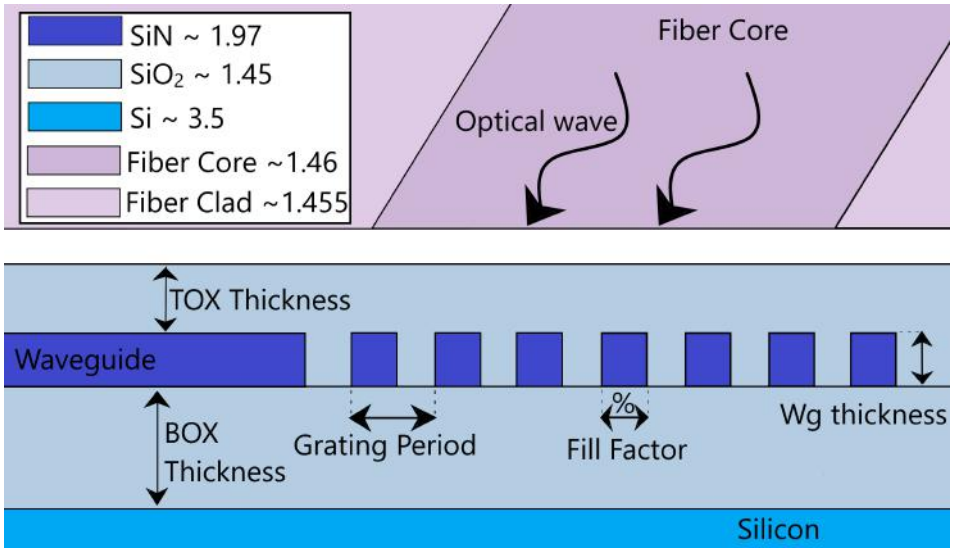

Figure 2.5: Illustration of the cross-section and key parameters of a full-etched binary grating coupler

coupling system [112, 113]:

$$n_{eff,grating} - n_c \sin(\theta) = \lambda/\Omega \tag{2.1}$$

where the EI of the grating can be determined by its RI profile and fill factor for guided propagation; then, (2) the grating's coupling strength, which typically depends on the RI contrast of the integrated waveguide materials, the fill factors and grating length superposition to the fiber core diameter interface, should be adjusted to optimize coupling; (3) destructive interference at the bottom oxide substrate should be obtained to prevent optical leakage into the substrate; and (4) constructive interference between the lead-in/lead-out fiber tip and the grating surface should be obtained as well. Fully etched grating couplers, which also benefit from the advantageous single-step lithographic fabrication process, are thus employed in this research to couple light in and out of the waveguides. Their performances can typically be analyzed in terms of (1) their maximum coupling efficiency, i.e. ratio of input to output light, and (2) their spectral bandwidth, that should be maximized to support broadband coupling.

To facilitate light coupling into the grating, standard SMFs with fiber tips polished to an 8° angle to the normal, also known as angled physical contact, are employed. The subsequent Bragg condition imposes a grating period of approximately 1 - 1.2 μm for coupling around 1550 nm. Hence, additional modeling work is used here to further refine the coupling behavior: 2D-FDTD simulation is applied on a grating coupler structure shown in figure 2.6, and a parametric analysis is performed to obtain an optimized pattern. Figure 2.7 illustrates the coupling efficiency of the grating coupler at 1550 nm for different values of grating parameters,

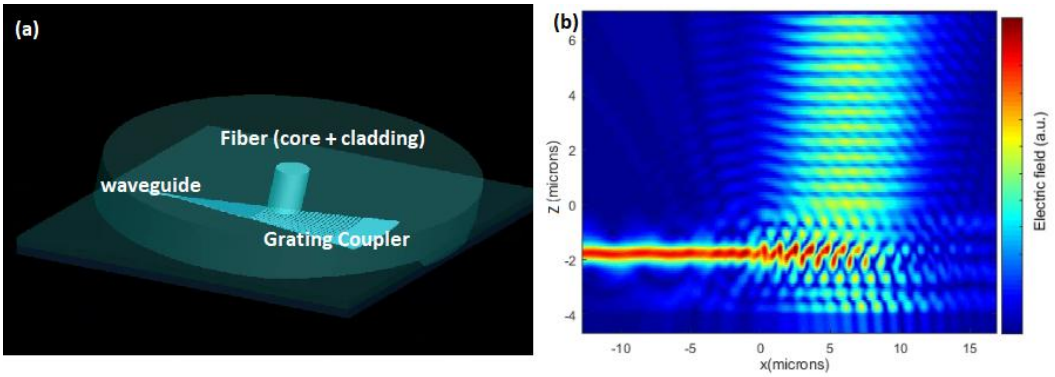

Figure 2.6: (a) Perspective of a grating coupler model, and (b) 2D FDTD simulated coupling profile at resonance

namely, grating period, fill factor, bottom oxide thickness and cladding thickness (for an SiO_2 cladding). These are obtained for a structure proposed in figure 2.5.

The grating period and duty cycle are subsequently adjusted to 1.14 µm and 0.55, respectively. Similarly, interference patterns are observed in figures 2.7 (c) and (d) for different thickness of bottom oxide and top cladding. Low insertion loss is obtained for constructive interferences at the cladding and destructive interference at the bottom oxide, for which thickness values are respectively set at 1.1 µm and 2.1 µm. The maximum simulated coupling efficiency and -3 dB transmission bandwidth are approximately 38% and 80 nm, respectively, for an excitation wavelength of 1550 nm . Additionally, near-symmetry of the scattering parameters has been achieved thus implying that the coupling transmission behavior is reciprocal.

2.1.3 Design Layout

The PIC layouts have been designed using the KLayout editor software, a free layout drawing tool for nano-techs that supports multiple scripting languages (Python, Ruby, etc) and provides the user with a very large and flexible panel of drawing functions. The photonic chip layouts have been produced using a combination of (1) personal scripts written in Ruby and Python, and (2) L. Chrotowski's open source photonic design libraries downloaded from github [23]. The layout process begins with the PIC floor plan which defines where each of the devices or optical functions of the chip will be located, as well as the placement of the primary input and output optical ports, i.e. grating couplers, to suit PIC packaging requirements. The masks for all the devices or optical functions are next drawn, according to the parameters from the simulated models. These devices are then connected via Bezier-apodized waveguides, whose maximum curvatures are verified. The final layout is subsequently compiled by using multiple dedicated programs in order to comply the lithographic machine requirements.

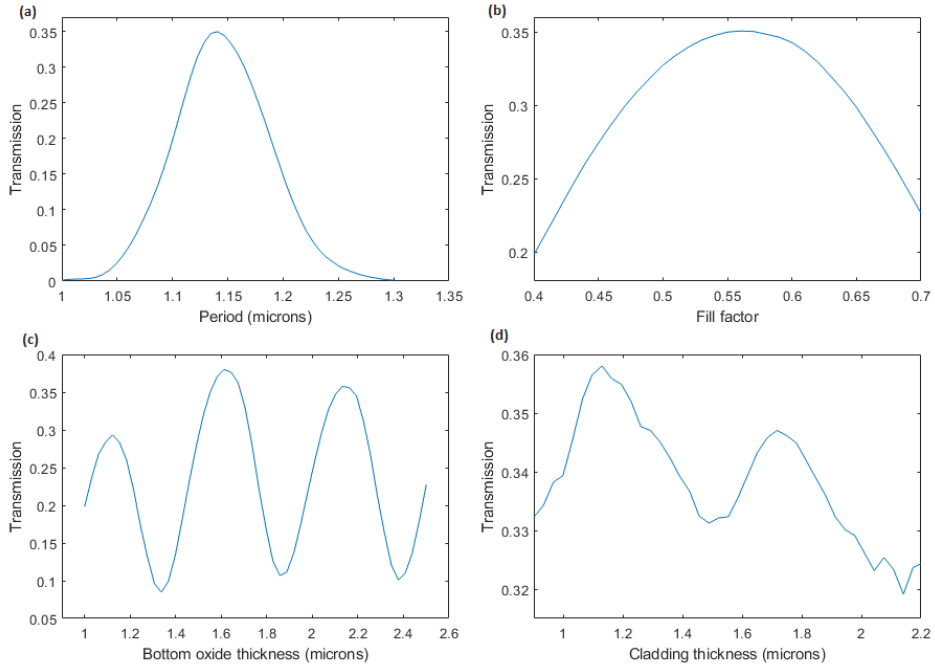

Figure 2.7: Grating coupler transmission characteristics for fiber-to-waveguide coupling at 1550 nm as a function of (a) grating period, (b) fill Factor, (c) bottom oxide thickness, and (d) cladding thickness.

2.1.3.1 Floor Plan for Optical Chip Coupling

In this work, a simplified optical probe station using fiber arrays has been developed to couple light into the optical chip through grating couplers (see figure 2.14 in Section 2.3). The fiber array (later shown in the experimental setup, figures 2.14 and 2.15) consists of a bundle of optical fiber ends arranged in one or two dimensional arrays simply by placing each fiber into v-grooves fabricated on a solid surface to ensure a periodic spacing (typically 127 µm or 255 µm). Such fiber arrays allow a relatively fast and easy positioning of the fiber cores with respect to the grating couplers on the PIC. This is carried out using active alignment which consists in measuring the quality of the transmission (typically through an alignment structure comprising a pair of input-output grating couplers) during the alignment process. This technique is comparatively more efficient than the lengthy process of separately positioning two fibers at the input and output grating couplers of the chip without any real feedback (i.e. only manual inspection via a camera).

2.1.3.2 Lithographic Requirements

The layout also needs to exactly fit the constraints imposed by the lithographic process. In particular, the resist properties (material type, photosensitivity, thermal and mechanical behaviors, etc) as well as the lithographic resolution and pattern-

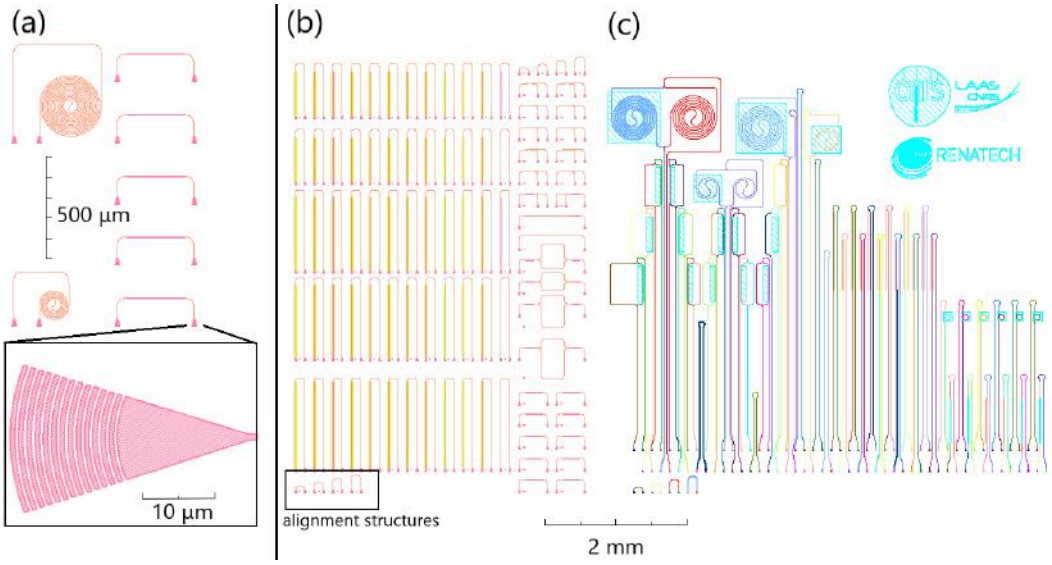

Figure 2.8: Layout pictures of (a) basic waveguides and grating couplers of fabricated photonic chips n° 1 - n° 2, (b) fabricated photonic chip n° 4 with alignment structures, and (c) fabricated photonic chip n° 6. Further details are given in appendix.

ing techniques should be taken into account to better predict their impact on the PIC performances. In this work, MaN2405 was used as a negative resist that is compatible with the RAITH electronic lithography equipment.

Here, the sub-type of the drawings must specifically correspond to the format supported by the Raith lithographic exposure modules. Each module specifies the exposure procedure and requires that the given geometries fit a specific format. As will be described in the following sections, normal and FBMS modes have been utilized in this thesis.

Figure 2.8 shows the related components of the designed layouts for PICs n° 1, n° 2, n° 4, and n° 6. Typical grating coupler pairs are also used as connectors for both the refractometric structure wiring and various structures that are introduced in the next chapters. The layout content is detailed in appendix A.1 for each fabricated chip n° 1 - n° 7.

2.2 Fabrication of Integrated Photonic Chips

2.2.1 Overview

Numerous processes have been utilized for the fabrication of photonic circuits. As previously mentioned, SiN-based technologies can significantly benefit from the techniques employed in CMOS process. In this section, the SiN process developed in this thesis is detailed. It has been conceived in close collaboration with LAAS'

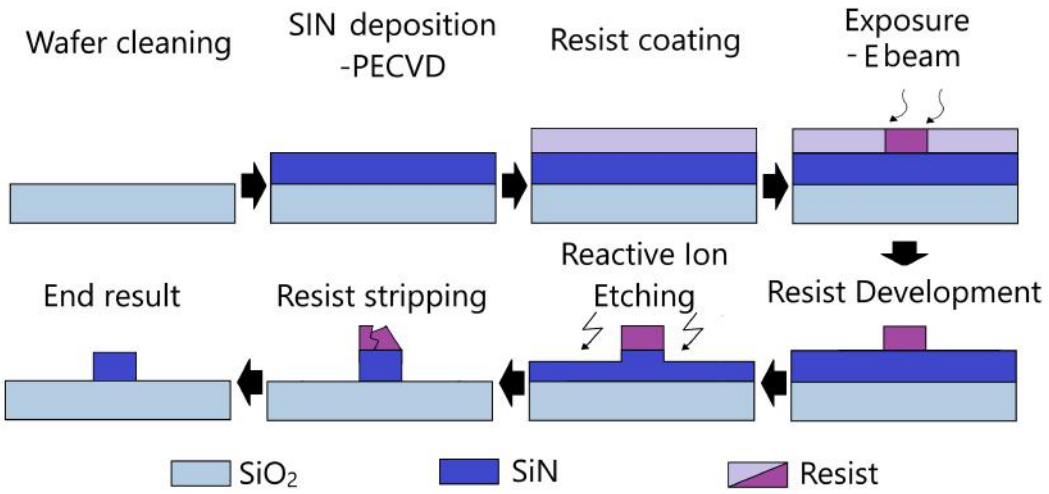

Figure 2.9: Illustration of typical electron-lithography process for integrated waveguide fabrication with negative resist

cleanroom engineering team to successfully fabricate operational PICs while taking into account the related equipment specifications. As illustrated in figure 2.9, the fabrication of waveguides and photonic devices is achieved through multiple successive steps of **(1) material deposition, (2) lithography, (3) material etching, and (4) cleaning**.

The most widely employed techniques for depositing solid materials are chemical vapor deposition (CVD), epitaxy and sputtering. The optical, mechanical and thermal properties of the deposited films usually depend on the technique utilized. Consequently, in order to inform the photonic models with the properties of the deposited films (e.g. RI) and parameters (e.g. thickness, non-uniformity, etc), it is necessary to accurately characterize the deposited films.

The patterning of photonic structures can typically be performed using different lithographic techniques which possess various exposure behaviors and resolutions. The achievable resolution mainly depends on the source wavelength and its distance from the surface to be exposed. These include step-and-repeat optical lithography systems (steppers) either at "standard" wavelengths (e.g. 436 nm ("g-line"), 405 nm ("h-line") and 365 nm ("i-line")) or deep ultraviolet lithography (e.g. 248 nm ("KrF") and 193 nm ("ArF")), or extreme ultraviolet lithography EUV (e.g. 13.5 nm) or, lastly, electron-beam lithography, for which the electron wavelength can be estimated at the picometer level. Finally, inscribing the patterns onto the previously deposited substrate is generally carried out by continuous chemical etching in a wet or plasma environment. Nanoimprint lithography technology that combines patterning and shape-transfer is also an alternative solution for high-resolution PIC fabrication [117] over large areas without stitching errors. NIL, however, requires a

mold to imprint patterns onto the resist by mechanical deformation but can enable mass-manufacturing of high-resolution patterns.

To summarize the whole fabrication procedure, the conceived fabrication process for SiN photonic circuits firstly consists in depositing SiO_2 and SiN materials onto a previously cleaned silicon 4-inch wafer using Plasma-Enhanced Chemical Vapor Deposition (PECVD). The wafer is subsequently sliced into multiple rectangular pieces. A negative resist coating is next deposited by spin-coating, followed by E-beam pattern exposure and development of the resist. The generated resist structure then serves as a layout mask for engraving the SiN by using a Reactive-Ion Etching (RIE) process. The chip is finalized by removing the remaining unwanted resist with wet chemical and plasma cleaning. The process is further described in the following subsections.

2.2.2 Plasma-enhanced Chemical Vapor Deposition

Plasma-Enhanced Chemical Vapor Deposition, as opposed to Low-Pressure Chemical Vapor Deposition (LPCVD), can enable thick films to be deposited on a wafer using plasma technology. On the one hand, LPCVD is a slow and costly technique that uses heat (SiN growth typically requires a temperature between 700°C and 850°C) to initiate the reaction of a precursor gas with the solid substrate while maintaining a sufficiently low gas pressure to both improve the deposited thickness and material uniformity as well as prevent other parasitic chemical reactions to occur. As a result, compared to PECVD, LPCVD generally incurs higher mechanical stress within the deposited layer, thus limiting the film thickness to approximately 300 nm - 400 nm [118]. PECVD, on the other hand, is a low temperature technique (SiN growth typically requires a temperature that is lower than 300°C) and thus exhibits much lower thermally induced mechanical stress in the substrate. Although PECVD could potentially result in lower film uniformity and material quality compared to LPCVD, as well as contribute to relatively higher intrinsic material optical absorption at the 1550 nm telecommunication wavelength if poorly operated [119, 118], its low temperature advantage and low cost process far outweigh the potential inconveniences. Consequently, for fabrication simplicity and cost effectiveness, PECVD is employed over LPCVD to obtain the desired waveguide thicknesses in our prototypes.

The equipment used for SiN and SiO_2 deposition is the ApSy PECVD 100. After cleaning the silicon wafer with O_2 Plasma, SiO_2 is deposited for 3.15 mins using plasma at 750 mT-300 W-380 kHz-300°C with a SiH_4/N_2 mixture. The film's RI and average thickness are then respectively measured with an UVISEL ellipsometer to be 1.475 @450 nm (estimated at 1.45 @1550 nm) and approximately 2 µm, as summarized in table 2.1. The SiN layer is next deposited over 3.10 mins using a 650 mT-185 W-380 kHz-300°C plasma with a $SiH_4/NH_3/N_2$ mixture. Its RI @1550 nm and average thickness are next estimated to be 1.97 and 405 nm, respectively. Two wafers have been produced and then diced into square pieces of 2×2 cm^2 by water jet-cutting, with prior deposition of protective resist to avoid

Material	Average	Maximum	Minimum	Uniformity
SiOx (nm)	1993,4	2119,4	1778,03	0,087
SiNx (nm)	404,5	417,2	392,0	0,031

Table 2.1: Thickness profiles of the deposited films

surface damage during the process.

2.2.3 E-Beam Lithography

Electron Beam Lithography (EBL) can achieve sub-10 nm patterning resolution by relying on accelerated electron sputtering onto electron-sensitive resists. This resolution, currently unmatched by conventional optical lithographic techniques, is highly interesting for integrated photonics requiring subwavelength patterns. Nevertheless, while EBL is particularly well adapted to address PIC prototyping with high-resolution and at relatively low-cost, the photonic structures and the associated circuit design should ultimately be made to conform to conventional techniques available in Multi-Project-Wafer fabrication dedicated to PIC manufacturing (e.g. via Europractice partners: IMEC, CEA-Leti, LioniX, etc).

The computer-controlled EBL equipment comprises (1) an electron gun that supplies and accelerates electrons to (2) a column system made of electromagnetic lenses that, in turn, shape and focus the electron-beam, to finally sputter the photonic chip that is placed on (3) a mechanical stage that is mainly used for macro-displacement under the electron column. EBL allows direct custom writing as it does not require any mask layer as opposed to photolithography. The beam is scanned in a sequential manner over the areas to pattern. Therefore, processing large surface areas can subsequently limit the exposure speed, rendering this technique unsuitable for mass-manufacturing (unless multi-parallel writing devices are employed). As previously explained, the resolution in optical lithography is mainly limited by the diffraction limit which, in turn, depends on the exposition wavelength (i.e. the De Broglie wavelength). The equivalent De Broglie wavelength for 10 - 100 keV of electron energy (energy typically emitted by EBL) is calculated to be approximately 5 - 20 pm, while the minimum EBL resolution is on the order of nanometers. The large difference ($\sim$ 3 orders of magnitude) between the EBL's attainable resolution and the electron wavelengths can be attributed to three major factors:

1. the spherical and chromatic aberrations of the lenses tend to complicate proper focusing of the beam. Several systems have been proposed to correct these problems [120].

2. electron-scattering is caused by both elastic and inelastic electron-material interactions. This results in electrons diffusing into the resist, thus statistically broadening the exposed area: this is known as the proximity effect.

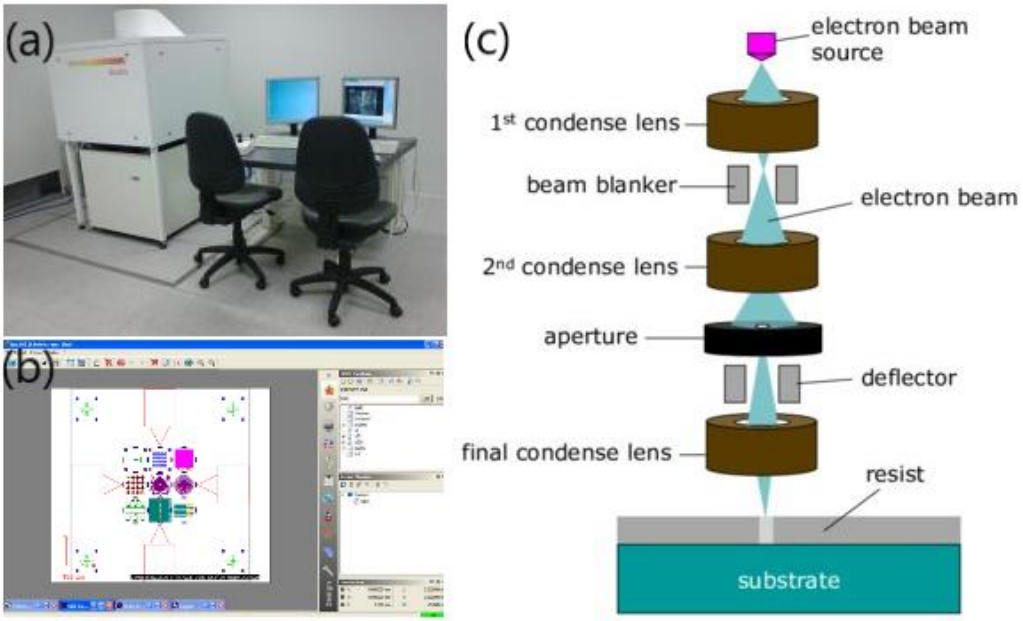

Figure 2.10: (a) Image of RAITH150 equipment in LAAS cleanroom [8], (b) overview of RAITH software [9], (c) E-beam operating schematic [10]

3. resist swelling and contraction occur during the development process and tend to slightly distort or even induce cracks in the resist layer.

Similar to [121], prior calibrations of the resist and exposure parameters (resist coating tests, dose adjustments, etc) are performed to achieve optimized patterning with the desired structure dimensions. These calibrations also enable one to deduce slight deformation that should be applied on the waveguide layouts to compensate the proximity effect. This adjustment is also known as proximity effect correction [9].

In most cases, the EBL process the layout by dividing it into multiple writing-fields, also called working areas, for which exposure is iteratively performed. The working areas are defined by the capacity of the electron optics to scan the surface without moving the mechanical stage that supports the exposed substrate. Usually much smaller than the area required by PICs, these working areas can generate stitch errors due to the imprecision of mechanical alignment between adjacent regions. This would normally cause mismatch of the waveguides at the interface and produce relatively high optical losses. Typical methods to reduce the effect of this fabrication flaw in the lithographic process include over-exposure at the working area junctions, enlargement of the areas at the interfaces, or minor extension of the working field's printing size to slightly superimpose on adjacent structures at the junction. However, these procedures are strongly dependent on the exposure parameters thus rendering it difficult to reduce the mismatches consistently. In this

thesis, the RAITH150 EBL offers a very specific pattern process known as Fixed Beam Moving Stage (FBMS). This writing mode enables certain types of pattern to be stitch-free by continuously exposing path-type structures over long distance with repetitive sweeping of the beam location to control path width, which is also expected to smoothen the waveguide curvatures. This operating mode, which requires its own calibrated exposure parameters and layout file formatting, is subsequently used for linking photonic components with waveguide patterning.

2.2.3.1 Sample Preparation Procedure for MaN2405 Coating

1. Chip blowing with N_2 gun
2. Flush with acetone
3. Flush with de-ionized (DI) water
4. Dry with N_2 gun
5. Dehydrate for 2 mins @200°C (ESSILOR Hotplate)
6. Plasma O_2 cleaning (Diener Electronic)
7. Hexamethyldisilazane (HMDS) primer deposition using OBDUCAT HMDS equipment - silanization facilitates resist adhesion to the chip surface
8. MaN2405 spin coating: 300 µL, 5000 rpm/60 s.
9. Dry for 2 mins @90°C
10. Electra92 spin coating: 5000 rpm/60 s - Electra is a protective resist used for charge dissipation during electron exposure. It is observed that post-coating drying could cause cracks to form here.

2.2.3.2 Electron Beam Lithography Parameters on MaN2405

1. set the column and electron gun parameters to: 20 kV acceleration voltage, 37 pA current, step size 10 nm
2. Set the writing fields at 127 µm and map origin so that no grating couplers are in between writing fields.
3. Set the exposure dose at 112 $\mu C/cm^2$ for normal exposure mode and with a dose factor of 1.25 for FBMS mode
4. Verify the exposure order
5. Set a 40 nm field decalibration in order to limit stitching error: Use a UV Zoom factor of 1.0003 in the "Writefield Alignment" window

2.2.3.3 maN2405 development

1. Develop in pure MF CD 26 for 50 s
2. Rinse in DI water for 1 min
3. Dry with N_2

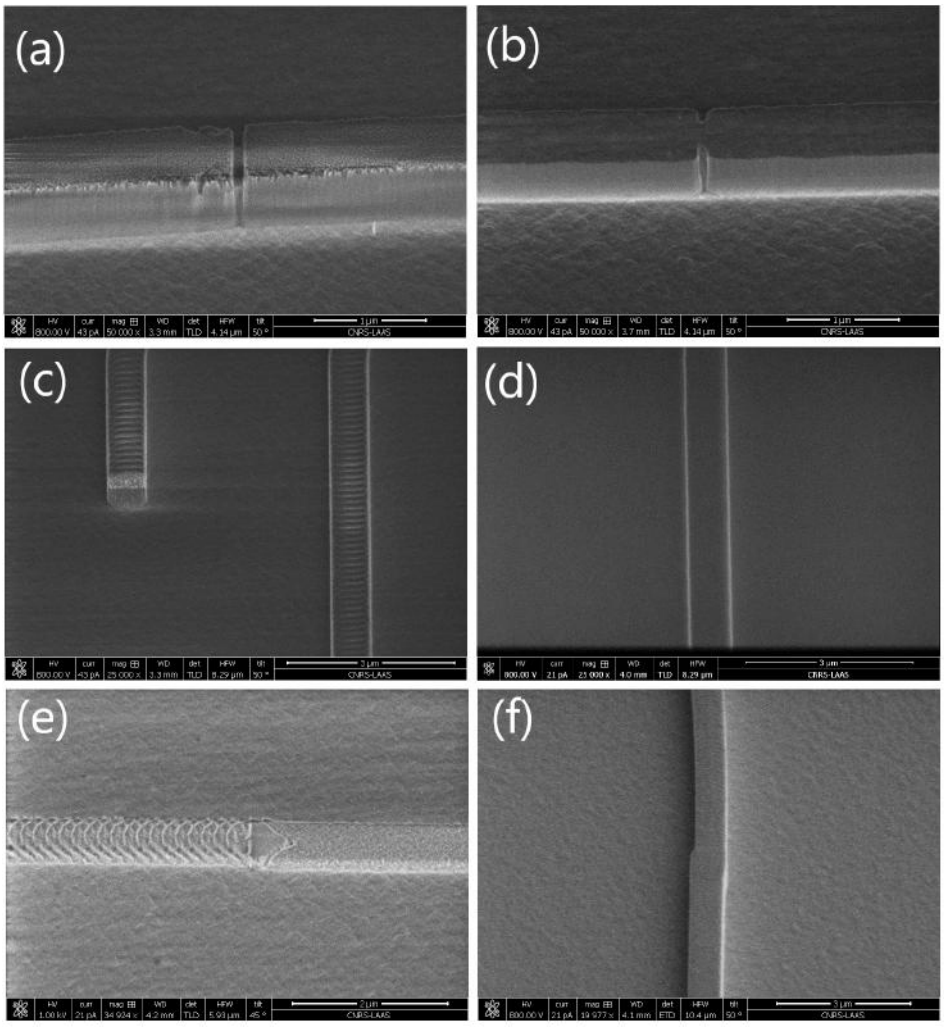

Figure 2.11: Scanning Electron Microscope (SEM) images of (a) normal exposure mode mismatch at working field junctions and (b) resulting waveguide cleave due to stitching effect after resist stripping, (c) FBMS exposure mode with small sweeping stripes on the resist and (d) resulting waveguide showing no cuts, and (e) resist after development on a normal/FBMS waveguide junction showing (f) minor waveguide dimensional variations

2.2.4 Reactive Ion Etching

Reactive ion-etching (RIE) is a dry etching technique commonly used in microfabrication. A plasma is firstly created by a strong radio-frequency EM field and induces ion collision with the wafer surface. Depending on the plasma's chemical nature, reaction can lead to anisotropic etching of the material on the surface, which is used here to transfer the resist patterns onto the substrate. Here, the Etchlab200 machine has been used to engrave SiN to form the photonic structures and waveguides. An integrated interferometer allows *in situ* tracking of the etching process by detecting the laser interference associated with the depth. In our RIE process, the main plasma gas flow rates for CHF_3 and O_2 are, respectively, 50 cm^3/min and 3 cm^3/min, while the plasma bias power is 100 W and the etching chamber pressure is 70 mTorr. The fabricated devices are illustrated in figure 2.12.

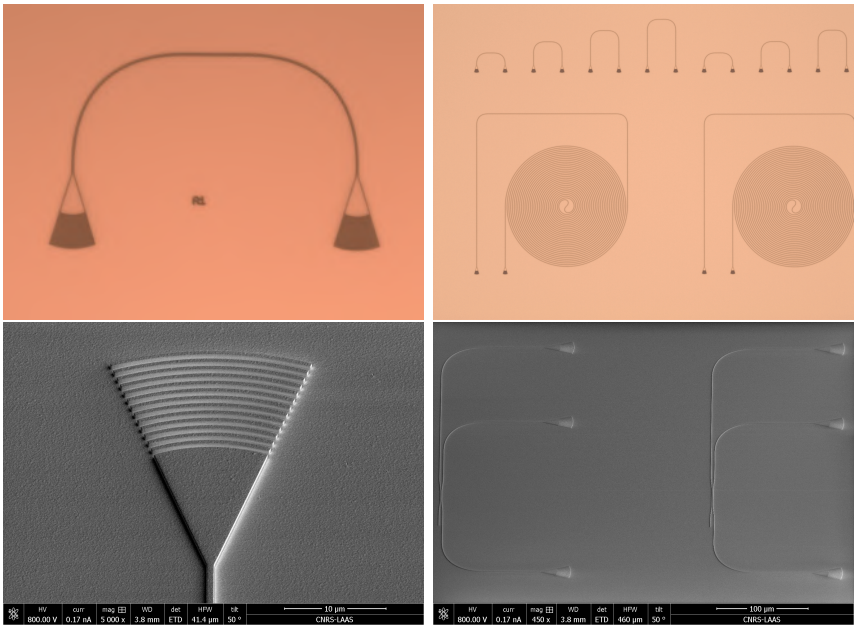

Figure 2.12: Images of fabricated devices of chips n° 1 and n° 2: (a) optical microscope (OM) image of grating coupler pair for chip in/out coupling, (b) OM image of spiral waveguide designed for waveguide loss measurement, (c) SEM image of fabricated grating coupler, and (d) SEM image of fabricated broadband coupler

2.3 Integrated Photonics Experimental Characterization

2.3.1 Overview of Experimental Setup

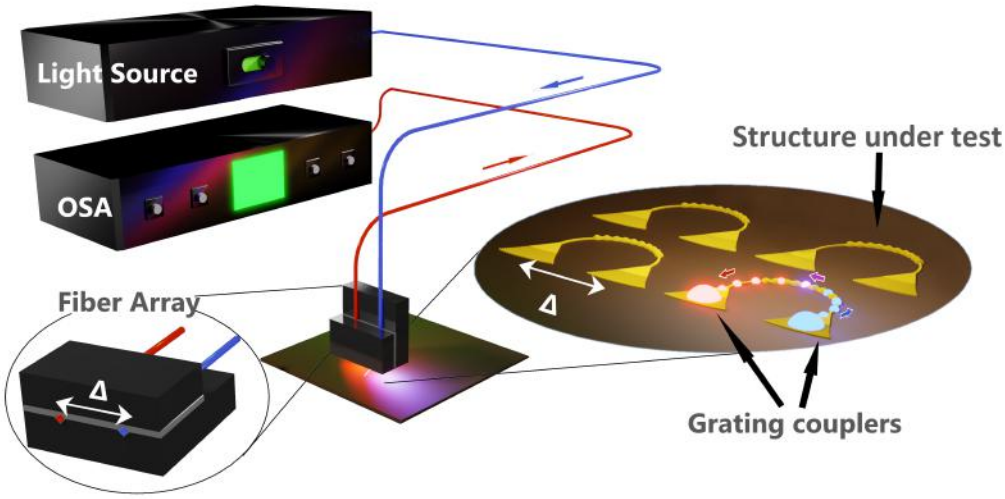

Figure 2.13: Illustration of experimental setup

The measurement setup developed for characterizing photonic structures consists of a broadband light source (BBS) , an optical spectrum analyzer (OSA) , a probe station with a fiber array and the chip under test, as illustrated in figure 2.13. As previously mentioned in Section 2.1.3, the fiber array incorporates a set of SMFs bound and held together by a support at one end, with each fiber core separated by a pitch of $\Delta = 127$ µm. Each structure to be characterized is connected to the respective input/output port of a grating coupler which allows the injection and recovery of the interrogating light through the fiber array positioned on top of the chip-integrated grating coupler pair. The coupling efficiency of the grating coupler generally depends on the polarization state of the injected optical mode which can randomly vary during propagation along the fiber. In order to ensure correct polarization of the injected light, polarization controllers and/or polarization maintaining fibers have been used in this thesis.

The fiber array is mounted onto XYZ motorized linear stages (ZABER) driven by a dedicated LabVIEW program for alignment purposes, as shown in figure 2.14. The alignment procedure relies on a few steps and is similar to that in [107]:

1. the PIC is placed on the sample holder stage with the correct orientation
2. a rough alignment of the PIC-fiber array is achieved by rotating both the sample stage and fiber array (yaw adjustment)

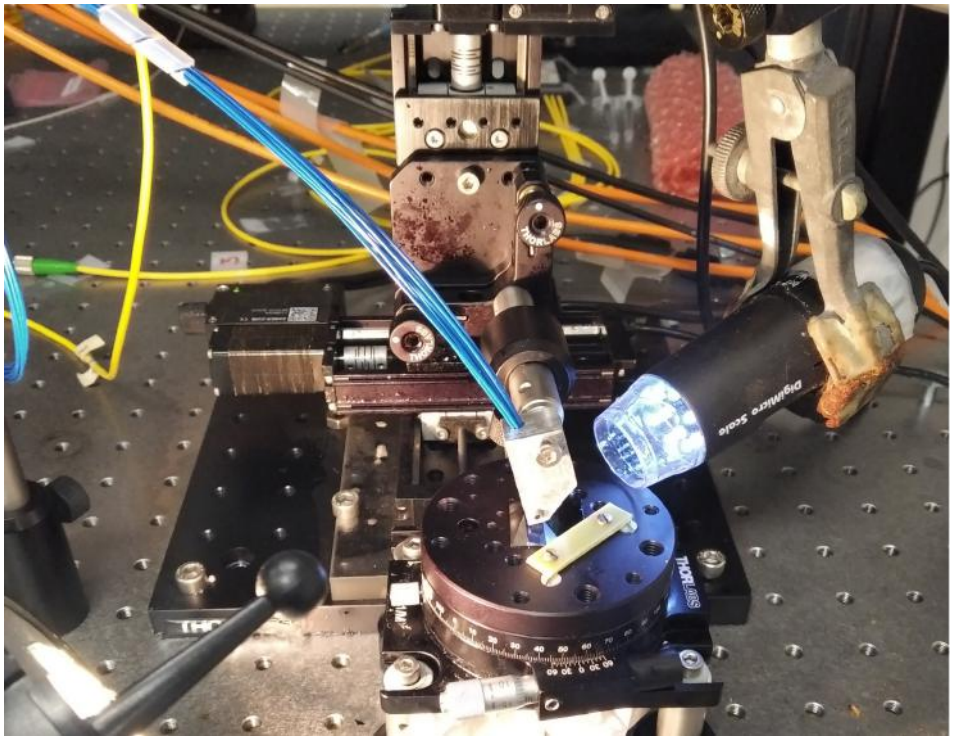

Figure 2.14: Picture of optical characterization setup

3. the fiber array is moved closer a few tens of micrometers to the sample stage, as seen in figure 2.15

4. a visible laser connected to the fiber array outputs and a microscope camera are used for angle adjustments and positioning of the fiber array on top of a pair of grating couplers

5. the laser is replaced by the IR source and finer alignment performed through feedback of the measured transmission of the components being aligned (similar to figure 2.12 (a)) or the functions under characterization

A bespoke algorithm is then incorporated into the program to enable automatic scanning of the entire chip's photonic structures or components via this feedback scheme. To ensure temperature stability, the chip is placed on a Thorlabs mount integrating a Thermo-Electric Cooler (TEC). The TEC additionally enables temperature tuning to study the temperature-induced spectral responses of these structures.

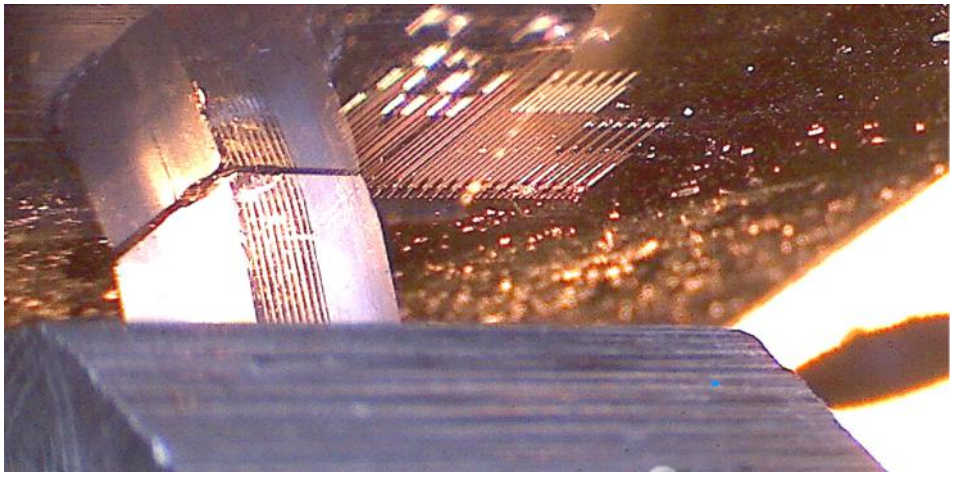

Figure 2.15: Enlarged image of the fiber array alignment with respect to the PIC chip

2.3.2 Optical Characterization of Grating Couplers

Multiple grating couplers with various grating pitches have firstly been fabricated, taking into account potential discrepancies of both the material and structural parameters from the simulated models. As shown in table 2.2, a blue shift of the coupling resonance pattern is observed in the measured transmission, when compared to simulated values. An SEM scan suggests this difference to be mainly attributed to a low electron-lithography exposure of the grating couplers, thus resulting in a reduced grating fill factor. It is also observed that the resonance centre could slightly shift as a function of the fiber array-grating coupler alignment. This slightly complicates the de-embedding procedure of the responses of the photonic structures. In addition, it has been decided to use SU8 coating instead of SiO_2 as the surface cladding for the future chips to facilitate chip fabrication and anticipate future modifications (such as window openings on waveguides or changes in cladding thickness). Maximum transmission is obtained by further optimization of the fiber array-to-chip angles and the associated contact areas, leading to a maximum coupling efficiency of - 6.5 dB, as shown in figure 2.16. However, in this thesis, all the measurements are performed with a safety gap between the fiber array and PIC (to prevent damage to both) so that coupling losses are slightly higher. Figure 2.17 displays the measured topography of the coupling efficiency of the grating coupler, showing that a micrometer precision is necessary for a relatively optimal coupling efficiency to be obtained.

Grating coupler n°	Simulated center resonance (nm)	Simulated bandwidth (nm)	Measured center resonance (nm)	Measured estimated bandwidth (nm)
1, period=1.12µm	1528	100	1520	86
2, period=1.14µm	1547	100	1539	90
3, period=1.16µm	1563	110	1549	92

Table 2.2: Measured transmission spectral parameters of the realized grating couplers

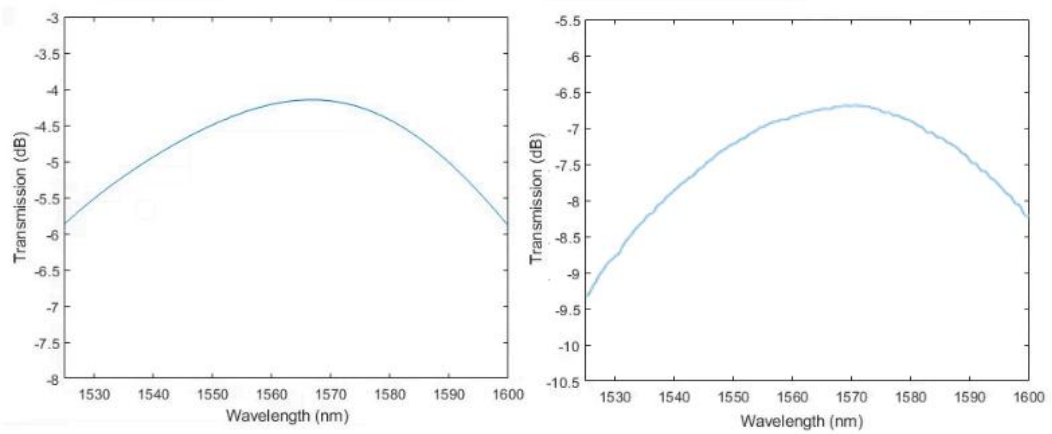

Figure 2.16: Typical transmission spectra of a grating coupler : (a) simulated, and (b) measured

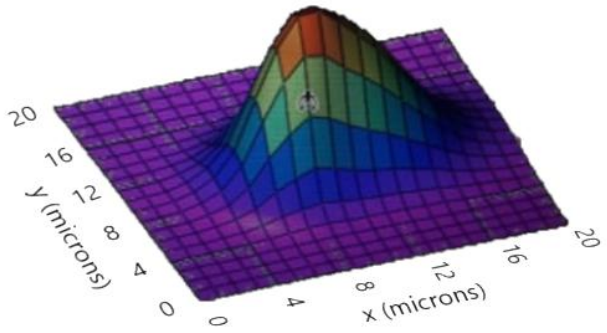

Figure 2.17: Topography of coupling efficiency of grating coupler

2.3.3 Optical Characterization of Waveguides

Once the grating couplers are characterized, the waveguide losses have to be determined for circuit scaling. This is carried out by measuring the transmission of the designed waveguides of different lengths varying between 100 µm and 3 cm. The waveguide losses for Chip n° 1 and Chip n° 2 are found to be higher in the case of

normal mode exposure during fabrication as compared to other chips fabricated under FBMS continuous exposure with respective propagation loss values at 15 dB/cm and 5.5 dB/cm. This is due to the higher number of waveguide mismatches induced in the waveguide coils for the normal exposure mode. The 5.5 dB/cm loss for FBMS-exposed waveguides, however, remains high in comparison to typical SiN waveguides which exhibit < 1 dB/cm losses for high-end waveguides [122, 118] or, recently, to the order of 1 dB/m [60] for unconstrained waveguides. A possible solution for reducing the relatively high propagation losses is to anneal the photonic chip (at 1150°C) as it has been demonstrated to considerably reduce N-H absorption in the SiN layer and smoothen waveguide sidewalls [118]. This solution is, however, not readily employable in the LAAS cleanroom as well as the time constraints involved to implement the new process. Another potential solution is to use a Damascene reflow process to exploit the structural properties of SiO_2 for SiN waveguide manufacturing [123]. This, however, complicates the fabrication process as well as it is unsuitable for some original structures that have been developed in this thesis.

Chapter 3

Integrated Refractometers

Contents

This thesis focuses on **integrated refractometers**, among other optical schemes, for the development of integrated gas sensors. The rapid technological progress in micro-technologies is continuously unlocking new possibilities to micro-engineer materials and structures, both at the wavelength and sub-wavelength scales. As suggested in Chapter 1, among the three main optical gas sensing schemes (absorption, fluorescence and refractometry), refractometric schemes demonstrate the highest potential for original design possibilities. Moreover, refractometers present the widest range of applications since the RI is a common property for all materials, and can thus be exploited for diverse sensing applications, such as pressure, temperature [39] or chemical sensing [101, 124]. The advancement in refractometric technology can therefore potentially have higher impact on the sensing industry compared to the other sensing schemes previously described.

A brief overview of the different optical schemes that are used for refractometric sensing in integrated optics is presented in this chapter. The chapter opens with a short theoretical treatment of the refractometric sensitivity, followed by a discussion on the tools and **figures of merit** that are widely employed by the photonics community to assess the performances of various refractometric designs. Secondly, the **five main refractometric sensing structure types** employed in integrated optics are described, namely **interferometers, resonators, plasmonics, diffraction gratings and photonic crystals**. A selection of simulation and experimental results from **state-of-the-art** conventional structures that have been

realized in this thesis is then displayed for each type of integrated refractometer. Finally, a non-exhaustive list of reported integrated refractometers is analyzed and discussed. Overall, this chapter proposes a model for analyzing the individual components and/or functions generally employed in integrated refractometers, both to give insight on **optimization patterns** and methods that can be exploited for the development of specific refractometers, and to underline the advantages and drawbacks of each refractometer type.

3.1 Refractometric Performances

3.1.1 Waveguide Sensitivity

Most integrated refractometric sensors are based on the variation of the effective index (EI) of an optical propagating mode induced by the change in RI of the sensitized layer placed in the vicinity of the waveguide surface. Similar to sensors based on the optical absorption of evanescent waves (EW) which operate on maximizing the evanescent field ratio (EFR) to the total mode field, a common optimization method of refractometric schemes is to maximize the dependence of the EI on the surrounding region's RI to be detected. Subsequently, this influence factor, generally known as the waveguide refractive sensitivity for a given mode, i, can be expressed as:

$$\Gamma_i\left(\lambda, n_{eff,i}\right) = \frac{\partial n_{eff,i}}{\partial n_c}\left(\lambda, n_{eff,i}\right) \tag{3.1}$$

This equation quantifies the ability of the waveguide structure to modify a mode's EI $n_{eff,i}$ when the RI of the surrounding cladding medium n_c is caused to change. Note that it is a common misconception to consider the field overlap ratio to the sensing region of a waveguide as being equal to the waveguide refractive sensitivity. By using the modal interference conditions for constructive interference in waveguides, an analytical formula for the waveguide evanescent refractometric sensitivity in 1D step-index models can be found to be [125, 126]:

$$\frac{\partial n_{eff}}{\partial n_c} = \frac{n_c}{n_{eff}} \frac{P_C}{P_{tot}} \left[2\left(\frac{n_{eff}}{n_c}\right)^2 - 1\right]^{\rho} \tag{3.2}$$

where P_{tot} and P_C respectively denote the total optical power and its fraction that propagates in the cladding, and ρ denotes polarization being equal to 0 for TE modes and 1 for TM modes. The demonstration for TE polarization is given in appendix A.4. This shows that the refractometric sensitivity is not only dependent on the power fraction in the cladding used as a sensing region, but also depends directly on parameters that are primarily dependent on the waveguide materials' index contrast. Marcatili's method for calculating EI of 2D models from 1D modal calculations can similarly be applied to obtain analytical formulas of the waveguide sensitivity for 2D models.

3.1.2 Chromatic Dispersion and Group Index

By analogy to waveguide sensitivity, it is obvious that any change of wavelength of the propagating modes can perturb the modal interference conditions and induce changes in the waveguide's mode power distribution, and therefore "see" its EI vary with the wavelength: this is the waveguide dispersion. The intrinsic material RI dependence with wavelength, defined as material dispersion, should also be taken into account to achieve higher model accuracy. The overall contribution is known as chromatic dispersion [127, 128] and induces the propagation constant to vary with the wavelength in many different ways. This phenomenon is present in most waveguides and affects the optical behavior of many RI-based architectures and systems. Chromatic dispersion particularly intervenes in the sensing analysis of most optical refractometers as they generally rely on the characterization of the spectral shift of an optical signature whose spectral position depends on EI. The first-order chromatic dispersion information of a waveguide's mode at a given wavelength is generally contained in the group index (GI), as given by [129]:

$$n_g(\lambda) = n_{eff}(\lambda) - \lambda \frac{\partial n_{eff}(\lambda)}{\partial \lambda} \tag{3.3}$$

which is generally used to analyze the instantaneous sensitivity of refractometric schemes. Higher-order dispersions are mostly utilized in more specific applications such as those based on the optical pulse-broadening Kerr-effect or in more advanced analysis.

3.1.3 Refractometric Sensitivity and Figure of Merit

As explained in Chapter 1, it is difficult to distinguish the efficiency of the optical scheme from the overall performance of the sensing system. For instance, the RI limit of detection (LOD) of a refractometer partially depends on the the equipment used to characterize the device, such as the measurement apparatus, source and coupling performances, noise resolution, precision, etc, which is not relevant for qualifying the intrinsic performance of the refractometric design. For this reason, different parameters commonly used for evaluating the performance of refractometric schemes have been proposed in the literature.

On the one hand, in the case of a single wavelength intensity-based measurement, the RI influence on the transmitted intensity, namely $S_{int} = \partial(I/I_0)/\partial n_{sens}$, can be evaluated in dB/RIU. One of the main issues of highly sensitive refractometric schemes based on intensity is that the operational range of the sensor is greatly reduced in most cases. On the other hand, for spectrally-based systems, the spectral sensitivity $S_\lambda = \partial\lambda_{shift}/\partial n_{sens}$ defines the ability of a structure's spectral response to shift with RI variation induced by environmental perturbation. Spectral interrogation techniques typically relies on tracking a spectral feature or characteristic (e.g. peak, dip, etc) of the sensor's spectral response, which could result in an increased measurement range compared to the intensity-based method (depending on the

performance of the optical spectrum analyzer, for example). Note, however, that S_λ primarily focuses on the spectral position analysis only and thus neglects other aspects: hence, the broader the spectral signature, the more difficult it is to track its position accurately. For this reason, the sharpness of the spectrum's peak(s) is an appropriate parameter for comparing refractometric schemes. Related parameters such as the Full-Width Half-Maximum (FHWM) , and other derivatives such as quality factor or Free Spectral Range (FSR) for sine-shaped spectral responses are commonly used figures of merit which characterize the broadness of the spectral features. Together with the spectral sensitivity, these parameters form the principal Figure Of Merit (FOM) which can be defined as

$$FOM = \frac{S_\lambda}{FWHM} \tag{3.4}$$

in units of RIU^{-1}. FOM can also be related to S_{int} around certain measurement regions for intensity-based measurements. Note that FOM alone can provide precious insight into the potential LOD of a refractometer. However, the determination of the pattern's position can be facilitated by curve-fitting using appropriate mathematical functions such as the Lorentzian. Such methods tend to integrate values over the measurement spectra, therefore reducing the effect of the measurement noise and consequently implying that S_λ becomes all the more important for comparing refractometric performances.

3.2 Refractometric Sensing Schemes

In this section, the operating principles of the main refractometric sensing schemes are presented. In particular, Mach-Zehnder interferometers as well as micro-ring resonators are also fabricated during this thesis to characterize the process technology and also to serve as reference. Note: most theoretical formulas that are given here for the different figures of merit of the sensing schemes are first-order approximations based on Taylor Series. After having briefly introduced the main different refractometric schemes that can be employed in integrated photonics for the realization of refractometers, each section proposes a non-exhaustive list of the respective integrated photonic structures that have been simulated and/or realized by the scientific community between 2016 and 2020. The objective here is to summarize the different sensor schemes that have been proposed to expose trends. Approximately 80 different structures operating in the NIR have been analyzed and figures of merit such as spectral sensitivities or spectral shape sizes have been extracted and compared from information reported in the articles. The sensors are classed according to the refractometer "family" and subtype as previously described, while outlining the specific core concept for each architecture.

3.2.1 Interferometers

Interferometers are devices based on the superposition of two (or more) coherent light beams to generate interference patterns which are dependent on the optical phase difference between the interfering beams. The interferometer can be employed for studying any parameters that can induce a relative **optical path difference (OPD)** (e.g. displacement, distance, propagation constants, RI variation, etc). Typically, a "sensing" wave propagates through the sensed region, which modifies its optical path, and interferes with an "unmodified" or a reference wave whose path length remains constant. Historically used for measuring distance variations, interferometers can also be applied to chemical sensing, as the OPD depends on the RIs of the media surrounding the sensing beam.

In guided-wave optics, a modification of the EI of a propagative mode via the EW leads to the creation of an optical phase delay that can be detected and measured by an interferometer. The main interferometric schemes used for refractometry in integrated photonics are based on the Mach-Zehnder interferometer (MZI) and multimode interferometers. MZIs have the simplest design: a light beam is first split into an arm going through the sensed region and a reference arm, typically using Y-splitters or broadband couplers, and then recombined after propagation. Figure 3.1 illustrates simulated and experimental results obtained from MZIs that have been designed, fabricated and tested as refractometers in this thesis (see appendix A.1.6). The phase difference typically induces sine-shaped spectral patterns that shift as a function of the OPD variations (due to EI variations that are induced by external perturbations). The MZI's spectral sensitivity can be approximated by [130]:

$$S_{\lambda,int}(\lambda,i,j) = \lambda \frac{\Gamma_i(\lambda)L_i - \Gamma_j(\lambda)L_j}{n_{g,i}L_i - n_{g,j}L_j} \tag{3.5}$$

where i and j are the two excited modes of the two optical paths, and L_i and L_j the respective path lengths (assuming L_i refers to the sensing arm).

Multimode interferometers, on the other hand, are based on the continuous coupling and interference occurring in a wave guiding structure that supports at least two propagative optical modes. In this case, the phase difference between the two modes primarily originates from the intrinsic difference between the GIs (or n_g) of the two modes, since $L_j = L_i$.

As deduced from equation (3.5), performance optimization techniques typically focus on either phase-matching of the propagative constants or enhancement of the waveguide's refractometric sensitivity. In spectral interrogation methods, increasing the sensing path length is mainly used to reduce the FSR (or equivalently the FWHM) of the transmission spectra which can be defined as:

$$FSR_{int}(\lambda,i,j) = \frac{\lambda^2}{n_{g,i}(\lambda)L_i - n_{g,j}(\lambda)L_j} \tag{3.6}$$

Interferometers are generally considered as tools of first choice for refractometric

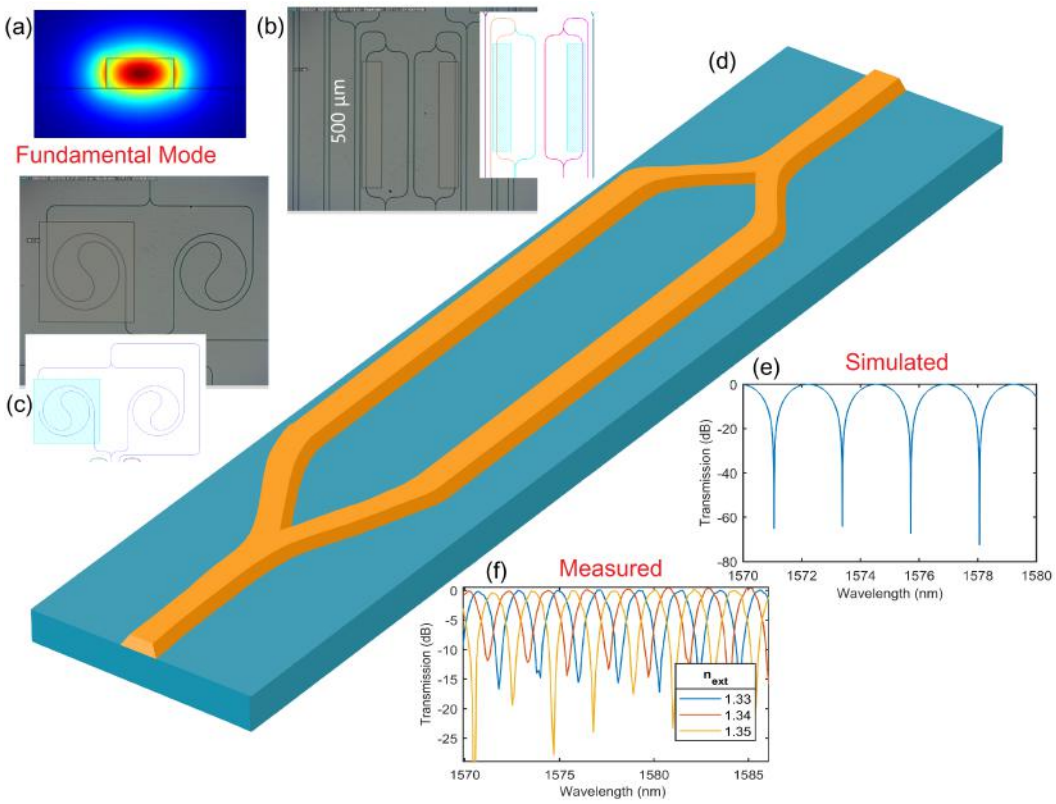

Figure 3.1: A typical integrated Mach-Zehnder interferometer design: (a) propagating fundamental mode in a strip waveguide simulated with Lumerical mode solver, (b)-(c) layouts and OM images of fabricated Mach-Zehnder interferometers for refractometry, (d) illustration of integrated strip Mach-Zehnder interferometer, (e) simulated spectral response of a designed MZI, and (f) measured spectral responses of a fabricated MZI for coated liquids of different RIs

applications in integrated optics not only for their simplicity of design and fabrication, but also because they potentially offer the highest sensitivities in the market. Table 3.2.1 summarizes the performances of the state-of-the-art of MZIs used as refractometric sensor from 2016 to 2020. The principal drawbacks of integrated MZI structures are: (1) the high waveguide loss that limits the optical arm length achievable on which the LOD greatly depends, but also (2) the spectral periodicity of the transmission pattern, which can complicate pattern tracking without continuous real-time measurement for highly sensitive architectures.

Ref	Year	Type	Specificity	sensitivity (nm/RIU)	FOM (RIU-1)	Materials	Wavelength range	RI Range	sim /fab
[131]	2019	multi-mode int	SPP interference	1930	214	SiO2-Gold	∼729nm	1.33-1.34	fab
[132]	2020	MZI	Plasmonic strip waveguide sensing arm	1300	∼87	SiN-LTO -SiO2-Al	∼1550nm	∼1.33	fab
[133]	2019	multi-mode int	bi-modal interferometer	789	∼158	Polymer	890-910nm	∼1.33	fab
[134]	2016	MZI	1D photonic crystal sensing arm	103	∼200	Si-SiO2	∼1550nm	∼1.34	fab
[135]	2016	MZI	slight asymetry	3498,6	∼500	Si-SiO2	∼1550nm	1.508-1.556	fab
[136]	2019	MZI	Multi-mode arms	826	∼63	Si-SiO2	∼1550nm	1.33-1.35	fab
[137]	2018	MZI	2D photonic crystal arms	200	-	Si-Air	∼1550nm	∼1	sim
[138]	2016	MZI	ring-assisted with slot waveguide	203	8.35	Si-SiO2	∼1550nm	∼1.33	fab
[139]	2019	MZI	Plasmonic waveguide Arm & variable attenuation	1930	161	SiN-Gold	∼1565nm	∼1.33	fab
[140]	2019	multi-mode int	bi-modal grating assisted interferometer	2270	85	Si-SiO2	∼1550nm	1.3183-1.3205	fab
[141]	2016	MZI	MMI-Coupled & Ring-assisted	593	∼210	Si-SiO2	∼1557nm	∼1.33	fab
[142]	2018	MZI	Femtosecond laser Microfabricated	122,4	∼102	Su8-SiO2	∼1560nm	∼1.33	fab
[143]	2019	MZI	MMI-Coupled & Ring-slot waveguide	625	∼75	Si-SiO2	∼1550nm	∼1	sim
[144]	2019	MZI	Plasmonic waveguide arms	2430	∼115	TiO2-gold -Su8-SiO2	∼1550nm	∼1.33	sim
[145]	2017	multi-mode int	MMI with low optical confinement	427	133	Si-SiO2	∼1550nm	∼1.33	sim

Table 3.1: List of recent integrated interferometers for applications in refractometry

3.2.2 Resonators

Resonators are essentially used as filters in optical telecommunications for signal multiplexing/demultiplexing because of their ability to separate wavelengths with high selectivity. They can also be used as refractometers displaying very sharp spectral features. In integrated photonics, they are typically implemented as micro-ring waveguides, also known as Micro-Ring Resonators (MRRs) [146, 147, 148, 149, 150], or in the form of waveguide cavities, such as Fabry-Perot Resonators [151, 152]. An optical ring resonator is obtained by forming a closed loop waveguide into which light can be coupled and is expected to make multiple round-trips. Figure 3.2 displays simulated and experimental results of MRRs that have been designed, fabricated and tested as refractometers in this thesis (see appendix A.1.6).

Fabry-Perot resonators (FPRs), contrary to MRRs, are based on the multiple reflections of a lightwave within an optical cavity enclosed by two or more reflectors. In both cases, the **multiple round-trips** of the optical beam result in self-interferences. Thus, resonance occurs when the loop properties satisfy the condition for constructive interference, for which the optical transmission is principally driven by the propagation constants. In this case, the RIs of the surrounding medium can be retrieved by analyzing the resonance spectral shifts. Although these resonator architectures also function on the principles of optical interferometry, they can nevertheless be distinguished from conventional interferometers here because they present specific behaviors that lead to different response patterns requiring different optimization methods. In particular, their spectral sensitivity and FSR can be defined as [153]:

$$S_{\lambda,res}(\lambda) = \lambda \frac{\Gamma(\lambda)}{n_g(\lambda)} \tag{3.7}$$

$$FSR_{res}(\lambda) = \frac{\lambda^2}{n_g(\lambda) L_{loop}} \tag{3.8}$$

where L_{loop} denotes the length over which the optical beam undergoes a complete round-trip propagation either in the loop for MRRs or the cavity in the case of FPRs.

Resonator performances however also depend on the cavity's coupling, propagation loss and reflector quality in case of FPR. In fact, these parameters will define the spectral sharpness of the resonance features, which is the main strength of resonators. They make up for their inherently limited sensitivity by their potential to achieve sharp resonance characteristics with structures of relatively small footprints (or dimensions). Table 3.2.2 summarizes the performances of the state-of-the-art of MRRs used as refractometric sensors from 2016 to 2020. Among the different ring resonator architectures, complex and original designs have been reported for refractometry, involving "exotic" shapes such as disk resonators [154], spiral resonators [155] or even designs based on whispering gallery modes [154]. FPR designs are, however, complicated by the difficulty to efficiently integrate reflectors. Resonator architectures are usually much more dependent on the quality of the fabrication

technology although they generally offer a much smaller footprint, thus making them highly promising candidates for multi-analyte sensing which could be implemented in sensor arrays.

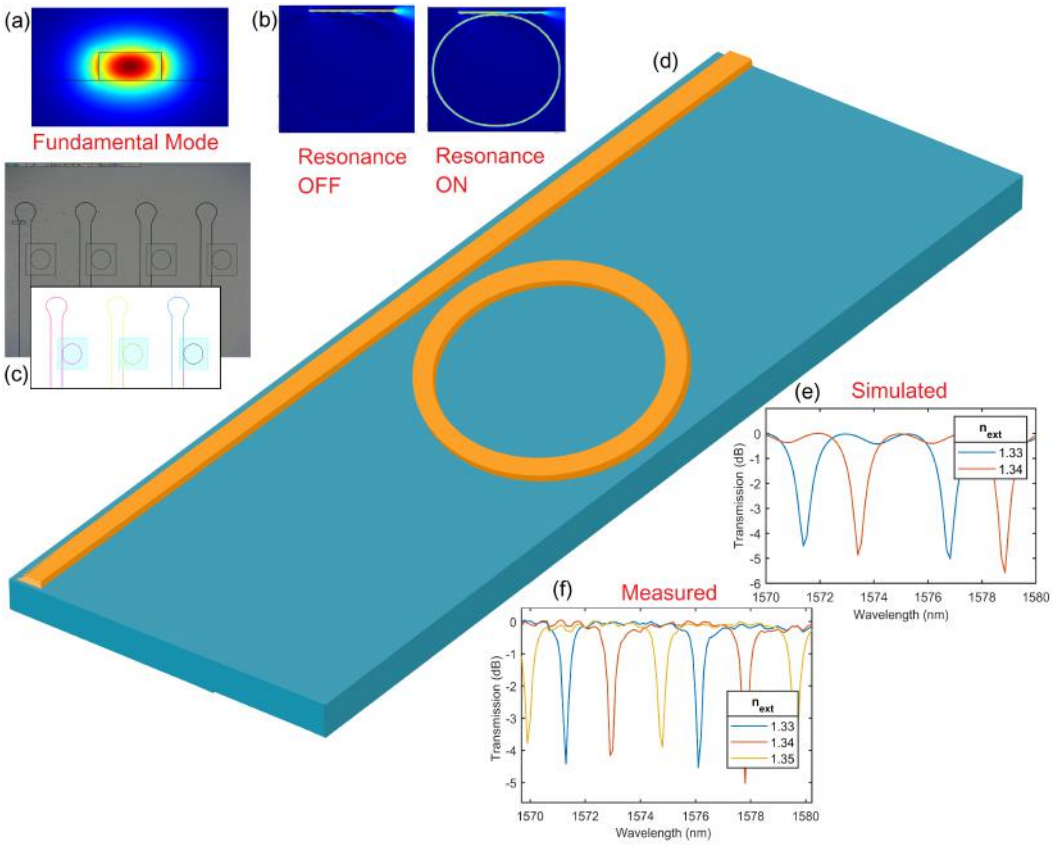

Figure 3.2: Micro-ring design as the typical integrated resonator: (a) propagating fundamental mode in a strip waveguide simulated with Lumerical's mode solver, (b) optical field distribution in the MRR out of and in resonance simulated with Lumerical's Finite-Difference Time-Domain solver, (c) design layouts and OM images of fabricated MRRs, (d) illustration of integrated strip MRR, (e) simulated spectral response of an MRR designed for different surface RIs, and (f) measured spectral responses of a fabricated MRR for measuring coated liquids of different RIs

Ref	Year	Type	Specificity	Sensitivity (nm/RIU)	Q Factor	Materials	Wavelength range	RI Range	sim /fab
[146]	2019	MRR	Fano Resonances in photonic Crystal	67	32000	Si-SiO2	1544.59nm	1.333-1.3346	sim
[147]	2020	MRR	Hybrid Plasmonic Wg	500	500	SiN-SiO2-Gold	1331nm	∼1.33	fab
[147]	2020	MRR	First Order mode Wg	200	10000	SiN-SiO2	1331nm	∼1.33	fab
[148]	2018	MRR	Hybrid Plasmonic Wg	800	70	Si-Gold	1470-1580	1-1.03	sim
[149]	2019	MRR	Metal-insulator-metal Wg Squared Ring	1320	∼19	Ag-Air	1300-1850	∼1	sim
[150]	2019	MRR	Transverse Magnetic Mode	233	6116	Si-SiO2	∼1570nm	∼1.33	fab
[156]	2018	MRR	2D Photonic Crystal ring resonator	690	1400	SiO2	∼1550nm	1.4-1.5	sim
[157]	2020	MRR	Plasmonic resonator w array of silver nano-dots	1240	20.9	Ag-Air	800-1600nm	∼1	sim
[158]	2016	MRR	Dispersion enhanced critical Coupling	57	15000	Si-SiO2	∼1550nm	1-1.477	fab
[159]	2017	MRR	Slot Waveguide	42	6500	GeAsSe-SiO2	1551.03	1.33-1.43	sim
[160]	2019	MRR	Wg dimension optimisation	229	1339	Si-SiO2	∼1550nm	1.35-1.401	sim
[161]	2016	MRR	Subwavelength grating Wg & TM mode	490	7000	Si-SiO2	∼1550nm	∼1.33	fab
[162]	2019	MRR	2D Photonic Crystal ring resonator	450	12245	Si	∼1550nm	∼1	sim
[163]	2020	MRR	Slot Wg	476	1900	Si-SiO2	∼1550nm	∼1.33	fab
[164]	2019	MRR	Double ring-resonator	1145	2820	Si-SiO2	∼1550nm	1-1.34	sim
[165]	2017	MRR	Fano resonances in subwg grating ring	366	12900	Si-SiO2	∼1550nm	∼1.33	fab
[166]	2016	MRR -MZI	MRR in an MZI	154,84	6400.8 -3902.5	Polymer	∼1550nm	1-1.33	fab
[167]	2017	MRR	Subwavelength grating Wg	427	9800	Si-SiO2	1550nm	∼1.33	fab
[168]	2018	MRR	Strip Wg	70,8	59000	Al2O3-SiO2	∼1565nm	∼1.33	fab
[169]	2017	MRR	Hybrid strip-slot Wg	106,29	18500	Si-SiO2	∼1550nm	∼1.33	sim
[170]	2019	MRR	Slot Wg	300	-	Si-SiO2	∼1550nm	∼1	fab
[171]	2018	MRR	Metal-insulator-metal Wg	1383	127	Si-Ag	1800-1960	1.33-1.35	sim
[151]	2019	Fabry -Perot	nano-hole array on gold reflector	593	210	SiO2-Gold	750-800nm	1.33-1.38	fab
[152]	2019	Fabry -Perot	Femto-Laser Micromachining	1181,4	-	SiO2	∼1550nm	1.2962-1.3828	fab

Table 3.2: List of recent integrated resonators for applications in refractometry

3.2.3 Plasmonics

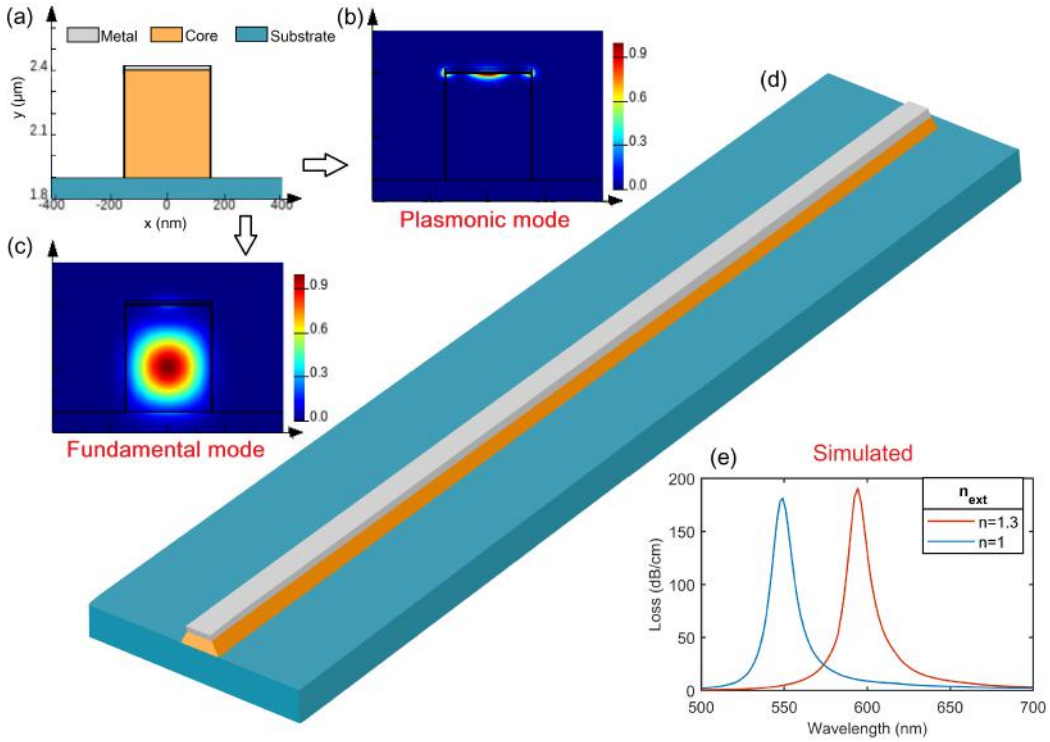

Figure 3.3: Hybrid plasmonic waveguide design for typical integrated plasmonic refractometer: (a) illustration of a hybrid plasmonic waveguide cross section, (b) simulated optical field of plasmonic mode, (c) simulated optical field of fundamental dielectric waveguide TM mode, (d) illustration of integrated hybrid plasmonic waveguide, and (e) fundamental mode loss versus wavelength for different surface RIs. Note: simulations have been performed with Lumerical's mode solver

Surface Plasmon Resonance (SPR) [172, 173, 174, 175] is exploited as the basis for numerous chemical sensors. SPR is based on the physical principle of resonant oscillation of free conduction electrons excited at the interface of two specific media (generally one dielectric and one **metallic**) by lightwave of a particular wavelength and angle of incidence. The optical coupling to a surface plasmon wave is defined by the relationship [176, 174] : $2\pi/\lambda \cdot n_c sin(\theta) = RE(k_{SP})$ where $RE(k_{SP})$ is the real part of the surface plasmon's (SP) propagation constant and θ the incident angle.

In integrated optics, plasmonic resonance is typically generated either using Kretschmann-based configurations [79] or with hybrid plasmonic waveguides [177, 178]. Refractometric measurements are generally performed by studying the reflectivity (or transmissivity in the case of a waveguide) of the device. Figure 3.3 simulates preliminary results from a typical plasmonic refractometer that has been

designed for illustration purpose.

SPR techniques can enable very sensitive probes to be developed for boundary perturbations and, while they are mainly directed toward bio-sensing [174] through the use of antigens-activated surface coating, they have also been widely demonstrated for gas sensing applications [63, 69, 79, 66]. However, despite their high sensitivity to the external environment, related to the large amplitude plasmon-induced evanescent field, SPR-based sensors exhibit very low Q-factors, which can complicate tracking of the resonance peak(s) and limit the sensor performance. SPs are also typically very lossy [174], which significantly limits the propagation length over which they can be used to interact with the external environment. Lastly, they rely on very strict manufacturing processes involving metals (thus increasing their fabrication difficulty) which render their integration on dielectric photonic infrastructures more complex. Nonetheless, plasmonic devices, with their promising properties, have been utilized in combination with multiple sensing schemes, such as interferometers [132] or resonators [148], to achieve a higher degree of optical interaction with the external environment. Table 3.2.3 summarizes the performances of the state-of-the-art on SPR used as refractometric sensors from 2016 to 2020.

Ref	Year	Type	Specifics	Sensitivity (nm/RIU)	FOM	Materials	Wavelength range	RI Range	sim /fab
[69]	2017	SPR-int	Reflectance study of GO coated gold	449,63	11	Graphene-Au-Si	500-900nm	1-1.44	fab
[175]	2020	SPR-int	grating-assisted coupling & based on Fabry-Perot Cavity	1820	293,15	Si-Ag-SiO2	∼2403.8nm	∼1.33	sim
[173]	2017	SPR-int	nano-slits structured metal layer	1020	614	MGF2-SiO2-Ag	1300-1500nm	1.33-1.8	sim
[177]	2019	SPR-hyb	nano-cavity based on hybrid plasmonic Wg	787,5	26.3	MoS2-BCB-PMMA	∼1701nm	1-1.24	sim
[178]	2016	SPR-hyb	Hybrid Plasmonic Wg	1423	128	Si-Ag-SiO2	∼1472nm	1-1.01	sim
[179]	2016	SPR-hyb	Rectangular cavity Fano resonance	1550	20	Gold-SiO2	1550-1630nm	∼1	sim
[180]	2017	SPR-int	Plasmonic grating	1140	271	Gold-GaN	∼1550nm	1.33-1.37	sim
[181]	2020	SPR-int	Periodic nano structures	1000	300	Gold-PMMA	∼1340nm	∼1.33	sim
[182]	2018	SPR-hyb	Side-Coupling to 2 fano-cavities	1295	54,13	Ag-Air	∼1300nm	1-1.2	sim
[183]	2017	SPR-hyb	nano-holes array above integrated photodiode	1200	14	al-Air	1100-1600nm	∼1	fab
[184]	2020	SPR-hyb	plasmonic crystal formed by nanogap tile array	216	-	Si-SiO2-Ag	1450-1650nm	1.5-1.65	fab
[185]	2017	SPR-int	Plasmonic squared resonator with nano-rods	2320	20	Ag-Air	∼2279nm	1	sim

Table 3.3: List of recent integrated plasmonic structures for applications in refractometry

3.2.4 Diffraction Gratings

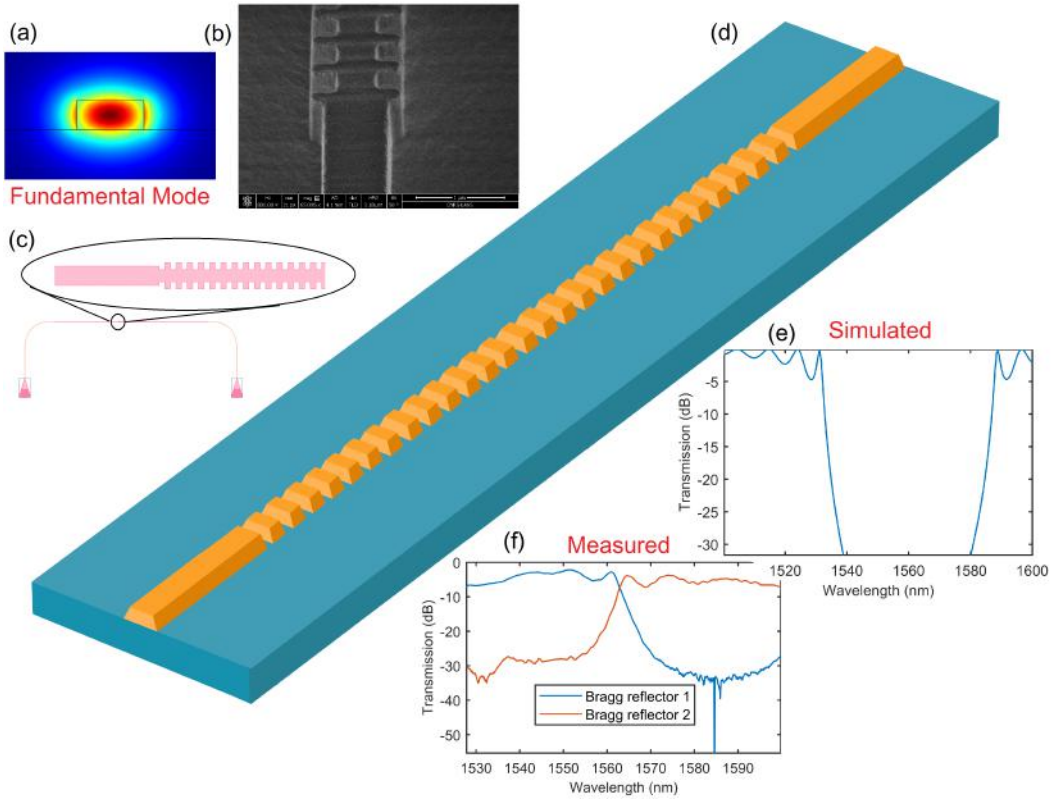

Figure 3.4: Bragg reflector design in typical integrated grating: (a) propagating fundamental mode in a strip waveguide simulated with Lumerical's mode solver, (b) SEM picture of a fabricated BG waveguide, (c) layout of the fabricated BG, (d) illustration of integrated strip BG waveguide, (e) EigenMode Expansion simulation of the spectral response (in transmission) of a designed BG waveguide, and (f) measured spectral responses (in transmission) of two fabricated BG waveguides

Diffraction gratings are **periodic** structures that are used to manipulate light to perform numerous optical functions. In integrated optics or fiber optics, they are usually implemented via periodic modulation of the RI profile of the waveguide core. Gratings diffract light at specific wavelengths so that different mode coupling functions can be obtained. These functions can generally be associated with three types of gratings, each depending on the grating's modulation period:

1. Bragg gratings (BGs): they serve mainly as wavelength-selective reflectors. BGs are typically modulated with short periods that satisfy the Bragg condition $\lambda_{Bragg} = 2n_{eff}\Omega$, where Ω is the grating period, and can therefore be used as refractometers if n_{eff} is made sensitive to the sensed region. They exhibit average-level sensitivities but can be designed to have high quality

factors as their spectral transmission features can be modified using various apodization functions [186], such as phase-shifted BG modulations.

2. Grating couplers: these are usually used for in-coupling of an incident beam to the surface of a photonic chip [113]. For the coupling to occur, the phase match between the grating and the incident beam must satisfy the condition $n_{eff} - n_c sin(\theta) = \lambda/\Omega$ where n_c is the cladding RI, and θ the beam's incident angle. This property renders grating couplers suitable as components to realize refractometers, or even gas sensors [187].

3. Long period gratings (LPGs): these structures can couple selected co-propagative modes at specific wavelength(s). This operation takes place when a phase-matching equation is satisfied between the two modes to couple, given by: $n_{eff_j} - n_{eff_l} = \frac{\lambda_{res}}{\Omega}$, where j and l are the two modes to couple, and λ_{res} is the resonant wavelength. In LPGs, grating periods are generally multiple times longer than the excitation wavelength. Typically used in fibers to allow optical energy to be coupled from the core mode to cladding modes that can interact with the external environment, LPGs can offer specific optical properties and these have been investigated for the design of high sensitivity refractometers in this thesis.

Table 3.2.5 summarizes the performances of the state-of-the-art of diffraction gratings used as refractometric sensors from 2016 to 2020.

3.2.5 Photonic Crystals

The propagation of electrons in a semiconductor is controlled by the interaction of electron waves with the **crystal lattice** of the material, forming electronic bandgaps that prohibit certain energy levels to be occupied. By analogy, photonic crystals (PhC) are micro/nano-structures that prohibit the propagation of certain electromagnetic waves through the principle of photonic bandgaps. PhCs are structures defined by macroscopic periodically arranged media of different dielectric constants where diffraction and interferences at their boundaries form the main mechanisms at the origin of their wavelength-selective transmission behavior.

As certain gratings can typically be approximated to 1D-PhCs, the unique properties of the multi-directional PhCs allow a very specific spectral tailoring that can be used for the design of integrated refractometers, and thus gas sensors. Most of these devices are based on 1D or 2D PhC waveguides [188], sometimes forming PhC cavities [189, 190, 191], or are based on free-space reflection from PhC surfaces [192]. Figure 3.5 shows simulated refractometric results of a PhC waveguide. The theoretical expressions of PhCs sensitivities and quality factors typically depend on the optical architecture, but is generally similar to those of resonators [193].

The main PhC properties that can generally be exploited for refractometry are: firstly, in PhC waveguides, the group velocity of the propagating waves can be manipulated to increase the penetration of the field into the cladding. This causes

a stronger interaction of the mode field with the analyte, which is a key advantage for better ease of integration to other refractometric schemes. Additionally, PhC cavities can exhibit very high quality factors, which can potentially enable high precision measurement. Similar to Bragg gratings, the introduction of local defects for phase-shifting is a method generally adopted for apodization of the spectral features. The main limitation for the commercialization of such sensors is, however, related to the need for both precision and resolution in the fabrication process of such structures. The design specificities for spectral tailoring of PhCs are still the subject of very active research in the scientific community.

Like PhCs, meta-materials are micro-structures that operate on the periodic micro-structuration of specific media for photonic manipulation. The main difference being that the lattice parameters are much smaller than the wavelength of light so that diffraction is negligible [194].Yet, while meta-materials are a recent field of research, their capacity to modulate RI to negative values makes them very promising candidates for integrated refractometry [195]. Table 3.2.5 summarizes the performances of the state-of-the-art of PhCs used as refractometric sensors from 2016 to 2020.

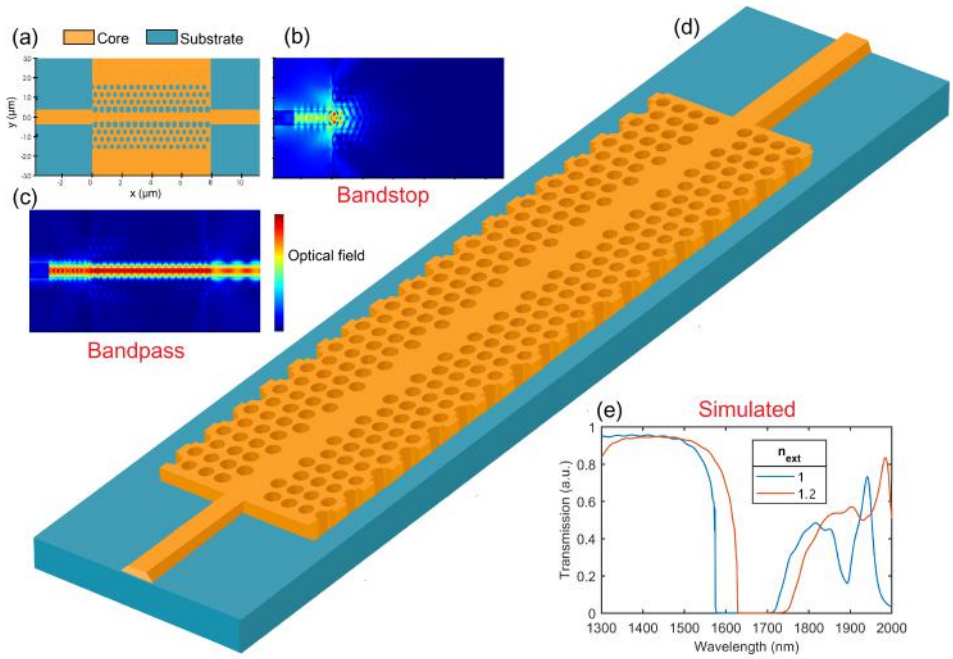

Figure 3.5: Waveguide design based on PhC: (a) surface profile of PhC waveguide, (b) optical field profile of waveguide for injected bandstop wavelength simulated with Lumercial's FDTD solver (cf [11]), (c) optical field profile of waveguide for injected bandpass wavelength, (d) schematic illustration of integrated PhC waveguide, and (e) simulated transmitted spectral response of PhC waveguide for different surface RIs

Ref	Year	Type	Specifics	Sensitivity (nm/RIU)	Q factor	Materials	Wavelength range (nm)	RI Range	sim /fab
[189]	2017	PhC cav	1D PhC nanobeam cavity	170,6	20000	Si-SiO2	1300-1450	∼1	sim
[188]	2016	PhC Wg	Complex refractive index sensing	139	35000	Si-SiO2	1500-1630	∼1.33	fab
[190]	2017	PhC cav	1D PhC nanobeam cavity with bandstop filter	252	12700	Si-Air	1521.74	∼1	sim
[196]	2016	PhC cav	Parallel 2D PhC cavities	62,5	15000	Si-SiO2	∼1550nm	∼1	sim
[192]	2017	PhC ref	Normal incidence Fano resonance measurement	94,5	32000	Si-SiO2	1465-1572	∼1.33	fab
[191]	2018	PhC cav	non-uniform 1D PhC cavity coupling	117	10000	Si-SiO2	∼1660nm	1.33-1.43	sim
[197]	2017	PhC cav	side-coupled 1D PhC nanobeam cavity air-mode	105,5	9055	Si-SiO2	∼1575.62	∼1.33	fab
[198]	2017	PhC cav	side-coupled 1D PhC nanobeam cavity dielectric-mode	254,6	1817	Si-SiO2	∼1522.65	∼1.33	fab
[199]	2018	PhC cav	2D PhC round cavity default	720	30	GaAs-SiO2	∼1310nm	∼1.36	fab
[200]	2019	PhC cav	1D PhC nanobeam cavity	326,1	1144	Si-SiO2	∼2000nm	∼1.33	fab
[193]	2019	PhC cav	Multi-Slot PhC Cavity	586	3500-4200	Si-SiO2	∼1550nm	∼1.33	fab
[201]	2016	PhC cav	Face-shaped 2D PhC cavity	359	477	Si-SiO2	∼1490nm	∼1.33	sim
[202]	2016	PhC cav	1D PhC nanobeam cavity with PhC filter	123,3	2200	-	∼1550nm	1-1.3	sim
[203]	2016	PhC cav	1D PhC nanobeam tapered cavity	390	13500	-	1621.7-1633.4	∼1.33	sim

Table 3.4: List of recent integrated photonic crystal structures for applications in refractometry

Ref	Year	Type	Specifics	Sensitivity (nm/RIU)	Q Factor	Materials	Wavelength range (nm)	RI Range	sim /fab
[204]	2018	Gratings GC	1D gratings with integrated photo-receptor	165	Q∼87.5	Si-SiN	400-700	∼1.33	fab
[205]	2018	Gratings BR	Cladding modulated bragg grating	322	4000	Si-SiO2	∼1550nm	1.33-1.38	sim
[206]	2018	Gratings BR	MRR-assisted slot phase shifted bragg grating	297,13	2000	Si-SiO2	∼1550nm	1.33-1.38	sim
[207]	2017	Gratings GC	Suspended grating coupler	400	20	SU8	∼1550nm	1.33-1.36	fab
[208]	2019	Gratings LPG	Rib Waveguide Long Period Grating	246	410	BK-7	1557.5nm	1.3154-1.3462	fab
[209]	2019	Gratings BR	Multi-Box subwavelength phase shifted bragg grating	579,2	8000	Si-SiO2	∼1550nm	∼1.33	fab
[210]	2020	Gratings BR	Comb-like assymetric double gratings	352	860	Si-SiO2	∼1550nm	∼1.33	fab
[211]	2019	Gratings BR	Plasmonic hybrid Wg	856	217	Si-SiN-SiO2-Ag	∼1550nm	∼1	sim

Table 3.5: List of recent integrated grating structures for applications in refractometry

3.2.6 State of the Art discussion

It can be observed in figure 3.6 that while interferometric and plasmonic sensors exhibit the highest sensitivities, they are typically associated with large or periodic spectral signatures, which can potentially complicate accurate readings of their spectral position and shift. Resonators and photonic crystals, while inherently limited in sensitivities, demonstrate high quality factors, which translate into very sharp spectral patterns. Although these can facilitate accurate determination of the resonance position, they are nevertheless comparatively more dependent on the manufacturing quality. Finally, diffraction gratings can potentially demonstrate spectral profiles of either types and appear to be flexible structures, which suggest an important potential for the design of high performance refractometers. In the rest of this thesis, the development of a grating waveguide type is presented: the integrated long period grating, or long period waveguide grating (LPWG) .

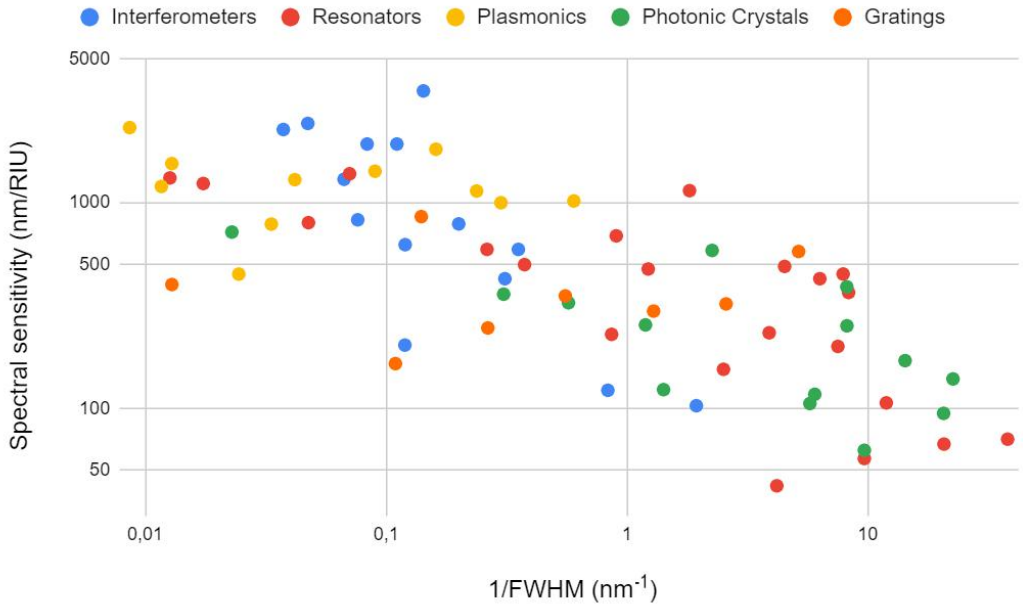

Figure 3.6: Spectral sensitivity versus inversed FWHM for five integrated refractometer types in NIR

Chapter 4

Theory of the Long Period Grating

Contents

4.1 Operating Principles of Long Period Gratings

This section focuses on the theory and principles behind Long Period Gratings (LPGs) with the aim to provide the tools and insight as to the choice of this particular structure for development into efficient integrated refractometers for gas sensing.

4.1.1 Brief History of the Long Period Grating

Beginning in the 1960s, research on the optical fiber was mainly devoted to reducing the optical attenuation in long fibers to cater to the fast developing field of optical telecommunication. The final aim then was to develop optical fibers as the superior component in the telecommunication sector as an alternative to the electrical wire in terms of price and performance (this was finally achieved in the 80s).

The optical losses in a fiber were found to be mainly related to manufacturing imperfections. The resulting non-uniform RI profile along the propagation axis of the early as-fabricated optical fiber was identified to be the cause of energy losses. This is largely due to diffraction that induces coupling to radiation modes. Further investigation led to the understanding that modulating the RI profile could be

used to enhance the exchange of energy between the different optical modes supported by a waveguide. In fact, in the years 1972-1974, Snyder, Taylor and Yariv, independently theorized on the power transfer between optical modes by means of internal waveguide perturbations and reviewed the main practical applications [57, 212]. In 1978, the photosensitivity in Germanium-doped optical fibers was first reported, enabling RI profile structuring of the fiber. This was rapidly followed, in the same year, by the demonstration of the first fiber Bragg grating (FBG) by Hill *et al* [213]. This FBG was used as a reflection filter, where contra-propagative mode coupling was induced by a periodic modulation of the fiber core (index) that had been inscribed by UV laser interference patterning. This was followed by the demonstration of the first LPG in 1990 by Hill *et al* to perform inter-modal energy exchange between fiber modes LP01 and LP11 [214]. However, the term "long period grating" was only connotated several years later in 1995 [215][216] after extensive analysis as these latter gratings, while similar to the original FBG, were composed of a much larger RI modulation pitch that was required for inter-modal coupling. Since then, numerous applications relying on this mechanism have been proposed for telecommunication [217] (filters, polarization couplers, multiplexers) and sensing applications [218]. Various technical approaches have also been proposed to fabricate LPGs in guided-wave media, in particular, to facilitate manufacturing LPGs in an optical fiber. These include local corrugation [219], tapering [220], laser irradiation, UV inscription, arc discharge [221], and, lately, lithography as will be presented in the following sections.

4.1.2 Coupled Mode Theory for Long Period Gratings

Solutions to Maxwell equations can typically be obtained by using the **Eigenmode approach**. This technique can be employed to significantly facilitate the understanding and modeling of the energy distribution and propagation of a mode within an optical waveguide, for which transverse and longitudinal electric and magnetic profiles can be separately formulated.

Snyder [57], and Taylor and Yariv [212] later proposed the use of a classical method for the analysis of vibrational systems coupling, widely known as **Coupled Mode Theory** (CMT) , to be applied on the mode equations to model optical coupling in perturbed waveguides. This approach was detailed a decade later by Snyder and Love in *Optical Waveguide Theory* [12], fully theorizing the optical effects of waveguide modulations (periodic structuring, apodization, etc) exerted on waveguides and predicting the future manipulation of the coupling effects. This section will review the mathematical demonstrations of the LPG's coupling mechanism, beginning with Maxwell equations to the simplified LPG coupling conditions. To summarize the following section, the Lorentz reciprocity theorem [222] together with Ostrogradski's divergence theorem are firstly formulated for optical waves to demonstrate **modal orthogonality** in a waveguide, from which (orthogonality) perturbation is shown to possibly enable energy coupling. The model is then analyzed to derive the mode coupling equations that depend on the perturbation pro-

files. Finally, the **resonance conditions** as well as **coupling rates** are described for the case of co-propagative mode coupling.

4.1.2.1 Reciprocity Theorem and Modal Orthogonality

Helmholtz's reciprocity theorem states that a ray of light and its reverse ray encounter matched "optical adventures". This can be related to the Lorentz reciprocity theorem that can be used to demonstrate the orthogonality of bound, radiative and leaky modes in waveguides [12]. The Maxwell curl equations [223] in dielectric material are given by

$$\begin{aligned} \nabla \times E &= -\mu \frac{\partial H}{\partial t} \\ \nabla \times H &= J + \varepsilon \frac{\partial E}{\partial t}, \end{aligned} \tag{4.1}$$

where E is the electric field vector, H the magnetic field vector, ε the permittivity, μ the permeability and J the electric current density. Since electromagnetic (EM) waves are oscillatory systems, the curls can also be expressed in the complex frequency domain using Fourier transform formulation:

$$\begin{aligned} \nabla \times E &= i\omega\mu H \\ \nabla \times H &= J - i\omega\varepsilon E, \end{aligned} \tag{4.2}$$

where ω is the angular frequency of the EM wave.

Using vector identities, the generalized Lorentz reciprocity theorem, can then be retrieved as given by [222]

$$H \cdot (\nabla \times E) - E \cdot (\nabla \times H) = \nabla \cdot (E \times H) \tag{4.3}$$

for each vector E and H. When two different EM wave systems *1* and *2* are studied, substituting equation (4.2) into equation (4.3) and considering the permeability μ as being equal to the free-space value μ_0 everywhere result in a vector identity of the form [57, 12]:

$$\nabla \cdot [E_1 \times H_2 - E_2 \times H_1] = i\omega(\varepsilon_2 - \varepsilon_1) E_1 \cdot E_2 + E_2 \cdot J_1 - E_1 \cdot J_2 \tag{4.4}$$

We now suppose a dielectric guided-wave system whose geometry supports several modal solutions by considering a dielectric lossless medium (material is reciprocal with $\varepsilon = \varepsilon*$). The solutions to the propagation in a z-invariant waveguide takes the form of a discrete set of modes j for which optical fields can be described as

$$\begin{aligned} E_j(x, y, z, t) &= e_j(x, y) e^{i(\beta_n z - \omega t)}, \\ H_j(x, y, z, t) &= h_j(x, y) e^{i(\beta_n z - \omega t)} \end{aligned} \tag{4.5}$$

where β_j is the modal propagation constant of a mode j, and e_j and h_j are the corresponding electric and magnetic mode profiles. The mode profile can be further described by the transverse and normal field components as [12]

$$\begin{aligned} e_j(x,y) &= e_{transverse,j}(x,y) + e_{z,j}(x,y)\cdot\widehat{z} \\ h_j(x,y) &= h_{transverse,j}(x,y) + h_{z,j}(x,y)\cdot\widehat{z} \end{aligned} \tag{4.6}$$

where $\widehat{z}$ is the unit space vector parallel to the waveguide [12]. The modal propagation can be seen as a continuum of cross-sectional solutions to Maxwell's equations along z-axis.

For simplicity, the normal field components of bound modes are neglected from here, without loss of generality. Note that the following calculations could incorporate normal components and still remain valid [57] but may require the use of a conjugated field form to ensure that the field norm is real.

Next, Ostrogradski's divergence theorem is applied on a volume of infinitesimal thickness to result in the general integral vector property F that is defined as [12]

$$\int_S \nabla\cdot F\ dS = \frac{\partial}{\partial z}\int_S F\cdot\widehat{z}\ dS + \oint_L F\cdot\widehat{n}\ dl \tag{4.7}$$

This two-dimensional form of the divergence theorem can be used to study the relationships between cross-sectional profiles of modes j and k. By firstly writing $F = [E_j \times H_k - E_k \times H_j]$ [1] in equation (4.7), the linear integral part is null when taking the infinite cross-section of the geometry, as it is supposed that the modes fields are the result of bound modes whose optical fields decay exponentially away from the guiding region. We then obtain the vector identity between bound modes j and k such that

$$\int_S \nabla\cdot[E_j\times H_k - E_k\times H_j]\ dS = \frac{\partial}{\partial z}\int_S [E_j\times H_k - E_k\times H_j]\cdot\widehat{z}\ dS \tag{4.8}$$

We next consider a waveguide region free from optical sources in order to study mode relationships. Hence, $J_j = J_k = 0$ and since the studied modes are solutions to the same cross-section profile of the waveguide, $\varepsilon_j = \varepsilon_k = \varepsilon(z)$, then the right term of equation (4.4) is equal to zero. Now, by substituting the stationary term of equation (4.5) into equation (4.8), the left term of equation (4.8) becomes null and we obtain [12] [2]:

$$(\beta_j + \beta_k)\int_S (e_j\times h_k - e_k\times h_j)\cdot\widehat{z}\ dS = 0 \tag{4.9}$$

Because the relationship between a forward-propagating mode k and its backward propagating counterpart -k can be described by [12]:

[1] This function relates to the Poynting vector used to describe power flux

[2] Note that in complex vector space we have $(c*V_1)\cdot V_2 = \overline{c}*(V1\cdot V2)$ and $(c*V_1)\times V_2 = c*(V_1\times V_2)$ where $\overline{c}$ denotes complex conjugate of c

$$e_{-k} = e_k \quad , \quad h_{-k} = -h_k \quad , \quad \beta_k = -\beta_{-k} \tag{4.10}$$

Equation (4.9) can be rewritten in the form

$$(\beta_j - \beta_k) \int_S (e_j \times h_k + e_k \times h_j) \cdot \hat{z} dS = 0 \tag{4.11}$$

By subtracting and adding both equations (4.9) and (4.11), the relationship between each bound mode supported by the waveguide demonstrates mode orthogonality as follows[12][3]dS :

$$\int_S e_j \times h_k \cdot \hat{z} dS = \int_S e_k \times h_j \cdot \hat{z} dS = 0 \qquad \text{if j}\neq \text{ k} \tag{4.12}$$

which can subsequently be normalized to [12]

$$\frac{1}{2} \int_S \widehat{e}_j \times \widehat{h}_k \cdot \hat{z} dS = \frac{1}{2} \int_S \widehat{e}_k \times \widehat{h}_j \cdot \hat{z} dS = 0 \quad \text{if j}\neq \text{ k or 1 if j=k} \tag{4.13}$$

where $\widehat{e}_{j,k}$ and $\widehat{h}_{j,k}$ are respectively the normalized electric and magnetic fields of modes j and k.

Modal orthogonality demonstrates that not only the modes form a basis from which any EM field propagating in a waveguide can be developed as a finite linear combination of its base vectors (modes), but also that they do not interfere. This implies that a perturbation of this orthogonality due to waveguide non-uniformities, for example, could subsequently lead to possible interference/coupling between modes.

4.1.2.2 Coupling Equations and Perturbational Approach

Now, accounting for the conservation of energy, the total transverse fields $E_{total,t}$ and $H_{total,t}$ within a waveguide can be described as [12]

$$\begin{aligned} E_{total,t}(z) &= \sum_j [b_j(z) + b_{-j}(z)]\widehat{e}_{t,j} + \sum_j \int_0^\infty [b_j(z,Q) + b_{-j}(z,Q)]\widehat{e}_{t,j}(Q)dQ, \\ H_{total,t}(z) &= \sum_j [b_j(z) - b_{-j}(z)]\widehat{h}_{t,j} + \sum_j \int_0^\infty [b_j(z,Q) - b_{-j}(z,Q)]\widehat{h}_{t,j}(Q)dQ, \end{aligned} \tag{4.14}$$

where b_j and b_{-j} denote forward and backward propagating modes, respectively, containing modal amplitude and phase dependence, and the right integral denotes the continuum of radiation modes Q. Radiation mode coupling will be ignored

[3]Note: To normalize, we either need the vectors to be real here, or a conjugated version of the theorem [224] can be applied by defining the dot product of complex vectors V1 and V2 as an inner product, therefore respecting $< V_1, V_2 >= \overline{< V_2, V_1 >} = \int_S \overline{V_2} V_1$

as we assume a slowly varying waveguide approximation. Further, $b(z)$ can be decomposed into the modal amplitude and phase variation as follows:

$$b_{\pm j}(z) = a_{\pm j}(z)e^{\pm i\int_0^z \beta_j(z)dz} \tag{4.15}$$

where a is the modal amplitude that is constant in unperturbed waveguides for a given mode.

We now consider a perturbation to the dielectric profile so that ε is z-dependent. The objective is to determine the z-dependent coupling characteristics as the wave propagates into the perturbed waveguide or perturbed region of the waveguide. Assuming a system with solely one excited mode k when a perturbation is introduced, we aim to determine the mode energy distribution to calculate E_{total} and H_{total}. The following dielectric profile $\varepsilon(x, y, z)$ at z differs so that $\varepsilon(z) \neq \varepsilon(z + dz)$ at $(z + dz)$, which, assuming energy conservation, results in the right term of equation (4.4) becoming non-null:

$$\nabla \cdot [E_k \times H_{Total} - E_{Total} \times H_k] = i\omega[\varepsilon(z + dz) - \varepsilon(z)]E_k \cdot E_{total} \tag{4.16}$$

where $E_{k,t}$ and $H_{k,t}$ are the transverse fields of the studied mode k. We now integrate over an infinite surface perpendicular to z both sides of equation (4.16) to obtain:

$$\int_{S_\infty} \nabla \cdot [E_k \times H_{Total} - E_{Total} \times H_k]dS = i\omega \int_{S_\infty} (\varepsilon_{z+dz} - \varepsilon_z)E_k \cdot E_{total} \cdot dS \tag{4.17}$$

Substituting the stationary part of equation (4.5) and equation (4.8) into equation (4.17), and the properties of the inner product in complex plane, we have:

$$\frac{\partial}{\partial z}\int_{S_\infty} [\widehat{e}_k \times H_{Total} - E_{Total} \times \widehat{h}_k] \cdot \widehat{z}e^{-i\beta_k z}dS = i\omega \int_{S_\infty} (\varepsilon_{z+dz} - \varepsilon_z)\widehat{e}_k \cdot E_{total}e^{-i\beta_k z}dS$$

giving:

$$(\frac{\partial}{\partial z} - i\beta_k)\int_{S_\infty} [\widehat{e}_k \times H_{Total} - E_{Total} \times \widehat{h}_k] \cdot \widehat{z}dS = i\omega \int_{A_\infty} (\varepsilon_{z=dz} - \varepsilon_{z=0})\widehat{e}_k \cdot E_{total}dS \tag{4.18}$$

Next, by substituting equation (4.14) into the left term of equation (4.18) and taking into account orthogonality of modes for a given waveguide cross-section in equation (4.12), we obtain:

$$
\begin{aligned}
&(\frac{\partial}{\partial z} - i\beta_k) \int_{S_\infty} [\widehat{e}_k \times \left(\sum_j [b_j(z) - b_{-j}(z)]\widehat{h}_j \right) - \left(\sum_j [b_j(z) + b_{-j}(z)]\widehat{e}_j \right) \times \widehat{h}_k] \cdot \widehat{z} dS \\
&= (\frac{\partial}{\partial z} - i\beta_k) \int_{S_\infty} [\widehat{e}_k \times [b_k(z) - b_{-k}(z)]\widehat{h}_k - [b_k(z) + b_{-k}(z)]\widehat{e}_k \times \widehat{h}_k] \cdot \widehat{z} dS \\
&= (\frac{\partial}{\partial z} - i\beta_k)[-4\, b_{-k}(z)]
\end{aligned}
\tag{4.19}
$$

Using the mode conventions of equation (4.10), the coupled mode equations for contra-propagative and co-propagative modes can respectively be found as

$$
\begin{aligned}
\frac{db_{-k}}{dz} + i\beta_{-k} b_{-k} &= \frac{i}{4}\omega_- \int_{S_\infty} (\varepsilon_{z+dz} - \varepsilon_z)\widehat{e}_{-k} \cdot E_{total} dS \\
\frac{db_k}{dz} - i\beta_k b_k &= -\frac{i}{4}\omega_+ \int_{S_\infty} (\varepsilon_{z+dz} - \varepsilon_z)\widehat{e}_k \cdot E_{total} dS
\end{aligned}
\tag{4.20}
$$

where angular frequency w_+=-w_-. Finally, by substituting equation (4.14) into the right term of equation (4.20), the general coupled mode equation can be found as [12]

$$
\frac{db_k}{dz} - i\beta_k b_k = i \sum_j [C_{kj} b_j + C_{k-j} b_{-j}] \tag{4.21}
$$

with **coupling coefficients** in the form of

$$
C_{kj} = -\frac{\omega}{4} \int_{S_\infty} (\varepsilon_{z+dz} - \varepsilon_z)\widehat{e}_{t,k} \cdot \widehat{e}_{t,j} dS \quad \text{k}\neq \text{j, C}_{kk}\text{=0,} \tag{4.22}
$$

An alternative form of equation (4.22) based on the RI profile can be found by introducing $\varepsilon = \varepsilon_0 n^2$ and $\omega = 2\pi c/\lambda$ such that:

$$
C_{kj} = \frac{\pi}{2\lambda} \left(\frac{\varepsilon_0}{\mu_0} \right)^{1/2} \int_{S_\infty} (n^2_{z+dz} - n^2_z)\widehat{e}_{t,k}\widehat{e}_{t,j} dS \quad \text{k}\neq \text{j, C}_{kk}\text{=0,} \tag{4.23}
$$

where n_z is the z-dependent RI profile and λ is the excitation wavelength.

4.1.2.3 Coupling Rate and Phase-Matching Condition

Let us now consider a multimode waveguide whose core is sinusoidally modulated along z with a profile described by

$$
n^2(x, y, z) = n_0^2(x, y) + \delta n^2(x, y) * \sin \left(\frac{2\pi z}{\Omega} \right), \tag{4.24}
$$

with a core modulation period of Ω. Figure 4.1 illustrates several examples of sinusoidal modulation of step-index waveguides. Note, also, that graded-index waveg-

uide modulation could also be analyzed in a similar manner.

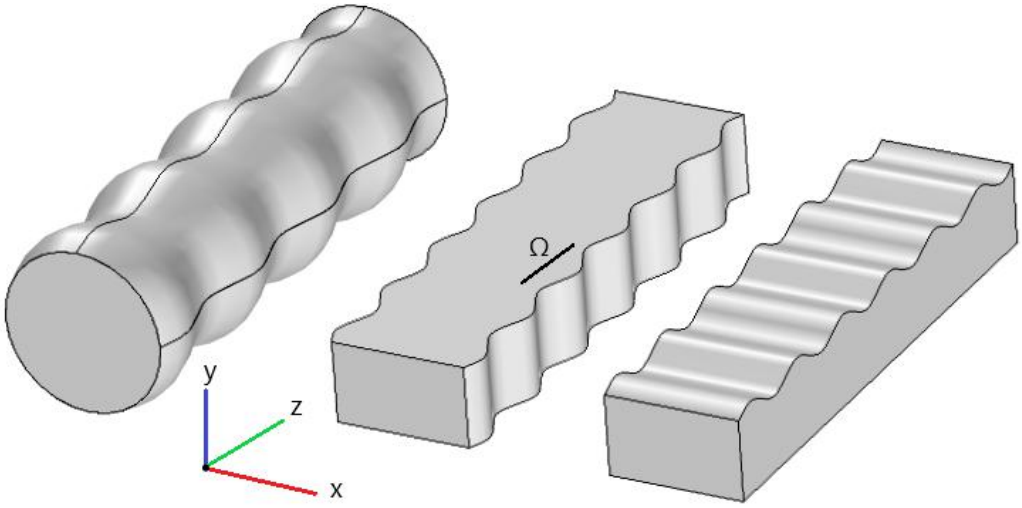

Figure 4.1: Examples of sinusoidally modulated step-index waveguides. Left to right: modulation in cylindrical waveguide, side modulation and surface modulation of a strip waveguide

To analyze the coupling between two modes k and j, equation (4.24) is introduced into equation (4.23). The z-profile of the coupling coefficient is then found to be of the form $C_{kj}(z) = \bar{C_{kj}} sin(2\pi z/\Omega)$. Here, we aim to study the modal amplitude of each mode along z. Substituting equation (4.15) into the coupled mode equation (4.21), and expanding the coupling coefficient using Euler's identity $sin(x) = (e^{ix} - e^{-ix})/2i$, we obtain the following system of differential equations:

$$\begin{aligned} \frac{da_k}{dz} &= a_j(z)\frac{\bar{C_{kj}}}{2}\left[e^{iz(\frac{2\pi}{\Omega}+\beta_l-\beta_k)} - e^{-iz(\frac{2\pi}{\Omega}+\beta_k-\beta_j)}\right] \\ \frac{da_l}{dz} &= a_k(z)\frac{\bar{C_{jk}}}{2}\left[e^{-iz(\frac{2\pi}{\Omega}+\beta_k-\beta_l)} - e^{iz(\frac{2\pi}{\Omega}+\beta_j-\beta_k)}\right] \end{aligned} \tag{4.25}$$

We set $\beta_k > \beta_j$, $a_k(z)_{z=0} = 1$ and $a_j(z)_{z=0} = 0$ and define the normalized modal power $P = |a|^2$. The differential equations can then be solved to obtain [12]

$$\begin{aligned} &P_k(z) = 1 - F^2 \sin^2\left(\frac{\bar{C_{kj}}}{2F}z\right) \quad \text{and} \quad P_j(z) = F^2 \sin^2\left(\frac{\bar{C_{kj}}}{2F}z\right) \\ &\text{with} \quad F = \frac{1}{\sqrt{1 + \frac{(\frac{2\pi}{\Omega}+\beta_j-\beta_k)^2}{\bar{C_{kj}}^2}}} \end{aligned} \tag{4.26}$$

The results are plotted in figure 4.2 illustrating that the exchange of energy

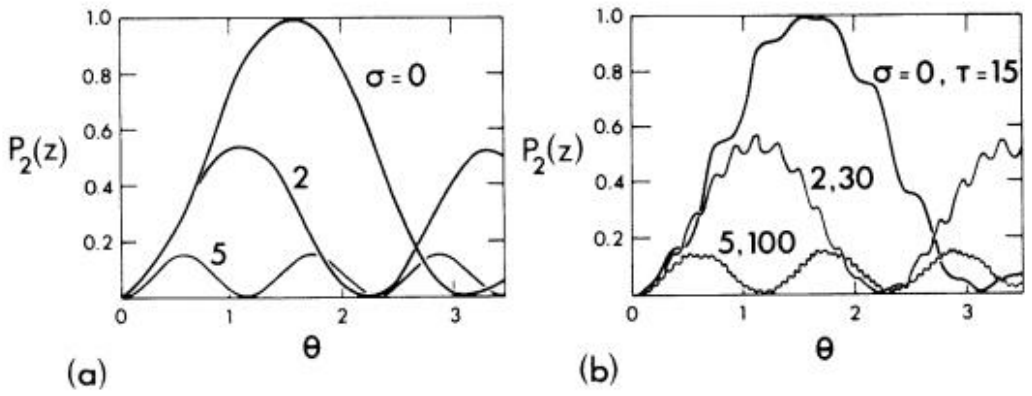

Figure 4.2: Illustration of the coupling profiles obtained for different values of the oscillatory terms in equation (4.25) [12]: (a) neglects the fast-oscillation terms, and (b) displays the effect of several values of the fast-oscillation terms on the coupling profile

depends on three main parameters:

1. Maximum coupling can be obtained when the modulation period satisfies the condition $\frac{2\pi}{\Omega} + \beta_l - \beta_k = 0$. In other terms, the **Phase-Matching Condition** can be given as

$$n_{eff_i} - n_{eff_j} = \frac{\lambda_{res}}{\Omega} \tag{4.27}$$

   where $n_{eff_{i,j}}$ denote the respective effective indices of modes i and j to couple, Ω the grating period and λ_{res} the center wavelength of the LPG's spectral pattern at which resonant energy transfer between modes is enabled.

2. The coupling coefficients determine the rate at which energy exchange is performed around resonance. The higher the coupling coefficient, the shorter is the distance for maximum coupling to occur. The minimum length for complete energy exchange between two modes at resonance can generally be approximated by $L_{opt} = \pi / \bar{C_{kj}}$. It can be deduced from equation (4.23) that the main contributions to the coupling strength, given by $\bar{C_{kj}}$, are the modulation amplitude and the optical field superposition in the modulated region, as previously detailed in [25].

3. Lastly, as illustrated in figure 4.2(b) [12], minor coupling oscillations of higher frequencies can be observed to superpose onto the main coupling resonance contribution. These are due to the "high frequency" oscillatory term in equation (4.25), i.e. $e^{iz(\frac{2\pi}{\Omega} + \beta_j - \beta_k)}$, when $\beta_j > \beta_k$. In most cases, this can be neglected as the oscillation amplitudes are inversely proportional to its frequency.

Additionally, it is suggested from the previous demonstration that other types of modulation profile with a suitable periodicity Ω that could satisfy the phase-matching condition could possibly lead to mode coupling. This can be explained by the modulation function that can be decomposed into a Fourier Series and expressed as

$$n^2(z) = n_0^2 + \sum_{m=1}^{\infty} a_m \cos\left(\frac{2\pi}{\Omega} mz\right) + \sum_{m=1}^{\infty} b_m \sin\left(\frac{2\pi}{\Omega} mz\right) \tag{4.28}$$

with a_m and b_m the Fourier coefficients. In case of odd functions, the cosine term is null. The coupling coefficients thus depend on these coefficients as well as the supported mode shapes (cf equations (4.23) and (4.24)).

In the context of this coupling behavior, LPGs are considered interesting candidates for the development of optical filters, as the coupling phenomenon is wavelength dependent. The phase-matching condition also influences or determines the diffraction angle of gratings and can thus be used to describe grating couplers and Bragg gratings. Moreover, it explains why longer periods are required to couple modes in long period fiber gratings (LPFGs) as they possess very close effective indices (EIs).

4.1.3 Simulation and Modeling Techniques for LPGs

4.1.3.1 Finite-Difference Time-Domain Techniques

Due to the difference in scale between its important longitudinal size and small width-modulation amplitude and wavelength, LPG simulations with standard techniques usually require large computing resources. In fact, LPFGs can generally size to several centimeters in length while their core are typically modulated over periods of hundreds of micrometers associated with micrometer-level amplitude variations and an RI varying over 10^{-3} RIU. Running parametric and optimization simulations would thus require high computing resources due to both the size of the LPGs and the mesh refinement constraints. Consequently, Finite-Difference Time-Domain (FDTD) or beam propagation method (BPM) are not suitable for fast and accurate simulation of LPGs. Nevertheless, these modeling techniques can provide interesting visual insights into the propagative coupling effects of LPGs. Figure 4.3 illustrates the longitudinal optical field profile of an LPWG on and off resonance, simulated with FDTD. Here, on resonance, the optical power is continuously transferred from the fundamental mode to a higher order mode.

4.1.3.2 EigenMode Expansion

EigenMode Expansion (EME) is an alternative method that has been intensively used to model integrated LPGs in this thesis. It is an efficient solution for analyzing periodically-modulated structures supporting bounded modes. In EME, the structure is firstly divided into slices transverse to the axis of propagation. The optical field of the supported modes is then calculated for each cross-section. Radiation modes here are taken into account by using simulation boundaries for which

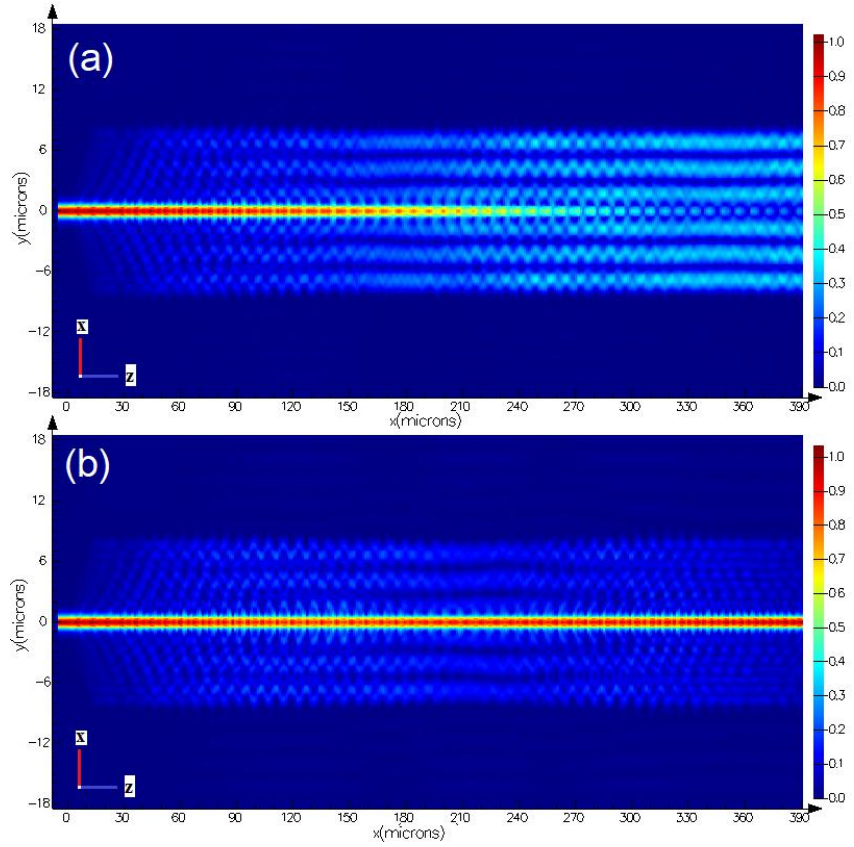

Figure 4.3: Optical intensity distribution seen from top surface: (a) on-resonance, showing a complete exchange of energy with HE7 mode, and (b) off-resonance, showing a negligible exchange of energy © 2021 IEEE

discretized expressions of radiation modes can be calculated. From this, scattering matrices are obtained from Maxwell equations applied on discrete boundaries, at slices interfaces. Then, an iterative field distribution is resolved along the propagation axis of the structure to study modal energy exchange. Because of the post-mode-calculation analysis which allows the setting of the structure's longitudinal profiles after the cross-sectional modal study, it is possible to optimize the LPG in terms of length and periodicity with relative ease.
While this modeling technique is widely employed among the photonic community, it is brought to light in this thesis that most commercial algorithms present some limitations that need to be addressed for accurate modeling of integrated waveguide coupling architectures such as LPG refractometers. In particular, two main issues might arise and prevent accurate simulation of the photonic circuits' wavelength responses:

1. High-order ($\geq$ 2) chromatic dispersion is usually neglected which prevents correct analysis of spectral characteristics and behaviors of certain structures. This could be critical, especially for highly sensitive LPG refractometers.

2. Variations of coupling coefficients over the spectrum are not taken into account, which can induce important variations in extinction ratios and transmission spectrum. This would typically affect integrated optical structures more than fiber components.

To circumvent these issues, custom algorithms using EME Lumerical solvers have been designed for all simulations in this thesis.

4.1.3.3 Coupled Local-Mode Theory for Long Period Waveguide Grating

Although the tools previously described are useful to simulate LPG response, these techniques still lack the ability to provide accurate insight on the photonic architecture's behavior, especially when certain parameters can affect simultaneously different properties of the structure's response. This subsection aims to summarize the published results in [25] where the modeling of a simple version of an integrated LPG was performed with EME and subsequently compared to a numerical solution of the Coupled Local-Mode Theory (CLMT) .

In practice, waveguide modulations cause the propagating mode shapes to vary along the propagation axis, hence modal equations might not be sufficiently accurate solutions to the Maxwell equations. Local modes are born from the concept that mode solutions of non-uniform waveguides can be used as approximations in finite regions [12]. The slowly varying waveguide approximation can also be used to more accurately model waveguides for which the mode field deformation induced by strong RI profile variations cannot be neglected. The main consequence here is that the propagation constants and coupling coefficients amplitudes may vary nonlinearly during propagation, and should be calculated for each cross-section of the waveguide before being injected into the coupled mode equations, henceforth denoted as CLMT equations.

We consider here a width-modulated strip waveguide structure, integrated on a Silicon-Nitride photonic platform, that supports a fundamental mode and several higher order modes. The structure will be developed in more detail in the next chapter. As previously explained, the structure is firstly sliced into multiple cross-sections for which modal analysis is used to obtain the mode profiles of the electric and magnetic fields. The coupling coefficients and propagation constants are then retrieved from the modal analysis and injected into a bespoke Matlab script to solve a set of the CLMT equations. EME is subsequently performed using Lumerical software to calculate scattering parameters and model the exchange of energy during propagation of the modes for comparison. Figure 4.4 shows the coupling behavior of the fundamental mode to several (selected) higher order modes during propagation, modeled using EME or CLMT for different mode coupling or wavelengths. Very similar results can be observed, which suggest the validity and accuracy of both models.

However, as discussed in detail in [25], each modeling method presents specific features. EME is a commercially available method that incorporates numerous add-

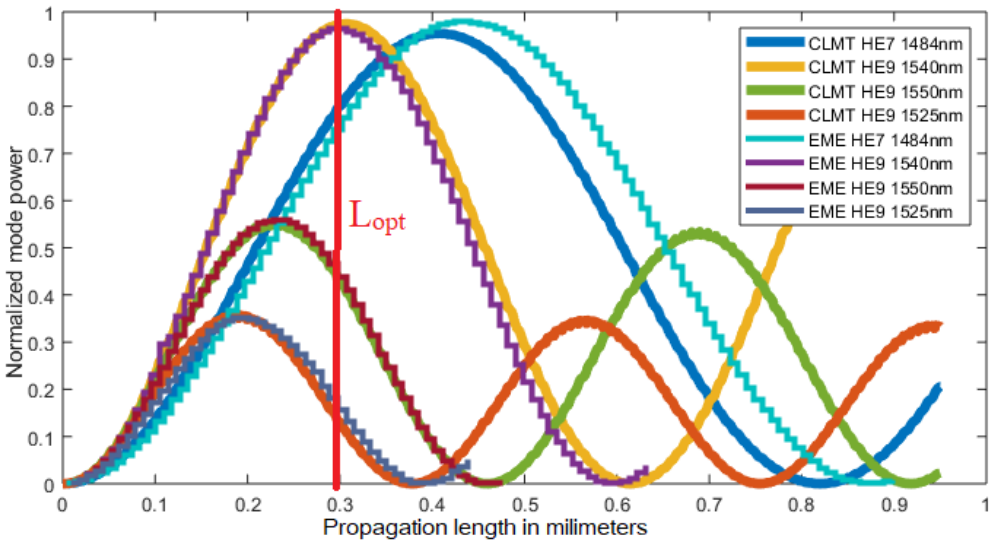

Figure 4.4: Example of normalized mode power versus propagation length for mode coupling of the fundamental mode to two higher order modes, HE7 and HE9, in an LPWG for different wavelengths, as simulated by CLMT and EME © 2021 IEEE

ons like parametric sweep, spectral study or includes modal analysis, which greatly facilitates optimization. EME also does not necessitate a slow-varying waveguide approximation to operate. On the other hand, CLMT is a more rigorous application of the coupling mechanism and provides relevant insight on the structure's behavior. By introducing the modulation profile's mathematical function into the coupling equations, the coupling coefficients can be derived to show that the coupling strength depends mainly on (1) the electric field superposition at the waveguide modulated interface for step-index modulations, (2) the modulation amplitude, and (3) the difference in EIs between coupled modes [25]. CLMT can thus greatly facilitate optimization of the waveguide design. Lastly, grating apodization simulation is facilitated by CLMT because the longitudinal modulation profile can be set separately from the transverse coupling coefficients.

4.1.3.4 Model for CLMT-induced Losses

As previously discussed, integrated waveguides tend to propagate modes at a much higher loss due to optical absorption and scattering that occur at the waveguide interfaces. This is due to the roughness and N-H bonds induced during waveguide fabrication. Modal propagation losses can be added to the CLMT model, by introducing modal scattering coefficients into the coupled mode equations. Both losses are proportional to the mode's optical amplitude [225], which modifies the general differential coupling equations (4.21) to become

$$\frac{db_k}{dz} - i\beta_k b_k = i\sum_j [C_{kj} b_j + C_{k-j} b_{-j}] - i * b_k * \alpha \tag{4.29}$$

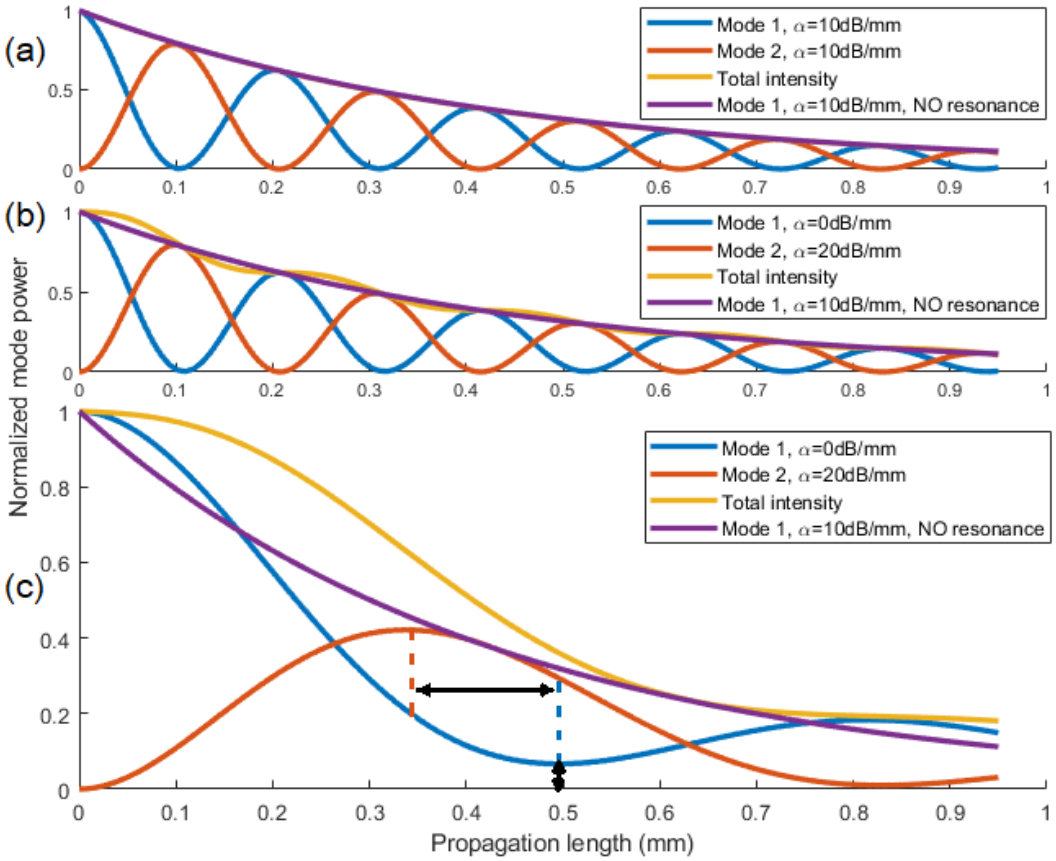

Figure 4.5: Mode power energy exchange versus propagation length for (a) modes of equal propagation losses, (b) modes of unequal propagation losses, and (c) modes of unequal propagation losses with low coupling strength

where α is the general loss coefficient.

Figure 4.5 plots the overall coupling behaviors for lossy waveguides. Figure 4.5(a) shows that, for a symmetrical loss behavior, the total mode intensity has the same behavior as that of a propagating non-coupling mode. Figure 4.5(b) shows that asymmetrical lossy behavior leads to irregular (oscillatory) energy loss over the propagation length. Figure 4.5(c) illustrates modes with lower coupling strength, which increases coupling perturbations due to propagation losses and asymmetrical behaviors. This further highlights the coupling dephasing and incomplete energy exchange (respectively indicated by arrows) that occur at each oscillation. Coupling losses should therefore be considered during the design of LPWGs in order to obtain qualitative extinction ratios.

4.1.4 Spectral Parameters

In addition to the position of the resonance on the spectrum given by equation (4.27), other LPG spectral features such as Full-Width Half-Maximum (FWHM or 3dB resonance bandwidth) or extinction ratio are, in most cases, critical. The FWHM of resonance dips/peaks that can be measured in the transmission spectra of LPGs can generally be derived from equation (4.26) by solving for half power transmission to obtain [40]:

$$FWHM \approx \frac{0.8\lambda_{res}^2}{L_{opt} \cdot \Delta n_{g,j,k}(\lambda_{res})} \tag{4.30}$$

where $\Delta n_{g,j,k} = n_{g,j} - n_{g,k}$. As described by equation (4.30) incorporating various group indices (GIs), the chromatic dispersion of the modes, propagation constants and optical profiles are wavelength dependent. Thus, to accurately determine the resonance spectral features would technically require the analysis of the modes as a function of the wavelength throughout the bandwidth of interest.

However, it is possible to numerically investigate the spectral characteristics of LPGs, in general, using different approximations. For example, over several simulation tests carried out, it is found that Lumerical approximates the propagation constant's dependence on wavelength with a first-order regression of the chromatic dispersion calculated at a single wavelength. However, this approximation becomes erroneous for systems that rely on dispersion enhancing techniques, as higher order dispersion contributions become significant. This concerns certain types of LPGs as will be described in the next sections.

4.2 LPG Theory for Refractometry

In this section, the use of LPGs for refractometric applications is described and theoretically analyzed. The subsequent optimization methods employed to improve the performance of the LPGs are also discussed.

4.2.1 Refractometric LPGs

The perturbation of an LPG refractometric system typically occurs through the interaction of the evanescent field of a mode with the target analyte, or external environment. This very interaction results in the modification of the propagation constants of the mode as a function of the RI variation associated with the concentration variation of the analyte. As defined by equation (4.27), the central wavelength of the resonance λ_{res} largely depends on the EI difference of the coupling modes. Changes in the LPG response can subsequently occur by performing mode coupling to a perturbed optical mode. LPGs have mainly been implemented in fiber platforms for their capacity in "unburying" inner core fields to induce relatively strong interaction with the external medium to be sensed. LPFG refractometers rely on the coupling between the fundamental core mode and a cladding mode; while

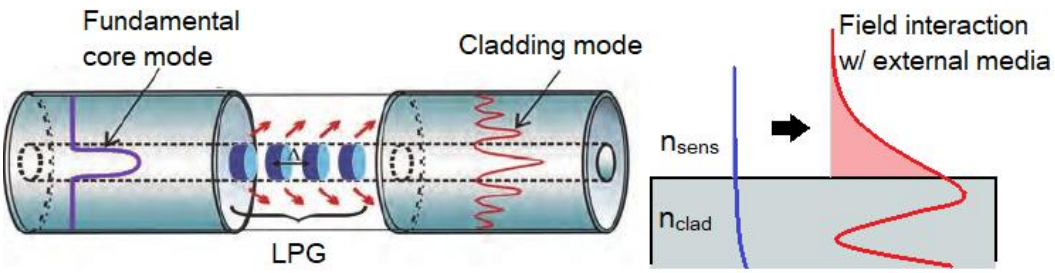

Figure 4.6: Illustration of fundamental mode coupling to cladding mode by an LPFG (left) [13], and the associated increase in field interaction with external media (right)

the core mode's EI is relatively insensitive to external influence, selected cladding modes can, on the other hand, interact substantially with the external medium or perturbation.

LPG refractometric sensors have been employed for numerous applications in the chemical sensing domain [226]. For example, solution concentration sensors are typically employed for saline [227] and glucose concentration [228] measurements due to the abundance of chemical processes that involve these two particular analytes. Further, since fiber LPGs can easily be deployed for *in situ* monitoring, they have been utilized to detect hydrocarbons [229] and monitor Volatile Organic Coumpounds (VOCs) in water [230]. In addition, LPGs have also been engineered to detect more complex bio-molecular analytes such as proteins [231], antibiotics [232], DNA [233] or even microorganism such as bacteria [234] and viruses [235]. These measurement schemes, however, require more elaborate chemical selectors, such as nano-particles [231], molecularly imprinted molecules [232], antigens [235] or antibodies [234] to functionalize the sensors.

Temperature sensing can also be achieved with LPGs, by either exploiting the difference between the intrinsic thermo-optic coefficients of the cladding and core materials or by coating the external region/surface with a material exhibiting high thermo-optic coefficient that can be sensed using an evanescent wave sensor configuration.

In the field of mechanical engineering or materials science, LPFGs have been principally been implemented for strain [236] and structural bend sensing [237]. The strain and torsion induced in the fiber lead to perturbation of the coupling mode parameters by the piezo-optical effect which can subsequently be demodulated to obtain the desired information.

An important point to be discussed is the particular property of the LPG response that is progressively created during the propagation of the coupling modes. For example, contrary to resonators or inteferometers (e.g. MZI), spectrum shifts are not the result of accumulated phase changes that are transcribed into interference patterns at multi-path junctions, but are actually due to the accumulation of

progressive coupling interferences which, in turn, depend on phase matching. This consequently enables LPGs to measure multiple RIs simultaneously while most interferometers only monitor the average RI "encountered" during propagation. A particular application of this feature is liquid level sensing [238] where the extinction ratio, which can simply be determined by measuring the transmission intensity at resonance, depends on the LPG length that is immersed in the target liquid. Further investigation of this property with different numerical models suggests that the correct operation of multi-RI analysis would require specific environmental conditions. The analysis shows that LPGs comprising multiple sequentially separated length sections with different external RIs can, in fact, scramble the optical response. This property could also be potentially utilized in the future for novel application areas if more reliable demultiplexing algorithms could be developed.

4.2.2 Analysis of LPG Refractometric Performance

The spectral sensitivity of evanescent wave LPG sensors is usually assessed by the resonance spectrum shift per unit change in RI of the external region. In order to clearly identify the main LPG parameters involved in the spectral sensitivity with the final aim to optimize the LPG structures, an analytical formula of the sensitivity that is derived from the previously demonstrated phase-matching condition as described by equation 4.27 is developed and proposed.

Suppose that an LPG of period Ω can support two modes j and k with EIs $n_{eff,j,1}(\lambda, n_{ext,1})$ and $n_{eff,k,1}(\lambda, n_{ext,1})$, respectively, where 1 represents a system with external index $n_{sens,1}$. We also assume that the coupling coefficients are non-negligible at resonance, and are obtained for a wavelength $\lambda_{res,1}$, defined by the phase-matching condition in equation (4.27). A disturbance of the external conditions now induces a change in the external RI from $n_{ext,1}$ to $n_{ext,2}$ that subsequently leads to variations in the modes' EIs, the values of which have been described at the beginning of the chapter during the definition of the waveguide sensitivity. The newly obtained resonance position on the transmission spectrum now becomes $\lambda_{res,2}$. Since the grating period has not changed, the phase-matching equation can thus be written as follows:

$$\Omega = \frac{\lambda_{res,1}}{n_{eff,j,1} - n_{eff,k,1}} = \frac{\lambda_{res,2}}{n_{eff,j,2} - n_{eff,k,2}} \tag{4.31}$$

It is assumed here that the perturbation is sufficiently small so that a first order Taylor approximation for each mode's EI can be used and expressed as:

$$n_{eff,n,2}(\lambda_{res,2}) = n_{eff,n,1}(\lambda_{res,1}) + \Delta_{\lambda_{res}} \frac{\partial n_{eff,n,1}}{\partial \lambda}(\lambda_{res,1}) + \Delta_{n_{ext}} \frac{\partial, n_{eff,n,1}}{\partial n_{ext}}(\lambda_{res,1}) \tag{4.32}$$

with $\Delta_{\lambda_{res}} = \lambda_{res,2} - \lambda_{res,1}$ and $\Delta_{n_{ext}} = n_{ext,2} - n_{ext,1}$.

By injecting equation (4.32) into equation (4.31), we then obtain:

$$\frac{\Delta_{\lambda_{res}}}{\Delta_{n_{ext}}} = \frac{\lambda_{res,2}\left(\frac{\partial n_{eff,k}}{\partial n_{ext}} - \frac{\partial n_{eff,j}}{\partial n_{ext}}\right)}{\Delta n_{eff} + \lambda_{res,1}\left(\frac{\partial n_{eff,k}}{\partial \lambda} - \frac{\partial n_{eff,j}}{\partial \lambda}\right)} \tag{4.33}$$

Now, by assuming $\lambda_{res_2}/\lambda_{res_1} \approx 1$, the LPG's spectral sensitivity in terms of waveguide sensitivity and GIs can be simplified to

$$\frac{\Delta_{\lambda_{res}}}{\Delta_{n_{ext}}}(\lambda) = S_\lambda = \lambda \frac{\Delta\Gamma_{j,k}(\lambda)}{\Delta n_{g,j,k}(\lambda)} \tag{4.34}$$

where Γ_j, Γ_k, $n_{g,j}$ and $n_{g,k}$ are respectively the waveguide sensitivities and GIs of modes j and k.

It should be noted that the resulting formula containing the difference in GIs as well as the waveguide sensitivities of two optical modes is highly similar to that of interferometers (see equation (3.5)). In fact, the LPG's FWHM (equation (4.30)) is also very similar to that of an MZI in transmission as can be derived from equation (3.6). One can conclude that LPGs behave similarly to interferometers whose response has been apodized to suppress spectral periodicity with continuous and selective interference.

An alternative expression for the LPG sensitivity can be found using equation (4.27):

$$S(\lambda, j, k) \approx \Delta\Gamma_{j,k}(\lambda) \cdot \Omega \cdot \gamma_{j,l}(\lambda) \tag{4.35}$$

where $\gamma_{j,k}$, also known as the dispersion factor, can be defined as [239][240]

$$\gamma_{j,k}(\lambda) = \frac{\Delta n_{eff,j,k}(\lambda)}{\Delta n_{g,j,k}(\lambda)} \tag{4.36}$$

Finally, the Figure of Merit (FOM) can subsequently be calculated to be:

$$FOM = \frac{S_\lambda}{FWHM} = \frac{\Delta\Gamma_{j,k}(\lambda) \cdot L_{opt}}{0.8\lambda} \tag{4.37}$$

showing that the performances of LPGs are ultimately limited by the interaction length during propagation.

4.2.3 Performance Optimization Methods

This subsection proposes an overview of the optimization methods that can be applied to increase either the FOM and/or sensitivities in LPG refractometric sensors, based on the previous formulas. The related LPG's design requirements are discussed as well.

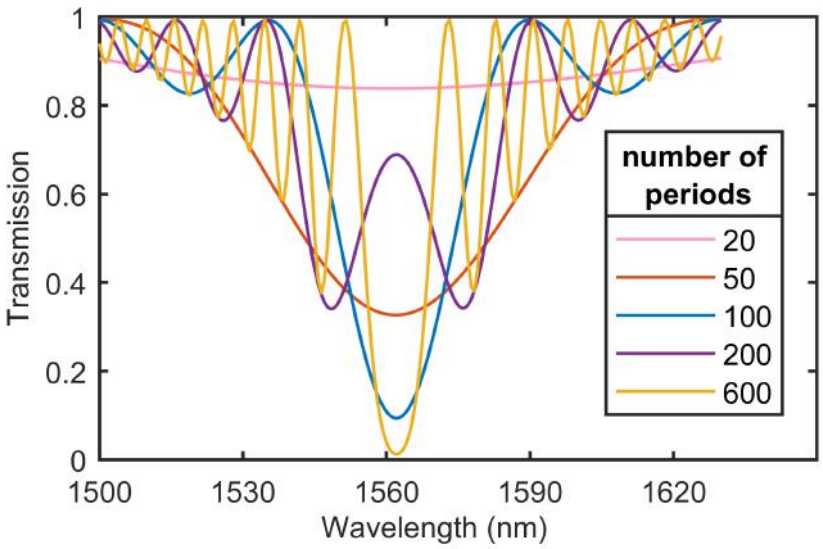

Figure 4.7: Resonance spectra in transmission of LPWG simulated with EME for various grating lengths

4.2.3.1 Length Optimization

Length optimization has an effect on the LPG performance as it can be used to reduce the FWHM of coupling resonances and, hence, increase the FOM. However, as shown in figure 4.4, the elongation of the LPG's modulated length results in recoupling of the optical modes. Simple length extension can effectively be used to reduce the FWHM of the central pattern, but increasing the length can rapidly lead to instability of the extinction ratio and merging of interference patterns, as illustrated in figure 4.7. For this reason, the LPG length increment should be accompanied by an inversely proportional reduction of the coupling coefficients. This can be implemented, for example, by decreasing the grating modulation amplitude or the optical field superposition of the coupling modes at the modulated interface. This optimization scheme is critical as it can potentially enable LPG performances to be easily multiplied.

4.2.3.2 Modal Interaction with the Sensing Region

In fiber LPGs, core modes couple to cladding modes. The interaction coefficient between the optical fields and the external sensing region is generally very low, of the order of 0.001-0.01 (typically 0.004) for conventional fibers [241] and slightly higher (0.013) for analyte-filled photonic crystal fibers [242]. Integrated photonic waveguides, on the contrary, typically exhibit high RI contrasts together with an intrinsic structural flexibility, which can facilitate the optimization of this sensitivity parameter. Waveguide sensitivity is typically optimized by increasing modal leakage for one coupling mode while reducing it for the other coupling modes. This is, however, complicated in LPG design since coupling modes are also required to

be partially overlapping for efficient coupling. Different concepts have thus been proposed to increase the waveguide sensitivity in LPWGs, including partial covering of the waveguide [243, 26], employing slot waveguides [243] or the use of porous waveguides [14].

4.2.3.3 Phase-Matching Turning Point

The phase-matching turning point (PMTP) optimization method consists in engineering the modal dispersion characteristics of a waveguide structure to bring the GIs of coupling modes closer together at a specific wavelength. As shown in equation (4.34), an equalization of the coupling modes' GIs in the denominator term $\Delta n_{g,i,j}(\lambda)$ can theoretically result in an infinite sensitivity.

Generally, chromatic dispersion is different for each mode, so that it is sometimes possible to have the coupled modes' GI values intersect for specific wavelengths, as illustrated in figure 4.8(a). This intersection or cross-over point for a pair of GIs is known as the Dispersion Turning Point (DTP) or Phase-Matching Turning-Point (PMTP). When the LPG's period is set accordingly for coupling to occur near the DTP wavelength, two resonance patterns can appear and will shift in opposite directions on the spectrum in accordance with the changes in the external RI. The spectral sensitivities of these resonances are extremely high around the DTP, but will decrease exponentially as the resonances shift away from the DTP, as illustrated in figure 4.8(b). This optimization method is typically performed by displacing the DTP near the wavelength of interest. In practice, this is achieved by adjusting or tailoring the waveguide structure to tune the chromatic dispersion of the coupling modes in order to counteract or balance their EI difference within the spectral window of interest. Both material and waveguide dispersions have to be taken into account. Nevertheless, the high index contrast intrinsic to the integrated nature of the waveguide enables the overall dispersion to be dominated only by the modal geometry so that material dispersion can be neglected [244].

Nonetheless, three major disadvantages of this optimization technique can be observed:

1. The FWHM of the resonance also depends on the GI difference between the coupling modes, implying that enhancement of the sensitivity proportionally multiplies the resonance spectral width, which can, in turn, complicate spectral reading. Consequently, it also limits the maximum sensitivity that can be read at the DTP, where the two resonance patterns start to merge.

2. The improvement of the sensitivity is very localized on the transmission spectrum. This is due to the high chromatic dispersion difference between modes, causing $\Delta n_{g,i,j}$ as well as γ to significantly vary with λ, thereby rapidly scrambling the sensitivity enhancement. The estimation of the RI of the external analyte will therefore be more complicated to achieve. In addition, because of the very high localized sensitivity, the achievable measurement range is considerably reduced.

3. The realization of such optimization requires simultaneously tuning the resonance around the wavelength of interest as well as the DTP, both of which rely on similar parameters. This can potentially complicate the design process, particularly in integrated optics where fabrication defaults are more frequent. While commonly used for optimizing LPFGs [245], this technique has also recently been proposed in integrated optics with a bi-modal asymmetric channel waveguide [246]

.

4.2.3.4 Proposed Approach based on Reduction of EI Difference of Modes with Similar Dispersion Profiles

Equation (4.35) shows that the sensitivity is proportional to the period when the dispersion contribution to the sensitivity can be neglected. In fibers, due to the low index contrast (typically ∼5mRIU contrast), propagation constants of coupling modes are found to be intrinsically close. As a consequence, from the phase-matching condition of equation (4.27), the LPFG periods Ω are typically found to be within 100 - 1000 µm for coupling in the NIR [66, 245, 230]. Based on equation (4.35), this explains why while there is little interaction with the external environment in LPFGs, their typical sensitivities (demonstrated) are within competitive levels in normal coupling regimes (without PMTP), as shown in table 4.2.4.

Contrary to PMTP optimization, which enables high γ dispersion coefficient to be obtained around the wavelength of interest and within only a very narrow spectrum, the objective here is to simultaneously bring the coupling modes' EIs closer together while maintaining or ensuring a similar dispersion behavior between these modes so that $\gamma \sim 1$. Achieving these conditions should theoretically enable the sensitivity to be both constant over a wider spectral range (if second and higher order dispersions are negligible) and significantly enhanced due to the decrease if the group index difference. As illustrated in figure 4.8(c), waveguides which support modes j and k fulfilling the condition $\Delta n_{g,j,k} = \Delta n_{eff,j,k}$ can lead to relatively stable sensitivities which are inversely proportional to Δn_{eff}. Note however that the sensitivity is also proportional to λ, which implies that, for instance, over a 100 nm optical spectral band centered at 1550 nm, the sensitivity is expected to vary by 7 %.

Also note that, by solving $\frac{dS_\lambda}{d\lambda}$, a truly stable S_λ can thus be obtained from coupling modes which satisfy the spectral profiles described by $\Delta n_{eff} = C_1 \cdot \lambda^{C_2}$, where C_1 and C_2 are constants associated with λ_{res} and S_λ. This optimization scheme depends entirely on the intrinsic properties of the waveguide which would require the use of higher level algorithms to be obtained.

Similar to PMTP, the proposed sensitivity enhancement technique also incurs an increase in FWHM, but it is simpler to implement on the integrated platform since it allows a greater flexibility for waveguide dispersion control. As proposed in the following chapter, certain waveguide architectures inherently favor this optimization concept.

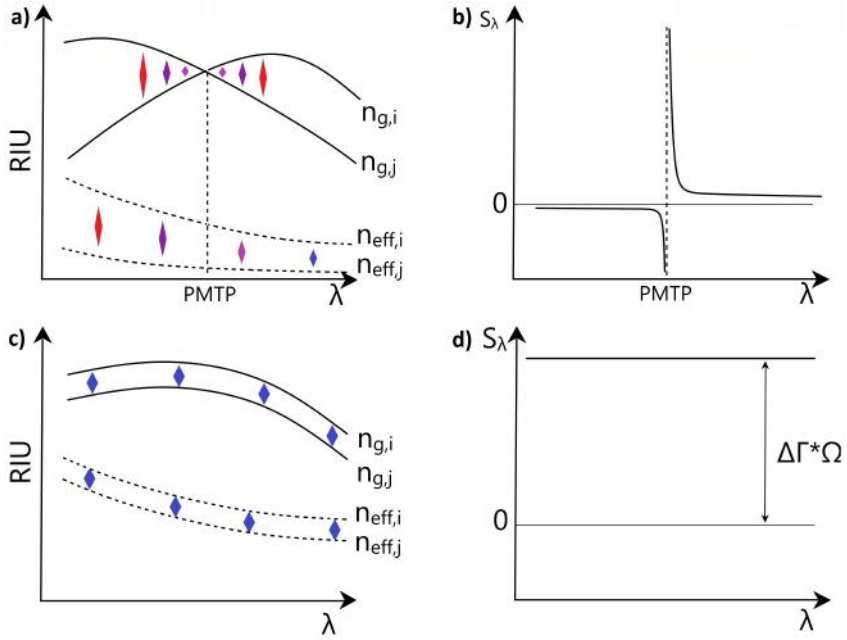

Figure 4.8: Illustration of the spectral sensitivity as a function of both GI and EI differences for different profiles of chromatic dispersion. Left column: spectral profiles of different propagation constants, and right column: resulting expected sensitivity behavior

4.2.4 State of The Art in LPGs

This subsection includes a non-exhaustive list of different refractometers based on LPGs implemented on both the fiber (Table 4.2.4) and the integrated photonic platforms (Table 4.2. The objective is to provide insight on the potential of LPGs as refractometers as well as to highlight the main optimization schemes and architecture trends utilized.

As can be observed, the grating sizes are of centimeter order for LPFGs and millimeter order in LPWGs. This is mainly due to the high propagation losses of integrated optics. The sensitivities of LPGs are on average relatively higher than other integrated refractometers while simultaneously exhibiting FWHMs on the order of nanometers. It can also be observed that the highest sensitivities are usually obtained with PMTP optimization; however, the corresponding FWHMs are also subsequently larger. In addition, with PMTP optimizations, the FWHMs can vary significantly and are sometimes impossible to retrieve from the measured transmission spectrum because of merging of the spectral patterns around the phase-matching turning point . In those cases, the spectral sensitivity also varies significantly with the sensed RI, indicating that the given sensitivity value is generally overestimated since it is estimated only around the PMTP, and thus should be considered carefully.

Ref	Architecture specificity	Grating Length (mm)	Sensitivity (nm/RIU)	FWHM (nm)	Optimization Pattern
[247]	Cascaded LPFGs w rotary modulation	22.5	27.77	≈ 10	-
[248]	Cascaded LPFGs w rotary modulation	245	58	≈ 100	-
[249]	Clad-etched Cascaded LPFGs	28	262	≈ 20	WG S
[250]	Clad-etched tilted modulation	-	507	≈ 10	WG S
[251]	Gold nanorods coating	-	167	≈ 20	WG S
[252]	Gold nanopcs coating	37	759	≈ 40	WG S
[253]	Sol-Gel coating	20	1067	≈ 15	WG S
[240]	-	50	1500	-	PMTP
[254]	Methane sensor	50	1500	≈ 20	PMTP
[255]	SiO2 nanopcs coating	30	1927	≈ 5	WG S
[256]	PhC fiber	50	243	≈ 10	WG S
[257]	SMF CO2 Laser radiation fiber tapering	2.4-4,8	30	≈ 40	-
[258]	Modified cladding	25.4	660	-	WG S
[259]	Tilted Gratings	55	602.86	≈ 40	-
[260]	Surface Plasmon Resonance	-	425-686.8	≈20-30	WG-S
[261]	Phase Matching Turning point optimization	30-50	887–2146	-	PMTP
[262]	Arc-Induced & dynamic study	15-30	112.3-6391.7	-	PMTP

Table 4.1: Reported LPFG characteristics and performances

Ref	Waveguide material	Architecture specificity	Grating Length (mm)	Sensitivity (nm/RIU)	FWHM (nm)	Optimization Pattern
our work [14]	SiN	Polymer wg coupling	1	240-1900	5	WG S
[263]	BK-7 glass	Rib wg	1.915	240	3	-
[243]	SiN	Strip-Slot wg coupling	2	1970	7	WG S
[246]	Si	asymmetric wg strip wg	1.5	5078	20-30	PMTP
Our work [26]	SiN	Rib wg	7.75	11500	25	index tailoring

Table 4.2: Reported LPWG characteristics and performances

Chapter 5

Simulation, Fabrication and Characterization of Integrated Long Period Grating Refractometers

Contents

5.1 Overview

This chapter describes the three different architectures of LPWG refractometers that have been designed, simulated, fabricated and tested in the course of this PhD.

Current outputs from this research include two corresponding peer-reviewed journal papers [14, 26] and one conference paper [25] that can be found in the Appendix at the end of the manuscript for consultation. Chapter 5 here will focus on synthesizing the objectives for each LPWG version in accordance with the previous chapter as well as summarizing both the **simulated and experimental results** obtained.

The first section describes the design, fabrication and testing of the first LPWG version denoted as LPWG n°1, whose structure is similar to that used in fiber LPGs as the coupled modes propagate in different materials. The principal aims are to optimize modal interaction with a porous medium for gas sensing. The main purpose here is to assess experimental issues related to LPWGs and better prepare for future gas sensing schemes. This section introduces the spectral study of multi-mode coupling and spectrum shift as a function of the grating period. It also presents the preliminary refractometric results obtained. A second LPWG version (LPWG n°2) then alternatively focuses on a more innovative design based on the rib waveguide [263]. The objective of the proposed structure is to increase the device sensitivity with a new dispersion-based optimization technique, as opposed to the more commonly used PMTP optimization technique. Experimental results obtained demonstrate a very high and constant sensitivity of more than 10,000 nm/RIU over a very wide dynamic range of 100 nm. The third section then presents a detailed simulation model of a simple LPWG architecture based on a modulated broadband coupler. This LPWG version, denoted as LPWG n°3, is found to exhibit figures of merit and sensitivities as high as 8000 and 300,000 nm/RIU, respectively. A parametric study on the proposed structure is also performed to assess the effect of the fabrication variability on the sensitivity and on the resonance spectral positions.

5.2 LPWG n°1

The two main objectives of this initial work are to (1) evaluate the fabrication and experimental issues that are inherent in integrated LPGs, and (2) propose a simple and flexible structure with optimized waveguide sensitivity for later gas sensing applications.

The first LPWGs have been designed to couple the fundamental mode of a Silicon Nitride (SiN) core waveguide to a higher order mode propagating in the cladding region. This latter region is fabricated in a different material with an RI lower than the core index, similar to most LPFGs, as previously illustrated in figure 4.6. However, contrary to LPFGs for which the functionalized gas-sensitive layer only interacts with the cladding mode's evanescent wave, here we aim to directly propagate a coupling mode in the porous layer. This would theoretically allow to greatly enhance the sensing waveguide sensitivity of the cladding mode $\Gamma_i = \partial n_{eff,i}/\partial n_{sens}$ in gas sensing schemes independently of the waveguide geometry.

The corresponding conference and journal papers are respectively [25] and [14].

5.2.1 Structure

The proposed LPWG architecture consists of an SiN (Si_3N_4 with RI = 1.97) width-modulated core waveguide covered by a multimode cladding waveguide [14], as illustrated in figure 5.1(a). A smooth sinusoidal width modulation is chosen to allow continuous and smooth coupling contrary to binary gratings where the waveguide is partly etched and can thus potentially induce loss of energy at the grating interfaces. In addition, the width modulation can be directly designed on the waveguide pattern, hence no additional process step is required.

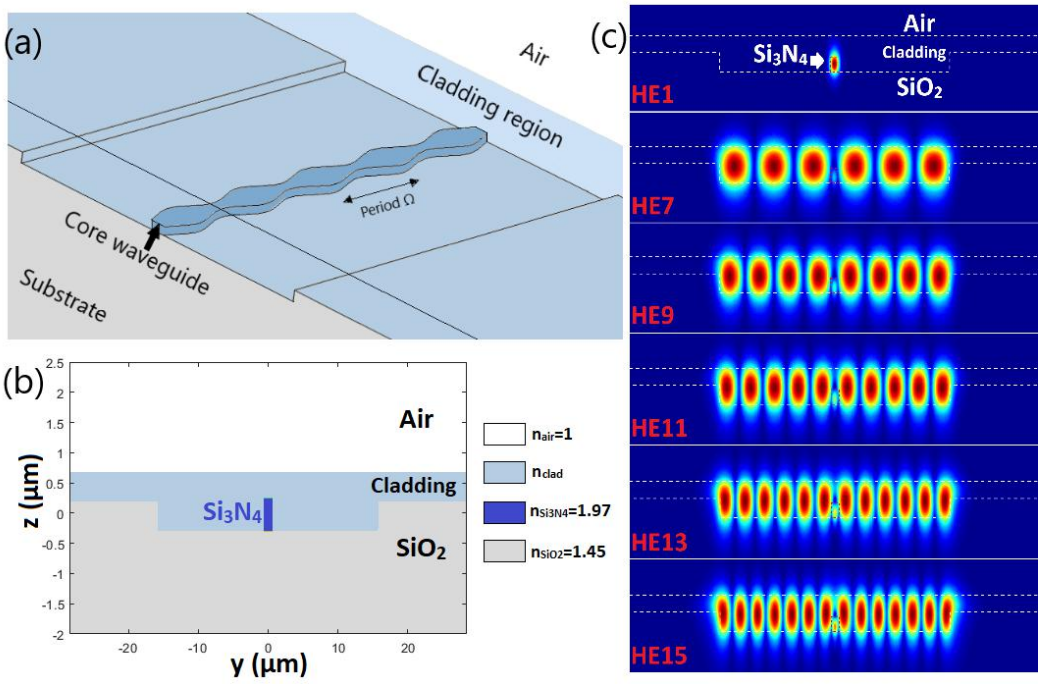

Figure 5.1: (a) illustration of LPWG structure, (b) cross-sectional material profile of LPWG, and (c) optical fields of propagative modes, © 2021 IEEE

To characterize the intrinsic properties of the designed LPWG, SU8, an epoxy-based negative photoresist commonly used in photolithography and waveguide fabrication [264], is initially employed as the cladding material. In fact, SU8 exhibits high optical transparency and an RI of 1.57 at 1550 nm, which are very similar to Styrene Acrylo-Nitrile (SAN) (RI 1.56) [66] and Polyhexamethylene biguanide (PHMB) (RI 1.55) [105] that are found to be promising polymer candidates for gas sensing. For a given cross-sectional dimension, the following relationship between the RIs of the materials permits separate confinement of the core and cladding modes: $n_{core} > n_{eff,1} > n_{clad} > n_{eff,n} > n_{sub} > n_{air}$, with $n_{core} = n_{Si_3N_4} = 1.97$ the core index, $n_{eff,1}$ the EI of the core's fundamental mode, n_{clad} the cladding index, $n_{eff,n}$ the EI of the n^{th} order cladding mode to couple, n_{sub} the index of the bottom SiO_2 layer and n_{air} the air index.

The SiN waveguide is designed with a cross-sectional dimension of 1000×400 nm incorporating a modulation width of ± 300 nm (see figure 5.1(b)). Preliminary experimental tests using waveguides of different widths have shown that no particular increase in optical propagation loss is expected for both maximas or minimas of the waveguide width over a full modulation period. The cladding cavity dimensions are designed to be 1.1 µm thick and 32 µm wide, for a 1 mm long sensor, thus allowing to support multiple propagative cladding modes which can be coupled to the fundamental core waveguide mode.

5.2.2 Modeling

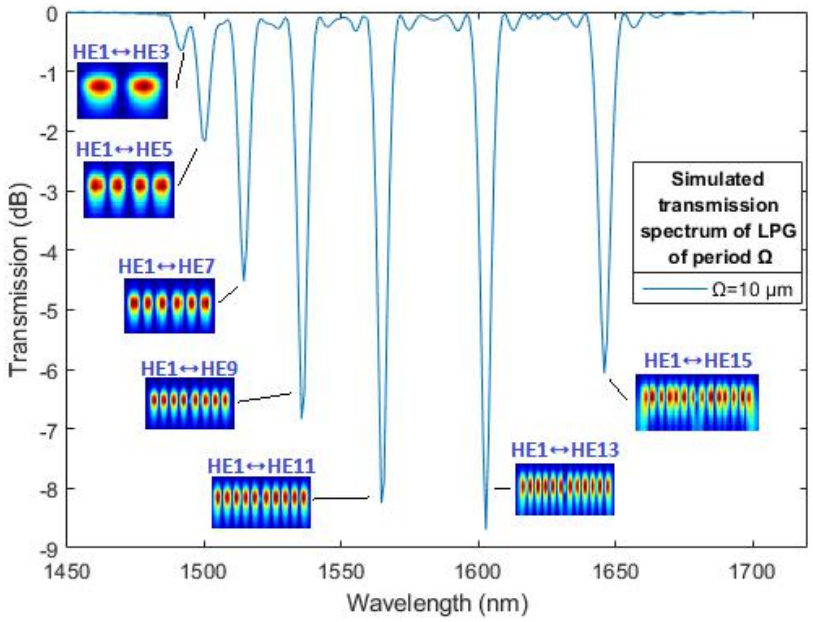

Figure 5.2: Simulated transmission spectrum of 1 mm long LPWG showing coupling between fundamental core mode and odd cladding modes. Insets illustrate various field profiles of coupled odd HEi modes © 2021 IEEE [14]

The optical fields of the core and cladding modes, propagation constants and coupling coefficients have been calculated by using COMSOL, Lumerical mode solvers and Matlab. Figure 5.1(c) displays the optical mode profiles of propagative modes of the structure. Coupling resonances between the fundamental mode and individual cladding modes are estimated to be obtained at 1550 nm for different periods around ≈10 µm. This coupling ultimately depends on the selected mode(s) to be coupled to, and can be calculated using the EIs of the modes and the phase-matching equation (4.27). Using EME and CLMT, the coupling coefficients are calculated to achieve an optimal coupling length of approximately 1 mm for the chosen parameters. However, since each cladding mode has a different propagation constant as well as different field superposition to the fundamental mode,

the coupling resonances are expected to occur at different wavelengths and rates, as shown in figure 5.2. Additionally, note that only odd modes can couple to the fundamental mode here since the structure's symmetry cancels out the even mode coupling coefficients.

5.2.3 Fabrication and Process Characterization

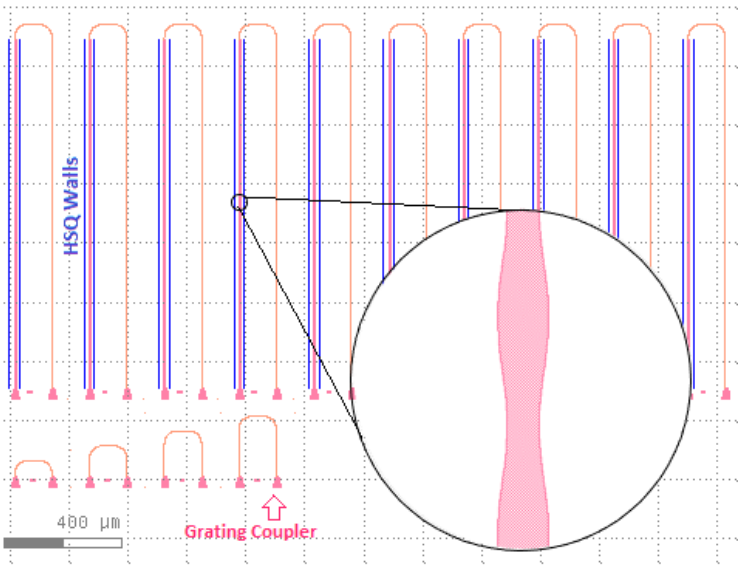

Figure 5.3: Layout of LPWG n°1 © 2021 IEEE

For simplicity of fabrication, the cladding waveguide cavity, as seen in figure 5.1(b), is delimited by incorporating SiO_2 slabs using Hydrogen Silesquioxane (HSQ) resist, whose constitution and RI are found to be very similar to those of SiO_2 after curing. The HSQ slabs are designed to be 3 µm wide and at least 0.6 µm thick to prevent multimode optical leakage as well as to ensure ease of coating and electron-patterning. Figure 5.2 shows simulated coupling resonances that are spread over a 250 nm spectrum, which greatly exceeds the measurement bandwidth of the optical spectrum analyser or OSA (of ∼100 nm) employed. To circumvent this issue, LPWGs with slightly different periods between 8 - 10 µm have been designed on the chip layout, as seen in figure 5.3, so as to induce a virtual shift of the coupling spectrum. Complete layouts can be found in the appendix for photonic chips n° 3 - n° 6.

A standard process is used for the fabrication of the SiN grating couplers, and FBMS is used for the connected waveguides. However, because the modulated region cannot be exposed using the FBMS exposure mode of the e-beam due to computational issues, the e-beam's normal mode is instead used with appropriate exposure parameters. These parameters have precedently been tested to reduce the waveguide mismatch that may occur at work-area junctions, as explained in Chapter 2. Following MaN2405 resist development and SiN waveguide patterning

with RIE, HSQ is deposited by spin coating for 1 min at 5000 rpm and cured for 2 min at 80°C. Note that an electra resist overcoating is employed to reduce charge effects. EBL of the HSQ slabs is performed using FBMS exposure mode with a 750 μC/cm^2 dose and an acceleration voltage of 30 kV. The development stage is carried out with 25 % TMAH for 1 min followed by water and methanol rinsing.

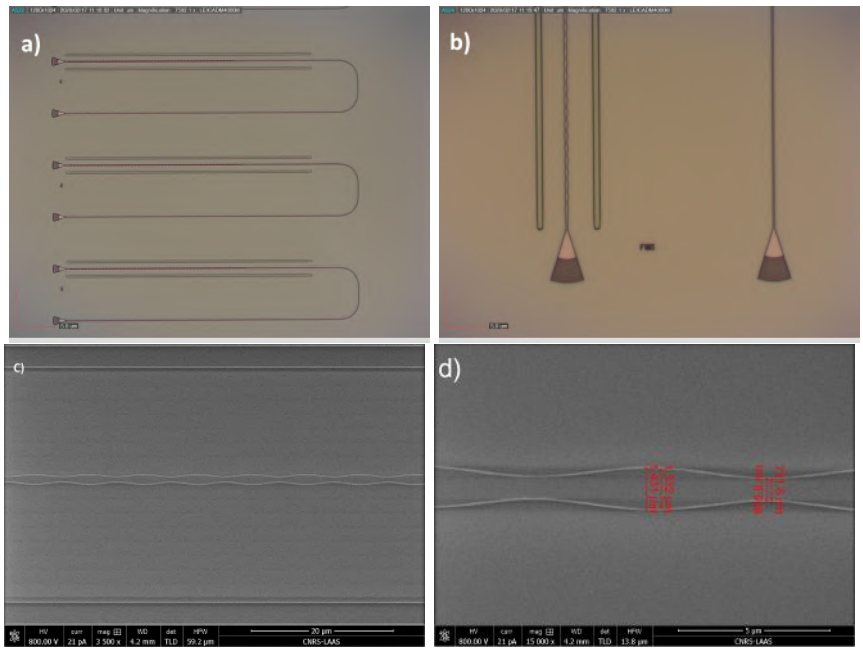

Figure 5.4: Photos of LPWG n°1 :(a) OM overview of photonic circuits and LPWGs, (b) OM image of grating couplers and related components, (c) SEM image of the modulated region of LPWG n°1, and (d) zoom of the modulated region showing slight variations in waveguide widths © 2021 IEEE [14]

Figure 5.4 shows OM and SEM images of the LPWGs fabricated for characterization and evaluation. A slight translation shift in figure 5.4(c) between the two patterned layers of the LPWG structure can be observed. This is attributed to a minor misalignment (overlay error) of the HSQ layer with the pre-patterned alignment marks. No waveguide mismatch has been observed at the work-area junctions. The SEM scan also shows the waveguides to be slightly larger than expected, due to a minor over-exposure of the waveguide patterns. The HSQ slabs are measured to be 1.1 μm thick by profilometry. Finally, SU8 is deposited by spin coating at a spin rate of 1700 rpm. This layer is also found to be 1.1 μm thick, as measured by profilometry.

5.2.4 Optical Characterization

As mentioned earlier, the theoretical transmission spectrum of the LPWG structure containing the first order resonance dip of every cladding mode is too large ($\sim$ 250 nm) to be measured over a single wavelength scan by the dedicated OSA. To solve

this issue, a set of LPWGs with identical cross-section and modulation amplitude but comprising different periods is first fabricated, followed by a virtual reconstruction of the combined spectra. To virtually reconstruct the entire coupling spectrum, the LPWGs' individual spectral contributions are firstly isolated by de-embedding the signal from contributions from the grating couplers and waveguides. The processed signals are next respectively shifted spectrally by values corresponding to the individual grating periods. Note that the LPWGs are found to exhibit little additional energy loss when compared to non-modulated waveguides of equal length. Further, no loss of data nor spurious overlapping during the spectral reconstruction has been observed. After the baseline correction, the LPWGs' transmissions are reassembled to result in the reconstructed spectrum plot as shown in Figure 5.5(b).

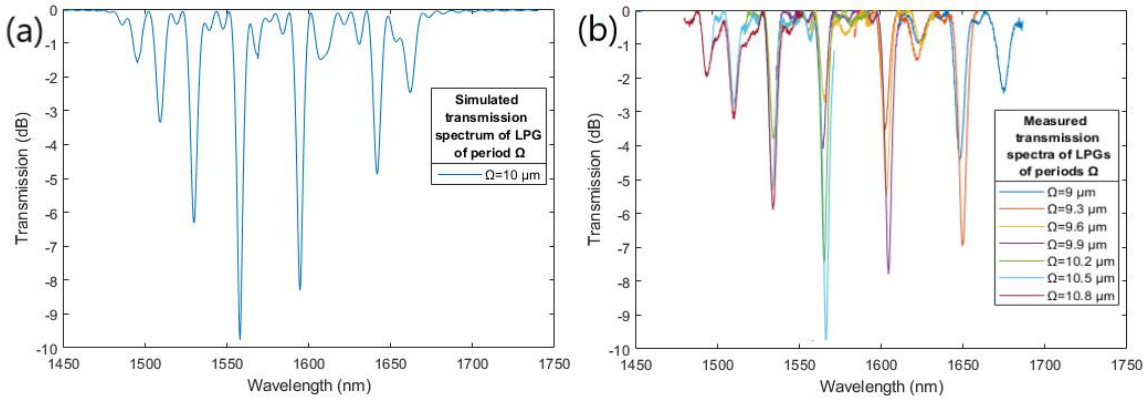

Figure 5.5: Transmission spectra for a 100-period long LPWG: (a) simulated with parametric adjustment, and (b) reconstructed from measurements © 2021 IEEE

Contrary to figure 5.2, shorter dips (of 1 - 3 dB amplitudes) have been observed between the main dips (3 - 10 dB amplitudes). They could be attributed to the slight asymmetry of the structure which disrupts the nullification condition of the optical modal field product at the lateral interfaces for even modes. This consequently leads to a minor rise in the coupling coefficients of the even modes, thus allowing partial coupling to these same even modes. Subsequently, when fabrication defaults such as asymmetry or waveguide width defects are reintroduced into the model, a very similar spectra can be found as illustrated in figure 5.5(a). Both the simulated and experimental results exhibit very similar FWHM of ∼5 nm but with slightly different extinction ratios. This is due mainly to the strong dependence of the coupling coefficients on the wavelength, thus manifesting as coupling amplitude flaws during the virtual reconstruction.

5.2.5 Refractometric Performance

It is difficult to directly assess the refractometric performances of the cladding section that is intended to function as the gas sensing layer. They have instead

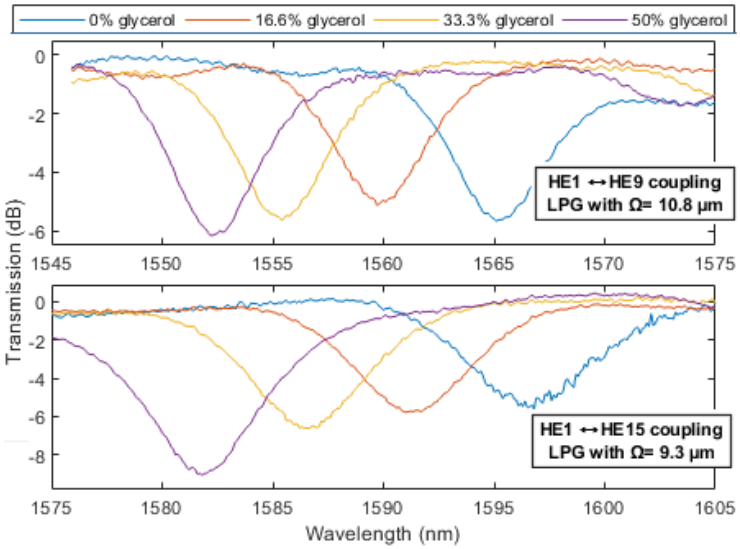

Figure 5.6: Measured spectrum of HE9 and HE15 mode resonance of LPWG using SU8 as cladding for different deposited concentrations of water and glycerol mixture © 2021 IEEE [14]

been evaluated via two indirect methods.

The first method relies on the study of the refractometric performance in a surface configuration, from which the resonance shifts could be measured for liquids of different RIs. The liquids under investigation are poured onto the chip surface. This technique would however lead to a much lower sensitivity than that achievable in refractometry of the bulk layer for gas sensing applications. Nevertheless, the responses could be compared with the simulated model.

Here, water and glycerol mixtures of different proportions are prepared to obtain varying RIs. The RIs are assessed using the initial RIs of water and glycerol around 1550 nm [265], and then applied on different LPWGs. The resonance shifts of the mode coupling dips are tracked and illustrated in figure 5.6 for the HE9 and HE15 modes. The measured surface sensitivities are then evaluated with Lorrentzian curve fitting and compared to simulation in table 5.1. The measured surface sensitivities, spectral bandwidths and extinction ratios are found to agree with the simulated model. This also suggests that the cladding refractometric performance should also agree with the simulated value when employed in later gas sensing experiments.

The second method consists in assessing the dependence of the resonance positions of the cladding index by temperature tuning, as the cladding material possesses a thermo-optic coefficient that is much higher than that of the core and the substrate. The temperature behavior of the sensor is firstly simulated with EME using the thermo-optic coefficients of SiN, SiO_2 and SU8, whose values at 1550 nm are, respectively, ∼24.5 µRIU/K, 9.5 µRIU/K [266] and −130 µRIU/K [267]. The temperature sensitivity of the LPWG model is estimated to be ∼330 pm/K and is

	Simulated surface sensitivity (nm/RIU)	Measured surface sensitivity (nm/RIU)	Simulated bulk sensitivity (nm/RIU)
HE9	198	195	1920
HE11	214	206	1915
HE13	231	227	1910
HE15	251	240	1820

Table 5.1: Calculated and measured sensitivities

similar for each mode resonance. To experimentally assess the temperature dependence, the photonic chip is placed on top of a Thorlabs laser diode mount with an integrated thermo-electric cooler (TEC). This enables temperature variation and stability control of the photonic circuits. In this method, the TEC temperature is swept from 15°C to 30°C by 5°C steps. A linear interpolation of the measured resonance wavelength values is then applied and leads to a temperature sensitivity of 340 pm/K, which is similar to the simulated value. From the temperature dependence analysis, the bulk sensitivity is approximated to be ∼1900 nm/RIU, which is in good accordance with simulation results (see table 5.1).

5.2.6 Discussion

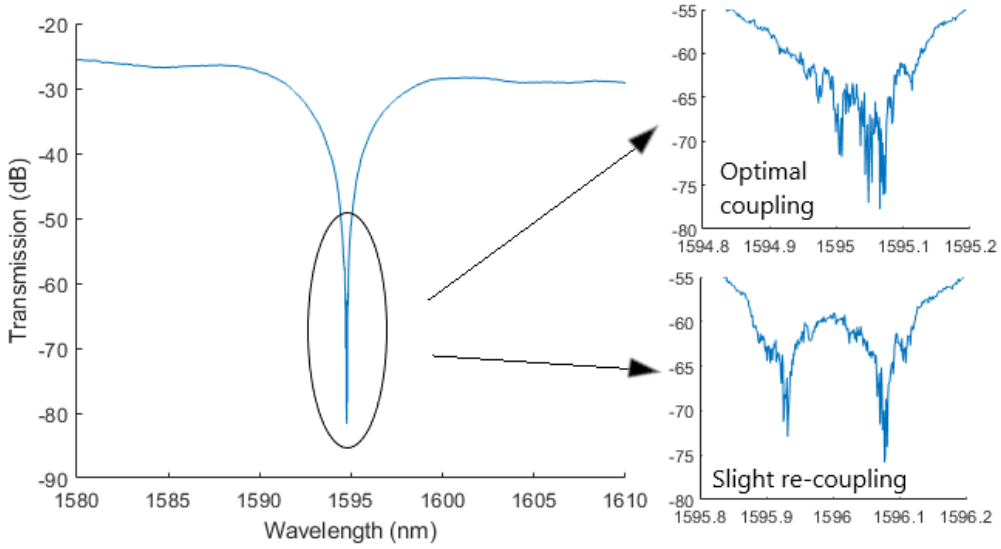

Figure 5.7: Raw transmission spectra of a perfectly coupled LPWG, with zoom on the central resonance region for optimal coupling (top left) and slight over-coupling (bottom left) generated by temperature change

From the experimental results, it is observed that the main limiting issues of LPWGs are static dimensional deviations (i.e. cross-sectional errors that are consistent on the waveguide) and propagation losses. However, the specific fabricated structures are deemed to be sufficiently resilient so that these errors are not critical and would only lead to minute spectral shifts and inaccuracy in the estimation of extinction ratios. These errors could otherwise be critical for other highly sensitive LPWG architectures since the resonance wavelength could be out of the optical spectrum range for example, as will be seen in the next sections. Off-align errors also lead to minor irregularities of the LPWG responses. Note, however, that stitching errors can be erased by writing field overlay. The estimated sensitivity and FOMs for gas sensing are calculated to be, respectively, 1900 nm/RIU and 400 RIU^{-1}, which are considerably high values for 1 mm structures when compared to other gratings or interferometers (see table 3.2.1).

Finally, the cladding is replaced by gas-porous polymers such as SAN and PHMB, using straightforward spin coating, and exhibited very similar spectral response, paving the way for later gas sensing experiments, as will be demonstrated in Chapter 6.

Additionally, it is possible to experimentally obtain LPWGs with optimal coupling if the structural parameters are correctly set. In such cases, the extinction ratio becomes maximal, as seen on figure 5.7. A small variation in temperature can, however, disrupt the optimal coupling condition and, in case of slight over-coupling, can lead to a deformation of the resonance shape, as illustrated in figure 4.7.

5.3 LPWG n°2

This section focuses on a second LPWG version that alternatively aims to enhance its refractometric sensitivity by reducing the value of the denominator in the theoretical formula for spectral sensitivity [26]: $S_\lambda = \lambda \Delta\Gamma_{j,k}(\lambda)/\Delta n_{g,j,k}(\lambda)$.

As previously explained in Chapter 4, this enhancement is typically achieved by PMTP optimization, which relies on using GI tuning. A noticeable problem with PMTP optimization is that the sensitivity enhancement significantly drops as the resonance shifts away from the PMTP, thereby considerably reducing the RI sensing or dynamic range (see figure 4.8). This is due to the large difference in chromatic dispersion between modes which causes $\Delta n_{g,i,j}$ to greatly vary with λ, thus causing the sensitivity to collapse.

Therefore, in order to maintain sensitivity enhancement over a wide spectral window, we propose an LPWG structure whose propagative modes possess not only close GIs but also very similar dispersive chromatic behaviors. The design guidelines for these LPWGs' cross-sectional structures are as follows:

1. The GIs of the core and slab modes must be in very close proximity to induce high sensitivity and significantly extend the measurement range.

2. The difference in chromatic dispersion between the two coupling modes should

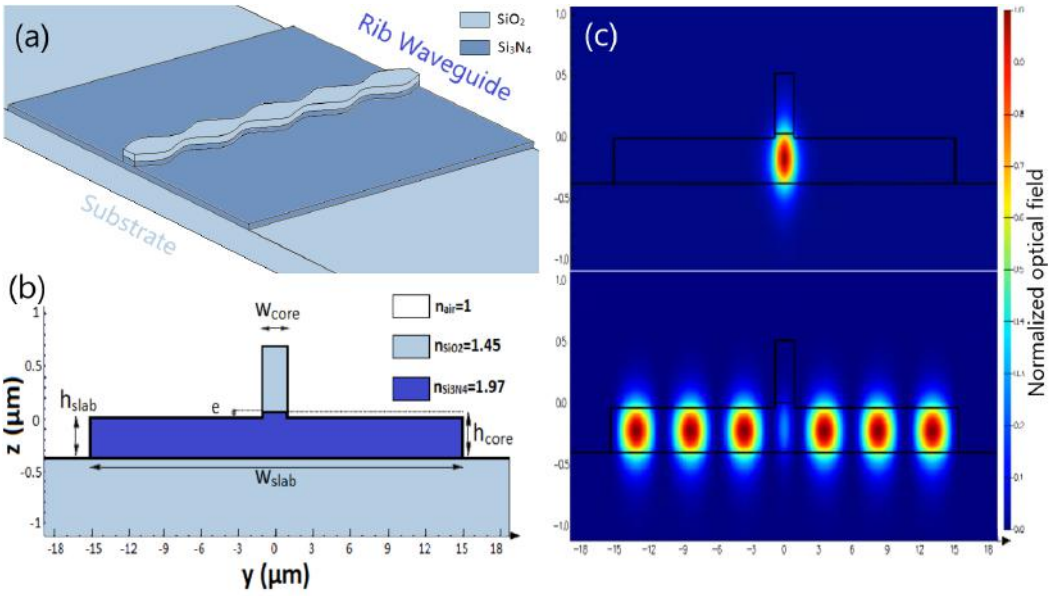

Figure 5.8: (a) illustration of LPWG structure, (b) LPWG cross-section material profile (c) optical fields of propagative modes HE1 and HE7

be as low as possible in the spectral region of interrogation. This means aiming for $\Delta n_g \sim \Delta n_{eff}$ in the measurement window.

3. The overlapping of the modal fields at the modulated interface must be tuned for coupling rate optimization [25, 224].

4. The modal interaction with the external region must be as strong as possible for the slab modes and almost null for the core mode.

Additionally, contrary to the first batch of fabricated LPWGs described in the previous section, an evanescent wave sensing configuration is preferred here to facilitate direct refractometric measurements. Temperature sensitivity should also be considered in the architecture's design for further optimization. Further details are described in the corresponding paper [26].

5.3.1 Structure

The proposed structure consists in a partially covered SiN hybrid rib-strip waveguide that hosts a fundamental mode in the central region and multiple higher order modes in the slab region, as illustrated in figure 5.8. The main advantage of this architecture lies in the intrinsic properties of rib-strip waveguides that respect the proposed guidelines. Since the optical profiles of the coupling modes are principally confined in the same material,

1. with respect to the structure geometry, the EIs and GIs of supported modes can be potentially induced to be very close and, hence, to behave similarly

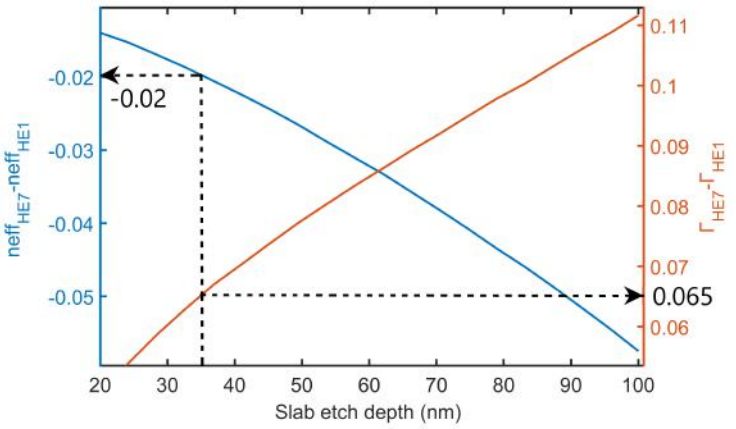

Figure 5.9: EI difference and variation of $\Delta\Gamma$ of coupling modes as a function of slab etch depth e with $w_{slab} = 30$ µm and $w_{core} = 1.65$ µm at 1550 nm. e is set at 35 nm and $h_{slab} = 365$ nm. Dashed lines: selected e with corresponding Δn_{eff} and $\Delta\Gamma$.

over a broad wavelength range, as will be demonstrated in the next subsection. Additionally, material dispersion can be neglected in this case

2. also, both modes are expected to be almost equally affected by temperature due to their co-propagation in the same material; the structure is thus inherently less prone to temperature crosstalk [268, 263].

Further, similar to the first fabricated version of LPWGs, the optical mode profiles partially superpose at the core region (see figure 5.8(c)) and can therefore be modulated for coupling. The central region's lithographic resist primarily employed to etch the core modulation profile can also be conveniently used here as a cover to further reduce the influence of the external environment on the EI of the fundamental mode. This is performed by using HSQ as resist for central region patterning.

5.3.2 Modeling and Parametrical Study

A parametric study is performed with Lumerical mode solvers and purpose-built scripts on the different structural parameters (core width and thickness, slab width and thickness) as illustrated in figure 5.8. First, the background RI is set around 1.33, as we aim to later experiment with water-based mixtures. The difference between the core and slab thickness, defined as the etch depth "e", is found to not only be the main contributor to the slab modes' waveguide sensitivity (Γ), as shown in figure 5.9, but also to highly influence coupling parameters and modal propagation behaviors.

In this study, e is set at 35 nm in order to minimize the EI difference between the fundamental mode and the higher order slab mode ($\Delta n_{eff} = neff_{HE1} - neff_{HE7}$).

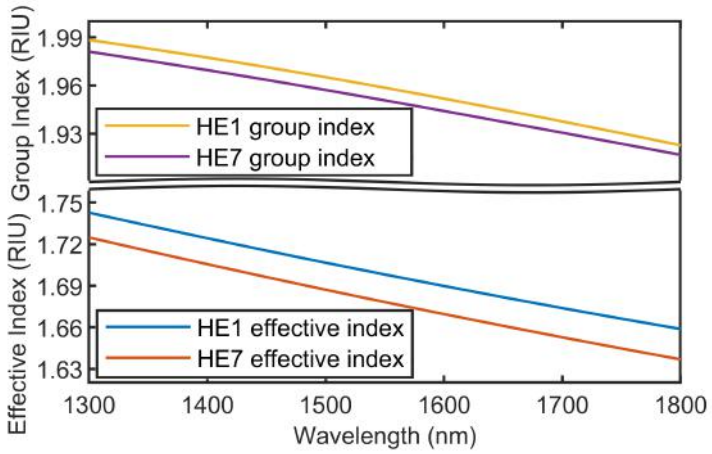

Figure 5.10: Simulated effective and group indices of modes HE1 and HE7 showing similar dispersion for LPWG with $e = 35$ nm, $w_{core} = 1.65$ µm and $w_{slab} = 30$ µm

The slab width (w_{slab}), on the other hand, allows to tune the propagation constants of the higher order modes. For $w_{slab} = 30$ µm, simulation results shown in figure 5.10 demonstrate that the GIs of the selected modes are not only very close together but also exhibit similar chromatic behaviors. As Δn_g is approximately constant over a relatively wide spectral range of 500 nm around 1550 nm, S_λ or spectral sensitivity is expected to remain relatively constant in this window. S_λ at 1550 nm is estimated to be ∼11,000 nm/RIU. The period for HE1 to HE7 mode coupling to occur at 1550 nm is, in turn, estimated to be approximately 77.5 µm using equation (4.27).

Further analysis plotted in figure 5.11 suggests the core width w_{core} to be the cross-sectional dimension that most contributes to the coupling coefficients, as it affects the modulated interface position with respect to the optical fields of the coupling modes. This parameter is used here to control the grating's optimal coupling length L_{opt} and resonance FWHM. Hence, an FWHM shorter than 25 nm has been selected for experimental purposes in order not to exceed the apparatus' measurement window limit of 100 nm. While w_{core} also slightly influences the GI and dispersion of the fundamental mode, it has been set at 1.65 µm as a good trade-off without increasing Δn_g nor altering the respective sensitivities of the modes to the external RI. Consequently, the FWHM is estimated at 25 nm for a grating length of 7.5 mm.

5.3.3 Fabrication and Characterization

Fundamental mode coupling in the rib waveguide is performed using 50 µm long strip-rib tapers at both ends of the LPWG [269]. In addition, as a safety margin against fabrication errors, several LPWGs with varying periods have been designed to ensure that LPWG resonances could be observed within the measurement spec-

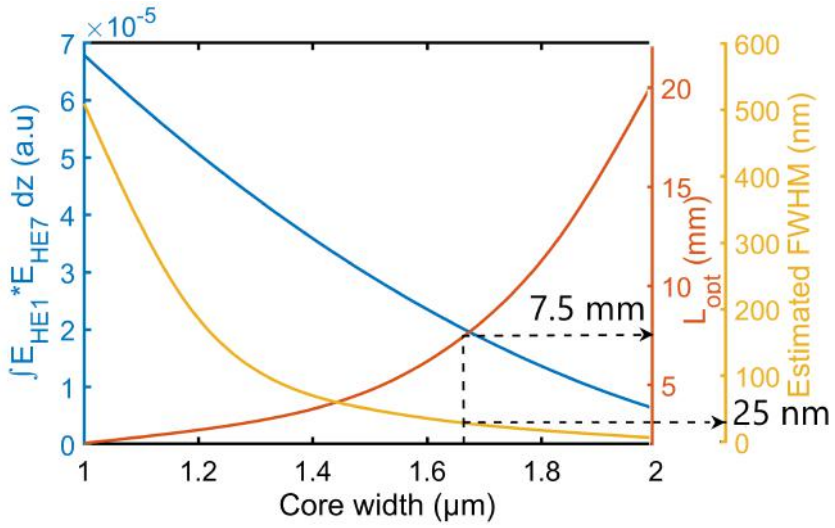

Figure 5.11: Coupling parameter and estimated full coupling length as a function of w_{core} for $e = 35$ nm and $w_{slab} = 30$ µm at 1550 nm. w_{core} is set at 1.65 µm. Dashed lines: selected w_{core} with corresponding L_{opt} and FWHM.

tral window, as shown in figure 5.12(a). In order to address the effects of fabrication tolerances on the LPWG performance, dimensional variations of the LPWG architecture with a normal distribution are introduced into the model. The widths and heights are varied in 3000 simulated models with a standard deviation or SD) of 3.8 nm and 1.3 nm, respectively, selected from an analysis of the manufacturing variability in silicon photonics lithography [17]. The overlay error between the slab and core layers is also introduced into the model with an SD of 300 nm. From the simulation results, it is found that ∼75% of the LPWGs exhibit resonance within the 1500 - 1600 nm range with a sensitivity variation as low as 3%. Further, the difference in thickness between the core and slab regions is also observed to be the highest contributor to and responsible for 90 % of the resonance shifts (see appendix A.8).

The fabrication procedure, as illustrated in figure 5.12(b), involves two lithographic processes:

1. the HSQ is firstly exposed as a pattern layer for the strip-rib waveguide core region, as well as for grating couplers and connecting waveguides. This prevents overlay errors from affecting the strip-rib's fundamental mode conversion

2. after development, the second exposure process is directly applied with MaN2405 to define the slab mode region. A first RIE step is carried out after which a second one is used to partially etch the slab region. Both etching steps are measured by closed loop laser interferometry to control the etch depth

Figure 5.13 displays SEM images of a rib-strip LPWG, highlighting a slight asymmetry that is due to a minor overlay error as seen in figure 5.13(d). However, when this error is reintroduced into the simulated model, a small resonance shift of only ∼20 nm is obtained.

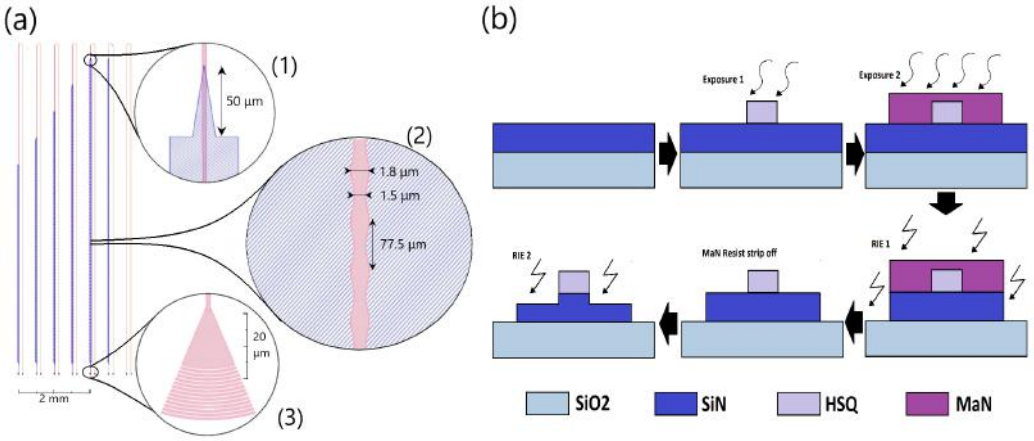

Figure 5.12: (a) Layout of the fabricated LPWGs, showing (1) strip-rib converter, (2) LPWG modulated core layer and (3) grating couplers, and (b) illustration of rib-strip LPWG fabrication process

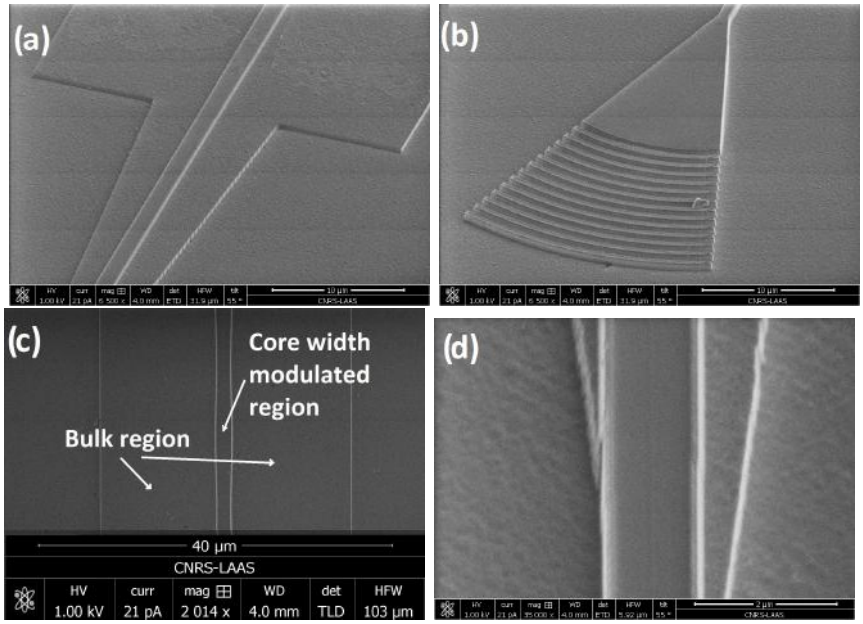

Figure 5.13: SEM images of integrated photonic components: (a) strip-rib converter, (b) grating coupler, (c) LPWG section, and (d) minor misalignment between strip and rib waveguides shown here at the beginning of the tapering region for the sake of clarity

5.3.4 Refractometric Performance

Commercially available liquids of calibrated RIs from Cargill are employed and mixed into different proportions to simulate indices varying between 1.33 and 1.35 RIUs. These RIs are first measured using a Hanna HI 96801 refractometer with a resolution of 0.2 mRIU. The optical liquids are then deposited on top of the chip to induce coupling resonance to be subsequently tracked over a spectral window of 100 nm. Resonance features which have been observed during optical characterization exhibit a 3 dB bandwith of 25 nm and an extinction ratio of 10 - 12 dB, as shown in figure 5.14(b). These are very similar to the simulated values in figure 5.14(a) which plots the corresponding transmission spectra after de-embedding and normalization. Baseline comparison to strip waveguides of the same length actually reveals lower rib-waveguide propagation losses that are assumed to be due to lower side-wall rugosity-induced scattering.

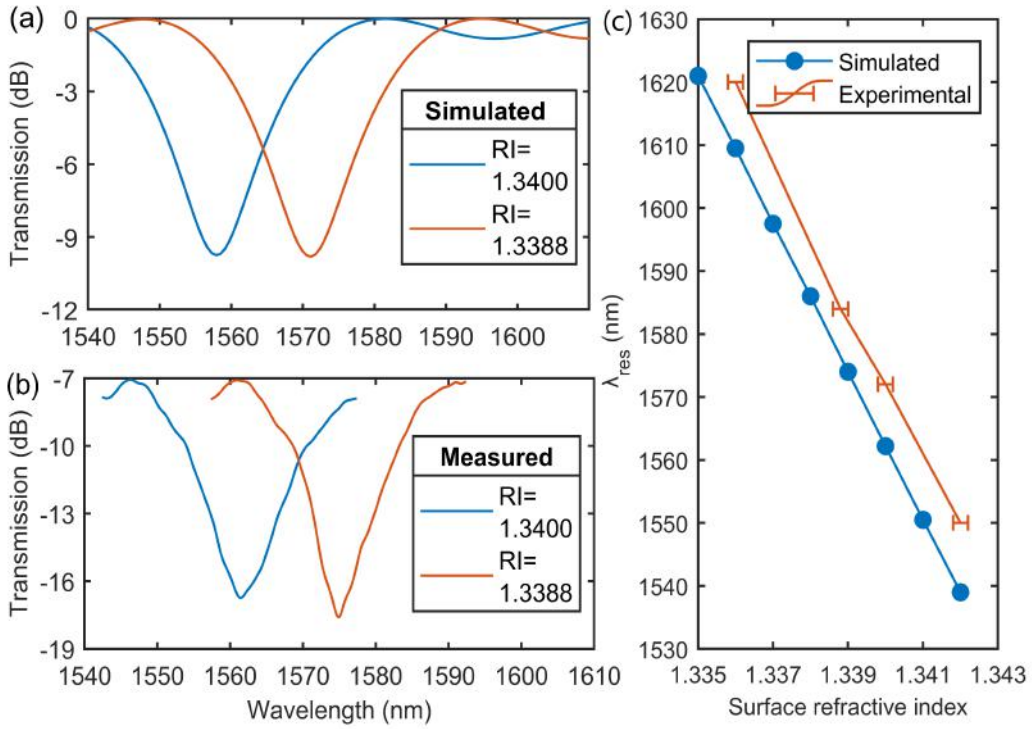

Figure 5.14: (a) Simulated and (b) experimentally measured normalized resonance spectra at surface RIs of 1.3388 and 1.34, and (c) corresponding resonance wavelengths displaying a relatively constant sensitivity of 11,500 nm/RIU.

Figure 5.14(c) plots the simulated and experimental resonance wavelengths of the LPWG against the analyte's RI, from which the sensitivity, calculated as the slope, can be extracted. Here, the experimentally measured sensitivity is estimated to be $S_\lambda \approx$11,500 nm/RIU. More significantly, it is found that S_λ remains almost stable (i.e. constant) over 100 nm, in good agreement with the simulated value.

5.3.5 Temperature Sensitivity

To study the influence of temperature on the structure, the thermo-optic coefficients of SiN and SiO_2 are introduced into the simulation model, similar to the first LPWG section, from which a very low temperature sensitivity of 150 pm/K is then obtained. Such a low value is to be expected since the coupled modes travel in the same materials and are thus subject to the same influence.

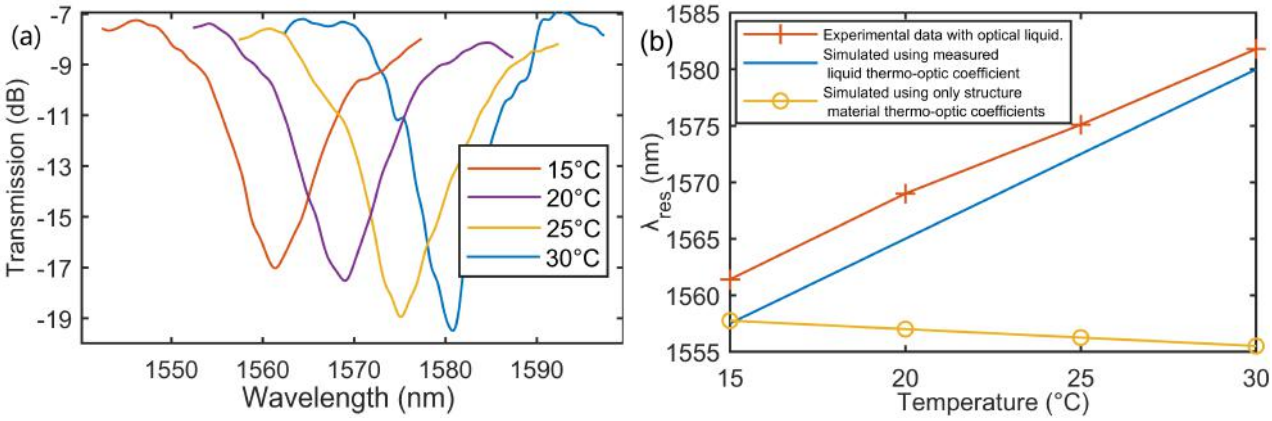

Figure 5.15: (a) Experimental transmission spectra, and (b) simulated and measured resonance wavelength variations versus temperature of the LPWG

To experimentally determine the temperature sensitivity of the LPWG sensor, the temperature of the TEC mount is tuned from 15 to 30°C, similar to previous Section 5.2.5. However, it is impossible here to directly measure the temperature sensitivity of the sensor in free space (i.e. without an external "cladding" medium) as the mode resonance would then not fall within the limits of the target spectral range around 1550 nm. In order to correctly measure this sensitivity without exceeding the spectral limits, the temperature dependence of the calibrated RI liquid is pre-characterized using a commercial refractometer inside a temperature incubator before being applied on the LPWG. The measured resonance wavelength shift due to the temperature induced variation of the liquid's RI is finally subtracted from the combined total resonance shift (from both the RI liquid and LPWG sensor) detected over the investigated temperature range. This thus enables the intrinsic temperature dependence of the LPWG sensor to be obtained, as shown in figure 5.15. The measured temperature sensitivity is found to corroborate the simulated value, which predicts a low intrinsic LPWG temperature dependence of ∼150 pm/K.

5.3.6 Discussion

A sensitivity of ∼11,500 nm/RIU with an FOM of 400 has been demonstrated with the proposed LPWG over a large measurement spectral window of 100 nm. Despite the unoptimized photonic waveguide manufacturing process, the measured LPWG coupling properties are found to be very similar to the simulated ones. In fact, the proposed architecture is less prone to certain structure's dimensional variations such as uncertainty in the RI of deposited materials, since both coupled modes propagate in very similar conditions sharing various structure parameters. This implies that they can be assumed to be equally affected by this kind of defects. In addition, as already mentioned, the temperature crosstalk is relatively low (∼0.15 nm/K), especially when compared to the high refractometric sensitivity.

Finally, the anisotropy of the sensed medium's RI induced by a heterogeneous coated liquid has been observed to generate irregularities in the transmission spectra, as seen in figure 5.16. This has been generated by using poorly mixed oils and has resulted in double resonance spectral shapes. This effect, however, rapidly vanishes with progressively improved liquid blending, but might be of more concern for LPWGs of higher sensitivities.

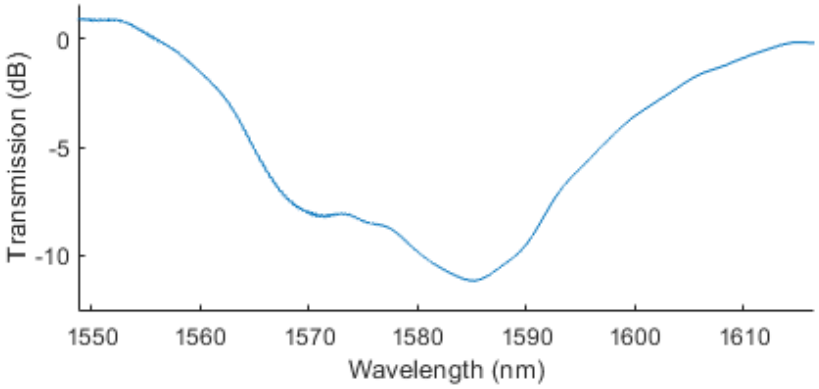

Figure 5.16: Transmission spectrum of a rib-strip LPWG with liquid-analyte RI anisotropy

5.4 LPWG n°3

In this section, the numerical analysis of an LPWG based on a pair of waveguides is performed to illustrate the importance of performance scalability of LPWG architectures for refractometric applications[1]. A detailed parametric analysis is applied to the proposed design to highlight the main design leverages and their effect on the refractometric performances. This modeling section shows that the proposed optimization techniques can be simultaneously used to scale the performances of LPWGs over a wide dynamic range. This is demonstrated through the analysis of several variants of the proposed architecture.

5.4.1 Structure

The studied structure consists of a pair of co-linear SiN strip waveguides, one of which is covered by an SiO_2 cladding layer, as illustrated in figure 5.17(a). This figure also shows the two associated fundamental HE mode profiles that are coupled by the LPWG at resonance. The dimensions of the waveguide with cladding are fixed at 650×550 nm which result in moderate optical mode confinement around 1550 nm. The RIs of SiN and SiO_2 are respectively given as 1.97 and 1.45. The cladding material is SiO_2, elaborated using HSQ resist which exhibits a lower RI of 1.37. HSQ is employed in part to that facilitate sensitivity optimization for sensing

[1]The associated paper is currently under review.

around 1.33 RIU. A long period binary modulation is applied to the covered waveguide's width for simulation purpose as well as for later fabrication. Note that similar coupling behavior could also be obtained by applying the same modulation on the exposed waveguide instead. In the next section, a parametric study is performed using 4 parameters related to the LPG dimensions: (1) exposed waveguide width w and (2) thickness t, (3) modulation amplitude a, and (4) waveguide interspace i (see figure 5.17(a)).

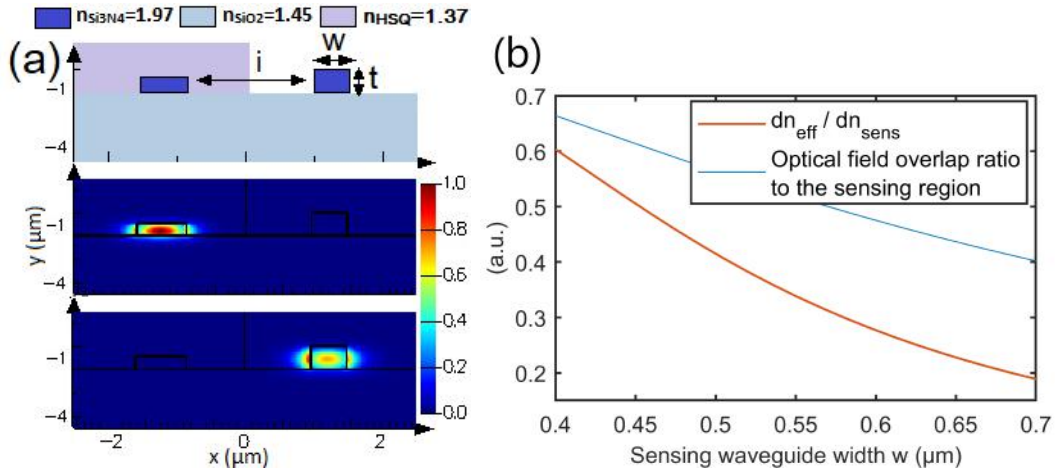

Figure 5.17: (a) Dual strip LPWG cross-section material composition and RI profile (top), and optical field profiles of coupled modes (bottom), and (b) waveguide sensitivity and field overlap ratio to the sensing region versus w

5.4.2 Modeling

The exposed waveguide's refractometric sensitivity, defined as $\partial n_{eff_j}/\partial n_{sens}$, is firstly optimized by reducing the optical confinement of the mode. As shown in figure 5.17(b), the waveguide sensitivity, $\partial n_{eff,j}/\partial n_{sens}$, of the exposed optical mode can be increased to nearly 0.5 by reducing w. A w as small as 450 nm enables optical mode propagation while exhibiting high index dependence on the external region at the same time. A wider waveguide would lead to lower sensitivity but could nevertheless reduce propagation losses induced by side-wall rugosity. The cladded waveguide sensitivity is negligible here.

Secondly, as previously discussed, the PMTP exists when $\Delta n_{g_{i,j}}(\lambda)$ tends to zero [246, 261]. This theoretically permits spectral sensitivity to locally reach an infinite value. However, the FWHM has previously been shown to be inversely proportional to $\Delta n_{g_{i,j}}(\lambda)$. Hence, S_λ and FWHM can be tuned here by controlling the GI difference $\Delta n_{g_{i,j}}(\lambda)$. This is carried out by adjusting the exposed waveguide thickness t, as shown in figure 5.18(a). Two LPWG examples with $t = 1$ µm and 1.4 µm are subsequently designed and simulated with EME algorithms. Their spectral sensitivities S_λ are theoretically estimated to be ∼30,000 and ∼300,000 nm/RIU,respectively,

as plotted in figure 5.18(a).

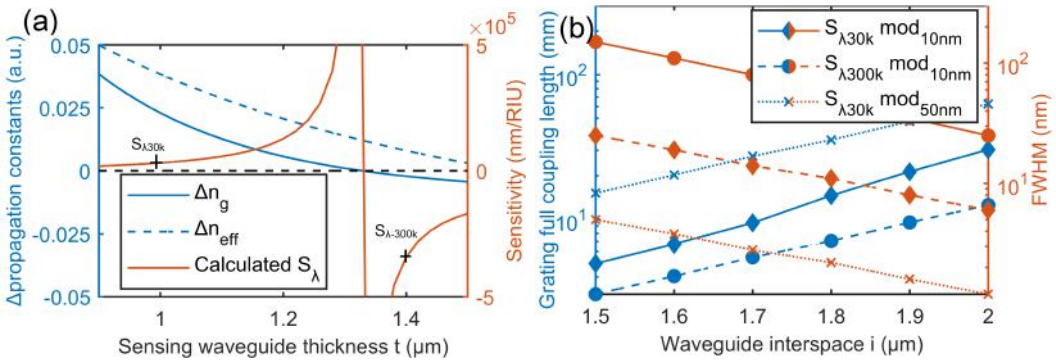

Figure 5.18: (a) GI and EI difference between coupling modes, and resulting estimated S_λ as a function of t; (b) grating length for full coupling and simulated FWHM at 1550 nm (log scale)

Lastly, after setting the grating periods accordingly to fulfill the resonance condition in equation (4.27) around 1550 nm, EME simulations are performed to study the effects of interspace i and modulation amplitude a on the spectral and coupling features. Note that prior to these simulations, i and a have been found to exert only minor influences on the propagation constants of the optical modes.

Figure 5.18(b) illustrates the FWHM and the behavior of the full coupling grating length L_{opt} versus i, demonstrating that the waveguide interspace is the main contributor to the optical field superposition of the coupling modes. Figure 5.18(b) also shows the modulation amplitude a to exert the strongest influence on the grating's optimal coupling length and spectral width. A nearly ideal inverse proportionality between L_{opt} and FWHM can be observed, as theorized in equation (**??**).

Table 5.2 summarizes the parameters and simulated performances of the different LPWG variants modeled here. Figure 5.19 plots the GIs of coupling modes in the wavelength region of interest for LPWG n° 3.1 to 3.4, while also illustrating simulated spectral sensitivities of $S_{\lambda 30k}$ = 30,000 nm/RIU and $S_{\lambda 300k}$ = -300,000 nm/RIU, respectively. Figure 5.19 also displays the EME-simulated transmission spectra of LPWGs n° 3.1 to 3.4 as listed in table 5.2 together with their spectral shifts induced by varying the external RI in the model. The magnitude of the spectral shifts corresponds to the calculated sensitivities while the FWHM of the LPWGs remains almost constant for each structure over the entire RI variation range. This is due to the very minor variations of $\Delta n_{g_{j,l}}$ of the coupled modes with λ, which renders both the sensitivities and the FWHM stable over the spectral range analyzed. Minor variations of the extinction coefficients are also observed and these are attributed to variations in the mode coupling strength with λ (note: this can only be achieved/obtained with advanced EME algorithms). Additionally, the FOMs of the simulated spectra are found to be proportional to the grating length

(L_{opt}), which is expected since $\partial n_{eff,j}/\partial n_{sens}$ is equal for each LPWG.

n^o	t (μm)	i (μm)	amp (nm)	$\Delta n_{eff_{j,1}}$ (a.u.)	$\Delta n_{g_{j,1}}$ (a.u.)	Period (μm)	L_{opt} (mm)	S_λ (μm/RIU)	FWHM (nm)	FOM RIU^{-1}
3.1	1	1.6	10	0.038	0.023	40.5	20	33	4	8250
3.2	1	1.6	50	0.038	0.023	40.5	4	33	20	1650
3.3	1.4	1.6	10	0.008	-0.0022	225	6.5	-310	115	2700
3.4	1.4	1.9	10	0.008	-0.0022	225	20	-310	38	8150

Table 5.2: Summary of parameters and simulated performances of 4 variants of the LPWG design n°3 at 1550 nm

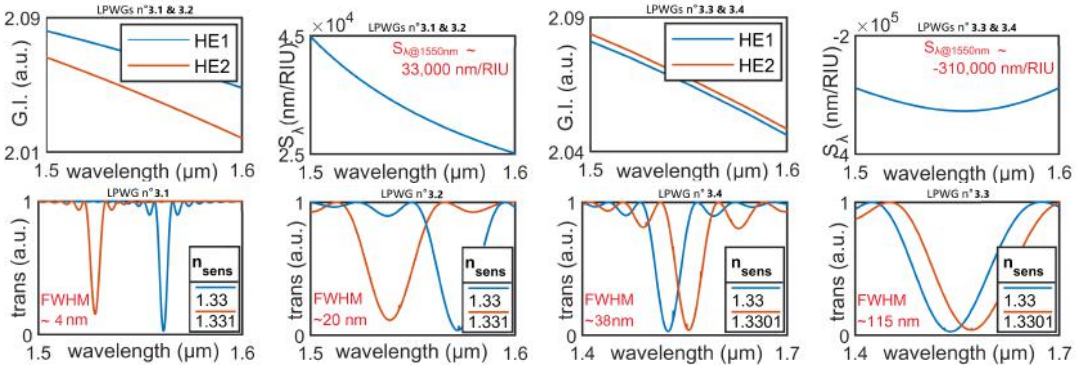

Figure 5.19: GI profiles, simulated transmission spectra (trans) and spectral sensitivities (S_λ) of different versions of LPWGs (n° 3.1-n° 3.4) for which the structure parameters are detailed in Table 5.2

5.4.3 Discussion and Fabrication Variability

The parametric analysis carried out above shows that a broad range of sensitivities as well as spectral features can be obtained by tuning or adjusting the optical mode properties. Spectrally stable sensitivities as high as 300,000 nm/RIU over a large dynamic range, with an FOM of 8000 have been simulated for 2 cm-long LPWGs. However, to achieve extremely high sensing potential, these LPWGs require the simultaneous control of multiple structure parameters. It is necessary to both obtain adequate resonance spectral position, shape and coupling magnitude, and also to ensure high but constant sensitivity levels over the entire measurement range. These simulations demonstrate that the most sensitive LPWG versions require very accurate structural parameters, and are subsequently more prone to manufacturing errors as well as experimental conditions.

To address the fabrication variability that can affect the LPWGs, a statistical study is performed: 2000 LPWG versions have been simulated by simultaneously introducing random geometrical deviations on w and t with standard deviations of $\sigma_w = 3.8$ nm and $\sigma_t = 1.3$ nm, respectively [17, 23, 270]. The simulated variations in EIs and GIs of the coupled modes and their subsequent dispersions are then

incorporated into the model to evaluate the resulting deviation from the expected resonance spectral positions and sensitivities. By considering LPWGs that exhibit resonance between 1500 and 1650 nm, and sensitivities varying by ± 25% of the typical simulated value as devices operating correctly, the proportion of working LPWGs with designed sensitivity levels of 30,000 and 300,000 nm/RIU are respectively estimated to be ~ 50 % and ~ 5 %.

Nonetheless, this estimation takes into account only static deviation of the waveguides' dimensions incurred during fabrication. LPWG non-uniformities[2] could lead to more significant transmission modifications, ranging from minor deformation of the LPWG's spectral signature to complete coupling signature scrambling. These modifications will depend on both the non-uniform longitudinal profile along the propagation axis and the dimensional amplitude variations. Note that future work will focus on studying the effects of non-uniformity on the LPWG response.

Therefore, in the design of high performance LPWG refractometers, the main criterion would lie in maximizing the impact of the waveguide materials' RIs on the propagation constants.This would minimize the influence of geometrical deviations that could occur during fabrication. Such optimization could be obtained by using waveguide materials of lower RI contrasts.

[2]Non-uniformities here include both dimension errors that are not uniform on the modulated waveguide and anisotropy of the sensed medium

Chapter 6

Application to CO_2 Gas Sensing: Preliminary Results

Contents

6.1 Chemical-Optical Transducer Layer

6.1.1 Carbon Dioxide Sensing

Carbon dioxide (CO_2) is the primary greenhouse gas emitted principally by anthropogenic activities. With over 30 billion tons released each year [15], CO_2 represents over 75% of the total mass in emitted greenhouse gases, as illustrated in figure 6.1(a). It is, in fact, estimated that CO_2 contributes 60% of the increase in greenhouse effect that is due uniquely to human-related activities [15], such as electricity generation, transportation and industrial processes, whereas the residential and commercial sectors account for "only" 11% in CO_2 emission. Since excessive exposure to or inhalation of CO_2 can induce severe health conditions, the related sensor market mainly focuses on indoor air-quality monitoring [16]. It is estimated that CO_2 sensors account for 31% of the gas sensing market share [16, 271], representing approximately 700 million US dollars. This is expected to grow by $\sim 80\%$ by the year 2028 [16]. The optical sensor share itself is expected to increase by an additional 25% to this date, thus underlining CO_2 sensing as a dominant sector for the design and fabrication of original photonic gas sensors.

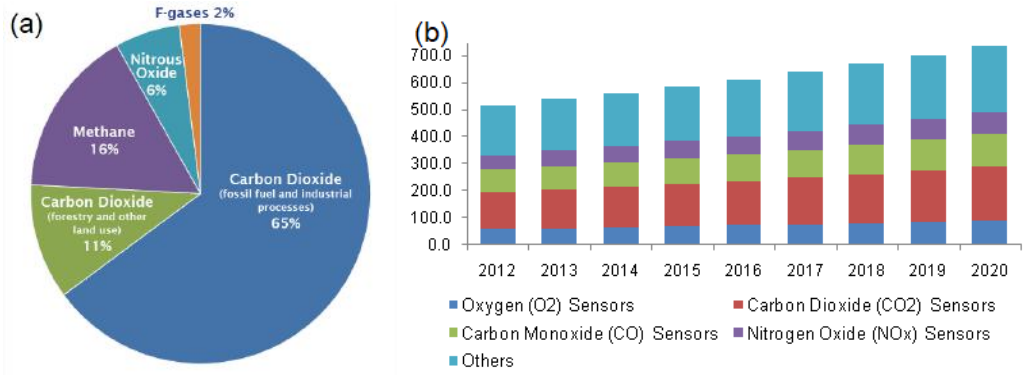

Figure 6.1: Global greenhouse gas emission by gaz [15] and Europe gas sensors market by product, 2012 – 2020 (USD Million) [16]

6.1.2 Introduction to Functionalized Polymer-based Gas Sensing

As previously explained in Chapter 1.4.1, the optical gas transducer quality depends on both its chemical affinity to the analyte and its structural properties that define its ability to diffuse the target gas into the porous medium. In this subsection, different possible engineering methods for manipulating these parameters are presented, together with the sensing film deposition process that is implemented for CO_2 sensing.

6.1.2.1 Engineering the Polymeric Structure

Gas-specific polymer functionalization requires several parameters to be considered to obtain a transducer with the desired properties:

1. The solvent used for dissolving the monomer before polymerization is the main contributor determining the morphology of the immobilization matrix. The solvent should allow sufficiently high solubility of the polymer and the functionalization indicators, when needed, to obtain films with high material homogeneity.

2. The solvent's volatility and mechanical properties are preponderant factors in defining the polymer's porosity and permeability. The porosity depends on the polymerization process during the evaporation of the solvent [36].

3. The viscosity (when dissolved in the solvent), flexibility and stability of the chemical and physical properties of the polymer over time can be engineered by the use of chemical additives such as plasticizers (to reduce viscosity), cross-linkers (to increase viscosity) or initiators (to initiate polymerization in aqueous solutions) [74, 77].

4. The macro structure of the polymer (such as surface smoothness) mainly

depends on the coating parameters as well as the polymer concentration in the solvent and the solvent volatility.

5. Surface treatment of the sensing area such as silanization can improve the coating process and physical stability of the sensing film. In fact, as shown in appendix A.9, water infiltration can cause coated polymer films to detach from the target surface when incorrectly treated.

6. Depending on the coated polymer, it is sometimes possible to restructure the sensing film using optical lithography [272] or nano-printing processes.

6.1.2.2 Coating Methods

Most common coating methods include spin coating, dip coating and spray coating [273]. Spin coating is a popular method that is also used for the coating of optical resists employed as mask layers in lithography techniques. This method relies on the deposition of a polymer in its liquid state (dissolved in solvent) on a planar substrate to be spinned at a specific rotation rate to obtain the desired thickness. Thermal curing can then be used to evaporate the solvent completely, thereby allowing the solidification of the polymer matrix. Dip coating is based on the continuous and controlled immersion of the substrate in the coating liquid to form a smooth polymer film. Spray coating is a more specific technique that involves directly spraying the liquid state polymer onto the planar substrate.

6.1.3 CO_2 Sensing Film

6.1.3.1 Polymer Material

Two materials considered to be suitable for elaborating the porous RI transducing layer have been employed in this thesis. Styrene-Acrylo Nitrile (SAN) is first examined as a potential candidate for gas sensing due to the following properties: high porosity potential [274] and chemical permeability, high transparency in the NIR and possible use for polymeric waveguide fabrication [272], high RI of $\sim$1.55 at 1550 nm for modal interaction enhancement to increase sensitivity, and, finally, its versatility to be engineered to incorporate macro-molecular selectors, such as Cryptophanes for methane specific detection [275, 66, 276, 254] or other suitable molecules as described in Chapter 1.

Polyhexanide (polyhexamethylene biguanide or PHMB) , is also considered and finally chosen as the polymer host as it has been previously demonstrated in photonic CO_2 sensing designs [105, 277, 172]. PHMB is a low-toxicity polymer that is typically used as disinfectant and anti-sceptic. Soluble in water, it is also commonly used for bio-regulation in swimming pools. In fact, the high affinity of the polymer to CO_2 makes it a promising candidate for selector-free gas sensing, which greatly facilitates fabrication of the porous film. Additionally, the RI of PHMB at 1550 nm is $\sim$1.54 [105], which is compatible with LPWG no. 1.0 previously described in Chapter 5.

6.1.3.2 Coating Process

The PHMB material is procured as a white powder with 95 % purity from JHSS China. Based on the chemical report of the scientific committee for the European Commission, the main PHMB solvents are methanol and water [278]. Methanol is hereby selected for its higher surface adhesion to silicon oxide and higher chemical volatility compared to water. The PHMB powder is dissolved with a ratio of 50 mg/mL of methanol, and mixed using a magnetic stirrer for 3 hours. A 1.4 µm thin film with a relatively smooth surface is next obtained by spin coating onto a silanized 2×2 cm^2 photonic chip at a spin rate of 800 rpm. The solvent is next evaporated by annealing at 90^oC for 30 minutes. Prior to obtaining the desired film characteristics, multiple tests are performed on SAN and PHMB with different solvents, coating spin speeds, polymer concentrations (in the solvent), chip surface types and annealing temperatures.

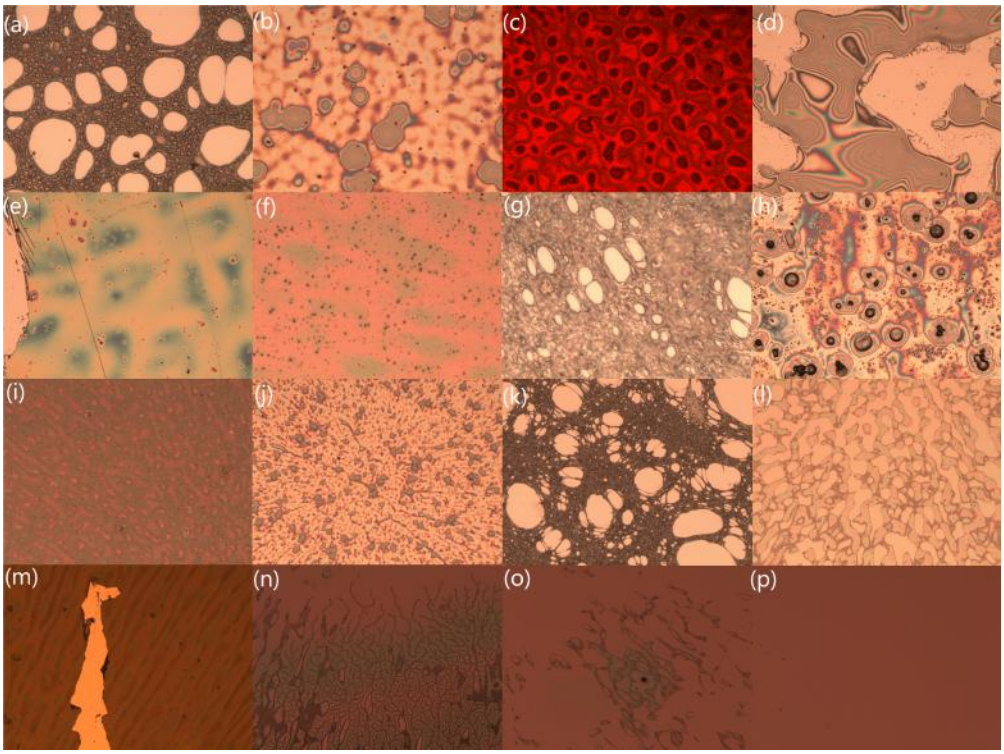

Figure 6.2: Optical microscope images of deposited polymer films: (a)-(l) coatings with unsuitable solvents and parameters displaying viscosity, adherence or solubility issues, (m) displaying a minor scratch, (n)-(p) showing the effect of progressive planarization on the surface topography

Figure 6.2 displays optical microscope images of the macro-state of the polymer materials after polymerization onto the target surface of the photonic chip. A wide range of behaviors in terms of surface adhesion, plasticity, viscosity and polymer solubility can be observed. Additionally, planarization processes are experimented

using nano-printing machines to smoothen the polymer surface, in anticipation of possible use of gas sensitive polymers directly as optical waveguides. These processes are found to effectively reduce the surface roughness when (1) the applied pressure is sufficiently high and (2) when the curing temperature is above the polymer's glass transition temperature, as seen in figure 6.2(p).

6.2 Experimental Results

6.2.1 Experimental Setup for Gas Sensing

Bottled CO_2 gas from Gazdetect in various pre-calibrated concentrations are employed in this thesis. To introduce the gas, a glass chamber is used as an impermeable container to allow the control of the gaseous environment into which the photonic chip is immersed, as shown in figure 6.3. The chamber has three openings: two for gas input and output, respectively, and the third to allow the fiber array to be aligned with the photonic chip for light injection and to perform the measurements. The third opening is sealed using a flexible rubber cover and silicone (as airtight seal) in order to prevent gas leakage and/or contamination of the gas chamber while enabling the fiber array to be moved and positioned onto the chip surface. A commercial CO_2 sensor (MH-Z16) is also inserted into the chamber as the reference sensor and interfaced to an Arduino card. Finally, the chamber is placed on top of the magnetic stirrer regulator (stirrer placed inside the gas chamber) in order to ensure a better homogeneity of the gaseous environment within the chamber itself.

6.2.2 Preliminary CO_2 Sensing Results

To detect the CO_2 gas, LPWGs on photonic chip n^{o}6 are coated with a PHMB film (see layout in appendix A.6). The LPWGs are positioned at least 2 mm away from the grating couplers on the layout, thereby allowing the fiber array to be in full contact with the chip without obstructing the interaction of the gas with the polymer in the sensing region. To interrogate the sensor (PHMB-coated LPWG), light is coupled from the fiber array into and out of the photonic chip via the grating coupler pairs (i.e. one pair of grating couplers to one LPWG). The grating pairs, positioned at both ends of the U-bend (see top of figure 6.3), are joint by waveguides in which the selected coupling modes are then propagated up to and through the LPWG sensing elements. Consequently, for the analysis of the output signal from the gas sensors, the superposed contributions from the grating couplers, waveguides, and coupling irregularities are first de-embedded from the total output. Subsequently, a normalized coupling spectrum is obtained, as illustrated in figure 6.4. Here, Lorrentzian curve fitting is applied to the obtained response and shown to superpose relatively well to the de-embedded resonance signal.

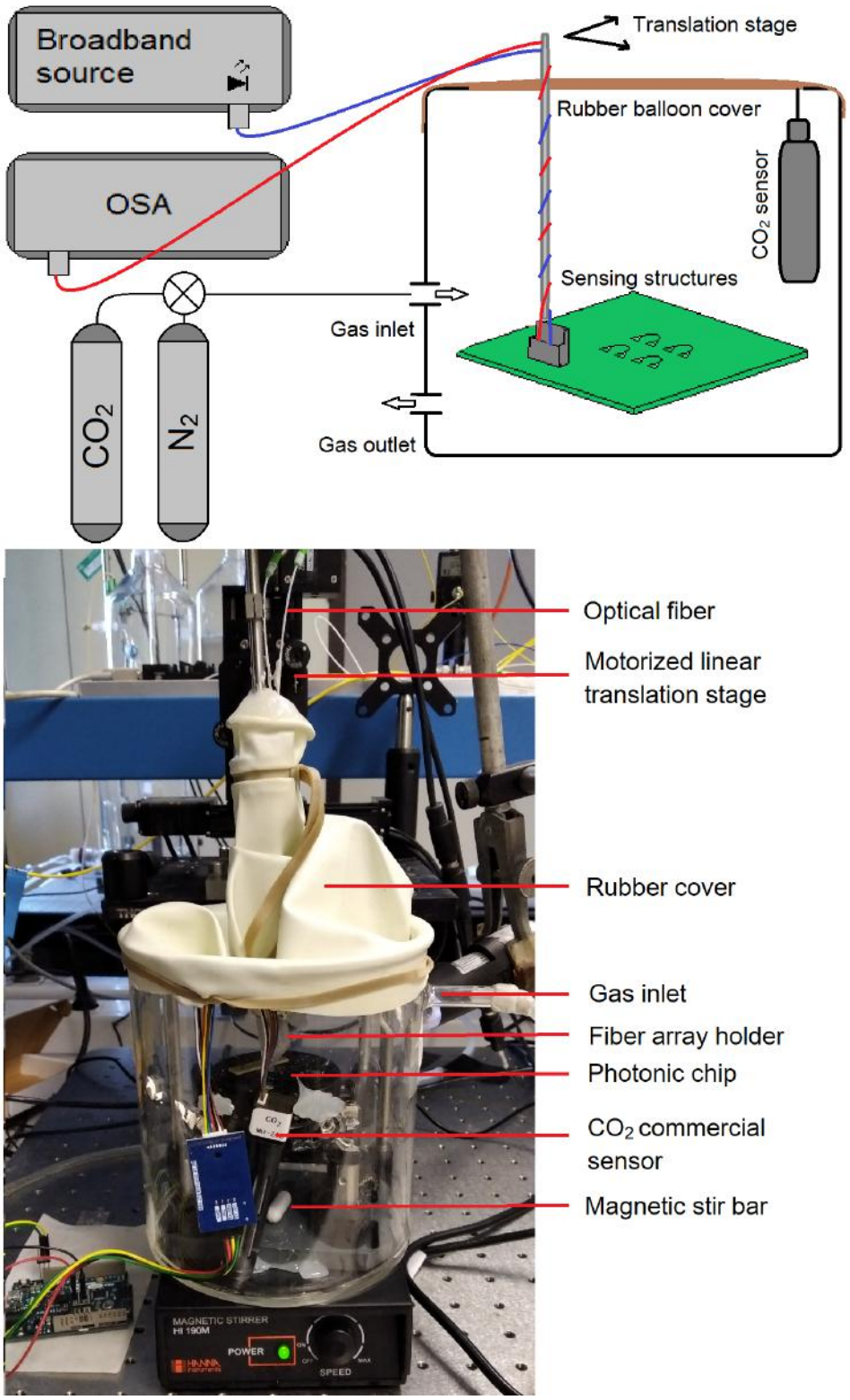

Figure 6.3: Schematic (top) and experimental setup (bottom) of the CO_2 gas sensor

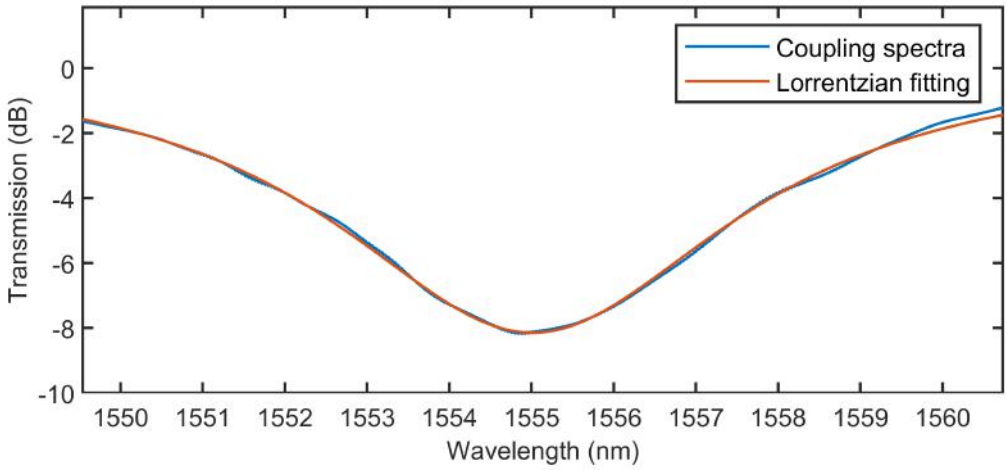

Figure 6.4: De-embedded coupling spectrum of LPWG 1.3

Initial gas sensing tests have been performed by using the low-resolution fast-scanning mode of the OSA, with each scan carried out iteratively every 15 seconds. The measured spectra are analyzed in real-time with a dedicated LabVIEW program, which additionally performs the curve fitting operation. Two experimental barriers are subsequently observed during the measurements:

1. During gas-flow opening, the applied gas pressure is found to lead to an instantaneous virtual spectral shift of the resonance. This could be attributed to a minor variation of grating coupling behavior induced by minor displacements or vibrations of the grating coupler upon initial gas flow.

2. The reference CO_2 sensor exhibits an inertia during the measurement, in part due to its small dimension compared to the relatively large volume of the gas enclosure. Depending on the concentration injected, the gas mixture or atmosphere is estimated to generally stabilize or homogenize after a few minutes. The mixing process is aided by the flux created by the magnetic stirrer.

Upon introduction of CO_2 into the chamber, the resonance shifts before stabilization of the gaseous atmosphere (i.e. after a few minutes) are detected and plotted in figure 6.5. The CO_2 concentration measured by the reference sensor after stabilization of the atmosphere in the chamber is displayed a few minutes after gas flow.

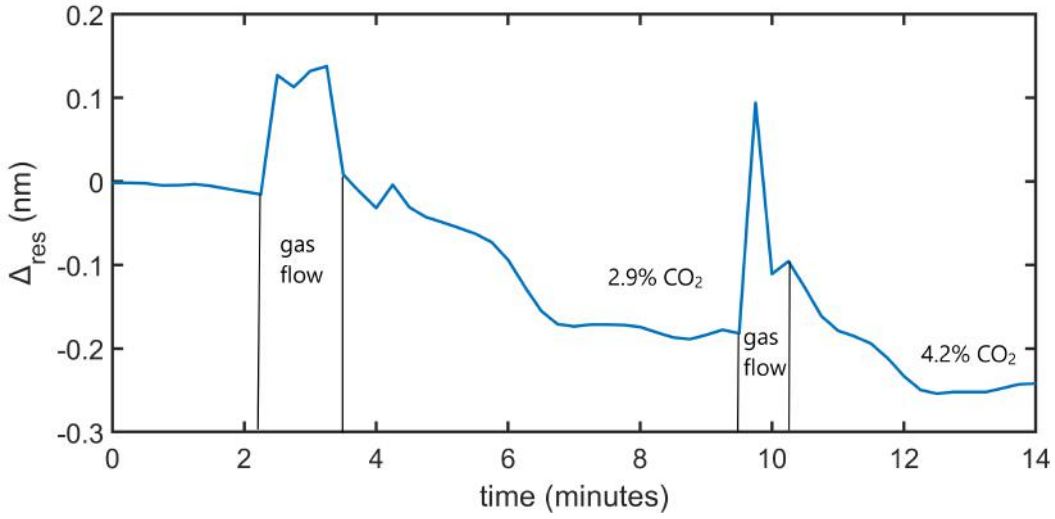

Figure 6.5: Preliminary results from CO_2 sensing experiment in enclosure under low-resolution fast-spectral scanning mode: resonance spectral position shift ($\Delta_{res}(nm)$) versus time for different CO_2 concentrations

To compensate perturbations induced during measurements due to gas surge immediately after valve opening and the relatively slow stabilization of the gaseous atmosphere in the chamber, the measurements have next been performed in a second experiment over 1h30 at very low gas flow. Here, high-resolution low-speed scans are instead performed and analyzed against referenced measurements. A quasi-linear spectral shift is observed, as illustrated in figure 6.6. Linear interpolation is then applied on the measured data to obtain a sensitivity of $6.8 \cdot 10^{-3}$ pm/ppm. Subsequently, based on the value of the LPWG sensitivity, the RI sensitivity of the PHMB layer is estimated to be $\sim 4.7 \cdot 10^{-9}$ RIU/ppm, corroborating the accepted value of $\sim 6 \cdot 10^{-9}$ RIU/ppm reported in the literature [105]. The discrepancy between these two sensitivity values can be attributed to different coating methods and parameters employed, thus giving rise to slightly different solubility characteristics.

6.3 Discussion

Preliminary results from gas sensing experiments have demonstrated the potential for high sensitivity CO_2-specific sensing using LPWGs coated with a sensitive PHMB polymeric film. Experiments have also been carried out to detect methane (CH_4) by functionalizing the LPWGs with a polymeric film of SAN incorporating cryptophane A molecules, which are CH_4-specific supramolecular traps. However, these attempts have proved unsuccessful to date as the sensors have been found to exhibit very low sensitivity or even no response when CH_4 is introduced into the instrumented gas chamber during tests. This could be attributed to several reasons, hitherto not investigated, such as poor quality of the cryptophane A molecules

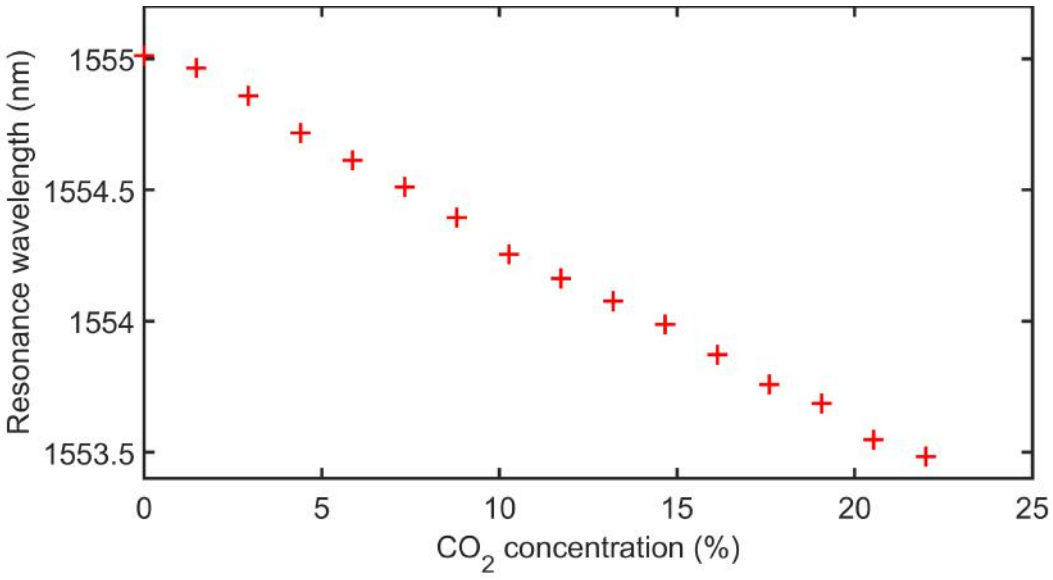

Figure 6.6: CO_2 spectral sensitivity

employed, polymer deterioration or destruction (instead of dissolution) of the cryptophane molecules by the highly aggressive solvent used (1,1,2,2 tetrachloroethane), etc.

During the experiments, several flaws in the gas-enclosure setup and photonic coupling components have been observed and could limit the complete evaluation of the LPWGs dedicated to gas sensing applications. Below is a brief summary of the principal flaws and their possible detrimental influence on the performance of the LPWG gas sensor:

1. the size of the enclosure and lack of proper gas-mixing components or equipment makes it very difficult to assess the exact response time of the porous polymer layer and to cleanse the enclosure. This also has an impact on the analysis of the gas desorption process from the sensitized polymer film when concentration is decreased.

2. the coupling irregularities and perturbations on the photonic chip currently limit the sensing resolution by drastically increasing the floor noise. Consequently, despite a very high spectral sensitivity, trace gas detection could be limited as the useful signal could easily be buried by noises from environmental perturbations such as pressure and temperature variations, and vibrations, in particular.

To resolve these issues, future experiments should account for:

1. a compatible airtight enclosure or chamber to introduce the target gas, with suitable dimensions to ensure rapid and uniform or homogeneous gas distribution throughout the chamber volume. An example could be a small-dimension

3D-printed enclosure that can provide atmospheric control at the surface of the photonic chip. A miniature chamber made of resin has been produced for this purpose (see appendix A.10) but presented leaks that have yet to be fixed.

2. direct butt-coupling to the photonic chip that could potentially enhance the coupling efficiency and eliminate coupling interferences. Securing the lead-in/lead-out fiber or fiber array to the chip by gluing or epoxy could subsequently be used to stabilize the coupling and significantly reduce mechanical perturbations.

3. the use of LPWGs with higher spectral sensitivities and temperature resilience. LPWG 2.0 is currently being adapted to sense PHMB refractive index in order to assess CO_2 gas concentration.

Conclusion

Integrated photonics is a very promising domain for the development of powerful embedded sensors, aiming for all sort of applications. In fact, the flexibility of design offered by the integrated platform and the intrinsic properties of optical systems for chemical sensing have led to a multitude of integrated architectures to be proposed over the years. The wide range of sensing mechanisms and measurement techniques has greatly complicated the analysis of such systems and made it difficult to identify the most promising structures.

A framework for optical-chemical sensors analysis has been initially suggested. It not only encompasses the different definitions that were presented in published reviews but also offers a model describing optical chemical sensor systems as a functional analysis. This model has subsequently been used to analyze the state-of-the-art of integrated optical gas sensors. As a result, the classification model suggests advantages and drawbacks of each sensing methods and system components, and reveals refractometric systems as one of the most promising candidate for gas monitoring since they could directly benefit of both the ever-improving micro-fabrication technology and chemical-material technology development. It was thus decided to investigate integrated refractometers.

Photonic Integrated Circuit (PIC) functions such as waveguides, grating couplers and fundamental refractometer structures (Mach-Zehnder Interferometers, Micro-Ring Resonators, Bragg Gratings) have been firstly designed, fabricated and characterized using the dedicated optical probe station developed during this thesis. The obtained propagation performances of our waveguides has proved to be the main limitation in the design of refractometers. Nevertheless, optical transmission has been found to be still sufficient to allow correct characterization of the intrinsic performances of the fabricated structures.

After an in-depth overview of the main refractometric structures, it has been decided to focus on a structure originally implemented on fibers: the Long Period Grating. The coupling mechanism and intrinsic sensing properties of LPWGs has been then analyzed using a mathematical model based on Coupled-Mode Theory, from which some performance optimization techniques have been derived and proposed.

As a first version of Long Period Waveguide Grating (LPWG), it has been decided to increase the influence of the analyzed media's refractive index on the propagation constants of the coupled modes to enhance the bulk sensitivity. This has been achieved by directly employing the gas-porous media as the LPG's cladding for modal propagation. Although a high sensitivity has been assessed, this LPG structure is mainly dedicated to gas sensing since its surface sensitivity used for refractive index of liquid analytes is an order of magnitude lower. A second version, based on a rib waveguide, has then been developed using dispersion tailoring methods, fabricated and characterized. A 6-fold sensitivity improvement has been

achieved reaching 11,500 nm/RIU, while having an extremely low cross-talk sensitivity to temperature of 0.15 nm/RIU, over a large measurement bandwidth of at least 100 nm. Having successfully demonstrated the important potential of LPWGs, a third LPWG architecture has been proposed and simulated, combining both optimization approaches, showing sensitivities up to 300,000 nm/RIU. We have however attempted in this thesis to prospectively assess the effects of the manufacturing and testing limitations that could arise, on the performances of these LPWG architectures.

Finally, preliminary results for CO_2 gas sensing application using the first LPWG have been obtained and discussed. It employs a polyhexamethylene biguanide polymer coating for CO_2 functionalization. However, the sensor performances are found to be mainly limited by the current test setup, especially due to mechanical perturbations. A new set-up, fabricated with 3D-printing, is thus under development.

This thesis demonstrates the great potential of LPWGs for sensing purposes, reporting models corroborated by experimental results of the highest performances. A total of one conference and two journal papers have been published, and a patent has been filed.

Both manufacturing resolution and the heterogeneity of the sensed environment have been found to greatly affect the optical response of a LPWG and create irregularities in the transmitted spectra.

Although this might prevent very sensitive LPWG from being feasible, it could also be used to develop new sensing applications. Our future work will be focused on monitoring heterogeneous profiles of chemical mixtures or possibly bent profiles of fibers, using LPGs. This could be performed with algorithms aiming at numerically retrieving the refractive history and/or profile of optical propagation in LPGs from the transmitted interference patterns.

Appendix A

Appendix

Contents

A.1 Layouts and Pictures of Fabricated Photonic Chips

A.1.1 Photonic Chip n°1

Photonic Chip n°1 (layout shown in figure A.1) was designed as a first attempt to perform photonic chip coupling, propagation and some fundamental functions. The objective here was also to characterize waveguide mismatch and the effects of overlaps at the connection or interface between components, and estimate dimensional errors in waveguides and components in terms of width and thickness. Grating couplers with different periods have been designed to address coupling errors, which resulted in slightly shifted coupling spectra because of slight errors in grating fill factors.

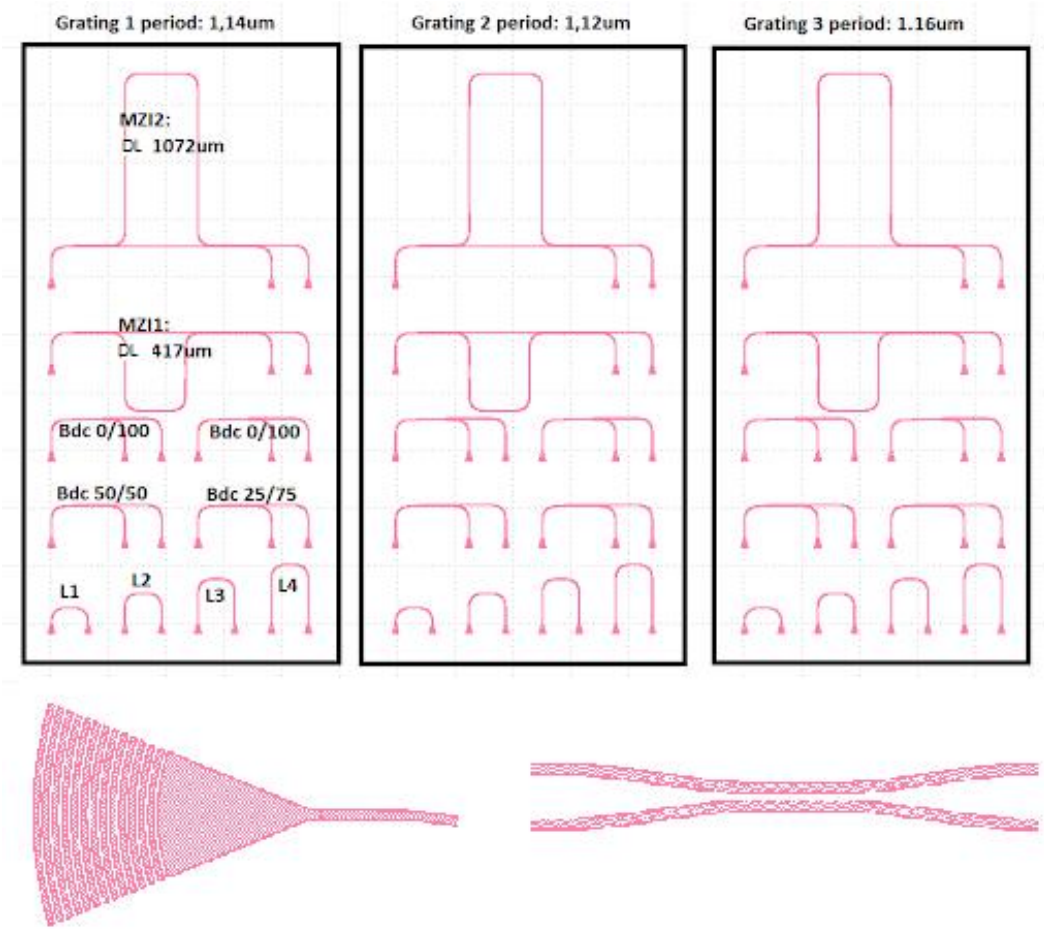

Figure A.1: Photonic Chip n° 1's layout

A.1.2 Photonic Chip n°2

Photonic Chip n°2 (layout shown in figure A.2) was designed to evaluate straight and bent waveguide losses and compare the effets of Normal mode exposure to FBMS mode exposure of propagation losses. Waveguide coils of different lengths have been designed and characterized. Two issues were observed for normal exposure mode: (1) waveguide mismatchs have been observed, as illustrated in figure A.2(d), which would require higher exposure intensity to remove, and (2) the RAITH150 exposure algorithm limits the amounts of point-coordinates per object to 4000. As a result, truncations were unavoidable when generating the 3 cm coil using the normal mode exposure configuration, which resulted in complete intensity loss. On the other hand, FBMS exposure mode showed much better results but required a specific transformation algorithm to be implemented in order to meet the RAITH150 requirements.

Consequently, for the following PIC tape-outs, waveguides were exposed with

FBMS mode to achieve better performances.

Additionally, an array of 5 Bragg-grating reflectors of varying periods was also designed and added to the chip. The measured responses were found to be very similar to the simulated values, as shown in figure 3.4, but their spectral position was slightly shifted, which suggests a grating effective index different from the simulation, probably due to fabrication smoothing of the binary corrugations of the grating [23].

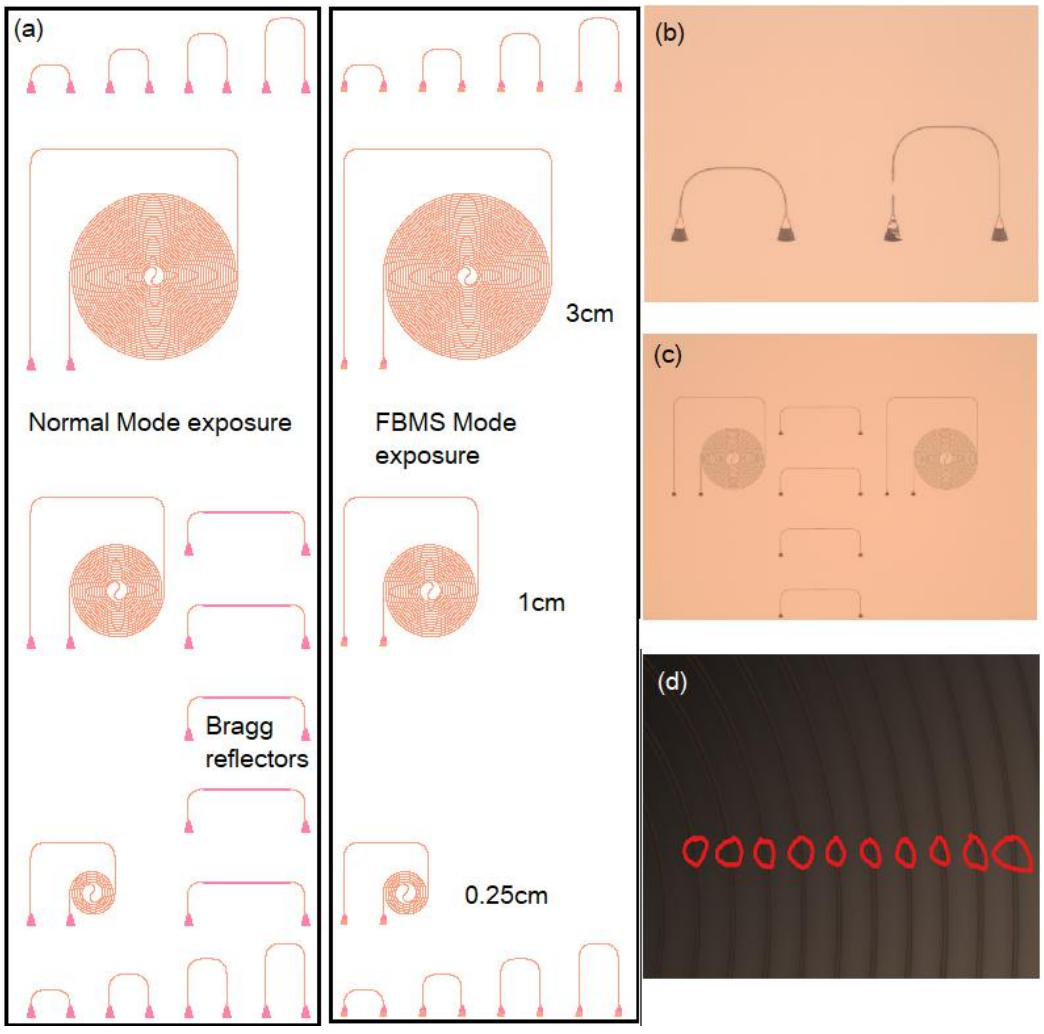

Figure A.2: (a) Photonic chip n° 2's layout, and optical microscope pictures of (b) grating coupler pairs showing defaults, (c) coil waveguides and Bragg Grating Reflectors, and (d) coil waveguide mismatches showing the working field junctions

A.1.3 Photonic Chip n°3

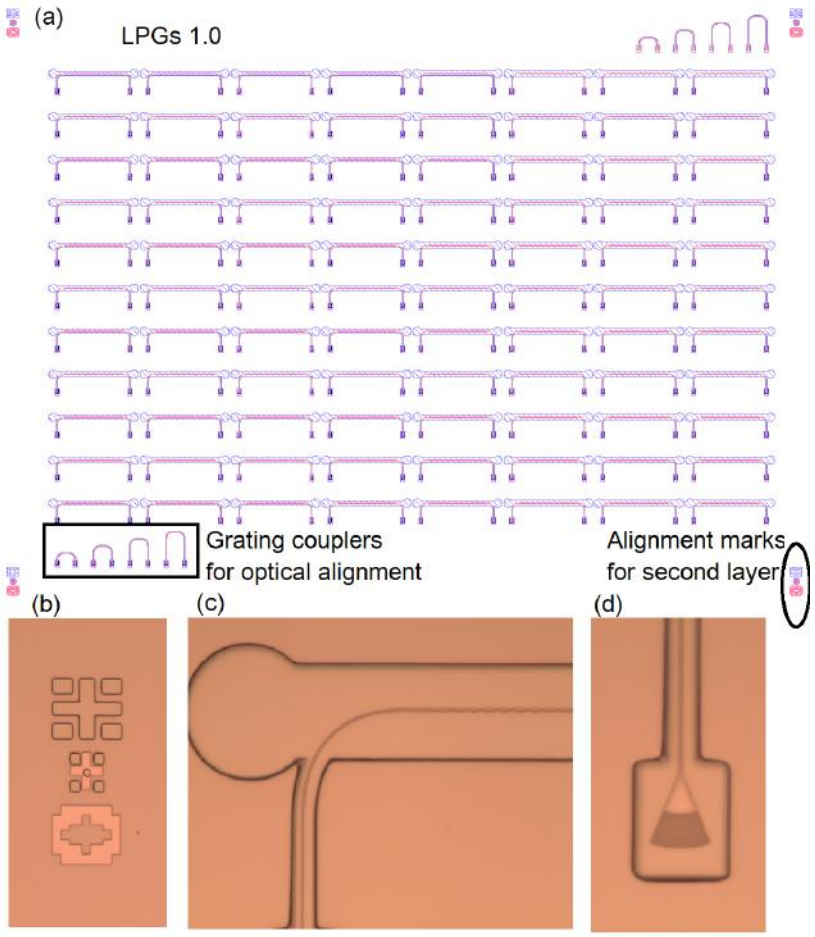

Figure A.3: (a) Photonic chip n° 3's layout depicting an array of the LPWGs 1.0 and optical microscope pictures of (b) alignment marks between SiN and SU8 layers, (c) multimode waveguide endpoint, and (d) SU8-cladded grating coupler

Photonic Chip n°3 (layout shown in figure A.3) was designed as a first attempt to perform multimode coupling with LPWGs (corresponding to version LPWG n°1.0). An array of LPWGs of varying widths and periods was designed to maximize the probability of observing a coupling resonance within the optical wavelength span of the optical spectrum analyser, and assess the variations of coupling resonance properties due to changes in the critical dimensions. Alignment marks have also been introduced in the layout to enable SU8 multimode waveguide fabrication in a second layer by laser lithography. The coupling spectra that have been observed demonstrated highly variable behavioral shifts (resonance, coupling amplitude...) compared to the simulation, and between structures with the same design properties. It was concluded from the measured spectra that the use of laser lithography resulted in too high variability for proper fabrication of this LPWG version.

A.1.4 Photonic Chip n°4

Photonic Chip n°4 (layout shown in figure A.4) was designed to fabricate LPWGs using HSQ side-walls for incorporating multi-mode waveguides. Four arrays of LPWGs with different widths and periods have been realized and characterized. A minor asymmetry in the obtained structures was observed due to poor calibration with the alignment marks. Nevertheless the coupling spectra measured between different LPWGs turned out to be consistent with each other and with the simulations. A small computational error in the definition of the absolute coordinates was found to induce a misalignment of the HSQ layer, as seen in figure A.4(d). This, however, had no major impact on the LPWG performances. Small resist peeling off can also be observed at certain LPWG field junctions in figure A.4(e), which caused the dysfunction of a significant part of the LPWGs. Additionally, transmission losses for different waveguide widths (300 - 1000 nm) were also characterized for straight waveguides. In fact, LPWG transmission losses were suspected to be due to the narrow waveguide regions occuring at each modulation period. This analysis found the transmission profile to exhibit a cut-off value around a 700 nm waveguide width, as shown in figure A.4(f). Lastly, a dedicated script for automatically labeling the structures was added to ease their visual identification by microscope and thus to facilitate their characterization, as seen in figure **??**(c).

A.1.5 Photonic Chip n°5

Photonic chip n°5 (layout shown in figure A.5) was designed and fabricated similarly to Photonic chip n° 4 except for the use of higher exposure doses to reduce the effect of mismatch at the working field junctions in LPWGs. Also, waveguide widths wider than 700 nm were employed to reduce optical losses. Longer versions of LPWGs were also realized as well. These LPWGs consequently exhibit much better results than PIC n°4. These results were used to reconstruct a coupling spectra displaying resonances with each multi-mode, as displayed in figure **??**. Additionally, splitters/couplers were also designed and realized, and used in Mach-Zehnder configurations. However, most of the Mach-Zehnder structures (only) have been found to be unusable due to an algorithm error which resulted in their associated grating couplers to be exposed twice. Lastly, Phase-Shifted Bragg-Grating (BG) Reflectors were also designed but found to achieve very poor responses to the phase-shift, often bypassing the phase-shift condition and acting as mere BGs. This was attributed to the lack of control of the propagation loss coefficient in such waveguide gratings.

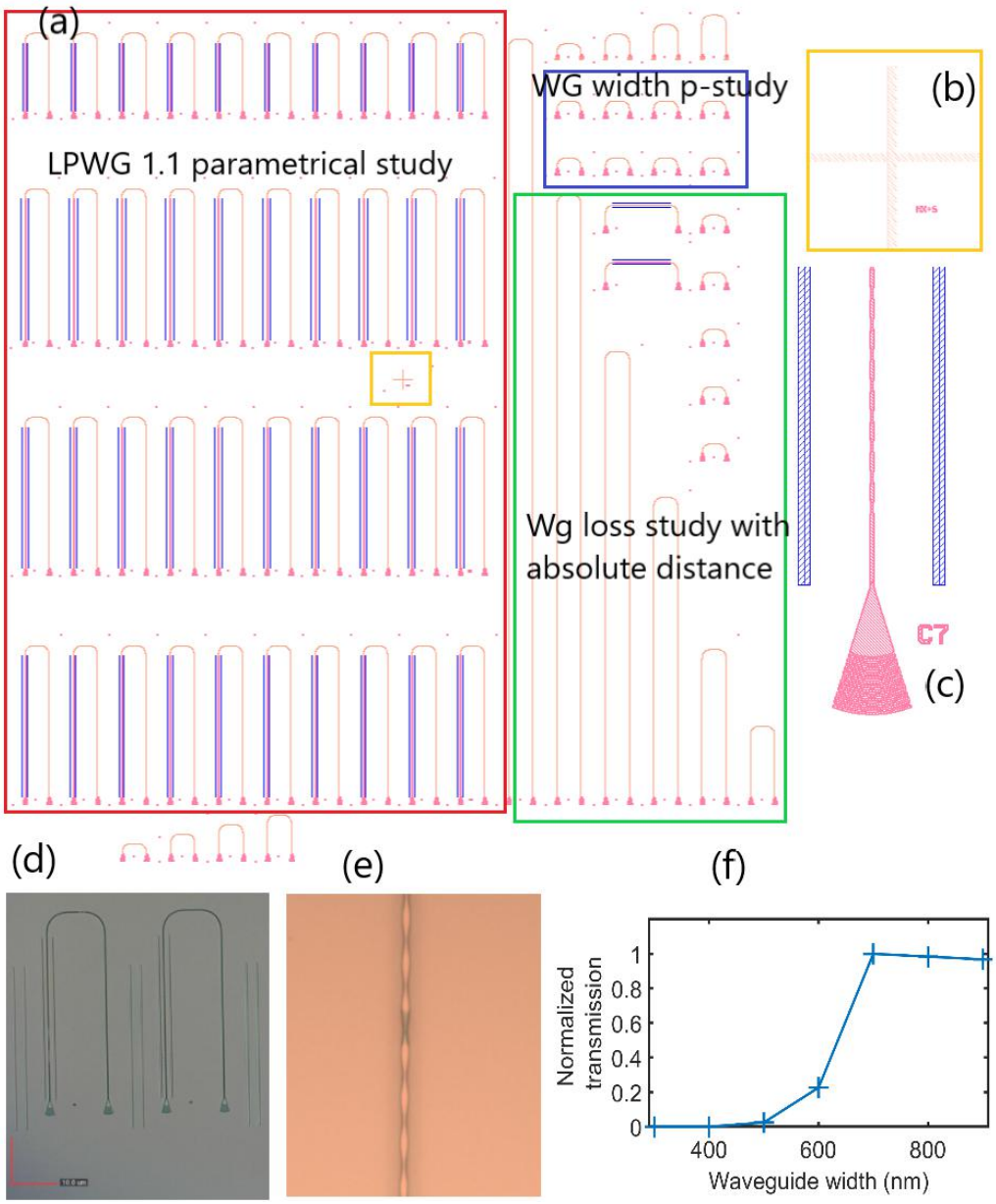

Figure A.4: (a) Photonic chip n°4's layout, depicting an array of LPWGs 1.1 with HSQ walls, and various waveguides for propagation loss study versus length and width, (b) alignment marks for E-beam, (c) structure numbering marks, (d) optical microscope pictures of HSQ layer's shifted exposure and (e) exposure default, and (f) measured transmission for waveguide of different widths exposing a cut-off value around 700 nm.

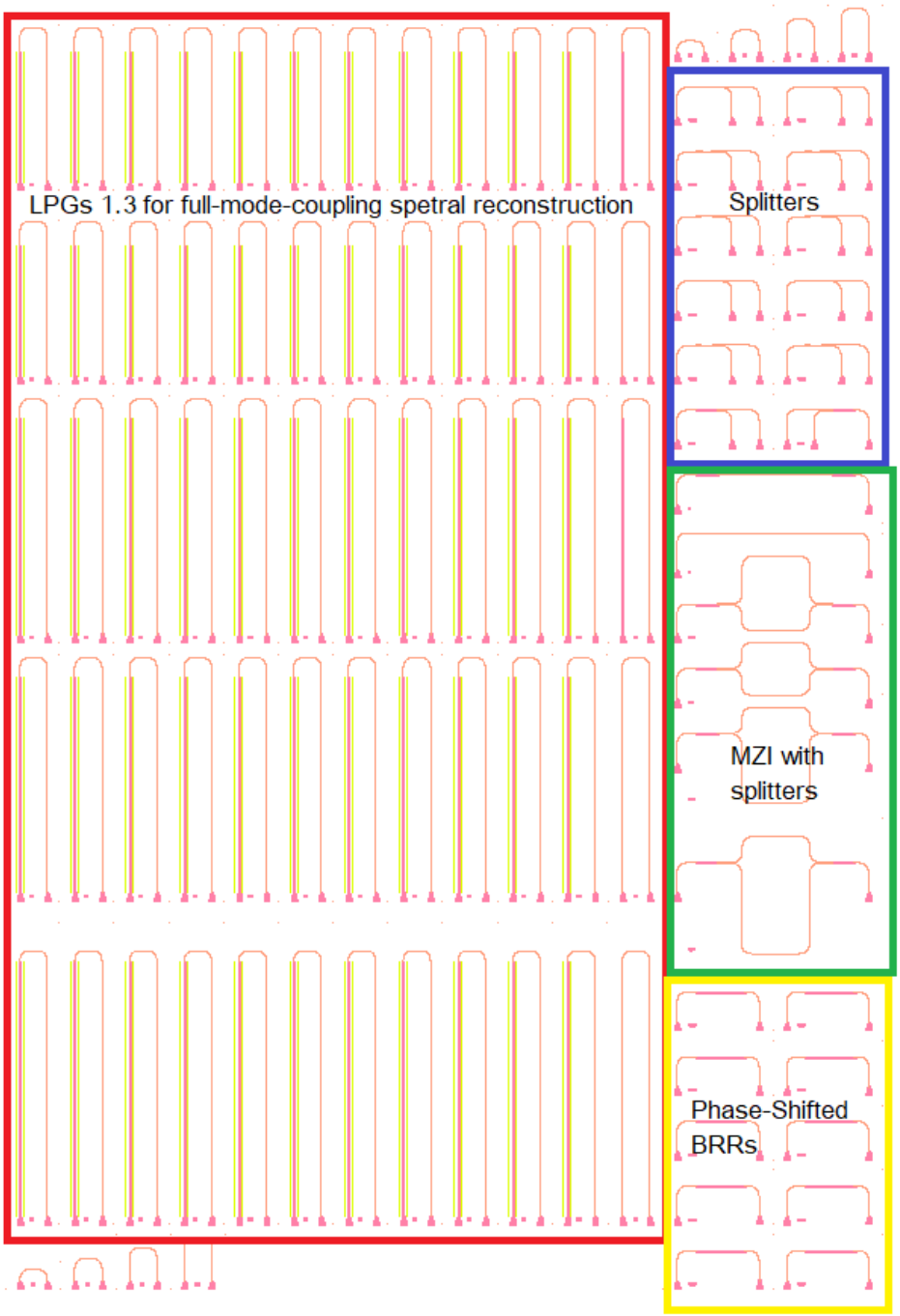

Figure A.5: Photonic chip 5's layout depicting array of LPWGs 1.2, waveguide splitters, Mach-Zehnder interferometers using splitters, and Phase-Shifted Bragg Grating reflectors

A.1.6 Photonic Chip n°6

Photonic chip n°6 (layout shown in figure A.6) was designed for the purpose of performing refractometric and gas sensing measurements. Unlike the previous PICs, the refractometric components have been placed at least 2 mm away from the grating couplers, so that the fiber array could be brought into contact without compromising the sensing surface of the LPWGs, Mach-Zehnder devices and ring resonators that were designed. A mask for SU8 opening in the sensing regions was produced by laser lithography. Additionally, waveguide converters have been used to perform coupling between SiN/Su8 waveguides to SU8/SiO2 and SU8/air waveguides, but were found to dysfunction due to overlap errors and incorrect exposure doses for the given dimensions. Lastly, a new layout script was produced to better control the exposure order of the components by using labeled layers, as illustrated by the multiple colors of each component in figure A.6. This has allowed working fields of structures to superpose without leading to double exposures (as encountered with MZIs in PIC n°4), thereby enabling a higher density of the components and waveguides to be obtained on the same chip. Consequently:

1. Multiple MZI refractometers have been designed, with various arm lengths to obtain multiple sensitivities and FSRs. Refractometric performances between 100 - 600 nm/RIU have been measured, with extinction ratios as low as 10 dB.

2. 6 MRRs have been realized with various coupling gaps, showing similar refractometric sensitivities ∼200 nm/RIU but different extinction ratios up to 10 dB.

3. LPWGs have been designed with spectral sensitivities of ∼1500 nm/RIU, and tested both with SU8, SAN and PHMB cover layers as the cladding material. Sensitivity to CO_2 has been measured, as discussed in Chapter 6.

A.1.7 Photonic Chip n°7

Photonic chip n°7 (layout shown in figure A.7) includes the first strip-rib LPWGs connected to grating couplers by strip waveguides and strip-rib converters, as discussed in Chapter 5. The LPWGs have shown refractometric sensitivities between +2000 and -11500 nm/RIU depending on the grating period. Figure A.7(a) shows the surface that was used for interferometric real-time monitoring of the RIE process. Figure A.7(d) shows HSQ-made cross structures that have been implemented in the first layer for automatic position re-calibration of the electron beam in order to reduce overlay errors on the second layer. The RAITH150 script employed was, however, found to be inefficient as the refractive index contrast between the HSQ layer and SiO_2 was too low for the calibration to be reliable.

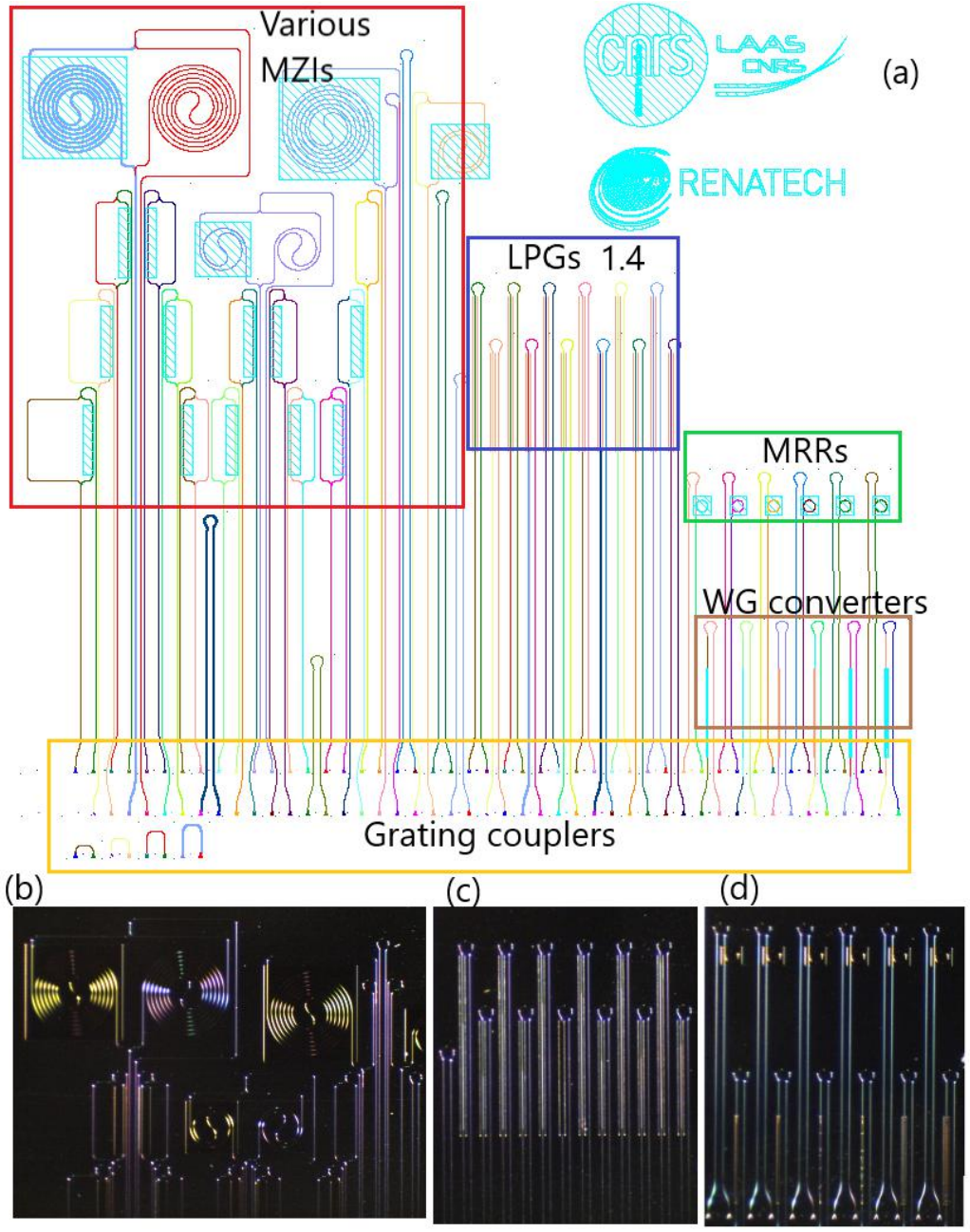

Figure A.6: (a) Photonic chip n°6's layout with MZIs, LPWGs 1.3, MRRs, waveguide converters, grating couplers and the appropriate logos (LAAS-CNRS and RENATECH). Also illustrated are magnified pictures of realized (b) MZIs, (c) LPWGs 1.3, and (d) MRRS and waveguide converters

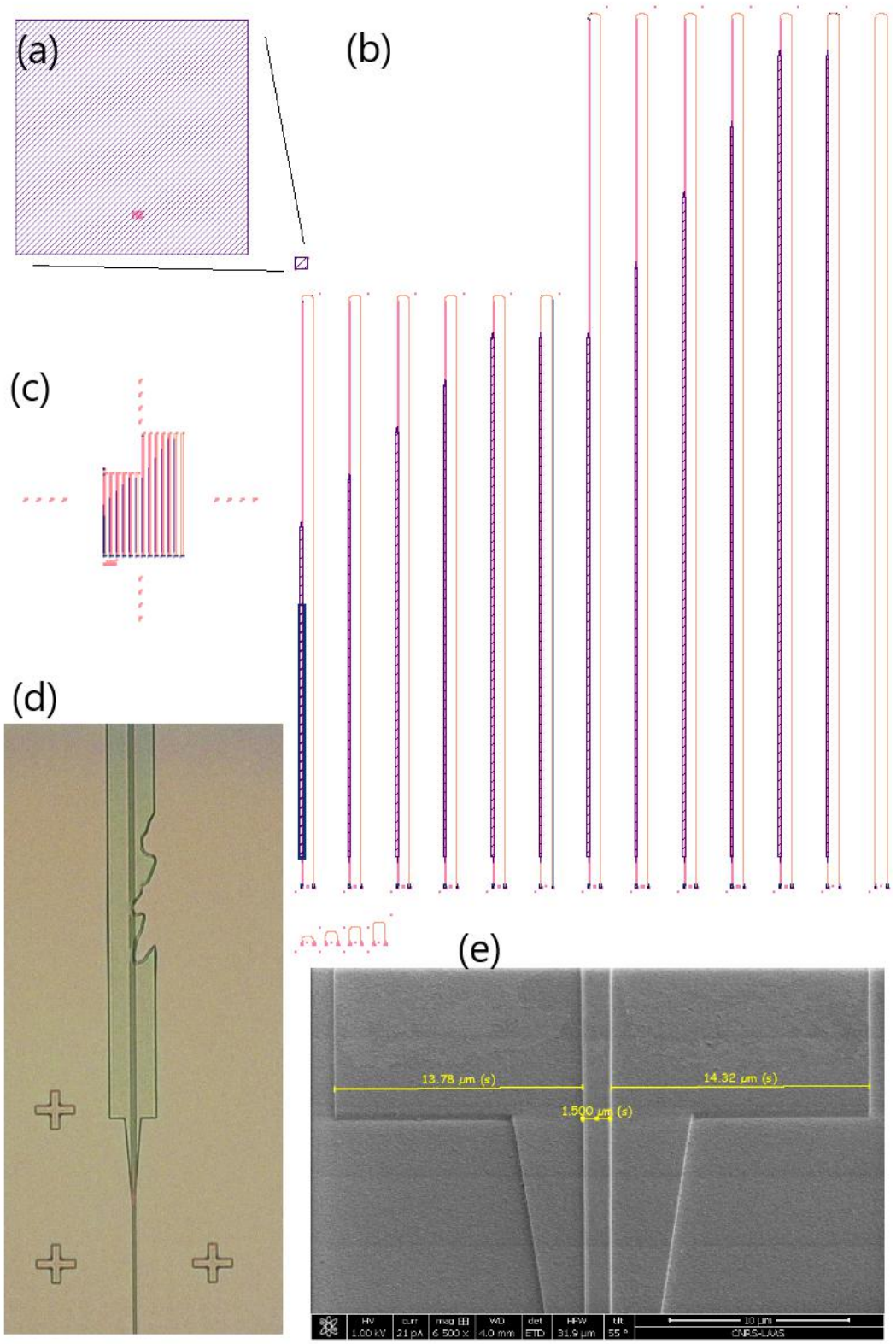

Figure A.7: Photonic chip n°7's layout depicting (a) square structure for RIE interferometric monitoring, (b) array of strip-rib LPWGs 2.0 of varying periods and lengths, (c) set of spatially distributed alignment marks, (d) optical microscope picture of LPWG with default and cross-marks for automatic position re-calibration, and (e) asymmetry of the rib-strip LPWG created by overlay error

A.2 Simulation

A.2.1 Statistical Analysis of Manufacturing Errors for LPWG2

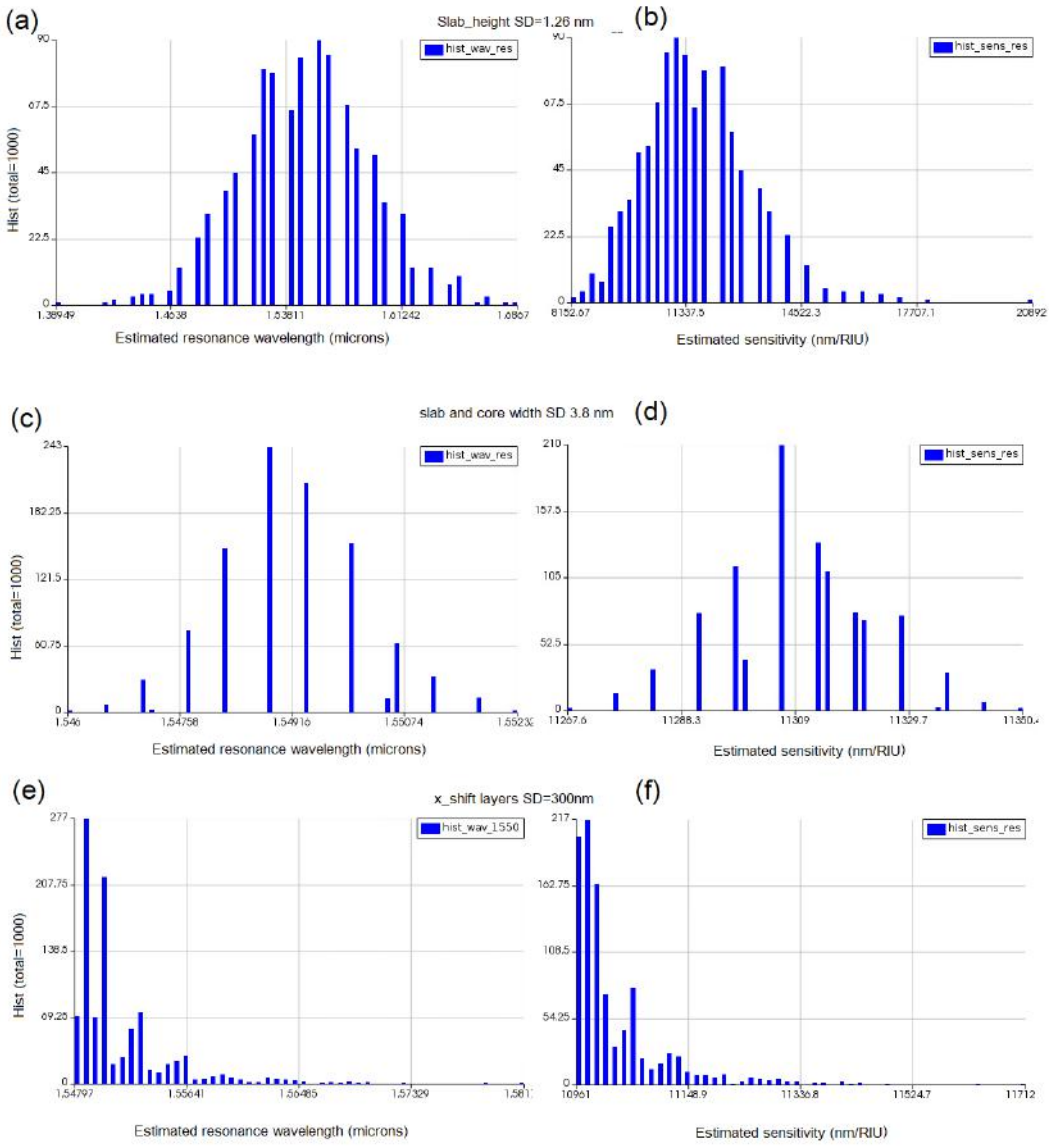

Figure A.8: Manufacturing tolerance analysis on LPWG2.0 (rib version), showing changes of resonance wavelengths and refractometric spectral sensitivities for random profiles of dimension variations: (a,b) slab thickness, (c,d) slab and core width and (e,f) translational core-slab shift [17]

Figure A.8 shows the simulated centre position of the resonance and sensitivity for 3000 versions of LPWG n∘2 (rib version). Random dimensional deviations have

been introduced on the slab thickness, the waveguide core, slab width and slab shift. The performance prediction analysis was based on the manufacturing variability of Deep-UltraViolet silicon photonics lithography [17, 23, 270]:

1. The slab and core widths were varied with a standard deviation SD = 3.86 nm
2. The core-slab etch depth was varied with a standard deviation SD = 1.26 nm
3. The off-align between different layers was varied with an arbitrary standard deviation SD = 300 nm.

It can be seen in figure A.8 that minor variations on all dimensions, except on the etch depth "e", have very little effect on the LPWG's spectral behavior (even at SD = 300 nm off-align, no significant effect is observed). The main variability contribution is "e", which is the difference in thickness between the core and slab regions.

Studies on the overall variability shows 78 % of the LPWGs' resonance wavelengths to remain within the spectral window of interest (1500 - 1600 nm) with a sensitivity variation of only ±15 %.

A.3 Experiment Results

A.3.1 Polymer Adhesion Issue

Figure A.9 shows a microscope image of Styrene-Acrylonitrile (SAN) polymer coating displaying a crack in which water has infiltrated because of poor adhesion to the surface. This could lead to sensor dysfunction due to polymer aging or water contamination. One could imagine using primer materials to enhance adhesion, like silanes.

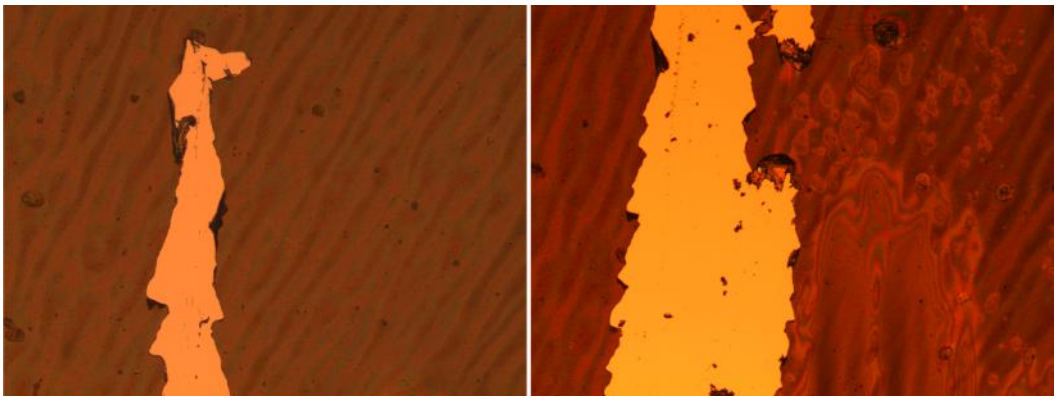

Figure A.9: Microscope pictures of physical fracture in a SAN polymer coated film, before and after contact with water, showing infiltration of water between the film and coated surface (from interferometric patterns)

A.3.2 3D-printed Piece for Atmosphere Control of Photonic Chip

Because of the perturbations that were introduced in the gas testing setup illustrated in figure 6.3, it was attempted to replace the enclosure with a 3D-printed resin-based piece (figure A.10) to be placed on the photonic chip. The piece was composed of two gas outlets that were connected inside the structure to a small cavity to be superposed on top of the sensing region of the photonic chip. Due to time constraints and minor leakage issues, testing was however not yet carried out.

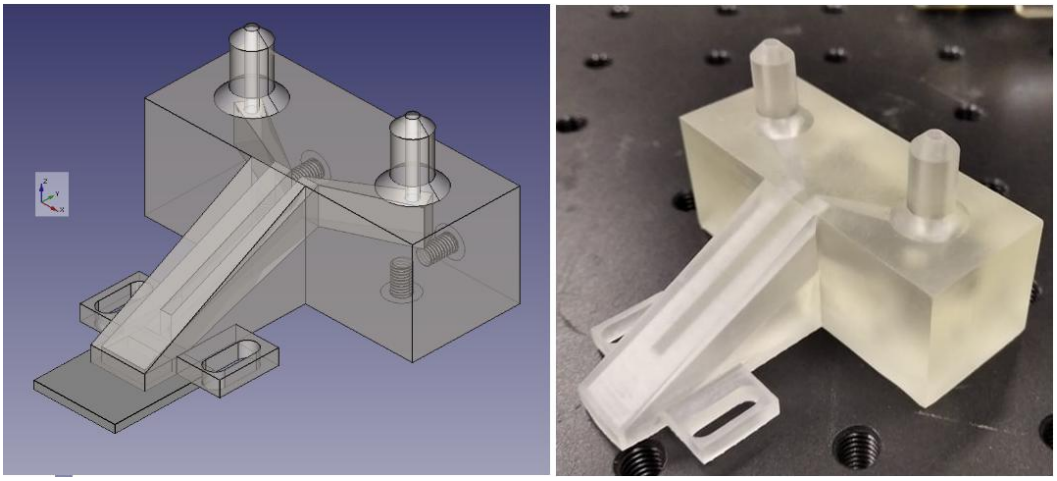

Figure A.10: Design model and 3D-printed piece for photonic chip atmosphere control

A.3.3 De-embedding

A.3.3.1 Definition

De-embedding is the action of removing the different contributions from related components along the optical path (grating couplers, splitters, broadband couplers, waveguides, etc) from a measured signal in order to isolate and extract the desired information content that is solely due to the component of interest. In the proposed setup, as illustrated in Chapter 3 [**?**], the photonic components are analyzed by removing the optical contributions of the connecting fiber and integrated waveguides as well as the coupling components and non-uniformities of the optical emission/reception. Since the transmission of integrated photonic structures is measured for refractometric purposes here, contributions of these optical components are analyzed spectrally.

A.3.3.2 Overall Method

Figure A.11 illustrates the main methods used for de-embedding measured signals to obtain uniquely the LPWG's optical response. Figure A.11(a) shows an initial signal that was measured using a SANTEC laser system and the optical coupling setup. To de-embed the signal related only to the LPWG, the measured signal of a test waveguide sample of length l (figure A.11(b)) that is equal to the connecting waveguide lengths of the device under test, was first subtracted. The light emission spectrum, coupling response, waveguide losses and analyzer spectral contributions were subsequently deducted altogether. The optical emission can actually present important intensity variations with the wavelength, as shown in figure A.12. Note, however, that the coupling contribution may slightly vary from device to device since the position of the fiber array highly influences the coupling spectral signature and efficiency. This incurred minor readjustments to be applied.

A.3.3.3 Advanced Filtering

The presence of small interferences has been observed, as shown in figure A.11(c), during the characterization of integrated optical components that have high losses (usually due to the important propagation length). Investigation has shown that the FSR of such interferences corresponds to the difference between the waveguide circuit length and the absolute distance between grating couplers. Subsequently, to remove this artefact without affecting other optical features, a bandstop filter whose central frequency corresponds to this particular FSR is applied on the signal. Finally, the de-dembedded signal is obtained, as shown in figure A.11(d), exhibiting resonance features from an LPWG's transmission spectrum (LPWG n°2) . To reduce the amplitude of such interferences, one could possibly increase the distance between the connected grating couplers, and/or use fiber arrays with wider pitch. This, however, also tends to complicate coupling which becomes more sensitive to angular errors.

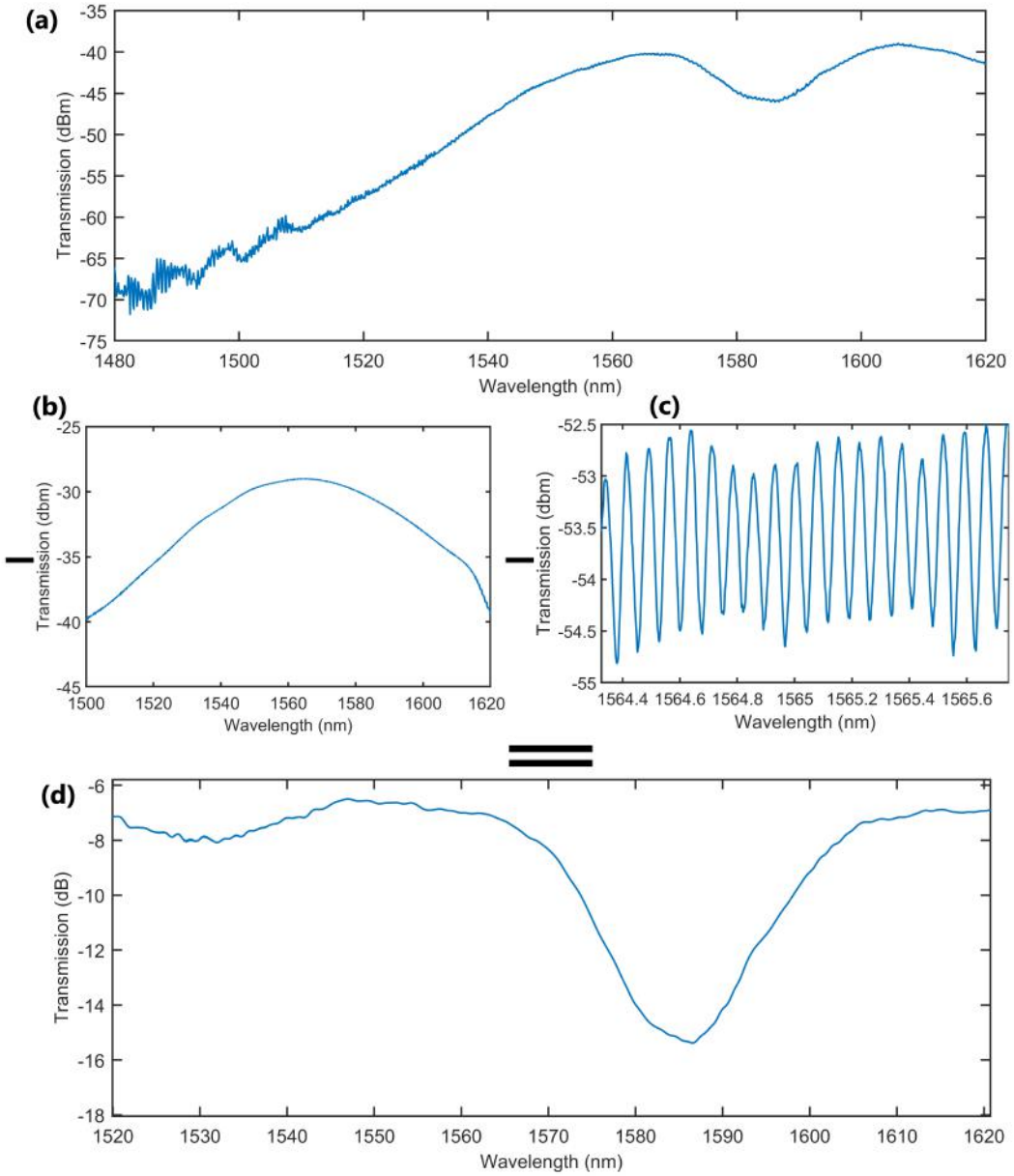

Figure A.11: Illustration of de-embedding method with (a) measured absolute transmission of a rib LPWG (PIC7) displaying resonance around 1580 nm, (b) measured absolute transmission of a test waveguide sample of specific length, (c) interference pattern that has been measured at low coupling, due to direct optical leakage from input fiber to output fiber as measured from a high-loss waveguide circuit and, (d) de-embedded LPWG spectral contribution

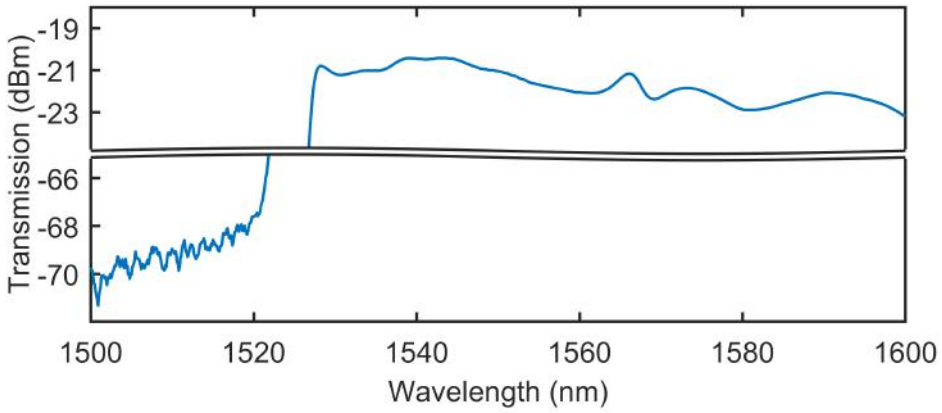

Figure A.12: Measured emission spectra of broadband IR source showing irregularities

A.4 Analysis of Waveguide Sensitivity for TE Mode in 1D-Model

The objective here is to analyze the influence of the refractive index of a cover region on the effective index of a guided mode in a 1-D three-layer slab waveguide. An analytical formula has been demonstrated in [126] for TM modes. Here, we aim to find a solution for the TE modes. Starting from the characteristic equation for the modal condition of a three-layer slab waveguide [279]:

$$\frac{2\pi t}{\lambda}\sqrt{n_f^2-N^2}-\arctan\left[\sqrt{\frac{N^2-n_s^2}{n_f^2-N^2}}\left(\frac{n_f}{n_s}\right)^{2p}\right]-\arctan\left[\sqrt{\frac{N^2-n_c^2}{n_f^2-N^2}}\left(\frac{n_f}{n_c}\right)^{2p}\right]-m\pi=0 \tag{A.1}$$

with m the mode order, $p=0$ for TE modes and $p=1$ for TM modes, and n_f, n_s and n_c the indices of the core layer, substate layer and cover layer, respectively.

By redefining the profile's refractive indices into dimensionless parameters as

$$\alpha_s=1-\left(\frac{n_s}{n_f}\right)^2;\qquad \alpha_c=1-\left(\frac{n_c}{n_f}\right)^2;\qquad X=1-\left(\frac{N}{n_f}\right)^2;\qquad T=\frac{2\pi n_f t}{\lambda} \tag{A.2}$$

equation (A.1) can be rewritten as

$$T=\frac{\arctan\left[\sqrt{\frac{\alpha_s-X}{X}}\left(\frac{1}{1-\alpha_s}\right)^p\right]+\arctan\left[\sqrt{\frac{\alpha_c-X}{X}}\left(\frac{1}{1-\alpha_c}\right)^p\right]+m\pi}{\sqrt{X}} \tag{A.3}$$

We aim to study the fundamental TE mode, with $m=0$ and $p=0$. We first

derive both sides of equation (A.3) with respect to n_c, giving:

$$\frac{\partial T}{\partial n_c} = 0 = \delta_c + \delta_s \tag{A.4}$$

with

$$\begin{aligned}
\delta_i &= \frac{\frac{\partial}{\partial n_c} arctan\left[\sqrt{\frac{\alpha_i - X}{X}}\right] \cdot \sqrt{X} - \frac{\partial \sqrt{X}}{\partial n_c} \arctan\left[\sqrt{\frac{\alpha_i - X}{X}}\right]}{X} \\
&= \frac{\sqrt{X}}{X} \cdot \frac{1}{2} \frac{\frac{\partial}{\partial n_c}\left[\frac{\alpha_i - X}{X}\right]}{\sqrt{\frac{\alpha_i - X}{X}}\left[1 + \frac{\alpha_i - X}{X}\right]} + \frac{\frac{\partial X}{\partial n_c}}{2X\sqrt{X}} \arctan\left[\sqrt{\frac{\alpha_i - X}{X}}\right] \\
&\text{using} \quad \frac{\partial}{\partial x}\left(\tan^{-1}(\sqrt{a(x)})\right) = \frac{a'(x)}{\sqrt{a(x)}(2a(x)+2)} \quad \text{and} \quad \frac{\partial}{\partial x}(\sqrt{a(x)}) = \frac{a'(x)}{2\sqrt{a(x)}}
\end{aligned} \tag{A.5}$$

The derivatives of the normalized parameters derivatives are then calculated as:

$$\frac{\partial \alpha_s}{\partial n_c} = 0 \qquad \frac{\partial \alpha_c}{\partial n_c} = -\frac{2 \cdot n_c}{n_f^2} \qquad \frac{\partial X}{\partial n_c} = -\frac{2 \cdot N}{n_f^2} \cdot \frac{\partial N}{\partial n_c} \tag{A.6}$$

which, when reintroduced into equation (A.4) with equation (A.5), gives:

$$\begin{aligned}
0 = \frac{\sqrt{X}}{X} \frac{\frac{-2n_c}{n_f^2} X + \frac{2 \cdot N}{n_f^2} \cdot \frac{\partial N}{\partial n_c} \cdot \alpha_c}{X^2 \sqrt{\frac{\alpha_c - X}{X}} \frac{\alpha_c}{X}} + \frac{\sqrt{X}}{X} \frac{\frac{2 \cdot N}{n_f^2} \cdot \frac{\partial N}{\partial n_c} \cdot \alpha_f}{X^2 \sqrt{\frac{\alpha_f - X}{X}} \frac{\alpha_f}{X}} \\
+ \frac{\frac{2 \cdot N}{n_f^2} \cdot \frac{\partial N}{\partial n_c}}{X\sqrt{X}} \left[\arctan\left[\sqrt{\frac{\alpha_c - X}{X}}\right] + \arctan\left[\sqrt{\frac{\alpha_s - X}{X}}\right]\right]
\end{aligned}$$

with $\frac{d}{dx}\left(\frac{a(x)-b(x)}{b(x)}\right) = \frac{b(x)a'(x) - a(x)b'(x)}{b(x)^2}$. We then obtain

$$\begin{aligned}
0 = \frac{\partial N}{\partial n_c} \left[\frac{N}{\sqrt{\alpha_s - X}} + \frac{N}{\sqrt{\alpha_c - X}} + \frac{N}{\sqrt{X}} \left[\arctan\left[\sqrt{\frac{\alpha_c - X}{X}}\right] + \arctan\left[\sqrt{\frac{\alpha_s - X}{X}}\right]\right]\right] \\
- \frac{n_c \cdot X}{\alpha_c \cdot \sqrt{\alpha_c - X}}
\end{aligned}$$

$$\begin{aligned}\frac{\partial N}{\partial n_c} &= \frac{n_c \cdot X}{\alpha_c \cdot \sqrt{\alpha_c - X}} \frac{1}{\left[\frac{N}{\sqrt{\alpha_s - X}} + \frac{N}{\sqrt{\alpha_c - X}} + N \cdot T\right]} \\ &= \frac{n_c}{N} \frac{\frac{1}{\sqrt{\alpha_c - X}}}{\frac{1}{\sqrt{\alpha_c - X}} + \frac{1}{\sqrt{\alpha_s - X}} + T} \cdot \frac{X}{\alpha_c} \\ &= \frac{n_c}{N} \cdot \frac{P_c}{P_{tot}}\end{aligned} \tag{A.7}$$

It can be seen that the sensitivity is proportional to the evanescent field ratio but also depends on the effective index and cover refractive index. This indicates that leaky modes could be an optimal solution for increasing the waveguide sensitivity.

Appendix B

Annex

Published articles :

Clement Deleau, Han Cheng Seat, Olivier Bernal, Frederic Surre. High-sensitivity integrated SiN rib-waveguide long period grating refractometer[J]. Photonics Research, 2022, 10(2): 02000564

C. Deleau, H. Seat, F. Surre, H. Tap, and O. Bernal, "Integrated Width-Modulated SiN Long Period Grating Designed for Refractometric Applications," J. Lightwave Technol. 39, 4820-4827 (2021).

C. Deleau, H. Seat, H. Tap, F. Surre and O. Bernal, "Integrated Silicon Nitride Horizontal Long Period Grating for Refractometric Gas Sensing applications," 2020 IEEE International Instrumentation and Measurement Technology Conference (I2MTC), 2020, pp. 1-6, doi: 10.1109/I2MTC43012.2020.9129170.

Note: the articles shall be removed before publication of the thesis online, as required by IEEE and OSA policies.

PHOTONICS Research

High-sensitivity integrated SiN rib-waveguide long period grating refractometer

Clement Deleau,[1,*] Han Cheng Seat,[1] Olivier Bernal,[1] and Frederic Surre[2]

[1]LAAS-CNRS, Université de Toulouse, CNRS, INP, Toulouse, France
[2]James Watt School of Engineering, University of Glasgow, Glasgow, UK
*Corresponding author: clement.deleau@laas.fr

Received 1 October 2021; revised 6 December 2021; accepted 15 December 2021; posted 16 December 2021 (Doc. ID 444825); published 27 January 2022

In this research, we demonstrate a high-sensitivity integrated silicon nitride long period grating (LPG) refractometer based on a rib waveguide with sinusoidally modulated width. While integrated LPG architectures typically achieve ultrahigh sensitivity only over a narrow optical bandwidth using a phase-matching turning-point optimization technique, our sensor exhibits a very high refractometric sensitivity that was designed to remain constant over a broad operational optical spectral bandwidth. The proposed design method relies on multi-modal dispersion tailoring that consists of homogenizing the spectral behaviors of both group and effective indices of the coupling modes. Experimental results are in agreement with numerical simulations, demonstrating not only a sensitivity reaching 11,500 nm/RIU but, more significantly, also that this sensitivity remains almost constant over a broad spectral range of at least 100 nm around 1550 nm. Additional advantages of the proposed sensor architecture encompass a low temperature sensitivity, down to −0.15 nm/K, and simplicity of the fabrication process. These results demonstrate the feasibility of chip-scale photonic integration to achieve both high sensitivity and large dynamic range of the proposed refractometer.

https://doi.org/10.1364/PRJ.444825

1. INTRODUCTION

Since their invention, refractometers have emerged as critical metrological tools extensively employed in industry for a broad range of applications, from chemical analysis [1] to temperature and strain sensing [2]. Refractometry-based sensors allow the estimation of the targeted physical or chemical parameter of interest via the optical measurement of its corresponding refractive index (RI). The inherent high versatility achievable among the wide variety of optical transducers contributes to driving research on refractometers toward increasingly higher sensitivities, resolution, and linearity. As the fundamental basis of many optical sensing solutions, refractometry has also been recently investigated for device implementation on the integrated photonic platform as a pathway to potentially achieve even higher performances while reducing the system's footprint [3]. Integrated silicon-based photonic sensors intrinsically benefit from major features such as electromagnetic immunity, compactness, and miniaturization, as well as their high flexibility of design [4]. These characteristics thus render the CMOS-compatible platform very attractive for high performance sensing schemes that require high resolution and precision while being cost effective. Integrated refractometers could be typically classified into five different categories: waveguide interferometers [5], resonators [6], photonic crystals [7], plasmonic devices [8], and diffraction gratings [9].

Long period gratings (LPGs) form a sub-family of the grating-based group. They consist of structures that operate on the exchange of energy between two or more co-propagative optical modes. This coupling is allowed by a periodic exchange of energy when the grating period and propagated wavelength satisfy a resonance condition. LPGs have been mainly investigated as fiber-based sensors because they allow optical energy to interact with the external environment by coupling a buried core mode to a leaking cladding mode [10] exposed to the external medium [11]. Any modification of the RI in the external environment results in a shift of a resonance wavelength. Their simplicity of fabrication using fiber tapering, irradiation, corrugation, inscription, or arc discharge has also rendered them attractive for mass fabrication. Moreover, LPGs have recently been subject to increasing interest for implementation in integrated photonics [12–16] due to their very high sensitivity potential, small footprints, and specific features that can be exploited on a design-flexible platform. In fact, when compared to typical interferometers or resonators, which exhibit periodic spectral patterns [17], LPGs offer the particular ability to create a localized spectral response while having similar performance potential. Obtaining such localized patterns is particularly advantageous, as it greatly facilitates the tracking of the LPG's spectral signature in highly sensitive refractometers.

In this work, we propose an integrated refractometric sensor operating on a long period waveguide grating (LPWG) implemented on a planar rib waveguide whose core width is sinusoidally modulated. Contrary to other optimization methods that generally improve the local sensitivity performance only around a narrow range of a few nanometers [14,18], we aim to show here that sensitivity can be uniformly enhanced over a broader spectrum by following certain design guidelines. This is performed on our structure by tailoring the effective indices of the coupled modes while simultaneously tuning the mode coupling strength. In Section 2, the LPWG sensing scheme is theoretically discussed and explained, and the design optimization method exploiting effective index (EI) tailoring is next described for sensitivity performance enhancement. In Section 3, the proposed architecture is detailed and modeled using modal analysis and eigenmode expansion (EME). The fabrication and characterization processes are then described in Section 4. Experimental results from optical refractometric measurements are subsequently presented and discussed in Section 5.

2. OPERATING PRINCIPLES

A. Long Period Grating Theory

LPGs are waveguide-based structures that employ periodic modulation to enable energy exchange between co-propagative optical modes. As each mode possesses a specific propagation constant and behavior, LPGs are designed to selectively couple modes at resonance wavelengths, as described by the phase-matching condition [19]

$$\Delta n_{\mathrm{eff},i,j}(\lambda_{\mathrm{res}}) \approx \frac{\lambda_{\mathrm{res}}}{\Omega}, \tag{1}$$

where $\Delta n_{\mathrm{eff},i,j} = n_{\mathrm{eff},i} - n_{\mathrm{eff},j}$, n_{eff_i} and n_{eff_j} are EIs of coupling modes i and j, respectively, Ω is the grating period, and λ_{res} is the resonance wavelength to achieve maximum coupling. For spectral features to appear around the resonance in the LPG's transmission spectrum, sufficient coupling strength and grating length are necessary to enable continuous coupling during the propagation of the injected mode. As described by the coupled mode theory [20] through numerous accepted LPG models, the continuous exchange of energy between modes around the resonance is periodic with respect to the LPG propagation length. Furthermore, when configured for specific sensor setups, this grating length has to be specifically set to enable complete mode coupling at resonance, so that energy is fully transferred between coupled modes. The coupling speed depends mainly on the coupling coefficients [20], which have previously been demonstrated to be mainly dependent on the optical field's modal superposition across the modulated area as well as on the modulation amplitude [15].

B. Long Period Grating as Refractometer

Perturbation of the optical system typically occurs through the interaction of the evanescent field of a mode with the target analyte, which results in modification of the propagation constants of the mode as a function of RI variation. As defined by Eq. (1), the central wavelength of the resonance λ_{res} largely depends on the EI difference of the coupling modes. Changes of LPG responses can subsequently occur by performing mode coupling to a perturbed optical mode. LPGs have mainly been implemented in fiber platforms for their capacity in unburying inner core fields and inducing interaction with an external medium to be sensed. Fiber LPG refractometers rely on the coupling between the fundamental core mode and a cladding mode; while the core mode's EI is relatively insensitive to external influence, selected cladding modes can, on the other hand, interact substantially with the external medium perturbation. The waveguide sensitivity of mode i, Γ_i, which represents sensitivity of the effective RI to the cladding index in evanescent optical waveguide sensors [21], can be expressed as

$$\Gamma_i(\lambda, n_{\mathrm{eff},i}) = \frac{\partial n_{\mathrm{eff},i}}{\partial n_{\mathrm{sens}}}(\lambda, n_{\mathrm{eff},i}), \tag{2}$$

where n_{sens} is the RI of the sensed region. Γ_i should not be confused with the sensed region's modal field overlap ratio, especially in high RI contrast waveguides [21]. Nevertheless, since Γ_i exhibits substantial correlation with the percentage of optical fields in the sensing region in most cases, it can thus be used as a tool to estimate the waveguide sensitivity.

Generally, LPG sensing systems rely on a wavelength interrogation technique. The sensitivity S_λ of the LPG is measured as spectral shifts of the resonance pattern per RI unit (RIU) of the sensed medium. Hence, the sensitivity equation can be calculated from Eq. (1) by applying a first-order Taylor series expansion [22], with respect to λ and n_{sens}, as detailed in Ref. [14], to result in

$$S(\lambda, i, j) = \lambda \frac{\Delta\Gamma_{i,j}(\lambda)}{\Delta n_{g,i,j}(\lambda)} \tag{3}$$

with $\Delta\Gamma_{i,j} = \Gamma_i(\lambda) - \Gamma_j(\lambda)$ and $\Delta n_{g,i,j} = n_{g,i} - n_{g,j}$, where $n_{g,i}$ denotes the modal group index (GI) of mode i, which can be expressed as $n_{g,i} = n_{\mathrm{eff},i} - \lambda \frac{\partial n_{\mathrm{eff},i}}{\partial \lambda}$ [23].

Two sensitivity improvement techniques have been previously employed in the design of integrated LPGs, namely, modal interaction optimization [12,15] and phase-matching turning-point (PMTP) optimization [14]. Modal interaction optimization relies on maximizing the sensing region's influence on the difference $\Delta\Gamma_{i,j}$ of the two coupling modes, while PMTP aims to minimize the GI difference $\Delta n_{g,i,j}$, thus significantly increasing spectral sensitivity, as illustrated by Eq. (3). In fact, by appropriately setting the grating period for coupling around the wavelength range of interest using Eq. (1), the sensitivity can be simplified into

$$S(\lambda, i, j) \approx \Delta\Gamma_{i,j}(\lambda) \cdot \Omega \cdot \gamma(\lambda), \tag{4}$$

where γ is known as the waveguide dispersion factor, defined as [22,24]

$$\gamma(\lambda) = \frac{\Delta n_{\mathrm{eff},i,j}(\lambda)}{\Delta n_{g,i,j}(\lambda)}. \tag{5}$$

Here, γ locally becomes infinite around the PMTP, whose associated wavelength can be obtained by solving $\Delta n_{g,i,j}(\lambda) = 0$, as illustrated in Fig. 1(a).

Optimization is typically performed by displacing the PMTP near the wavelength of interest using GI tuning to increase the γ contribution to overall spectral sensitivity. In practice, this is equivalent to engineering the chromatic dispersion of coupling modes to counteract or balance the difference

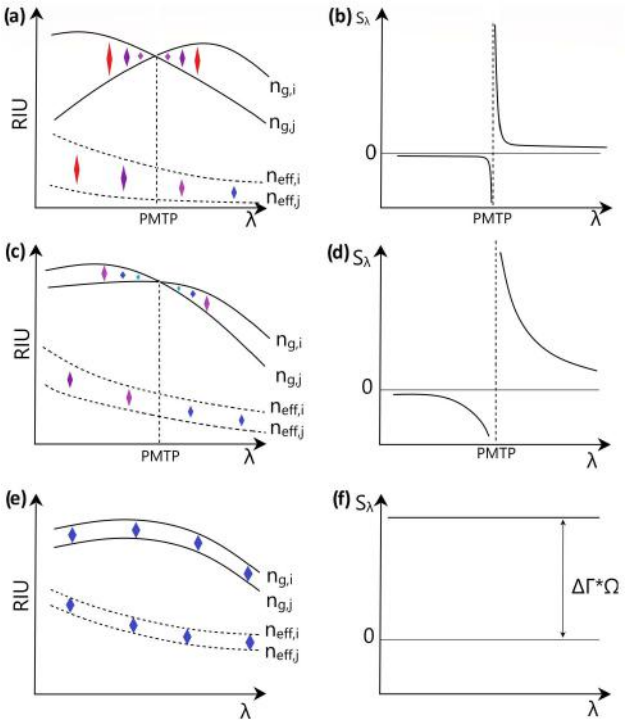

Fig. 1. Illustration of spectral sensitivity optimization behavior. (a), (c), (e) Different propagation constant spectral profiles and (b), (d), (f) subsequent expected sensitivity behavior versus wavelength.

between the EIs of coupling modes within the spectral window of interest. A notable problem with PMTP optimization is that the sensitivity enhancement significantly drops as the resonance shifts away from the PMTP, as illustrated in Fig. 1(b), thereby considerably reducing the RI sensing range. This is due to the high chromatic dispersion difference between modes that causes $\Delta n_{g,i,j}$ to greatly vary with λ, thus causing the sensitivity to collapse.

To circumvent this issue, we propose in this research another method based on the tailoring of the coupling modes so that the coupled modes' chromatic dispersion behaviors and EIs could be brought as close as possible. This should result in a sensitivity improvement similar to the PMTP method, with the additional characteristic of the resulting sensitivity response remaining almost constant over a much wider wavelength measurement range, as illustrated in Figs. 1(e) and 1(f). In this case, γ becomes nearly constant and close to one, and the sensitivity enhancement is mainly derived from the extended grating period Ω that is needed for coupling modes with close EIs, as shown in Eq. (1).

In addition to the sensitivity, the full-width at half-maximum (FWHM) can be utilized for comparing refractometric schemes, as it can provide insight on the resolution achievable in tracking both the induced resonance location and shift, thus accounting for the sensor performance. FWHM can be estimated as follows [25]:

$$\mathrm{FWHM}(\lambda_{\mathrm{res}}) \approx \frac{0.8\lambda_{\mathrm{res}}^2}{L_{\mathrm{opt}} \cdot \Delta n_{g,i,j}(\lambda_{\mathrm{res}})}, \tag{6}$$

where L_{opt} is the optimal LPG length for which full coupling is obtained at λ_{res}. Shaping of the spectral widths of the LPGs' resonance patterns can thus be performed by engineering the grating profile, coupling parameters, and grating length.

C. Proposed Structure

The proposed structure consists of a partially covered silicon nitride (SiN) hybrid rib–strip waveguide of RI $n_{\mathrm{SiN}} = 1.97$ whose core width is modulated to form an LPG as illustrated in Fig. 2. SiN on silicon oxide technology is chosen for its simplicity of fabrication and patterning, and for its relatively low index contrast in comparison with silicon on insulator (SOI), which facilitates modal tailoring. Also, rib waveguides possess significant advantages when employed for the design of LPWGs. As previously reported in Ref. [13], tailoring of the rib etch dimensions can enable the structure to support a fundamental mode confined within the waveguide core region together with higher-order modes spread out over the slab region. The optical fields of the propagating fundamental HE1 mode and the higher-order odd slab mode HE7 are simulated and plotted in Fig. 3. As the optical fields of both core and slab modes are partially overlapping in the modulated region, the field product integral at the modulated interface is non-null for odd modes. This is necessary to enable energy coupling between modes near λ_{res} during mode propagation, as previously illustrated in Ref. [15]. Moreover, since the optical profiles of the coupling modes are principally confined in the same material, two major features that can be exploited for sensing can be expected. First, as will be shown in Section 3.C, an intrinsic property of the rib structure is that it can support modes whose EIs and GIs can potentially be induced to be very close and to behave similarly over a broad wavelength range, thus favoring our optimization scheme. Second, since the LPG resonance relies on a differential mechanism as described by Eq. (1), both modes are expected to be almost equally affected by temperature or material dispersion due to their co-propagation in the same material: the structure is inherently less prone to temperature cross talk [13,26], and material dispersion can be neglected in the simulated models. In addition, the waveguide grating modulation is designed to be continuous along the core section width, which further reduces propagative losses due to optical leakage that would otherwise occur in typical binary-etched gratings, as shown in Ref. [14]. It further facilitates the theoretical analysis of mode coupling via coupling local mode theory [20], which is exact only in the case of

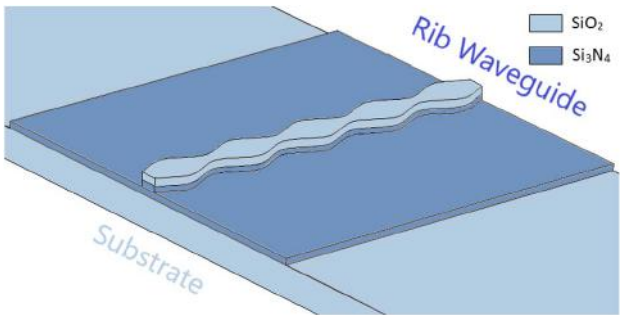

Fig. 2. Illustration of the implemented rib waveguide LPG structure with sinusoidally modulated width.

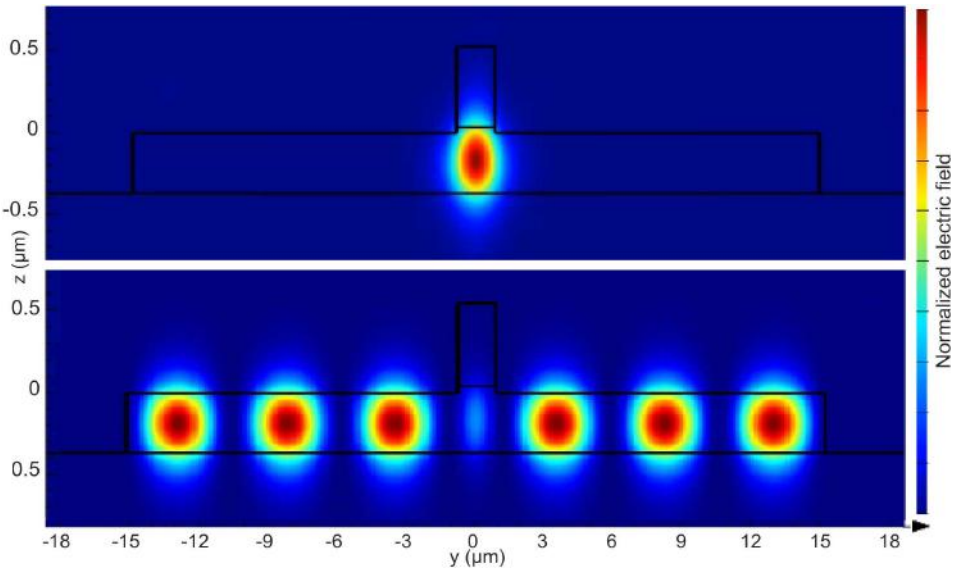

Fig. 3. Simulated mode profiles for a rib LPWG: HE1 (top) and HE7 (bottom).

"slowly varying waveguide approximations," thereby allowing to accurately model the LPWG for optimization purposes, as demonstrated in Ref. [15]. Nevertheless, converting our sinusoidally modulated LPWG to a binary one remains possible. The last particularity of our structure is that the core region is partially covered by silicon oxide (SiO_2), thus attenuating the sensitivity of the fundamental mode in the core to perturbations in the sensing region while the slab modes, on the contrary, substantially interact with this region. The SiO_2 layer is efficiently implemented during the fabrication process by using a specific resist without requiring any supplementary process step, as will be detailed in the next section.

3. DESIGN OPTIMIZATION AND LPWG ARCHITECTURE

A standard 400 nm SiN core thickness, h_{core}, has been chosen to facilitate optical injection into the photonic chip via grating couplers as well as for relatively unconstrained fundamental mode propagation. Further, as illustrated in Fig. 4, the remaining rib waveguide parameters, such as slab thickness, h_{slab}, which depends on the etch depth e, core width w_{core}, and slab width w_{slab}, have been optimized with respect to the following guidelines.

1. The EIs of the core and slab modes must be in very close proximity to induce high sensitivity and significantly extend the measurement range.
2. The modal interaction with the external region must be as strong as possible for the slab modes and almost null for the core mode.
3. The overlapping of the modal fields at the modulated interface must be tuned for coupling rate optimization [15,20].
4. The difference in chromatic dispersion between the two coupling modes is small in the spectral region of interrogation.

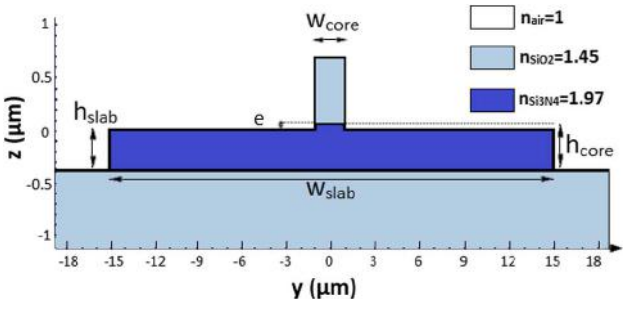

Fig. 4. LPG cross-sectional profile.

The following subsections describe the LPWG structural parameters that are chosen. In this research, we employ Lumerical's mode solver to simulate the rib LPWG [27] for which the mesh resolution has been set at 1 nm in the core region and surrounding interfaces. Note that both metal and perfectly matched layer boundary conditions lead to identical results, as they are positioned sufficiently far from the waveguide.

A. SiO_2 Strip

As previously described, $\Delta\Gamma_{i,j}$ can be increased by controlling the optical field overlap of the respective coupling modes to the sensing region. This is performed by minimizing the optical leakage of the fundamental mode into the sensing region while enabling slab modes to expand in the external environment. To minimize the core mode sensitivity to the sensing region $\Gamma_{HE1}(\lambda)$, a strip of SiO_2 is deposited on top of the core region. Here, Γ_{HE1}, as evaluated by simulation, has been lowered to $\approx$0.02. Additionally, as described in more detail in Section 4, during the fabrication process, the SiO_2 strip can also be advantageously used as the mask for patterning the modulated waveguide, thereby reducing further the required number of process steps. A minimum strip thickness of 0.5 μm is determined to be sufficient to prevent additional leakage.

B. Slab Thickness

We observe that the etch depth, e, appears to be the most influential parameter on the LPWG behavior. As the slab region becomes thinner, the slab mode's evanescent field expands into the cladding and substrate regions. It first enhances the sensed region's influence on the propagation constants of the slab modes by increasing $\Gamma_{\text{slabmodes}}$ because a higher proportion of the modal field now interacts with the sensed region. However, if e is too small, the fundamental mode will no longer be confined in the core region and will, instead, start leaking horizontally into the slab region, thereby increasing Γ_{coremode}. Second, e is the main contributor to the EI difference between the slab–core modes, where stronger vertical confinement will cause the EIs of the slab modes to further decrease. Since they are already inherently lower than that of the core mode, it would result in a lower LPG spectral sensitivity. Last, e also significantly influences the LPG's coupling strength since the latter depends on the modulated area (which, in turn, is proportional to e) [15,20]. Figure 5 shows the influence of e on both $\Delta n_{\text{eff},\text{HE}_7,\text{HE}_1}$ and $\Delta\Gamma_{\text{HE}_7,\text{HE}_1}$. As a trade-off among Γ coefficients, EIs, and coupling coefficient optimization, the slab thickness h_{slab} is chosen to be 365 nm.

C. Slab Width

Mode calculations suggest that the EIs of slab modes tend to increase and approach the EI of the fundamental mode with increasing slab width (w_{slab}). However, since large w_{slab} will also spread the slab's mode field, the electric field superposition at the modulated interface will tend to decrease, thereby reducing the amplitude of the coupling coefficient and, consequently, increasing the required sensor length. A 30 μm wide slab is found to be a good compromise to enable full optical coupling to the first slab modes over a millimeter-scale propagation length. Figure 6 illustrates the simulated propagation constant EIs and GIs of modes HE1 and HE7, respectively, in the NIR spectral band (from ≈1.3 to 1.8 μm). It can be observed that the coupling modes' EIs behave very similarly so that $\Delta n_{g,i,j}$ and $\Delta n_{\text{eff},i,j}$ are relatively small and constant over a large wavelength band, similar to Figs. 1(e) and 1(f). These suggest that both very high sensitivities up to $S_\lambda = 10{,}000$ nm/RIU [as demonstrated by Eq. (3)] at a relatively constant level over the entire C-band could simultaneously be attained.

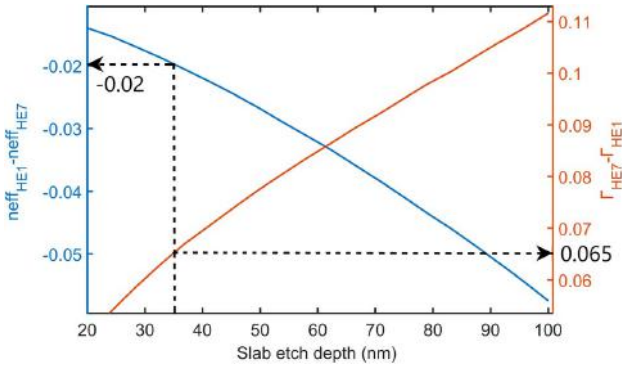

Fig. 5. Coupling modes' EI difference and waveguide sensitivity Γ difference versus slab etch depth with $w_{\text{slab}} = 30$ μm and $w_{\text{core}} = 1.65$ μm at 1550 nm. Etch depth is set at $e = 35$ nm and $h_{\text{slab}} = 365$ nm. Dashed lines: chosen etch depth and corresponding Δn_{eff} and $\Delta\Gamma$.

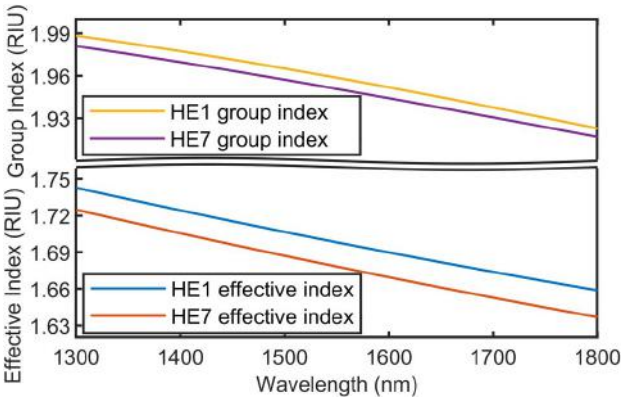

Fig. 6. Simulated effective and group indices of modes HE1 and HE7 showing similar dispersion with $e = 35$ nm, $w_{\text{core}} = 1.65$ μm, and $w_{\text{slab}} = 30$ μm.

D. Core Width

The core width is found to have little effect on the EIs of both core and slab modes when tuned between 1 and 3 μm. Nevertheless, two criteria have to be taken into account for the proper design of the LPWG. First, single mode propagation within the core region has to be ensured to minimize Γ_{coremode} and maximize $\Gamma_{\text{slabmodes}}$. Second, the core width also determines the geometrical location of the modulated interfaces on the slab surface. This parameter has to be optimized to obtain a specific modal field superposition for a particular coupling strength to be achieved. Furthermore, as demonstrated by Eqs. (3) and (6), the FWHM of the resonance can be determined with L_{opt} and the propagation constants. Hence, to facilitate experimental measurements, an FWHM lower than or equal to 25 nm has been estimated as the maximum measurable FWHM permissible to accurately observe the coupling spectra for different external indices, as our apparatus' measurement spectral window is only approximately 100 nm wide. Figure 7 illustrates the influence of the core width on the main coupling strength parameter, $\int_e E_{\text{HE1}} \cdot E_{\text{HE7}}\, dz$, which can further be used to estimate the expected coupling length for a given modulation amplitude of 0.15 μm, for example, as previously demonstrated in Ref. [15]. The average width of the core, w_{core}, is set to 1.65 μm to achieve a 25 nm wide spectral dip with full mode coupling, corresponding to a grating length of 7.5 mm.

E. LPWG Period and Length

As described by Eq. (1), when the EIs of the coupling modes are closer, the LPWG period greatly increases. To couple the HE1 and HE7 modes around 1550 nm, whose EIs are found to be, respectively, 1.693 and 1.673, the period has to be set to ≈77.5 μm. Here, EME is employed as an efficient technique to model mode propagative periodic structures [28], as previously demonstrated in Ref. [15]. In this work, one single period of the LPWG architecture is first sliced into 20 partitions along the propagation axis. The modes and field overlaps are then calculated for each local cross section. Subsequently, after a numerical reconstruction of the LPWG profile along the

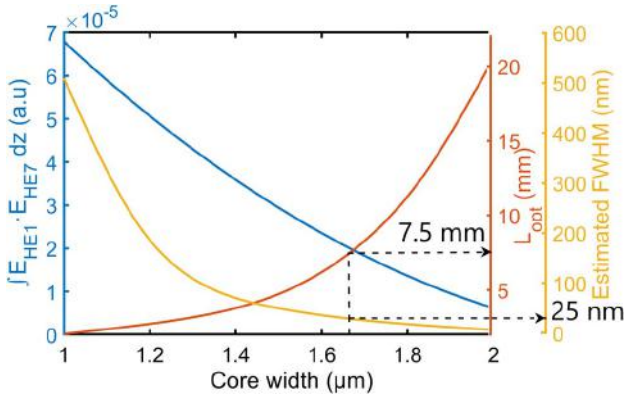

Fig. 7. Coupling parameter and estimated full coupling length versus core width with $e = 35$ nm and $w_{slab} = 30$ μm at 1550 nm. w_{core} is set at 1.65 μm. Dashed lines: chosen core width and corresponding coupling length L_{opt} and FWHM.

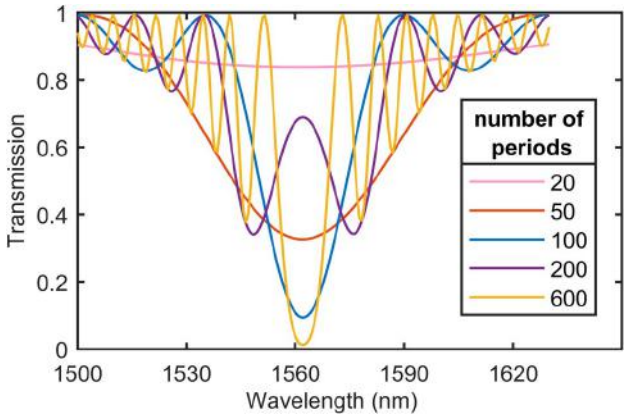

Fig. 8. Resonance spectra simulated with EME for different LPWG lengths with a period of 77.5 μm, $e = 35$ nm, $w_{slab} = 30$ μm, and $w_{core} = 1.65$ μm.

propagation axis, the continuous optical coupling in the LPWG over the propagation length is calculated with successive optical energy distribution by superposition of the scattering matrices. Figure 8 plots the simulated output spectra for different grating lengths, illustrating a simulated coupling length very similar to the calculated length. The model demonstrates a 25 nm FWHM that can be obtained over 100 periods, which is similar to the designed grating length of 7.5 mm.

4. FABRICATION

A. Layout

To facilitate optical injection into the photonic chip, standard grating couplers are used, as they enable easy characterization of the optical structures [4]. Fundamental mode coupling in the rib waveguide is then performed using 50 μm long strip–rib tapers at both ends of the LPWG [29]. Since fabrication defaults due to both variations of material RIs and geometrical dimensions of the patterned waveguides, and also high sensitivity ($S_\lambda > 10{,}000$ nm/RIU), are expected, several LPWGs of slightly different periods are fabricated to optimize the chances to obtain the coupling resonance within our measurement spectral range. Figure 9 illustrates the layout of the fabricated photonic chip, including LPWGs and grating couplers that have been designed.

B. Process

As illustrated in Fig. 10, a SiO_2 layer of approximately 2 μm thickness is first deposited on a pre-cleaned Si wafer by plasma-enhanced chemical vapor deposition (PECVD). A 400 nm thick SiN core layer is next deposited on top of the SiO_2 film, also by PECVD. The index of this core is measured by ellipsometry to be $n_{core} \sim 1.97$. The SiO_2 top strip is then fabricated using electron-sensitive hydrogen silsesquioxane resist (HSQ), whose constitution is found to be very similar to SiO_2 after curing, with an RI of 1.37 [30]. Moreover, the resist is also used as the etching protective layer for patterning the core waveguide and grating couplers. Subsequently, electron-sensitive MaN2405 resin is deposited by spin coating, followed by an Electra92 resin layer used for electronic charge dissipation during electron-beam lithography with a RAITH150 E-beam writer. This lithography step is used to pattern the slab region of the waveguide. The main E-beam exposure parameters, namely, acceleration voltage, beam current, step size, and dose, are respectively 20 kV, 37 pA, 10 nm, and 112 μC/cm^2 for MaN2405 resist, and 30 kV, 325 pA, 10 nm, and 375 μC/cm^2 for HSQ. After the resist development, the SiN layer (thickness ~400 nm) is etched using reactive ion etching (RIE) to obtain grating couplers and slab waveguides that are fully delineated. The remaining MaN2405 resist is removed using pirhana solution followed by plasma O_2 cleaning without affecting the SiO_2 strip generated from HSQ or the unetched SiN layer. Finally, a 35 nm etch is performed on the slab region of the rib waveguide using the SiO_2 strip as the layer mask. This particular process has two advantages: (i) the core and grating mask layer are also used as the protective strip of the core region to enhance sensitivity, and (ii) the fully etched grating couplers and partially etched rib-waveguide core region are patterned with the same mask, thereby reducing

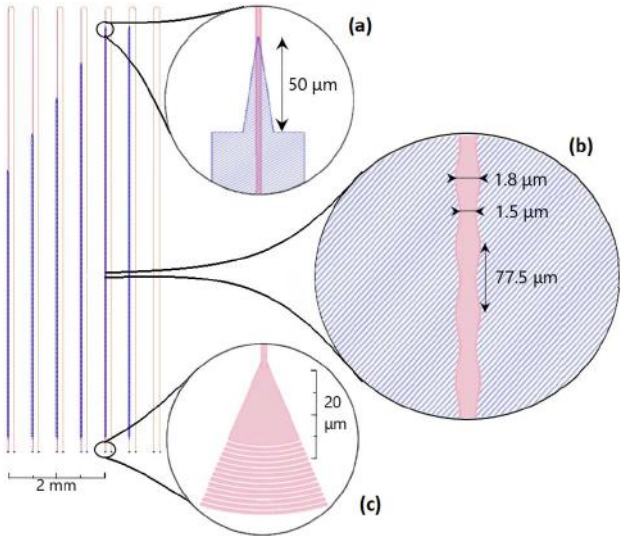

Fig. 9. Layout of the designed photonic chip showing (a) strip–rib converter, (b) LPWG, and (c) grating coupler.

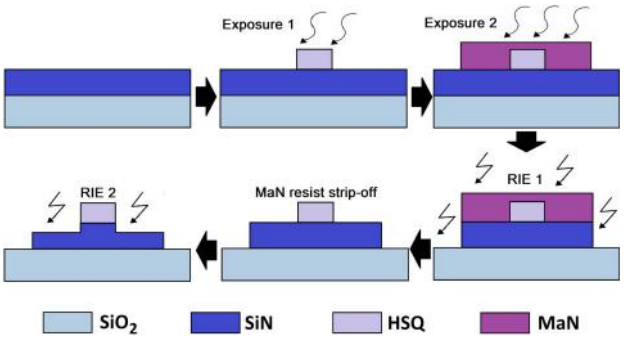

Fig. 10. Illustration of LPWG fabrication process.

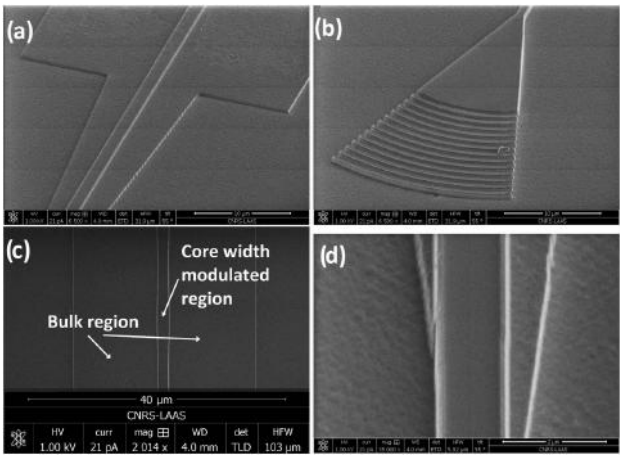

Fig. 11. SEM pictures of photonic circuit components: (a) strip–rib converter; (b) grating coupler, (c) LPWG section, and (d) minor misalignment between strip and rib waveguides shown here at the beginning of the tapering region for the sake of clarity.

possible mismatch during the strip–rib fundamental mode conversion.

C. Structure Characterization

The rib LPWGs are first physically characterized using a scanning electron microscope (SEM) as seen in Fig. 11(d). A transverse shift of 600 nm is observed on the second patterned layer. This 600 nm off-alignment is reintroduced into the simulation model and found to cause a minor resonance shift of ~20 nm with ~3% sensitivity variation.

5. EXPERIMENTAL RESULTS

A. Experimental Setup

The experimental setup for optical characterization consists of a Santec TSL550 tunable laser source, a fiber array mounted on a motorized linear stage driven by a dedicated LabVIEW program, and an optical powermeter, as illustrated in Fig. 12. The injection and recovery of the interrogating light into the photonic circuit is obtained by positioning the fiber array on top of a chip-integrated grating coupler pair. The injected laser wavelength is next scanned over the spectral region of interrogation from which the transmission spectrum is then measured. The transmission spectra of the LPWGs are obtained after de-embedding the transmitted signal to isolate both the LPWG's and tapers' spectral contributions from those of the grating couplers, tunable laser output, and lead-in/lead-out waveguides. It is first observed during optical characterization of the LPWGs that the background loss of ~7 dB, which includes contribution from each taper, is slightly lower for rib waveguides relative to a control sample based on strip waveguides. This can be attributed to the overall reduction of the sidewall surface area in the rib waveguides, which alleviates the roughness-induced refraction losses during optical propagation.

B. Sensitivity

Commercially available liquids of calibrated RIs from Cargill are employed and mixed into different proportions to simulate

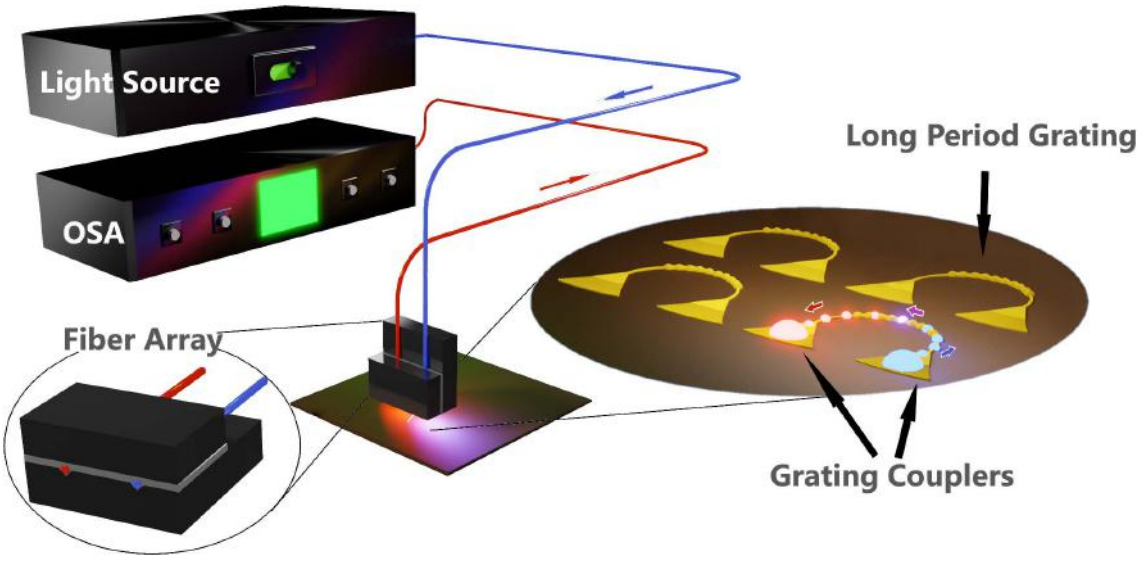

Fig. 12. Illustration of the experimental photonic characterization setup.

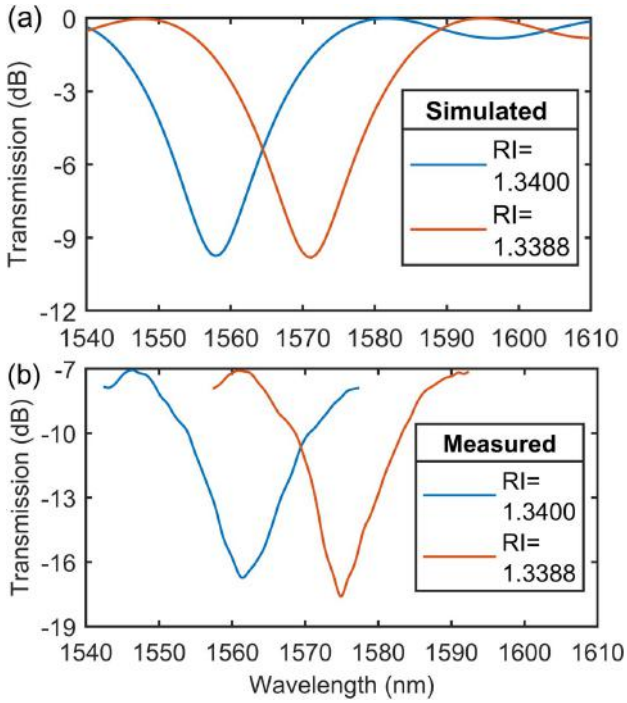

Fig. 13. (a) Simulated and (b) experimentally measured normalized resonance spectra at surface RIs of 1.3388 and 1.34.

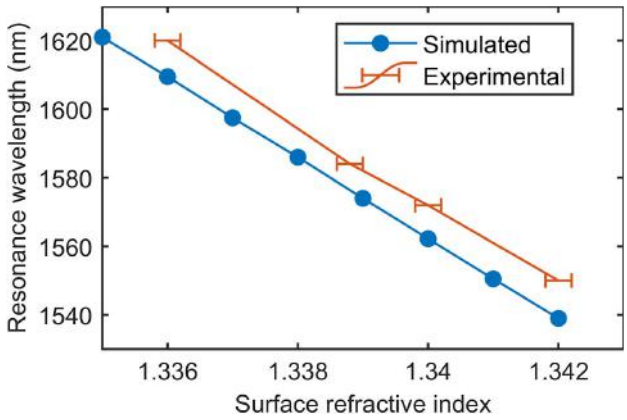

Fig. 14. Simulated and measured resonance wavelength of LPWGs obtained for different surface RIs.

indices varying between 1.33 and 1.35 RIUs. These RIs are first measured using a commercial Hanna HI 96801 refractometer with a resolution of 0.2 mRIU. The optical liquids are then deposited on top of the chip to induce RI variations in the LPWG resonance, which is subsequently tracked over a spectral window of 100 nm. Resonance features observed during the optical characterization of an LPWG with a 77.5 μm period, as shown in Fig. 13, exhibit a 3 dB bandwith of 25 nm and an extinction ratio of 10–12 dB, which are very similar to the simulated values. Figure 14 plots the simulated and experimental resonance wavelength of the LPWG against the analyte's RI, from which the sensitivity calculated as the slope can be extracted. Here, the experimentally measured sensitivity is estimated to be $S_\lambda \approx 11{,}500$ nm/RIU and highly stable over 100 nm (limited by the SANTEC TSL550 measurement range), in good agreement with the simulated value.

Table 1 summarizes the sensitivities and specific properties of our proposed structure in comparison with previously reported fabricated LPWGs. Other LPWG designs based on waveguide sensitivity enhancement [12,16] or the PMTP optimization technique [14] exhibit either limited sensitivity enhancement or measurement range, respectively. On the other hand, our proposed sensor demonstrates ultrahigh sensitivity that, more significantly, is found to remain constant over a broad measurement range.

C. Temperature Dependence

To study the influence of temperature on our structure, the thermo-optic coefficients of SiN and SiO_2 are first determined to be 2.45×10^{-4} RIU/K and 9.5×10^{-5} RIU/K, respectively [31]. These are then introduced into our simulation model from which a very low temperature sensitivity of 150 pm/K is obtained. This low value is to be expected since the coupled modes travel in the same materials and are thus subject to the same influence. To experimentally study the temperature sensitivity of our sensor, the temperature of the laser mount is tuned using a Thorlabs thermo-electric cooler (TEC) with a 0.02°C precision. Nevertheless, it is impossible here to directly measure the temperature sensitivity of the sensor in free space (i.e., without an external "cladding" medium), as the mode resonance would then not fall within the limits of the target spectral range around 1550 nm. To correctly measure this sensitivity without exceeding the spectral limits, a calibrated RI liquid with a pre-characterized temperature dependence is applied on the LPWG surface. The resonance wavelength shift due to the liquid's RI variation induced by the temperature

Table 1. Comparison with Other Fabricated LPWGs

References	Material	Structure Type	LPG Length (μm)	Measured Sensitivity (nm/RIU)	FWHM (nm)	Period (μm)
[16]	Silicon nitride	Polymer waveguide coupling	1000	240–900	5	10
[13]	BK-7 glass	Rib waveguide	1915	240	3	180
[12]	Silicon nitride	Strip–slot waveguide coupling	2000	1970	7	15.1
[14]	Silicon	Asymmetric strip waveguide	1500	5078	20–30	7.8
Our work	**Silicon nitride**	**Rib waveguide**	**7750**	**11,500**	**25**	**77.5**

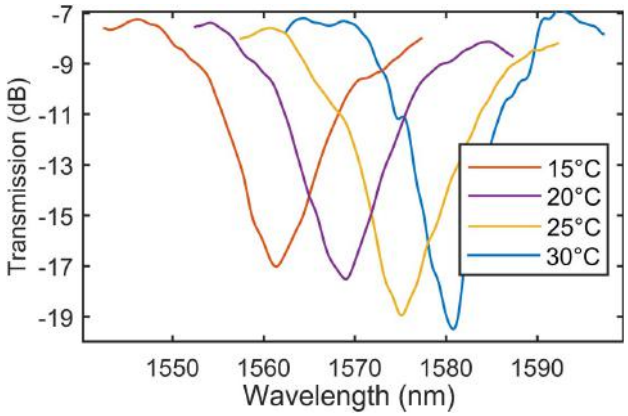

Fig. 15. Experimental wavelength resonance pattern shifts with temperature of the LPWG.

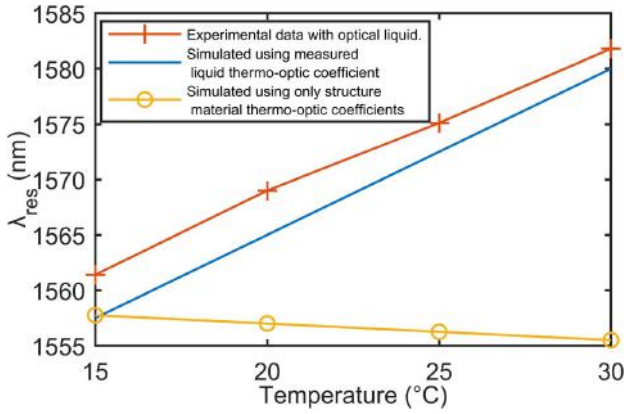

Fig. 16. Simulated and measured resonance wavelength variations versus temperature of the LPWG.

variation is finally subtracted from the combined total resonance shift (from both the RI liquid and LPWG sensor) to obtain the intrinsic temperature dependence of the LPWG structure (Figs. 15 and 16). The measured temperature sensitivity is found to corroborate the simulated value, which predicts a low intrinsic LPWG temperature dependence of ~150 pm/K.

6. CONCLUSION

Integrated refractometers are under intense investigation as the current state of the art in nano-fabrication lends unprecedented flexibility in the design of wavelength-scale complex photonic structures. In this paper, we proposed a novelty integration of a structure typically implemented on fiber platforms, i.e., the LPG. Indeed, alongside interferometers, LPWGs are photonic structures that benefit most from current advances in waveguide manufacturing technology [32], as their performance ultimately scales to the propagation length. However, unlike high-sensitivity interferometers for which the analysis of their spectral shift is complicated by the output spectral periodicity, LPWGs, on the other hand, which present localized spectral patterns, are promising candidates for constructing ultrahigh performance refractometers. The proposed structure, consisting of a rib-waveguide LPG, has been designed, fabricated, and characterized. A very high sensitivity of $S_\lambda \approx 11{,}500$ nm/RIU together with a figure of merit (FOM $= S_\lambda$/FWHM) of approximately 400 has been measured over a wide spectral window of 100 nm, in agreement with theoretically calculated and simulated values. This design has been found to demonstrate the efficiency of EI tuning and could, additionally, be further combined with other methods to potentially increase the sensitivity to values hitherto unmatched on the integrated platform. In this work, we also demonstrated the significant design capabilities of rib LPWGs, which exhibited critical features such as minimal temperature cross talk and simplicity of fabrication. Finally, an ongoing study further suggests that certain types of similar waveguides can possess inherent dispersive behaviors that allow their sensitivity to be multiplied by one to two orders without any reduction in sensitivity stability over the entire measurement range. Results from our new study shall be published in a future paper.

Funding. Institut National Polytechnique de Toulouse (Toulouse Tech Interlabs 2019).

Acknowledgment. All fabrication and characterization of the integrated photonic long period waveguide gratings were supported by both TTIL 2019 (Toulouse Tech Interlabs) and RENATECH (French Network of Technology Platforms) within LAAS-CNRS cleanroom infrastructure. The authors thank A. Lecestre, F. Carcenac, J.-B. Doucet, and L. Mazenq for their technical assistance with the fabrication and characterization process of the photonic integrated circuits.

Disclosures. Other than a patent filing application that is in progress on certain elements of this work, the authors declare no conflicts of interest.

Data Availability. Data underlying the results presented in this paper are not publicly available at this time but may be obtained from the author upon reasonable request.

REFERENCES

1. A. Urrutia, I. Del Villar, P. Zubiate, and C. Zamarreño, "A comprehensive review of optical fiber refractometers: toward a standard comparative criterion," Laser Photon. Rev. **13**, 1900094 (2019).
2. M. Ramakrishnan, G. Rajan, Y. Semenova, and G. Farrell, "Overview of fiber optic sensor technologies for strain/temperature sensing applications in composite materials," Sensors **16**, 99 (2016).
3. E. Luan, H. Shoman, D. M. Ratner, K. C. Cheung, and L. Chrostowski, "Silicon photonic biosensors using label-free detection," Sensors **18**, 3519 (2018).
4. L. Chrostowski and M. Hochberg, *Silicon Photonics Design: From Devices to Systems* (Cambridge University, 2015).
5. X. Guan and L. H. Frandsen, "All-silicon interferometer with multimode waveguides for temperature-insensitive filters and compact biosensors," Opt. Express **27**, 753–760 (2019).
6. S. Chandran, R. K. Gupta, and B. K. Das, "Dispersion enhanced critically coupled ring resonator for wide range refractive index sensing," IEEE J. Sel. Top. Quantum Electron. **23**, 424–432 (2017).

7. P. Xu, J. Zheng, J. Zhou, Y. Chen, C. Zou, and A. Majumdar, "Multi-slot photonic crystal cavities for high-sensitivity refractive index sensing," Opt. Express **27**, 3609–3616 (2019).
8. E. Chatzianagnostou, A. Manolis, G. Dabos, D. Ketzaki, A. Miliou, N. Pleros, L. Markey, J.-C. Weeber, A. Dereux, B. Chmielak, A.-L. Giesecke, C. Porschatis, P. J. Cegielski, and D. Tsiokos, "Scaling the sensitivity of integrated plasmo-photonic interferometric sensors," ACS Photon. **6**, 1664–1673 (2019).
9. X. Wang, J. Flueckiger, S. Schmidt, S. Grist, S. T. Fard, J. Kirk, M. Doerfler, K. C. Cheung, D. M. Ratner, and L. Chrostowski, "A silicon photonic biosensor using phase-shifted Bragg gratings in slot waveguide," J. Biophoton. **6**, 305–828 (2013).
10. E. Simões, I. Abe, J. Oliveira, O. Frazão, P. Caldas, and J. Pinto, "Characterization of optical fiber long period grating refractometer with nanocoating," Sens. Actuators B **153**, 335–339 (2011).
11. H. Hu, C. Du, Q. Wang, X. Wang, and Y. Zhao, "High sensitivity internal refractive index sensor based on a photonic crystal fiber long period grating," Instrum. Sci. Technol. **45**, 181–189 (2016).
12. Q. Liu, Z. Gu, M. K. Park, and J. Chung, "Experimental demonstration of highly sensitive optical sensor based on grating-assisted light coupling between strip and slot waveguides," Opt. Express **24**, 12549–12556 (2016).
13. U. Tripathi and V. Rastogi, "Temperature insensitive long period waveguide gratings in rib waveguide," Optik **186**, 15–21 (2019).
14. J. Høvik, M. Yadav, J. W. Noh, and A. Aksnes, "Waveguide asymmetric long-period grating couplers as refractive index sensors," Opt. Express **28**, 23936–23949 (2020).
15. C. Deleau, H. Seat, H. Tap, F. Surre, and O. Bernal, "Integrated silicon nitride horizontal long period grating for refractometric gas sensing applications," in *IEEE International Instrumentation and Measurement Technology Conference (I2MTC)* (2020), pp. 1–6.
16. C. Deleau, H. C. Seat, H. Tap, F. Surre, and O. D. Bernal, "Integrated width-modulated sin long period grating designed for refractometric applications," J. Lightwave Technol. **39**, 4820–4827 (2021).
17. M. Kitsara, K. Misiakos, I. Raptis, and E. Makarona, "Integrated optical frequency-resolved Mach-Zehnder interferometers for label-free affinity sensing," Opt. Express **18**, 8193–8206 (2010).
18. R. Wong, D. Hu, M. Ibsen, and P. Shum, "Optical fibre long-period grating sensors operating at and around the phase matching turning point," in *Applications of Optical Fibers for Sensing* (IntechOpen, 2019), https://www.intechopen.com/chapters/63687.
19. H. Taylor and A. Yariv, "Guided wave optics," Proc. IEEE **62**, 1044–1060 (1974).
20. A. W. Snyder and J. Love, *Optical Waveguide Theory* (Springer, 2012).
21. G. Veldhuis, O. Parriaux, H. Hoekstra, and P. Lambeck, "Sensitivity enhancement in evanescent optical waveguide sensors," J. Lightwave Technol. **18**, 677–682 (2000).
22. T. MacDougall, S. Pilevar, C. Haggans, and M. Jackson, "Generalized expression for the growth of long period gratings," IEEE Photon. Technol. Lett. **10**, 1449–1451 (1998).
23. E. A. J. Marcatili, "Modal dispersion in optical fibers with arbitrary numerical aperture and profile dispersion," Bell Syst. Tech. J. **56**, 49–63 (1977).
24. X. Shu, L. Zhang, and I. Bennion, "Sensitivity characteristics of long-period fiber gratings," J. Lightwave Technol. **20**, 255–266 (2002).
25. L. Rindorf and O. Bang, "Sensitivity of photonic crystal fiber grating sensors: biosensing, refractive index, strain, and temperature sensing," J. Opt. Soc. Am. B **25**, 310–324 (2007).
26. Q. Liu, K. S. Chiang, and K. P. Lor, "Condition for the realization of a temperature-insensitive long-period waveguide grating," Opt. Lett. **31**, 2716–2718 (2006).
27. http://www.lumerical.com.
28. D. Gallagher and T. Felici, "Eigenmode expansion methods for simulation of optical propagation in photonics - pros and cons," Proc. SPIE **4987**, 69–82 (2003).
29. T. Aalto, K. Solehmainen, M. Harjanne, M. Kapulainen, and P. Heimala, "Low-loss converters between optical silicon waveguides of different sizes and types," IEEE Photon. Technol. Lett. **18**, 709–711 (2006).
30. C. W. Holzwarth, T. Barwicz, and H. I. Smith, "Optimization of hydrogen silsesquioxane for photonic applications," J. Vac. Sci. Technol. B **25**, 2658–2661 (2007).
31. A. Arbabi and L. Goddard, "Measurements of the refractive indices and thermo-optic coefficients of Si_3N_4 and SiO_x using microring resonances," Opt. Lett. **38**, 3878–3881 (2013).
32. M. H. P. Pfeiffer, J. Liu, A. S. Raja, T. Morais, B. Ghadiani, and T. J. Kippenberg, "Ultra-smooth silicon nitride waveguides based on the damascene reflow process: fabrication and loss origins," Optica **5**, 884–892 (2018).

Integrated Width-Modulated SiN Long Period Grating Designed for Refractometric Applications

Clément Deleau, *Member, IEEE,* Han Cheng Seat, *Senior Member, IEEE,* Frederic Surre, *Senior Member, IEEE,* Hélène Tap and Olivier D. Bernal, *Member, IEEE*

***Abstract*—A novel integrated photonic structure based on Long Period Waveguide Gratings (LPWGs) relying on channel-width modulation is proposed and tested for refractometric applications. These LPWGs have been fabricated through a Silicon Nitride process and experimentally characterized in terms of both surface and bulk sensitivities. Surface sensing configuration is first achieved by propagating one of the coupling optical modes into an epoxy-based negative photoresist SU8 cladding region that is in contact with the analyte via its outer surface. We subsequently show that the proposed LPWGs cladding layer can be advantageously replaced by a gas-porous polymeric bulk layer such as Styrene-co-AcryloNitrile (SAN) as the cladding region to be directly sensed to anticipate future gas sensing applications. Here, bulk sensing is optimized by increasing the analyte's influence on the modal propagation constants as it is demonstrated to be currently the most promising solution to effectively enhance the figure of merit of long period gratings of given lengths. Using varying water-glycerol mixtures, the surface sensitivity of these LPWGs has been measured at up to 240 nm per RI unit (RIU) that is in agreement with simulation. In addition, the bulk sensitivity has been indirectly estimated to be ∼1900 nm/RIU via temperature measurements, which corroborates simulation results, thereby paving the way towards gas sensing applications.**

***Index Terms*—Integrated photonics, long period grating, refractometry, coupled-local-mode theory, silicon photonics.**

I. Introduction

In recent years, integrated photonics has been intensely investigated for the development of highly sensitive lab-on-chip sensor applications. Due to their high degree of flexibility, they enable a multitude of functional designs to be implemented in a miniaturized circuit. The immunity of integrated photonic devices to electromagnetic and radiofrequency interferences coupled to their potential high resolution also render them very attractive [1] for *in situ* measurements and monitoring in harsh environments. Numerous embedded functions, once implemented, can thus be simultaneously driven or interrogated by a unique optical source on a thermally and mechanically robust platform. These characteristics have led to growing interest from the industry to develop and commercialize integrated optical sensors for indoor chemical monitoring, elevating the limits of detection towards ever-increasing sensitivities. Integrated optical chemical sensors can detect and measure the concentration of an analyte by accessing a particular optical parameter. Various designs for integrated refractometric measurements have been proposed over the years, including integrated interferometers [2], ring resonators [3], plasmonics [4], photonic crystals [5] and gratings [6]. These are principally reagent-mediated sensors [7], implying that they monitor the optical response of an intermediate species (typically a solid porous matrix) whose optical properties depend on the presence of the target gaseous analyte. This is advantageous in several ways; firstly, a very high selectivity to a particular analyte can be achieved since some material matrices or chemical transducers are uniquely responsive to a specific biochemical species, and secondly, it permits chemical interaction enhancement by focusing effort on optically optimizing and sizing of the material matrix. Amongst the three principal interrogation techniques, namely intensity-based measurements, wavelength or spectral interrogation and phase demodulation, wavelength-based techniques technically guarantee measurements which are relatively independent of any input intensity variations from the optical source.

In this work we propose a novel type of integrated refractometer using a planar multimode Long Period Grating (LPG). LPGs are structures operating on wavelength-selective coupling of two or more co-propagative modes whose effective indices can be analyzed by using the resonance spectral features. The LPG structure typically consists of a periodic longitudinal index or spatial modulation of a multi-mode supporting architecture with the modulation of the order of several times the wavelength to allow selective optical mode resonance. Historically, LPGs have been principally implemented on fiber-based platforms, as the introduction of such modulation can simply be performed by irradiation or tapering of the fiber core or cladding but have recently found interest in the integrated platform [8] [9]. In fiber LPGs, which couple core modes to cladding modes, the interaction coefficient between the optical fields and the external sensing region is usually very low, of the order of 0.001 - 0.01, (∼0.004) [10] for conventional fibers and slightly higher (∼0.013) [11] for analyte-filled photonic crystal fibers. Nevertheless, the sensitivities that are obtained in these fiber-based devices are still within competitive levels. We hereby propose to exploit the design flexibility offered by integrated photonics in this work to create a highly sensitive and original chip-integrated sensor based on modal interaction optimization with the analyte of interest. Our design focuses on the coupling of the single core mode (in the silicon nitride layer) to cladding layer mode(s) by using periodic waveguide width-modulation as a pattern, as illustrated in Fig. 1. To

C. Deleau, H. C. Seat, H. Tap and O. Bernal are with LAAS-CNRS, Université de Toulouse, CNRS, INP, 31000 Toulouse, France, e-mail: clement.deleau@laas.fr.

F. Surre is with James Watt School of Engineering, University of Glasgow, Glasgow, G12 8QQ, United Kingdom.

Manuscript published 15/05/2021

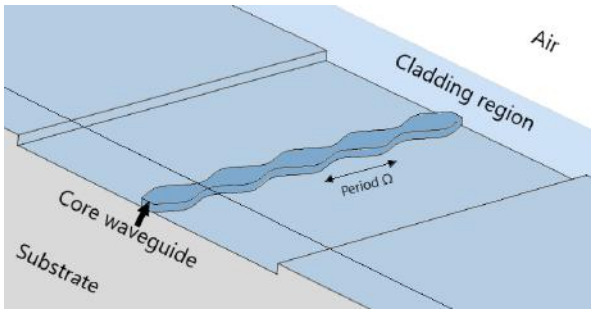

Fig. 1. Illustration of the proposed SiN integrated Long Period Grating

address future gas sensing applications, these LPGs could employ bulk sensing to benefit from the enhanced sensing matrix-optical field interaction with the cladding layer.

Section II describes the sensing scheme and structure features, and briefly discusses the different optimization methods that can be applied on an LPWG. The architecture's optical behavior is then modeled in Section III through EigenMode Expansion (EME) techniques whose advantages and limitations are discussed. Subsequently, Coupled-local-mode Theory (CLMT) [12] is introduced as a means to provide more insight on the optical behavior of the design and to facilitate coupling rate optimization. In Section IV, the fabrication and characterization of the LPWGs are presented, and the effects of the process variations on the optical system are analyzed in detail. In the last section, to assess the performance of the proposed LPWG, experimental and simulation results of the LPWG transmission spectrum and surface sensitivity are first presented using a cladding layer of epoxy-based negative photoresist SU8. Regarding bulk sensitivity, we will then show that it can be inferred from the temperature dependence tests. Finally, the SU8 cladding layer is replaced by a gas porous layer of Styrene-co-AcryloNitrile (SAN) that is demonstrated to be compatible with our LPG, thereby paving the way towards future gas sensing applications.

II. Design

A. Theory

Long Period Gratings have been successfully exploited in Fiber Optic Chemical Sensors due to their ease of fabrication and, in particular, their capacity for coupling energy to outer cladding modes, thereby allowing the optical power to interact with the external environment. As duly reported in various papers [13] [14], a phase-matching condition between two co-propagative optical modes must be fulfilled to enable resonance to result in an exchange of energy :

$$n_{eff_j} - n_{eff_l} = \frac{\lambda_{res}}{\Omega} \tag{1}$$

where n_{eff_j} and n_{eff_l} are the effective indices (EIs) of the two coupled modes j and l, respectively, λ_{res} the center resonant wavelength and Ω the grating period. The formula is derived from the well-known Coupled Mode Theory (CMT) [12], from which coupling equations can be expressed as

$$\frac{db_{\pm j}}{dz} \mp i\beta_j b_{\pm j} = \sum_j \left(C_{\pm j,l} b_l + C_{\pm j,-l} b_{-l}\right) \tag{2}$$

where $b_{\pm j}$ is the modal amplitude of the forward $(+)$ or backward $(-)$ propagating mode j, β_j is the propagation constant of mode j, and $C_{j,l}$ is the mode coupling coefficient between modes j and l. Then, straightforward development and conservation of energy show that when the mode coupling coefficients $C_{j,l}$ are periodically modulated along the longitudinal axis, with a modulation period corresponding to the accumulated phase difference between the two modes, coupling can occur. The rate of energy exchange upon resonance further depends on other parameters, including the modulation amplitude and optical field superposition at the modulated guide interfaces, as previously detailed in [15]. In refractometric sensing schemes employing LPGs, the presence of the analyte generally modifies the refractive index (RI) of the equivalent sensing layer which, in turn, modifies the propagation constants of the incident modes propagating in the layer. The difference in EI variation between the two coupled modes leads to a spectral shift of the optical resonance. This spectral shift can finally be measured to determine the RI variations of either the analyte deposited on top of the cladding layer (*i.e.* surface sensing configuration) or of the cladding layer itself (*i.e.* bulk sensing configuration). To a certain extent, in correlation with the modal overlap, which is defined as the modal optical field superposition ratio to the region of interest, the dependency of the EI of the i^{th} mode on the RI of the sensing layer n_{sens} (used here as the cladding layer) can be expressed as the coefficient Γ_i:

$$\Gamma_i\left(\lambda, n_{eff,i}\right) = \frac{dn_{eff,i}}{dn_{sens}}\left(\lambda, n_{eff,i}\right). \tag{3}$$

Now, by considering the phase-matching condition (equation (1)), the sensitivity of the LPG can thus be established as

$$S = \frac{d\lambda_{res}}{dn_{sens}} = \lambda \frac{\Gamma_j\left(\lambda, n_{eff,j}\right) - \Gamma_l\left(\lambda, n_{eff,l}\right)}{n_{g,j} - n_{g,l}} \tag{4}$$

where $n_{g,j}$ and $n_{g,l}$ are the group indices of the mode j and l, respectively. Subsequently, the sensitivity of an LPG can be improved either by increasing the numerator term or decreasing the denominator term in equation (4). Based on the former, we propose to enhance the sensitivity of the LPWG by extensively increasing the Γ_l coefficients by improving the modal overlap of the modes to couple in the sensing region. This could be achieved by inducing one of the modes to directly propagate in the sensing region, which is particularly applicable to gas sensors using gas-porous solid cladding layers. Moreover, due to the relatively large spectral width of the typical LPG resonance, to the order of several nanometers, the minimum detectable spectral shift is typically limited by the full-width half-maximum (FWHM) of the resonance instead of the optical analyser spectral resolution [16]. By using the CMT

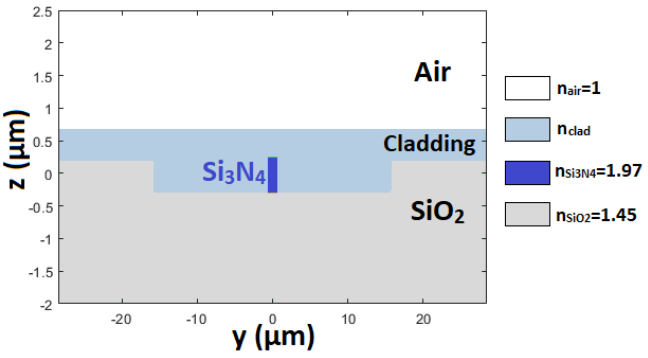

Fig. 2. Cross section material and refractive index profile of the proposed LPWG with n_{clad} = 1.58 for SU8 and 1.57 for SAN

approach and taking into account modal dispersion effects, the figure of merit (FOM) can be expressed as follows :

$$F.O.M. = \frac{S}{FWHM} \approx \frac{(\Gamma_j - \Gamma_l)L_{opt}}{0.8\lambda_{res}} \quad (5)$$

where L_{opt} is the minimum LPG length for full mode coupling at resonance. The expression shows that for an LPG of a given length the FOM is ultimately limited by the coefficients $\Gamma_{j,l}$ and that tailoring of the spectral features can be performed by engineering L_{opt} which depends on the coupling coefficients $C_{j,l}$, as will be detailed in the next section. Additionally, as it can be deduced from equations (4) and (5), improvements of the FWHM can be achieved by either reducing the coupling strength and proportionally increasing the grating length, or engineering the coupled modes propagation constants. The former method however decreases the optical transmission level with longer propagation in lossy integrated waveguides while the latter reduces the spectral sensitivity in proportion to the FWHM change, thus resulting in a constant FOM.

B. Structure

The proposed LPWG architecture consists of a Silicon Nitride (Si_3N_4) width-modulated core integrated waveguide and a multimode cladding waveguide, as shown in Fig 1. Smooth width modulation is advantageous as it allows continuous coupling, contrary to binary gratings where the waveguide is partly etched, thus potentially inducing loss of energy at the grating interfaces. In addition, the width modulation can be directly designed on the waveguide pattern, hence no additional process step is required.

The principal objective of our design is to obtain resonant coupling between the fundamental mode and a multi-mode in the cladding waveguide. As a main difference to fiber-based LPGs, whose cladding mode interaction with the sensing layer is generally very low, we elect to directly use the cladding cavity as the sensing layer, thus potentially increasing the coefficient Γ_l to nearly 1. To perform this operation, a polymeric layer of Styrene-co-AcryloNitrile (SAN) is selected for its important material properties pertaining to future potential gas sensing applications. Firstly, SAN has been previously proven as a suitable gas sensing host layer [2], and allows incorporation of selective reagents such as Cryptophane for functionalization to methane, for instance. Secondly, its RI n_{SAN} (=1.57) is superior to the standard oxide material index of n_{SiO_2}=1.45, thereby enabling the confinement of modes in a sufficiently large sensing layer without significant field leakage to the bottom oxide layer. It was also previously demonstrated as an acceptable integrated waveguide [17], and is thus expected to exhibit relatively minor diffractive imperfections which could arise due to the porosity of the polymer. Considering suitable cross-sectional dimensions, the following relationship between material RIs permits confinement of core and cladding modes: $n_{core} > n_{eff,1} > n_{clad} > n_{eff,n} > n_{sub} > n_{air}$ where the indices are respectively the RI of the core $n_{core} = n_{Si_3N_4}$=1.97, $n_{eff,1}$ the EI of the core's fundamental mode, n_{clad} the RI of the cladding, $n_{eff,n}$ the EI of the nth order cladding mode to couple, n_{sub} the RI of the bottom SiO_2 layer and n_{air} the RI of air.

The SiN waveguide is designed at standard dimensions with a cross-section of 1000×400 nm with a modulation width of $\pm$ 300 nm (see Fig. 2). Unlike waveguide Bragg grating reflectors whose periods are lower than the interrogating wavelength, waveguide LPGs could be subject to relatively higher energy loss at the period width minimas if the mode is too constrained. Preliminary experimental tests have, however, shown that no particular increase in optical loss is expected for both maximas or minimas of the waveguide width over a full modulation period. The cladding cavity dimensions are designed to be 1.1 μm thick and 32 μm wide, for a 1 mm long sensor, thus allowing to support multiple propagative cladding modes which can be coupled to the fundamental core waveguide mode.

III. Modeling

A. Mode calculation and Eigenmode Expansion

The waveguide structure supports a fundamental core mode, denoted by HE1, and multiple cladding modes (i.e. HEi with i= 2, 3, 4...), whose optical fields are shown in Fig. 3 for odd modes from HE7 to HE15. Each cladding mode possesses an EI slightly inferior to that of SAN that slowly decreases with the order of the mode. The cladding dimensions have been chosen to support up to eight hybrid odd HE modes which should result in eight resonant dips over a 200 nm spectral range. Moreover, as will be discussed in the next section, they also allow coupling parameters of different levels to be obtained which will translate into various dip amplitudes. As it is intended to couple the fundamental mode to cladding modes around 1550 nm, the LPWG modulation period values are chosen to be between 8 and 10 μm, depending on the selected mode(s) to be coupled to. This is achieved by satisfying equation (1) and using the cross-section of the waveguide at zero-modulation amplitude for modal calculation. It is, however, important to understand that due to the nonlinear EI dispersion of the modes, the period-averaged EI is slightly different from the average width profile's EI, hence a small resonance shift can be expected between calculated (equation (1)) and simulated/experimental results. EigenMode Expansion (EME) is found to be an efficient solution for analyzing

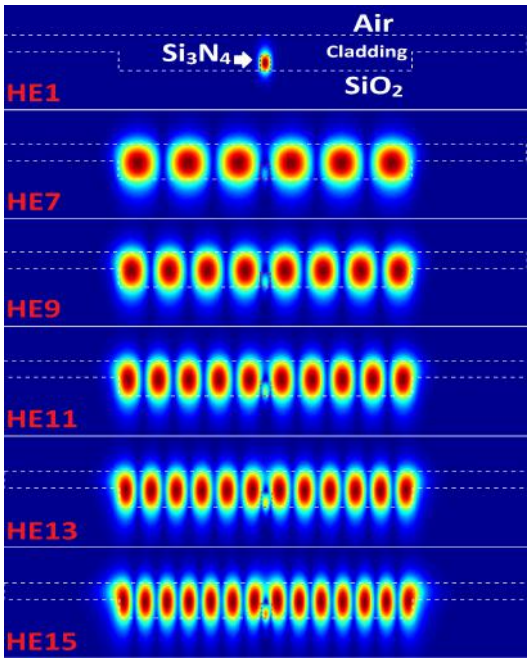

Fig. 3. Optical fields of cross-sectional odd modes

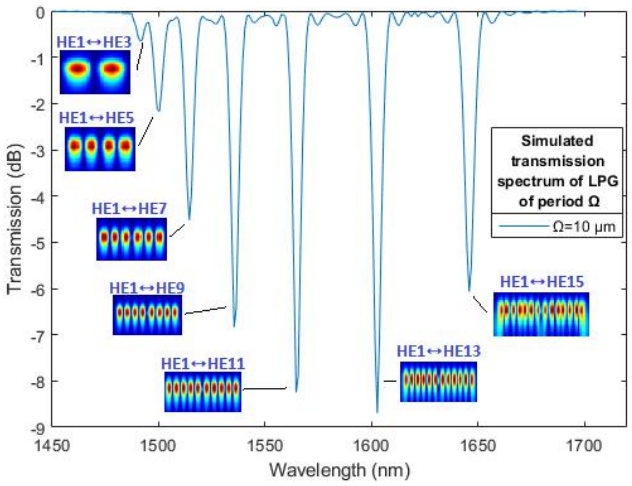

Fig. 4. Simulated transmission spectrum of 100-period LPWG showing coupling between fundamental and odd cladding modes. Insets illustrate various field profiles of coupled odd HEi modes

periodically-modulated structures. In EME, the structure is firstly divided into slices transverse to the axis of propagation. The optical fields and dispersion behaviors of the modes are then calculated for each cross-section after which a contingent iterative superposition of the scattering parameters is resolved to obtain the modulated modal information. Because of the post-mode-calculation analysis, which permits the setting of the structure's longitudinal profiles after the cross-sectional modal study, it is possible to optimize the LPWG in terms of length and periodicity with relative ease. Moreover, since EME studies the exchange of energy between modes, it is highly suitable for the design of our filter-type structure based on a multi-modal resonant coupling behavior. Figure 4 shows the output spectrum of the fundamental mode which exhibits multiple dips due to the different cladding mode resonances.

B. Coupled-local-mode Theory approach

Coupled-local-mode Theory (CLMT) provides an analytical model of the LPWG's response using parametric inputs such as its geometrical dimensions. Similar to EME, it requires the slicing of the structure and a modal calculation for each cross-section. However, mode coupling coefficients in CLMT are calculated analytically using the modulation parameters for each cross-section as shown in equation (6). The propagation calculation is then performed by the resolution of a set of differential equations as given in equation (2), contrary to CMT [12]. In addition, CLMT takes into account the important waveguide dimensional variations as well as polarization effects by using the coupling coefficient between the j^{th} and l^{th} modes, denoted $C_{j,l}$, calculated for a large number of cross-sections slices over a modulation period and defined by :

$$\forall j \neq l, \quad C_{jl} = \frac{k}{4}\left(\frac{\varepsilon_0}{\mu_0}\right)^{\frac{1}{2}} \frac{1}{\beta_j - \beta_l} \int_{A_\infty} \hat{e}_j^* \hat{e}_l \frac{\partial n^2}{\partial z} dA, \qquad (6)$$
$$C_{jj} = 0,$$

where A_∞ is the infinite cross-section, ϵ_0 and μ_0 the free-space dielectric and permeability constants, respectively, Γ the free-space wavenumber $2\pi/\lambda$ and * denotes the complex conjugate. The development of the coupling coefficients provides important information. First, through the differential RI integration over the modulation interfaces, it is seen that only odd modes can be coupled to the fundamental mode for a structure with vertical plane symmetry along the propagation axis: the calculated coefficient becomes null for even modes because of the opposite polarization states of the fields at the two modulated waveguide interfaces as described in detail in [15]. Secondly, the coupling length at resonance for total energy transfer can be adjusted by controlling the amplitude of the coupling coefficients. This can firstly be performed by optimizing the electric field superposition at the lateral core-cladding interface. As an example, from Fig. 3, it is observed that the HE9 mode has a higher optical field strength at the core-cladding interface than the HE7 mode, hence a greater coupling coefficient is achieved. Additionally, the coupling strength also depends on the modulation amplitude. A deeper modulation thus leads to longitudinal shortening of the optimized sensor, but can also increase extrinsic waveguide loss with thinner waveguide widths or widen the resonance spectral pattern as described in equation (5). In Fig. 4, one also notices the tendency of the coupling dips of the higher-order mode (HE15) to be smaller, despite having a greater Γ_i coefficient, as previously explained. This is because the energy starts coupling back to the fundamental mode after being exchanged completely; the exchange of energy is periodic. In most fiber-based LPGs, the coupling coefficients vary only slightly over a full period. As a result, the optimal grating length L_{opt} for the

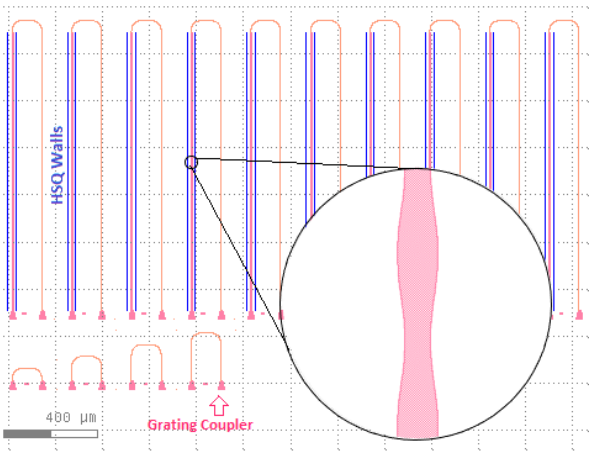

Fig. 5. LPWGs layout designed on Klayout

j^{th} and l^{th} mode coupling can be approximated by $\pi/(2C_{jl})$ [16]. However, for LPWGs, as previously demonstrated in [15], L_{opt} must be found numerically. This is due to larger variations of the coupling coefficient induced by typical profile modulations in integrated photonics.

IV. Fabrication

A. Materials and Cross Section

To validate the proposed LPWG architecture's operating principle and assess its surface sensitivity, a first set of LPWGs has been initially designed (Fig. 5) and fabricated using SU8 instead of SAN. Since both SU8 and SAN have very similar RIs and since SU8 has the particular advantage of being more easily deposited (in terms of flatness and thickness), SU8 is firstly used as cladding to investigate the operationality of the LPWG and characterize it as a prototype. Note that SU8 is an epoxy-based negative photoresist commonly used in photolithography, hence its optical and viscosity characteristics are widely known. This enables a greater control to be achieved on the cladding layer. It is, however, not porous to gaseous species and is only used here to validate the operating optical principle. For simplicity of fabrication, the cladding is delimited by incorporating SiO_2 walls using Hydrogen Silesquioxane (HSQ) resist, whose constitution and RI are found to be very similar to those of SiO_2 after curing. The HSQ walls are designed to be 3 μm wide and 0.6 μm thick to prevent multimode optical leakage as well as to ensure ease of coating and electron-patterning.

B. Process

To fabricate our waveguide, a 2 μm SiO_2 layer is first deposited by plasma-enhanced chemical vapor deposition (PECVD) on a clean Si wafer. Parasitic substrate optical leakage during waveguide modal propagation has been previously investigated for this material thickness and found to be negligible. A 400 nm thick Si_3N_4 (or simply SiN) layer is next deposited on top by PECVD, with n_{core} (∼1.97) measured by ellipsometry. An electron-sensitive resist MaN2405 is deposited by spin-coating, followed by an Electra92 resist layer,

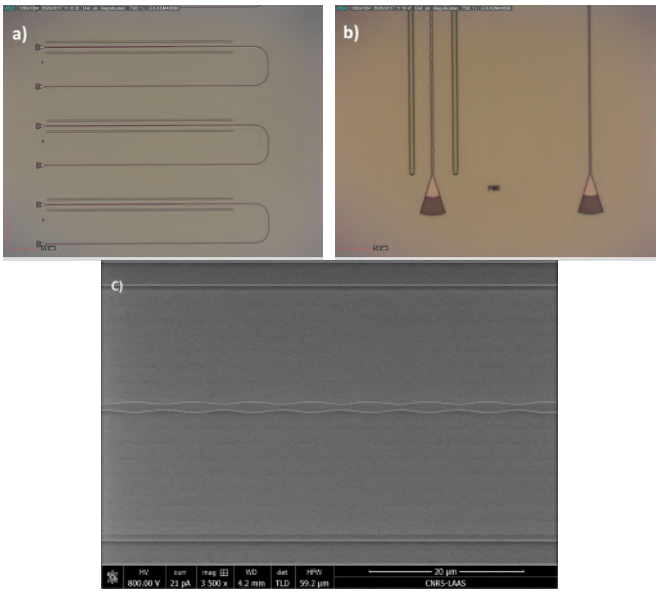

Fig. 6. Fabricated LPWGs die microscope photographies: (a) overview, (b) grating couplers zoom and (c) SEM image of the grating modulation

principally used for the dissipation of electronic charges that are induced during the electron-beam lithography stage. After development of the waveguide patterns, the unwanted parts of the SiN layer are removed by reactive ion etching (RIE). The remaining parts of the resist are then removed using acetone and Plasma O_2 cleaning. Both the HSQ and Electra92 resists are then deposited by spin-coating. After curing of the HSQ walls, a final layer of SU8 is deposited by spin-coating at a spin-rate of 1700 rpm. This layer amounts to 1.1 μm thick as measured by profilometry. Figure 6 shows optical microscope pictures and a zoomed scanning electron microscope (SEM) image of the fabricated LPWGs.

C. Post-Fabrication Characterization

Scanning electron microscopy has revealed a slight asymmetry of the structure, due to a minor translation shift between the two patterned layers. As will be shown in the next section, this asymmetry has only minor consequences on the output spectrum as well as on the sensor's sensitivity. The measured waveguide width has also been found to be slightly different from the design, which should induce a small resonance shift in the transmission spectrum since it slightly modifies the average EI of the core mode.

V. Experimental Results

A. Experimental Setup

The experimental setup for characterizing our structure consists of a broadband light source (BBS), an optical spectrum analyzer (OSA), a fiber array and the chip under test, as illustrated in Fig. 7. The fiber array incorporates a set of multiple fibers bound and held together by a support at one end, with each fiber core separated by 127 µm. Each structure to be characterized is connected at each respective output to a grating coupler, which allows the injection and recovery of

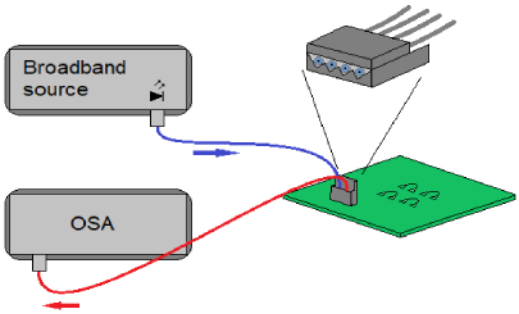

Fig. 7. Illustration of the experimental setup

the interrogating light through the fiber array positioned on top of the chip-integrated grating coupler pair. The fiber array is mounted onto a motorized linear stage driven by a dedicated LabVIEW program for alignment purposes. An algorithm has also been incorporated into the program to enable automatic scanning of the entire chip via feedback of the measured transmission spectra of the components or functions under characterization. For temperature stability, the chip is placed on top of a Thorlabs mount with integrated thermo-electric cooler.

B. Virtual Reconstruction Of The Entire Coupling Spectrum

As shown in equation (1), the position of the resonance peak due to coupling resonance within the structure depends proportionally on the period of the LPWG for a given cross-section. Furthermore, Fig. 4 shows that the theoretical transmission spectrum of the structure containing the first-order coupling resonance dip of every cladding mode is ∼200 nm wide and too large to be measured over a single wavelength scan by our setup. Hence, a set of LPWGs with different periods but identical cross-section and modulation amplitude has been designed and fabricated instead. It then becomes possible to virtually reconstruct the entire spectrum by firstly de-embedding the signal to isolate the LPWG's individual spectral contribution and, secondly, by shifting the processed signals respectively to the corresponding LPWGs periods. The LPWGs exhibit little or no additional energy loss when compared to non-modulated waveguides of equal length. After base-line correction, the LPWGs transmissions are shown on the reconstructed spectrum in Fig. 8(b). Subsequently, when fabrication defaults such as asymmetry or waveguide width defects are reintroduced into the model, a very similar spectra can be found as in 8(a).

Contrary to Fig. 4, shorter dips (1-3dB) have been observed between the main dips (3-10dB). They may be attributed to the slight asymmetry of the structure which disrupts the nullification condition of the optical modal field product at the lateral interfaces for even modes. This consequently leads to a minor rise in the coupling coefficients of the even modes, thus allowing partial coupling to these same even modes. Nonetheless, a flaw in the virtual spectrum reconstruction is highlighted by the differing measured amplitudes for the same coupling dips and can be attributed to the high spectral

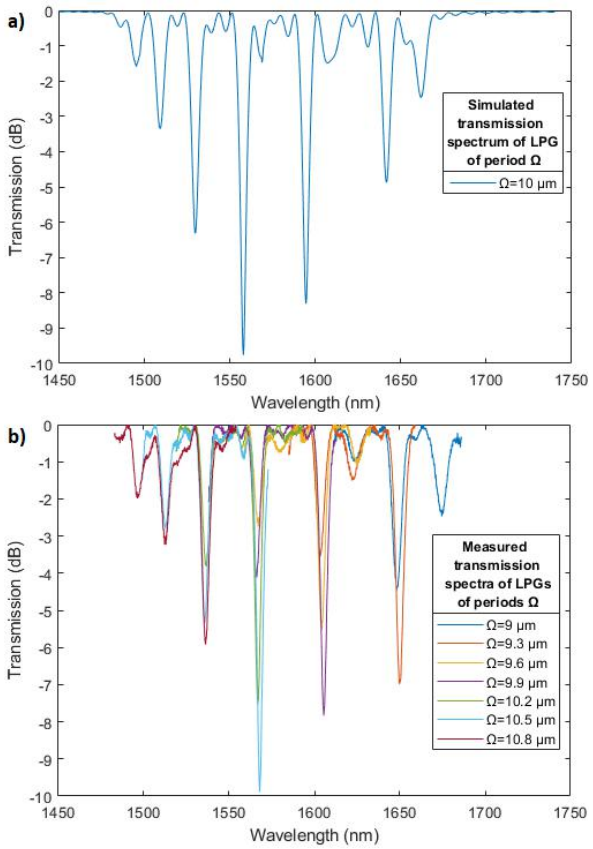

Fig. 8. Transmission spectra for a 100-period long LPWG: (a) Simulated with parametric adjustment and (b) reconstructed from measurements

dispersion of the modal coupling coefficients in high index-contrast gratings. This is because with higher wavelengths, the fundamental mode becomes more leaky and results in large variations of the optical field product at the waveguide's modulated interfaces, thereby changing the coupling strength. The different coupling dips are found to exhibit extinction ratios of several dBs. The dips also exhibit an average FWHM of approximately 5 nm in this work. Using the SANTEC tunable laser (TSL-550 C model) with its swept test system, which has a ± 1 pm repeatability and resolution, 200 wavelength scan measurements have been performed over an hour with a regulated temperature of 23°C to estimate the precision σ_{sensor} of the resonance wavelength of the HE9 mode's transmission spectrum. After applying a Lorentzian curve fitting, $\sigma_{sensor} = 1.5$ pm is obtained, which is similar to the laser system precision.

C. Refractometric measurements

A cladding refractometric measurement configuration is difficult to achieve here since a gas-porous sensing region is a solid layer which cannot be filled or saturated with liquids. We thereby propose a simple surface-based experimental configuration where the target liquid is poured onto the top surface of the sensor. Because of the relatively thin SU8 cladding, Γ_l is of the order of 0.1 which remains higher than the coefficients of the cladding modes in most fiber LPGs,

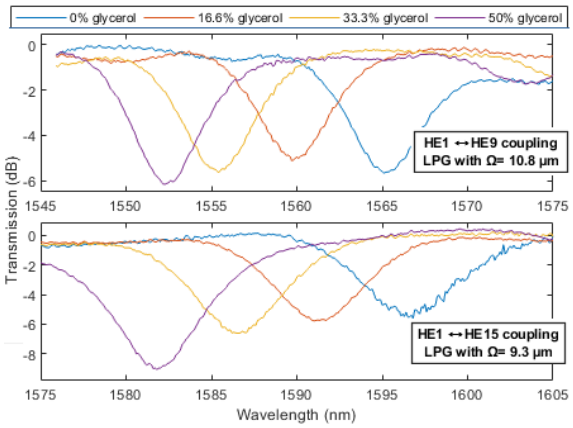

Fig. 9. Measured spectrum of HE9 and HE15 mode resonance of LPWGs using SU8 as cladding for different deposited concentrations of water and glycerol

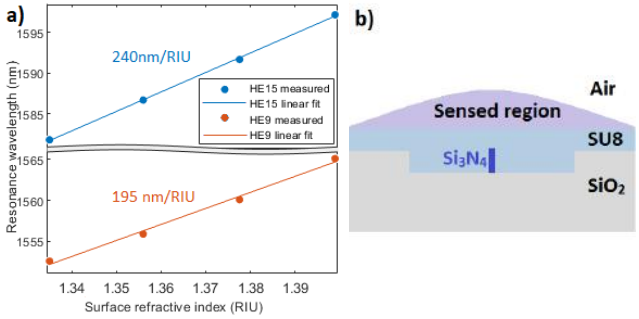

Fig. 10. (a) Measured surface spectral sensitivities of modes HE9 and HE15 and (b) Surface sensing configuration illustration

when the surface of the structure becomes the sensing region. Water and glycerol mixtures of different proportions are then applied on different LPWGs and the resonance shifts of mode coupling dips tracked, as shown in Fig. 9 for the HE9 and HE15 modes. Using the RIs of water and glycerol around 1550 nm [18], the surface sensitivities are measured (Fig. 10) and compared to simulation, for both surface and cladding measurements in Table I. A sensitivity up to 240 nm/RIU has been measured for the HE15 mode's resonance dip, whose bandwidth and extinction ratio values are both found to agree with the simulated spectrum. Additionally, it is observed that when fleeting impurities interact with the cladding layer during measurement, the resonance features are not shifted, due to the inertial behavior of the LPWG. Because the modal energy exchange during propagation is driven by a coupling momentum, the LPWG sensor's resonance wavelength depends on the sensed layer's median RI and not the average RI, thus rendering it robust to disturbance by impurities. Additionally, a cross-sectional modification on a small segment of the LPWG does not lead to any significant shift in the LPWG resonance but can, however, contribute to reduce the coupled energy, making LPWGs highly interesting candidates for sensing of gases whose RI profiles are generally homogeneous within a given volume. As the measured and simulated sensitivities are found to be very similar for the surface measurement configuration, the experimental measurements are taken to corroborate the model and the subsequent simulations without loss of generality, thus validating the operation of our sensor with data-processed inputs. The comparison also suggests that the cladding measurements can further be expected to conform to the simulated values. Using our measured sensor resolution, a detection limit of 2 μRIU in the case of bulk sensing can be estimated.

TABLE I
CALCULATED AND MEASURED SENSITIVITIES

	Simulated surface sensitivity (nm/RIU)	Measured surface sensitivity (nm/RIU)	Simulated bulk sensitivity (nm/RIU)
HE9	198	195	1920
HE11	214	206	1915
HE13	231	227	1910
HE15	251	240	1820

D. Temperature dependence

The temperature behavior of the sensor is firstly simulated with EME using thermo-optical coefficients of SiN, SiO_2 and SU8, whose values at 1550 nm are respectively $\sim$24.5, 9.5 [19] and -130 μRIU/K [20]. The temperature sensitivity of the wavelength resonances is estimated to be $\sim$330 pm/K and is similar for each mode resonance. For experimental validation, the TEC temperature is swept from 15 to 30°C at 5°C steps. Linear interpolation of the measured values gives a temperature sensitivity of 340 pm/K as plotted in Fig. 11. In addition, from the temperature dependence analysis, an approximation of the bulk sensitivity can be inferred. This is estimated to be $\sim$1900 nm/RIU.

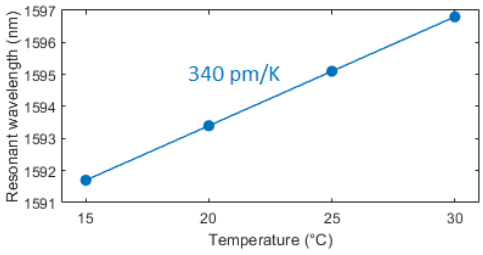

Fig. 11. Measured temperature dependence of the wavelength resonance

E. SAN coating

As previously mentioned, SU8 cannot, in practice, be used as a gas sensing layer as it is a hermetic layer. Instead, a porous polymeric layer of similar RI such as SAN can be used for gas sensing applications [2]. To ensure SAN compatibility with the proposed design architecture as the cladding, coating and characterization are performed on SAN as follows: 50 mg of SAN are dissolved in 10 mL of methylethylketone and the mixture is spin-coated onto the pre-cleaned photonic chip. As seen in Fig. 12, the coupling phenomenon occurs very similarly to that of the SU8-coated LPWG. Small changes of

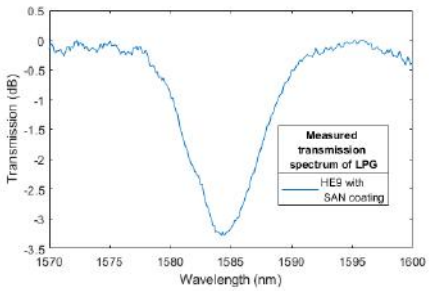

Fig. 12. Measured transmission spectrum of HE9 mode resonance on LPWG with SAN cladding

coupling are due to minor variations in the film thickness and layer RI deviation as compared to the previously-characterized LPWGs. Consequently, employing SAN as an external sensing layer provides a pathway to gas sensing based on the bulk sensitivity of the proposed LPWG. In addition, since the thermo-optical coefficients of SAN and SU8 are of the same order [21], the thermal behavior in a SAN-clad LPWG is not expected to significantly vary from the presented results.

VI. Conclusion

In this work, SiN width-modulated LPWGs have been designed, fabricated and characterized to achieve RI measurements with high sensitivity. Surface sensitivities up to 240 nm/RIU have been attained and agree with both the proposed CLMT model and EME simulations. In addition, from temperature tests, the bulk sensitivity has been estimated to be approximately 1900 nm/RIU, in accordance with EME simulations. This is an improvement of almost an order of magnitude and demonstrates possibly a very high sensitivity for potential gas sensing applications. A specific use of SAN's high RI is demonstrated to allow modal propagation, which could improve both the sensitivity and FOM of our sensor by eight-fold based on a bulk measurement configuration. The results from this work will serve as a baseline for the design of LPWGs combining modal interaction optimization with other sensitivity enhancement techniques such as phase-matching turning point optimization [14].

Acknowledgment

The fabrication and characterization of the integrated photonic long period gratings are supported by a TTIL (Toulouse Tech Interlabs) 2019 grant and by LAAS-CNRs micro and nanotechnologies platform, a member of the Renatech french national network. The authors would like to thank A. Lecestre, F. Carcenac, J-B. Doucet, L. Mazenq and P-F. Calmon for their technical support during the fabrication and characterization processes of the photonic integrated circuits.

References

[1] L. Chrostowski and M. Hochberg, *Silicon Photonics Design: From Devices to Systems*. Cambridge University Press, 2015.

[2] F. T. Dullo, S. Lindecrantz, J. Jágerská, J. H. Hansen, M. Engqvist, S. A. Solbø, and O. G. Hellesø, "Sensitive on-chip methane detection with a cryptophane-a cladded mach-zehnder interferometer," *Opt. Express*, vol. 23, no. 24, pp. 31 564–31 573, Nov 2015. [Online]. Available: http://www.opticsexpress.org/abstract.cfm?URI=oe-23-24-31564

[3] N. A. Yebo, S. P. Sree, E. Levrau, C. Detavernier, Z. Hens, J. A. Martens, and R. Baets, "Selective and reversible ammonia gas detection with nanoporous film functionalized silicon photonic micro-ring resonator," *Opt. Express*, vol. 20, no. 11, pp. 11 855–11 862, May 2012. [Online]. Available: http://www.opticsexpress.org/abstract.cfm?URI=oe-20-11-11855

[4] A. Zaki, K. Kirah, and M. Swillam, "Integrated optical sensor using hybrid plasmonics for lab on chip applications," *Journal of Optics*, vol. 18, p. 085803, 08 2016.

[5] M. Danaie and B. Kiani, "Design of a label-free photonic crystal refractive index sensor for biomedical applications," *Photonics and Nanostructures - Fundamentals and Applications*, vol. 31, pp. 89 – 98, 2018. [Online]. Available: http://www.sciencedirect.com/science/article/pii/S1569441017303735

[6] S. Jain, S. Srivastava, S. Rajput, L. Singh, P. Tiwari, A. K. Srivastava, and M. Kumar, "Thermally stable optical filtering using silicon-based comb-like asymmetric grating for sensing applications," *IEEE Sensors Journal*, vol. 20, no. 7, pp. 3529–3535, 2020.

[7] C. McDonagh, C. S. Burke, and B. D. MacCraith, "Optical chemical sensors," *Chemical Reviews*, vol. 108, no. 2, pp. 400–422, 2008, pMID: 18229950. [Online]. Available: https://doi.org/10.1021/cr068102g

[8] Q. Liu, K. S. Chiang, and K. P. Lor, "Condition for the realization of a temperature-insensitive long-period waveguide grating," *Opt. Lett.*, vol. 31, no. 18, pp. 2716–2718, Sep 2006. [Online]. Available: http://ol.osa.org/abstract.cfm?URI=ol-31-18-2716

[9] U. Tripathi and V. Rastogi, "Temperature insensitive long period waveguide gratings in rib waveguide," *Optik*, vol. 186, pp. 15 – 21, 2019. [Online]. Available: http://www.sciencedirect.com/science/article/pii/S0030402619305406

[10] E. Simões, I. Abe, J. Oliveira, O. Frazão, P. Caldas, and J. Pinto, "Characterization of optical fiber long period grating refractometer with nanocoating," *Sensors and Actuators B: Chemical*, vol. 153, no. 2, pp. 335 – 339, 2011. [Online]. Available: http://www.sciencedirect.com/science/article/pii/S0925400510008518

[11] H. Hu, C. Du, Q. Wang, X. Wang, and Y. Zhao, "High sensitivity internal refractive index sensor based on a photonic crystal fiber long period grating," *Instrumentation Science & Technology*, vol. 45, no. 2, pp. 181–189, 2017. [Online]. Available: https://doi.org/10.1080/10739149.2016.1215994

[12] A. W. Snyder and J. Love, *Optical waveguide theory*. Springer Science & Business Media, 2012.

[13] L. Jin, W. Jin, J. Ju, and Y. Wang, "Coupled local-mode theory for strongly modulated long period gratings," *Journal of Lightwave Technology*, vol. 28, no. 12, pp. 1745–1751, 2010.

[14] R. Y.-N. Wong, D. H. J. Juan, M. Ibsen, and P. P. Shum, "Optical fibre long-period grating sensors operating at and around the phase matching turning point," *Applications of Optical Fibers for Sensing*, 01 2019.

[15] C. Deleau, H. Seat, H. Tap, F. Surre, and O. Bernal, "Integrated silicon nitride horizontal long period grating for refractometric gas sensing applications," in *2020 IEEE International Instrumentation and Measurement Technology Conference (I2MTC)*, 2020, pp. 1–6.

[16] L. Rindorf and O. Bang, "Sensitivity of photonic crystal fiber grating sensors: Biosensing, refractive index, strain, and temperature sensing," *Journal of the Optical Society of America B*, vol. 25, 08 2007.

[17] G. Qureshi, N. Padha, V. Gupta, M. Kamalasanan, A. Singh, A. Kapoor, and K. Tripathi, "Styrene acrylonitrile (san) based polymeric waveguides," *Optics and Laser Technology*, vol. 35, no. 5, pp. 401 – 407, 2003. [Online]. Available: http://www.sciencedirect.com/science/article/pii/S0030399203000379

[18] J. E. Saunders, C. Sanders, H. Chen, and H.-P. Loock, "Refractive indices of common solvents and solutions at 1550 nm," *Appl. Opt.*, vol. 55, no. 4, pp. 947–953, Feb 2016. [Online]. Available: http://ao.osa.org/abstract.cfm?URI=ao-55-4-947

[19] A. Arbabi and L. Goddard, "Measurements of the refractive indices and thermo-optic coefficients of si3n4 and siox using microring resonances," *Optics Letters*, vol. 38, 10 2013.

[20] M. Ibrahim, J. Schmid, A. Aleali, P. Cheben, J. Lapointe, S. Janz, P. Bock, A. Densmore, B. Lamontagne, R. Ma, D. Xu, and W. Ye, "Athermal silicon waveguides with bridged subwavelength gratings for te and tm polarizations," *Optics express*, vol. 20, pp. 18 356–61, 07 2012.

[21] N. G. Sultanova, S. N. Kasarova, and I. D. Nikolov, "Characterization of optical properties of optical polymers," *Optical and Quantum Electronics*, vol. 45, no. 3, pp. 221–232, Mar 2013. [Online]. Available: https://doi.org/10.1007/s11082-012-9616-6

Integrated Silicon Nitride Horizontal Long Period Grating for Refractometric Gas Sensing applications

Clément Deleau
LAAS-CNRS
University of Toulouse, INP
Toulouse, France
clement.deleau@laas.fr

Han-Cheng Seat
LAAS-CNRS
University of Toulouse, INP
Toulouse, France
seat@toulouse-inp.fr

Hélène Tap
LAAS-CNRS
University of Toulouse, INP
Toulouse, France
helene.tap@toulouse-inp.fr

Frédéric Surre
School of Mathematics, Computer Science and engineering
University of London
London, United Kingdom
f.surre@ieee.org

Olivier Bernal
LAAS-CNRS
University of Toulouse, INP
Toulouse, France
Olivier.bernal@toulouse-inp.fr

***Abstract*—We designed an integrated long period grating based on the horizontal periodic tapering of a silicon nitride channel waveguide. The structure is studied for gas sensing applications, using Styrene AcryloNitrileas sensitive layer. Simulation results from the proposed architectureshow ahigh sensitivity beyond1700 nm/RIU using awavelength interrogation method centered at 1550 nm for a 20µm large and 300µm long structure.**

Keywords—Integrated photonics, gas sensor, modeling, long period grating, coupled local mode theory.

I. INTRODUCTION

For the past two decades,long period fiber gratings (LPFGs) have beenintensely investigated for communication [1] and sensing applications [2]. A wide diversity of LPFG-based systems has been demonstrated and used in various applications, such as optical filters [3], gain flatteners, polarization couplers, multiplexers and particularly refractometric sensors [4-7]. However, to the best of our knowledge, the design of these structuresis typically limitedto standard dimensions and intrinsic parameters of the host fibers, rendering them unsuitable for integration and optimization.

Following the enormous impact of integrated electronics on our society, integrated photonicshave been subject to an exponentially growing interest since its earliest inception as laser diode devices for telecommunication applications in the 1960sand is now widely studied for the design of original, power-efficient and high-resolutioncompact sensors. In 2003, Tsoi and al. [8] demonstrated the first integration of a long period waveguide grating (LPWG)having similar properties to conventional LPFGs. The LPWGarchitectureusing a periodic perturbation of the width or height of the waveguide enables strong coupling between the fundamental mode and a copropagating cladding mode.It can thus be designed to **selectively perform coupling under specific conditions**, makingthem very interesting candidates for in-situ chemical monitoring. Using a suitablefunctionalizing chemical layer for the cladding window surrounding the LPWG core, the detection and quantification of a specific analyte has been demonstrated through various techniques[4,5,7].

The fabrication of index-modulated structures required for long period gratings can be performed through local corrugation [9], tapering [6], laser irradiation, ultraviolet inscription, arc discharge [10]. We propose here to introduce a grating perturbation on the fundamental mode of a simple channel waveguide through a smooth periodic change of the waveguide width.Unlike binary gratings, this type of grating enables smooth power coupling and can be studied underthe slowly-varying envelope approximation assumptions. The design is studied to analyzethe LPWG response to a change of analyte concentration through the change of the sensing materialrefractive index.

This paper is organized in three parts. First, in Section II, the general design of the horizontal LPWG is presented and compared to other reported types of LPWG. In Section III, the Coupled Local-Mode Theory (CLMT) [11] is used to introduce and describe the principle of the LPWG's mechanism This approach is formulated as a proof-of-concept but can subsequently beextended to accurately model the LPWG response and characteristics[12,13]. In Section IV, CLMT is applied on our structure andan EigenMode Expansion (EME) method is performed with Lumerical suite tools as a comparison and simulation results of the sensor's sensitivity are discussed.Finally, in section V,two fabrication methods are proposed.

II. ARCHITECTURE

A. *Proposed structure*

The proposed LPWG sensor structure consistsofa periodically-modulated(along the z-axis) channel width(x-axis) waveguide inside of a polymeric sensing regionas illustratedin Figure 1.

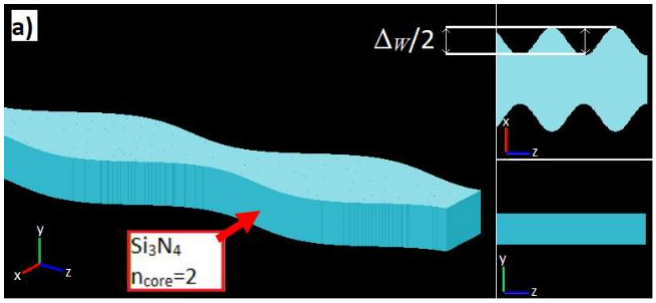

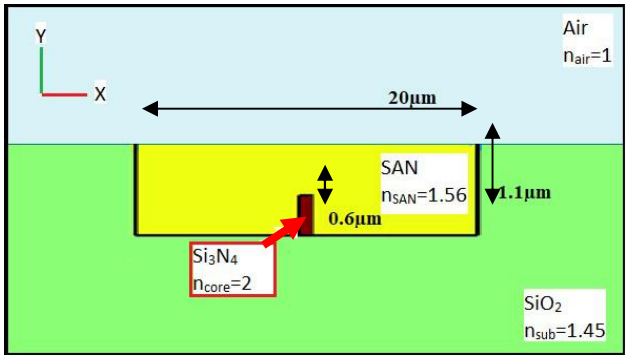

Fig. 1. (a)*Horizontal LPWG coreprofiles and (b)cross-sectional material architecture where the Si3N4 and the Styrene AcryloNitrile(SAN) are the core and cladding waveguides respectively*

As explained in the next section using CLMT [11], the excitationof the coupling phenomenon between core and cladding modes is performedvia a periodic modification of the local modes along the propagation z-axis. Two different grating types can allow this mechanism. The most common grating is one with a local index variation inscribed in the waveguide or core [1,10]. It usually requires a specific and complex apparatus as well as accurate calibration on each material to be engraved. The second grating structure, more commonly employedin integrated photonics structures, are corrugatedwaveguides[9,14], which can be achieved by an additional vertical etching step to createrelief, leading to optical coupling to cladding modes above the waveguide core. On the contrary, our structure is designed to incorporatea horizontal modulation via a periodic waveguide width variation and the design of a specific cladding box. Hence, no further process step is necessary. This is advantageous since the modulation pattern is directly drawn on the layout.

B. Materials and dimensions

The sensing mechanism is based on the coupling between two different modes; the fundamental core mode, HE1 of effective index $n_{eff,1}$, and an n^{th} cladding mode of effective index $n_{eff,n,}$ which is mostly confined in the cladding whichcan later be functionalized to a specific chemical. Since grating-assisted coupling involves coupling the core mode to higher-order modes, which are modes with lower effective indices, the following conditionmust be fulfilledto have mode confinement

$$n_{core} > n_{eff,1} > n_{clad} > n_{eff,n} > n_{sub} > n_{air}$$

where n_{core}, n_{clad}, n_{sub} and n_{air} are the refractive indexes of the Si_3N_4 waveguide core, the cladding, the SiO_2 substrate, and the air respectively.

Aspecific set of materials and structure dimensions must thenbeconsidered to allow both standard manufacturing process and functionalization for potential gas sensing. Silicon nitride (Si_3N_4 or more commonly SiN)isemployed for its ease of growth in the domain of integrated photonics and optical properties(i.e. for its relatively mediumindexcontrast with silicon oxide). The sensitive layeremployed as cladding must be a porous polymer, in which the gas is soluble.In addition, the sensitivity and selectivity can be enhanced by employing supramolecular compounds which have a cage-like structure within which molecules can be reversibly trapped [21].For example, Cryptophane-A which presents the smallest relative cavity, a methane trap,can be incorporated into a Styrene AcryloNitrile (SAN) film of index n=1.56, forming the sensing layer of a Mach-Zehnder-based methane sensor[15,16]. It is referred to here as cladding, as it almost entirely encompasses the Silicon Nitride core(Fig. 1.(b) and 2.(a))

Figure 1. (b) describes the cross-sectional refractive index profile of the LPWG, with n_{core}=2, n_{clad}=1.56, n_{sub}=1.45, n_{air}=1. A sensing window thickness of ~1 µmallows uniform and relatively quick diffusion of the gas species to be detected as demonstrated in [5,7,8,15].The cladding and waveguide are respectively designed to have a20 and 0.8 (w_{core}) µm width and a 1.1µm and 0.6(h_{core})µmthicknessto ensure single mode propagation only within the core while allowing multiple higher order modes within the cladding.Moreover, the cladding dimensions determine the maximum order of the propagating cladding modes, which directly influences the coupling strength, as demonstrated later in section III and IV.Themaximum width variation Δ_W(see Fig. 1. (a))and grating length period Ω are chosen to be 0.6µm and 8.76µm, respectively (Fig. 1 a)so that Ω corresponds to the standard LPG phase-matching condition [11,12,13]on thepropagationconstants $\beta_j(z)$ and $\beta_l(z)$ of the two modes to couple at the resonance wavelength around 1550 nm:

$$\beta_j(z=0) - \beta_l(z=0) = \frac{1}{\Omega}, \qquad (1)$$

Here, coupling occurs between the fundamental mode HE1, andhigher order propagating cladding modes, out of which one exhibits a higher coupling at a specific wavelength as described in the next section.More precisely, it will be further shown that only odd cladding modes can be coupled to the fundamental mode through the LPWG.Their respective effective indices and profiles were simulated with Lumerical,as shown in Fig. 2 for 2 higher-order modes only, to calculate the resonant grating period. We see that for the two multi-modes, most of the optical field is confined into the SAN, therefore called cladding-modes. These modes thus become inherently more affected by a change of the SAN refractive indexn_{clad}.Using eq. (1), the resonance wavelength can be approximated by the average of the values of each coupled-mode effective indicesalong z-propagation. Note, however, that the real resonance wavelength values will be slightly shifted as the functions of the mode effective indicesversuscore width are not linear.

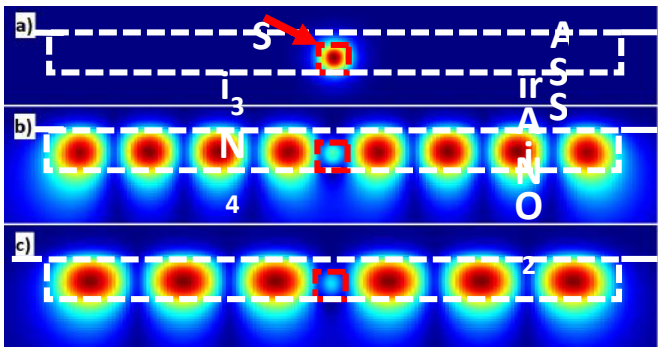

Fig. 2. *Mode profiles at 1550nm for Fundamental* (a)*HE1 mode, and cladding* (b)*HE9 and*(c) *HE7 modes calculated with Lumerical mode solver*

III. LPG MODEL

Different methods have been used to model the light propagation when introduced into the LPG. However, certain types of simulation methods find difficulty to model accurately this type of sensor as the behavior of the distribution of light is very continuous and highly depends on small structure variations.

A. Finite-Difference Time-Domain

As an example, Finite-Difference Time-Domain (FDTD) gives an interesting insight of the overall sensor mechanism as shown in Fig 3, where coupling happens between HE1 and HE7, but its high dependence onfine discretization makes it inadequate for accurate modeling in our case using our computing resources.The need for both high temporal and mesh resolution over a relatively large area, especially at the interfaces where refraction happens, leads to large memory needs, otherwise simulations will present larger numerical errors than other methods. However, comparing Fig. 3. (a) and (b) clearly illustrates that, only at resonance, most of the optical power is transferred from the core mode to the higher order cladding mode after a brief propagating length.

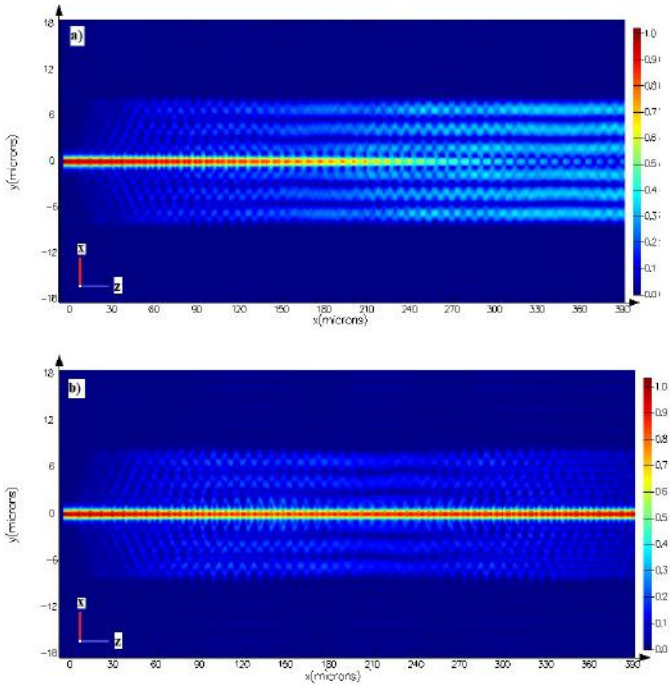

Fig. 3. (a)*Illustration of the intensity distribution seen from above at resonance (b)Normalizedintensity distribution seen from above with a slightly different cladding index*

To circumvent these computing issues, two different methods can be used instead: the common EigenMode Expansion method and, more specific to our LPG application, the CLMT [11].

B. Eigenmode Expansion method

The Eigenmode expansion method (EME), also referred to as mode matching method, is a rigorous technique used for modeling waveguides [17,18], which relies on a scattering parameter superposition approach to calculate the amplitude of each mode at any propagation distance. This technique has very good efficiency for periodic and/or long components and provides flexible post-calculations analysis. It is thus ideal for modeling long period grating-based systems [18] as, due to the structure periodicity, it is possible to calculate the structure scattering parameters fromone single period. The method is available in various commercially available software such as Lumerical© suite tools, which was used to simulate the results presented on fig. 2.

Figure 2. shows (a) the fundamental mode profile and (b)-(c) the profile of two cladding modes that can couple to the fundamental mode at certain conditions. The gratingperiod is longitudinally divided into 40 block objects and the guided mode calculation considers 40 modes per block similarly to [12].

C. Coupled Local-Mode Theory application

On the other hand, the CLMT application is performed through the characterization and calculation of the continuous refraction at the interfaces between the core and sensing window, which provides**a more physical model** on the coupling behavior in the LPG. The application of the theory was performed throughMatlab© and COMSOL© linked scripts.

Conventional Coupled Mode Theory (CMT)[11]is usually used to describe the coupling between modes when small perturbations are assumedand modes remain almost unchanged along the propagation direction.Further, the general coupled mode equations are restricted to weakly guiding waveguides where polarization effects are ignored.CMT can thus model very accurately the first category of LPGs mentionedin Section II, where the waveguide dimensions remain constant and only local refractive indices are modified. However, in the presenceof significant cross-sectional dimension modulations [13], CMT can no longer be applied, and a more specific approach, such as CLMT [11], is required. CLMT achieves good results [12,13] when used to describestructures with large but slowly varying non-uniformitiesalong the waveguide and can thus be potentially used to describe our structure. In this section, a brief introduction to CLMT is formulated together with a method to calculate coupling coefficients. It will allow better understanding of the structure behavior and provide more insightto further optimize the design architecture.

Generally, there isno exact solution to Maxwell's equations for propagation along a perturbed waveguide.It is, however, possible to obtain accurate approximations of modes within local regions, known as local modes [11]whichsuperpose to form the transverse field components as

$$\Phi_t(x,y,z) = \sum_j \left\{ b_j(z) + b_{-j}(z) \right\} \hat{\varphi}_{tj}(x,y,\beta_j(z)), \qquad (2)$$

where $\hat{\varphi}_{tj}$ representsthe orthonormal electric or magnetictransverse field profiles of the j^{th} mode, and $b_{\pm j}$ *(z)*areboth modal amplitude and phase for forward (+) or backward (-) propagation.

The coupling behavior between local modes is formulated by the general coupled local-mode equation [11]

$$\frac{d\,b_{\pm j}}{dz} \mp i\,\beta_j b_{\pm j} = \sum_j \left\{ C_{\pm j,l}\, b_l + C_{\pm j,-l}\, b_{-l} \right\}, \qquad (3)$$

withC_{jl} the coupling coefficient between the local modes *j* and *l*which can be expressed as[11]

$$C_{jl} = \frac{1}{4}\left(\frac{\varepsilon_0}{\mu_0}\right)^{\frac{1}{2}} \frac{1}{\beta_j - \beta_l} \int_{A\infty} \hat{e}_j^* . \hat{e}_l \frac{\partial n^2}{\partial z} dA, \quad j \neq l; \;\; C_{jj} = 0 \quad (4)$$

The squared index component of the horizontal grating structure can be expressed here as

$$n^2(x,y,z) = \begin{cases} n_{clad}^2 & y > \dfrac{h_{core}}{2} \\ n_{core}^2(1 - \Delta_n H(x - \rho(z)) & |y| \le \dfrac{h_{core}}{2} \\ n_{box}^2 & y < -\dfrac{h_{core}}{2} \end{cases}, \qquad (5)$$

with $\Delta_n = 1 - \dfrac{n_{clad}^2}{n_{core}^2}$, $\rho(z) = \dfrac{\Delta_w}{4} sin\left(\dfrac{2\pi z}{\Omega}\right) + \dfrac{w_{core}}{2}$ and where $x = y = 0$ at the center of the waveguide. *H* denotes the Heaviside function and ρ the periodic width variation of the LPWG along the z axis. By substituting eq. (5) into (4), we obtain the coupling coefficient for localmodes of an integrated horizontalgrating in the form of

$$C_{jl}(z) = \frac{1}{4}\left(\frac{\varepsilon_0}{\mu_0}\right)^{\frac{1}{2}} \frac{n_{core}^2 \Delta_n}{\beta_j - \beta_l} \frac{d\rho(z)}{dz} \left[\begin{array}{l} \displaystyle\int_{-\frac{h_{core}}{2}}^{\frac{h_{core}}{2}} ((\hat{e}_j^* . \hat{e}_l)_{x=\rho(z)} dy) \\ + \displaystyle\int_{-\frac{h_{core}}{2}}^{\frac{h_{core}}{2}} ((\hat{e}_j^* . \hat{e}_l)_{x=-\rho(z)} dy) \end{array} \right], \qquad (6)$$

with C_{jj}=0.

Further, the transverse electric field at the interfaces of a step-index waveguide of relatively high index contrast is discontinuous, which complicates the calculation of the integrand. A bypass method [11] is to recognize that $n^2 e_t$ is continuous across the interfaces. As a result, the transverse component of the integrand can be replaced by

$$\left(\frac{n^2 \hat{e}_{t,j}^*}{n_{core}^2}\right).\left(\frac{n^2 \hat{e}_{tl}}{n_{clad}^2}\right)$$

As previously mentioned, one of the main advantages of this CLMT compared to the EME method consists in providing a better insight of the phenomena taking place in the LPG. In particular, important LPWG properties can be deduced from this equation (eq. 6):(1) onlycoupling of the fundamental mode to odd cladding modes is possible as the even mode coupling coefficients are null;(2) the coupling amplitude can be increasedby modifying the grating amplitude $\Delta_w$and period Ω (via ρ) or by optimizing the field superposition at the waveguide interfaces. The increase of the coupling coefficient amplitude fastens the rate at which energy is exchanged between modes, as described in eq. (3), thereby reducing the minimumrequiredLPWG's length to achieve maximum coupling.

To obtain a good estimation of the remaining integral in $C_{jl}(z)$ (eq. 6), COMSOL mode-solver, based on finite-element method, can be used as it allows a convenient way to extractthe interface fields of each modes, their effective indices, and Poynting vectors for normalization. Ten cross-sections were simulated by sweeping the waveguide width between minimum and maximum values to constitute a dataset of values.These calculations are only required over half a period of the 3D model because of the structure's periodicity. This dataset is then transferred to Matlab, coupling coefficients are calculated and extracted, and only then, the LPG geometry is taken into account to model energy distribution. Another advantage of the proposed model based on CLMT is thatusing this predetermined dataset, any LPG geometry can be designed and simulated easily. CLMT only requires a dataset of coupling coefficients for given cross-sections and directly calculates energy distribution as a function of $C_{jl}(z)$, while EME superposes each mode to calculate scattering parameter between each section.

IV. SIMULATIONRESULTS

A. Model validation

Figure4 shows the cladding mode power versus the propagating length along the LPWG for different wavelengths obtained withbothCLMT and EME techniques. It clearly shows that comparable results can be achieved with the CLMT.In addition, here, the highest order propagating mode (HE9, for our LPWG's dimensions)shows higher coupling than anylower order modes (e.g. HE7) at their respective resonant wavelengths (HE9@1540nm and HE7@1484nm), as previously demonstrated by the CLMT equations, due to a higher field product integrand at the core/cladding interface. This results in a reduced LPWG's length to achieve maximum coupling.The "HE9 normalized power" at wavelengths 1550nm and 1525nm clearly describes the coupling behavior of the LPWG when the injected wavelength drifts from the resonance, resulting in a reduction of the coupled energy at a the optimal sensor length (the shortest length where coupling reaches its peak at resonance), L_{opt} = 300µm here.

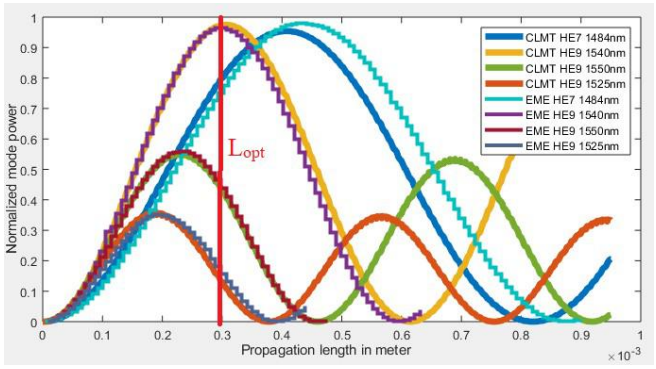

Fig. 4. *Cladding mode normalized power versus propagation length (SI) forHE7 and HE9 modes at different wavelengths simulated by CLMT application and EME*

B. Sensor sensitivity

The system interrogation can be performed through the wavelength interrogation method [4-7]. The refractive index

sensing mechanism relies on the disruption of the resonance of the LPWG which occurs when the cladding mode propagation constant changes. As a main difference with typical LPFG chemical sensors, which usuallyinvolve SPR as the cladding material cannot be modified easily, the cladding mode here is mostly confined in the sensing layer incorporated with the selective transducer. It is expected to lead to a relatively large modification of the mode propagation constant when the material indexchanges, i.e.analyte-inducedperturbations, which enhances sensor sensitivity.

Figure 5. (a) shows the coupling spectrafordifferent cladding refractive indices. From these results,thesensitivity can be calculated (cf. Fig. 5. (b)). The average sensitivity is found to be 1768nm/RIU (refractive index unit).

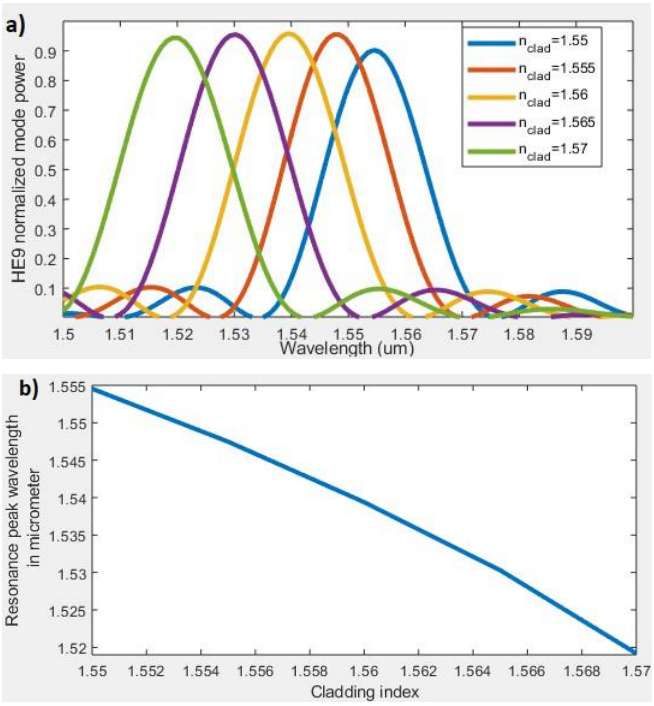

Fig.5. (a) *HE9 normalized mode power spectra for a 33 periods long grating at different cladding refractive indices, calculated with EME method and* (b) *resulting resonance peak shift for wavelength interrogation*

As it is difficult to measure the output spectra of the higher mode the measurement is made directly at the output of the core, which allows to get the same wavelength via detecting a dip in the light in the core.

We assume here that the output core intensity is equal to the input intensity minus the coupled energy to cladding modes along propagation, which could easily be measured using grating couplers, for example.

One can also notice a LPG peak is larger than other resonance peak found in integrated optics, which prevents it from large linewidth source issues.

V. FABRICATION PROPOSALS

This new type of integrated refractometric sensor is based on a specific coupling mechanism which allows several profile configurations, and therefore multiple realization processes. As described in the first section, the effective indices of each region must respect a certain relationship.Two different approaches can be employed to fabricate the LPWG.

A first method would be to simply create an opening into the buried core of a photonic chip and cover it with a sensing film to fill the etched region as seen in Fig. 6. (a). A downsize to this method is the lack of control of the thickness of the film at certain areas where the cladding could form a rib multi mode waveguide instead of a strip one. It could simply be bypassed to a certain extent by performing spin coating to different speeds until the thickness reaches a value corresponding to a desired $n_{eff,n}$of the rib cladding mode.

A second method (Fig. 6. (b)) currently being investigated would be to perform lithography on the polymer layer, creating polymer waveguides encompassing the core waveguide. (19) This type of structure could also be translated to an electro optical multi-mode coupler, enabling selected coupling of the fundamental mode into a specific higher order mode.

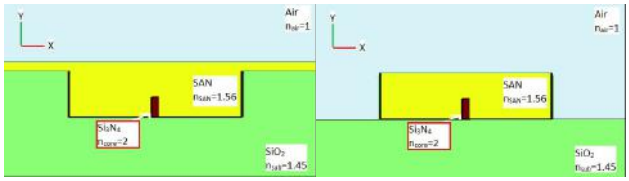

Fig. 6. (a)*Rib cladding structure and* (b)*Strip cladding structure*

VI. CONCLUSION

We have presented a new sensor architecture based on a long period horizontal gratingstructure. We have also proposed to describe the LPWG using the CLMT which provides more insight on the physics of the structure.For example,it indicates that a higher index contrast and therefore higher n_{core} values could increase the coupling, rendering the architecture an interesting candidate for silicon on-chip integration.This approach has been successfully compared to and verified using a standard method based on EME. Moreover,CLMT is more flexible to common grating profile modulations [12,20] as we work on the reconstruction of the coupling coefficient shape along propagation. The calculated overall sensor sensitivity reaches 1768 nm/RIU, and further improvement could increase the sensitivity to over 2000nm/RIU. Based on [21], from the achieved Mach Zehnder sensitivity of 0.768 mrad/ppm, the SAN and Cryptophane layer sensitivity to methane in terms of RIU/ppm canbe estimated to be approximately 6.3 nRIU/ppm. As a result, using a similar sensitive layer with our proposed LPG architecture, an 11 fm/ppm theoretical wavelength sensitivity could be expected.This new type of design appears promising and can benefit from improvements or hybridations, potentiallyinvolving new sensing mechanisms, like plasmonics[18] or photonic crystals[22].

REFERENCES

[1] K.S .Chiang and Q. Liu, “Long-period grating devices for application in optical communication,” 2006.

[2] H. Tsuda and K. Urabe, “Characterization of long-period grating refractive index sensors and their applications, *Sensors* vo.9, 2009

[3] A .M. Vengsarkar, P .J. Lemaire, J.B. Judkins, V. Bhatia, T. Erdogan and J.E. Sipe, “Long-period Fiber gratings as band-rejection filters”, *Journal of Lightwave Technology*, vol. 14, no. 1, pp. 58-65, June, 2007.

[4] J.A. Barnes, R.S. Brown, A.H. Cheung, M.A. Dreher, G. Mackey and H.-P. Loock, “Chemical sensing using a polymer coated long-period fiber grating interrogated by ring-down spectroscopy”, *Sensors and Actuator* B 148, April 2010.

[5] J.A. Barnes, M.A. Dreher, K. Plett, R.S. Brown, C.M Crudden and H.-S. Loock “Chemical sensor based on a long period fibre grating modified by a functionalized polydimethylsiloxane coating”, *The Analyst,* vo. 133, no. 11 pp. 1541-1549, November, 2008

[6] W.B. Ji, S.C. Tjin and C.L Ng,”Highly sensitive refractive index sensor based on adiabatically tapered microfiber long period gratings”, *Sensors* vo.13, 2013

[7] S. W. James, S. Korposh, S.-W. Lee and R.P.Tatam, “A long period grating-based chemical sensor insensitive to the influence of interfering parameters” *Optics express* vol. 22, no.7, April, 2014.

[8] H.C. Tsoi, W. H. Wong and E.Y.B. Pun, “Polymeric long-period waveguide gratings”, *IEEE Photonics technology letters*, vol. 15, no. 5, May, 2003.

[9] S. Pal, A. Chauhan, M. Singh, P. Kumar, M. Sharma, N. Pradhan, K. Singh and C. Dhanavantri, “Realization of long-period corrugated grating in silica-on-silicon based channel Waveguide”, *IEEE photonics Technology Letters*, vol. 21, no. 20, October 2009.

[10] J.M. Estrudillo-Ayala, R.I. Mata-Chavez, J. C. Hernandez-Garcia, R. Rojas-Laguna, *“*Long period fiber grating produced by arc discharges*”*, *Fiber optic sensors*, 2006, pp. 295-313.

[11] Allan W. Snyder and John D. Love, *Optical waveguide theory*. London, New York: Chapman and Hall, 1983

[12] Qingning Li,”Coupled-local-mode theory and study of optical peoperties of a gaussian fiber grating”, *J. Opt. Soc. Am.A*, vol. 16, vo. 6, June 1999.

[13] Long Jin, Wei Jin, Jian Ju, and Yiping Wang, “Coupled local-mode theory for strongly modulated long period gratings”, *Journal of lightwave technology*, vol. 28, no. 12, June, 2010.

[14] D. Zhang, Y. Zhang, Y. Cui, C. Chen, and E.Y.B. Pun, “Long period grating in/on planar and channel waveguides: a theory description”, *Optics & Laser Technology 39* 1204–1213, September, 2006.

[15] F. Dullo, S. Lindecrantz and J. Jagerska, “Sensitive on-chip methane detection with a cryptophane-A cladded Mach-Zehnder interferometer” ,*Optics express* vol. 23, no.24, November, 2015.

[16] Haris Apriyanto. “Study, analysis and experimental validation of fiber refractometers based on single-mode, multimode and photonic crystal fibers for refractive index measurements with application for the detection of methane.”, *Hal archives-ouvertes* March, 2019.

[17] *EME*. [online] Kb.lumerical.com. Available at: https://kb.lumerical.com/solvers_eigenmode_expansion.html

[18] Yue Jing He, “Investigation of LPG-SPR sensors using the finite element method and eigenmode expansion method”, *Optics express* vol. 21 no.12, June 2013.

[19] Martin F. Broglia, Diego F. Acevedo, Denise Langheinrich, Heidi R. Perez-Hernandez, Cesar A. Barbero, and Andrés F. Lasagni, “Rapid Fabrication of Periodic Patterns on Poly(styrene-co-acrylonitrile) Surfaces Using Direct Laser Interference Patterning,” *International Journal of Polymer Science*, vol. 2015, Article ID 721035, 7 pages, 2015.

[20] T. Erdogan, “Cladding-mode resonances in short- and long-period fibers,” *J. Opt. Soc. Am. A*, vol. 14, no. 8, August 1997.

[21] Martin Ingvaldsen “Sensitivity to pressure and methane of a cryptophane-A doped polymer” *semanticscholars*, 2015

[22] P. Steinvurzel, E.D. Moore, E.C. Magi, B.T. Kuhlmey, and B.J. Eggleton, “Long period grating resonances in photonic bandgap fiber”, *Optics express* vol. 14, no.7, April, 2006.

Bibliography

[1] Yole developpement, editor. *Gas and Particle Sensors 2018*. Micronews, 2017. (Cited in pages iv, 19, and 20.)

[2] I.E. Gordon, L.S. Rothman, C. Hill, R.V. Kochanov, Y. Tan, P.F. Bernath, M. Birk, V. Boudon, A. Campargue, K.V. Chance, B.J. Drouin, J.-M. Flaud, R.R. Gamache, J.T. Hodges, D. Jacquemart, V.I. Perevalov, A. Perrin, K.P. Shine, M.-A.H. Smith, J. Tennyson, G.C. Toon, H. Tran, V.G. Tyuterev, A. Barbe, A.G. Császár, V.M. Devi, T. Furtenbacher, J.J. Harrison, J.-M. Hartmann, A. Jolly, T.J. Johnson, T. Karman, I. Kleiner, A.A. Kyuberis, J. Loos, O.M. Lyulin, S.T. Massie, S.N. Mikhailenko, N. Moazzen-Ahmadi, H.S.P. Müller, O.V. Naumenko, A.V. Nikitin, O.L. Polyansky, M. Rey, M. Rotger, S.W. Sharpe, K. Sung, E. Starikova, S.A. Tashkun, J. Vander Auwera, G. Wagner, J. Wilzewski, P. Wcisło, S. Yu, and E.J. Zak. The hitran2016 molecular spectroscopic database. *Journal of Quantitative Spectroscopy and Radiative Transfer*, 203:3–69, 2017. HITRAN2016 Special Issue. (Cited in pages iv and 23.)

[3] Daniel Popa and Florin Udrea. Towards integrated mid-infrared gas sensors. *Sensors*, 19(9), 2019. (Cited in pages iv and 23.)

[4] P. J. Harmsma R. P. Ebeling D. M. R. Lo Cascio et al. M. Hoekman, J. Dingjan. Poster in 'esa round table on micro and nano technologies' (2014). (Cited in pages iv and 24.)

[5] Harmsma P J Ebeling R P Cascio D M R L Leeuwis H Hoekman M Dingjan J and Heideman R G. Towards a space-based on-board photonic calibration stimulus. Poster at ESA Meeting, 2014. (Cited in pages iv, 23, and 24.)

[6] Daniel Mariuta, Stéphane Colin, Christine Barrot-Lattes, Stéphane Le Calvé, Jan G. Korvink, Lucien Baldas, and Jürgen J. Brandner. Miniaturization of fluorescence sensing in optofluidic devices. *Microfluidics and Nanofluidics*, 24(9):65, Aug 2020. (Cited in pages iv and 26.)

[7] Giuseppe Antonacci, Jeroen Goyvaerts, Haolan Zhao, Bettina Baumgartner, Bernhard Lendl, and Roel Baets. Ultra-sensitive refractive index gas sensor with functionalized silicon nitride photonic circuits. *APL Photonics*, 5(8):081301, 2020. (Cited in pages iv and 28.)

[8] Franck Carcenac. Raith150 (n-rait). lims-LAAS-CNRS. (Cited in pages v and 43.)

[9] RAITH nanofabrication. Nanosuite software reference manual. RAITH nanofabrication. (Cited in pages v and 43.)

[10] Alongkorn Pimpin and Werayut Srituravanich. Review on micro- and nanolithography techniques and their applications. *Engineering Journal*, 16:37–56, 01 2012. (Cited in pages v and 43.)

[11] O. Ivanova, Remco Stoffer, L. Kauppinen, and Manfred Hammer. Variational effective index method for 3d vectorial scattering problems in photonics: Te polarization. 01 2009. (Cited in pages vi and 67.)

[12] A .W. Snyder and J. Love. *Optical Waveguide Theory*. Springer, 1 edition. (Cited in pages vi, 16, 17, 71, 72, 73, 74, 76, 77, 78, and 81.)

[13] Catarina Silva, Joao Coelho, Paulo Caldas, and Pedro Jorge. *Fibre Sensing System Based on Long-Period Gratings for Monitoring Aqueous Environments*. 02 2012. (Cited in pages vii and 85.)

[14] Clement Deleau, Han Cheng Seat, Helene Tap, Frederic Surre, and Olivier D. Bernal. Integrated width-modulated sin long period grating designed for refractometric applications. *Journal of Lightwave Technology*, pages 1–1, 2021. (Cited in pages vii, 3, 89, 92, 95, 96, 97, 99, and 101.)

[15] The Intergovernmental Panel on Climate Change, editor. *AR5 Climate Change 2014: Mitigation of Climate Change*. 2014. (Cited in pages viii, 117, and 118.)

[16] Grand View research, editor. *Gas sensor market size by product,technology, ebd use, region and segment Forecasts,2021-2028*. 2021. (Cited in pages viii, 117, and 118.)

[17] Zeqin Lu, Jaspreet Jhoja, Jackson Klein, Xu Wang, Amy Liu, Jonas Flueckiger, James Pond, and Lukas Chrostowski. Performance prediction for silicon photonics integrated circuits with layout-dependent correlated manufacturing variability. *Opt. Express*, 25(9):9712–9733, May 2017. (Cited in pages ix, 107, 115, 139, and 140.)

[18] *Global Sensors in Internet of Things (IoT) Devices Market, Analysis Forecast: 2016 to 2022; (Focus on Pressure, Temperature, Light, Chemical, Motion Sensors; and Applications in Healthcare, Manufacturing, Retail, Transportation)*. BIS research, 2017. (Cited in page 2.)

[19] Intergovernmental Panel on Climate Change. *Climate Change 2013 – The Physical Science Basis: Working Group I Contribution to the Fifth Assessment Report of the Intergovernmental Panel on Climate Change*. Cambridge University Press, 2014. (Cited in page 2.)

[20] Denise Wilson. History of chemical sensing. University of Washington. (Cited in pages 2 and 19.)

[21] Yole developpement, editor. *Gas and Particle Sensors - Technology and Market Trends 2021 report*. 2021. (Cited in page 2.)

[22] Colette McDonagh, Conor S. Burke, and Brian D. MacCraith. Optical chemical sensors. *Chemical Reviews*, 108(2):400–422, 2008. PMID: 18229950. (Cited in pages 2, 6, 11, 12, and 13.)

[23] Lukas Chrostowski and Michael Hochberg. *Silicon Photonics Design: From Devices to Systems*. Cambridge University Press, 2015. (Cited in pages 2, 19, 31, 33, 37, 115, 131, and 140.)

[24] Paddy French, Gijs Krijnen, and Fred Roozeboom. Precision in harsh environments. *Microsystems & Nanoengineering*, 2(1):16048, Oct 2016. (Cited in page 2.)

[25] C. Deleau, H. Seat, H. Tap, F. Surre, and O. Bernal. Integrated silicon nitride horizontal long period grating for refractometric gas sensing applications. In *2020 IEEE International Instrumentation and Measurement Technology Conference (I2MTC)*, pages 1–6, 2020. (Cited in pages 3, 78, 81, 82, 95, and 104.)

[26] Clement Deleau, Han Cheng Seat, Olivier Bernal, and Frederic Surre. High-sensitivity integrated sin rib-waveguide long period grating refractometer. *Photonics Research*, 10(11):02000564, 2 2022. (Cited in pages 3, 89, 92, 95, 103, and 104.)

[27] A. G. Correa-Mena, L. A. González, L. J. Quintero-Rodríguez, and I. E. Zaldivar-Huerta. Review on integrated optical sensors and its applications. In *2017 IEEE Mexican Humanitarian Technology Conference (MHTC)*, pages 170–173, 2017. (Cited in page 6.)

[28] Hummad Qazi, Abu bakar Mohammad, and Muhammad Akram. Recent progress in optical chemical sensors. *Sensors (Basel, Switzerland)*, 12:16522–56, 12 2012. (Cited in pages 6, 11, 12, 13, and 14.)

[29] Paul V Lambeck. Integrated optical sensors for the chemical domain. *Measurement Science and Technology*, 17(8):R93–R116, jun 2006. (Cited in pages 6 and 13.)

[30] Aleksandra Lobnik, Matejka Turel, and Spela Korent Urek. *Optical Chemical Sensors:Design and Applications*. 01 2012. (Cited in pages 6 and 11.)

[31] Vikas Kumar, Nicola Coluccelli, and Dario Polli. Chapter 5 - coherent optical spectroscopy/microscopy and applications. In V.P. Gupta, editor, *Molecular and Laser Spectroscopy*, pages 87–115. Elsevier, 2018. (Cited in page 8.)

[32] Jane Hodgkinson and Ralph P Tatam. Optical gas sensing: a review. *Measurement Science and Technology*, 24(1):012004, nov 2012. (Cited in pages 8, 14, and 15.)

[33] Sulaiman Khan, David Newport, and Stephane Le Calvé. Gas detection using portable deep-uv absorption spectrophotometry: A review. *Sensors*, 19:5210, 11 2019. (Cited in page 8.)

[34] Ann-Kathrin Elger and Christian Hess. Application of raman spectroscopy to working gas sensors: From in situ to operando studies. *Sensors*, 19(23), 2019. (Cited in page 8.)

[35] Otto S Wolfbeis. Chemical sensing using indicator dyes. 1997. (Cited in page 9.)

[36] Ghenadii Korotcenkov. *Handbook of Gas Sensor Materials: Properties, Advantages and Shortcomings for Applications Volume 2: New Trends and Technologies, chapter 15.* 2013. (Cited in pages 9, 11, 12, 20, 21, and 118.)

[37] Joseph R Lakowicz. *Topics in fluorescence spectroscopy: volume 4: probe design and chemical sensing*, volume 4. Springer Science & Business Media, 1994. (Cited in pages 9 and 15.)

[38] Byeong Ha Lee, Young Ho Kim, Kwan Seob Park, Joo Beom Eom, Myoung Jin Kim, Byung Sup Rho, and Hae Young Choi. Interferometric fiber optic sensors. *Sensors*, 12(3):2467–2486, 2012. (Cited in page 10.)

[39] Manjusha Ramakrishnan, Ginu Rajan, Yuliya Semenova, and Gerald Farrell. Overview of fiber optic sensor technologies for strain/temperature sensing applications in composite materials. *Sensors (Basel, Switzerland)*, 16(1):99, Jan 2016. 26784192[pmid]. (Cited in pages 10 and 52.)

[40] Lars Rindorf and Ole Bang. Sensitivity of photonic crystal fiber grating sensors: Biosensing, refractive index, strain, and temperature sensing. *Journal of the Optical Society of America B*, 25, 08 2007. (Cited in pages 10 and 84.)

[41] Volker Nock, R.J. Blaikie, and Tim David. Micro-patterning of polymer-based optical oxygen sensors for lab-on-chip applications. volume 6799, 12 2007. (Cited in pages 11 and 27.)

[42] Rainer Klein and Edgar I. Voges. Integrated optic ammonia sensor. In Joseph R. Lakowicz and Richard B. Thompson, editors, *Advances in Fluorescence Sensing Technology*, volume 1885, pages 81 – 92. International Society for Optics and Photonics, SPIE, 1993. (Cited in pages 11, 25, and 27.)

[43] Ghenadii Korotcenkov. *Handbook of Gas Sensor Materials: Properties, Advantages and Shortcomings for Applications Volume 2: New Trends and Technologies, chapter 9.* 2013. (Cited in pages 12, 20, and 21.)

[44] Benedetto Troia, Francesco De Leonardis, and Vittorio M.N. Passaro. Cascaded ring resonator and mach-zehnder interferometer with a sagnac loop for vernier-effect refractive index sensing. *Sensors and Actuators B: Chemical*, 240:76–89, 2017. (Cited in pages 13 and 15.)

[45] Abderrahmen Trichili, Mitchell A. Cox, Boon S. Ooi, and Mohamed-Slim Alouini. Roadmap to free space optics. *J. Opt. Soc. Am. B*, 37(11):A184–A201, Nov 2020. (Cited in pages 13 and 16.)

[46] Min Wei, RuiFeng Kan, Bing Chen, ZhenYu Xu, ChenGuang Yang, Xiang Chen, HuiHui Xia, Mai Hu, Yabai He, JianGuo Liu, et al. Calibration-free wavelength modulation spectroscopy for gas concentration measurements using a quantum cascade laser. *Applied Physics B*, 123(5):149, 2017. (Cited in page 15.)

[47] Pietro Patimisco, Gaetano Scamarcio, Frank K Tittel, and Vincenzo Spagnolo. Quartz-enhanced photoacoustic spectroscopy: a review. *Sensors*, 14(4):6165–6206, 2014. (Cited in page 15.)

[48] Austin Griffith, Ryan Lau, Jaime Cardenas, Yoshitomo Okawachi, Aseema Mohanty, Romy Fain, Yoon Lee, Mengjie Yu, Christopher Phare, Carl Poitras, Alexander Gaeta, and Michal Lipson. Silicon-chip mid-infrared frequency comb generation. *Nature communications*, 6, 08 2014. (Cited in page 15.)

[49] T. H. MAIMAN. Stimulated optical radiation in ruby. *Nature*, 187(4736):493–494, Aug 1960. (Cited in page 16.)

[50] Mario F S Ferreira, Enrique Castro-Camus, David J Ottaway, José Miguel López-Higuera, Xian Feng, Wei Jin, Yoonchan Jeong, Nathalie Picqué, Limin Tong, Björn M Reinhard, Paul M Pellegrino, Alexis Méndez, Max Diem, Frank Vollmer, and Qimin Quan. Roadmap on optical sensors. *Journal of Optics*, 19(8):083001, jul 2017. (Cited in pages 16 and 17.)

[51] Serge Valette, editor. *Integrated Optics: The history and the future*. Ecio-Conference. (Cited in pages 16, 17, 18, and 19.)

[52] Dietrich Marcuse, editor. Academic Press, first edition edition, 1974. (Cited in page 16.)

[53] Christopher Doerr. Silicon photonic integration in telecommunications. *Frontiers in Physics*, 3:37, 2015. (Cited in pages 17 and 18.)

[54] Eli Yablonovitch. Inhibited spontaneous emission in solid-state physics and electronics. *Phys. Rev. Lett.*, 58:2059–2062, May 1987. (Cited in page 17.)

[55] D. G. Dalgoutte and C. D. W. Wilkinson. Thin grating couplers for integrated optics: an experimental and theoretical study. *Appl. Opt.*, 14(12):2983–2998, Dec 1975. (Cited in page 17.)

[56] P. Del'Haye, A. Schliesser, O. Arcizet, T. Wilken, R. Holzwarth, and T. J. Kippenberg. Optical frequency comb generation from a monolithic microresonator. *Nature*, 450(7173):1214–1217, Dec 2007. (Cited in page 17.)

[57] Allan W. Snyder. Coupled-mode theory for optical fibers. *J. Opt. Soc. Am.*, 62(11):1267–1277, Nov 1972. (Cited in pages 17, 71, 72, and 73.)

[58] Lars Thylen. A moores law for photonics. In *2006 International Symposium on Biophotonics, Nanophotonics and Metamaterials*, pages 256–263, 2006. (Cited in page 18.)

[59] Andreas Hänsel and Martijn J R Heck. Opportunities for photonic integrated circuits in optical gas sensors. *Journal of Physics: Photonics*, 2(1):012002, jan 2020. (Cited in pages 18 and 23.)

[60] Junqiu Liu, Guanhao Huang, Rui Ning Wang, Jijun He, Arslan S. Raja, Tianyi Liu, Nils J. Engelsen, and Tobias J. Kippenberg. High-yield, wafer-scale fabrication of ultralow-loss, dispersion-engineered silicon nitride photonic circuits. *Nature Communications*, 12(1):2236, Apr 2021. (Cited in pages 19 and 51.)

[61] Shaobin Feng, Fadi Farha, Qingjuan Li, Yueliang Wan, Yang Xu, Tao Zhang, and Huansheng Ning. Review on smart gas sensing technology. *Sensors (Basel, Switzerland)*, 19(17):3760, Aug 2019. 31480359[pmid]. (Cited in page 19.)

[62] Ghenadii Korotcenkov. *Handbook of Gas Sensor Materials: Properties, Advantages and Shortcomings for Applications Volume 2: New Trends and Technologies, chapter 12*. 2013. (Cited in pages 19 and 20.)

[63] Ayushi Paliwal, Anjali Sharma, Monika Tomar, and Vinay Gupta. Carbon monoxide (co) optical gas sensor based on zno thin films. *Sensors and Actuators B: Chemical*, 250:679–685, 2017. (Cited in pages 20, 22, and 63.)

[64] Arne Schleunitz, H. Steffes, R. Chabicovsky, and E. Obermeier. Optical gas sensitivity of a metaloxide multilayer system with gold-nano-clusters. *Sensors and Actuators B-chemical - SENSOR ACTUATOR B-CHEM*, 127:210–216, 10 2007. (Cited in pages 20 and 22.)

[65] V.M. Aroutiounian. 12 - porous silicon gas sensors. In Raivo Jaaniso and Ooi Kiang Tan, editors, *Semiconductor Gas Sensors*, Woodhead Publishing Series in Electronic and Optical Materials, pages 408–430. Woodhead Publishing, 2013. (Cited in page 20.)

[66] Firehun Tsige Dullo, Susan Lindecrantz, Jana Jágerská, Jørn H. Hansen, Magnus Engqvist, Stian Andre Solbø, and Olav Gaute Hellesø. Sensitive on-chip methane detection with a cryptophane-a cladded mach-zehnder interferometer. *Opt. Express*, 23(24):31564–31573, Nov 2015. (Cited in pages 20, 22, 63, 90, 96, and 119.)

[67] V.C. Gonçalves and D.T. Balogh. Optical vocs detection using poly(3-alkylthiophenes) with different side-chain lengths. *Sensors and Actuators B: Chemical*, 142(1):55–60, 2009. (Cited in pages 20 and 22.)

[68] Shilpa Kulkarni and Sujata Patrikar. Detection of propane gas adsorbed in a nanometer layer on silica nanowire. *Optik*, 127(1):465–470, 2016. (Cited in pages 20 and 22.)

[69] Shawana Tabassum, Ratnesh Kumar, and Liang Dong. Plasmonic crystal-based gas sensor toward an optical nose design. *IEEE Sensors Journal*, 17(19):6210–6223, 2017. (Cited in pages 20, 22, 28, 29, 63, and 64.)

[70] Nestor Bareza Jr., Kavitha K. Gopalan, Rose Alani, Bruno Paulillo, and Valerio Pruneri. Mid-infrared gas sensing using graphene plasmons tuned by reversible chemical doping. *ACS Photonics*, 7(4):879–884, Apr 2020. (Cited in pages 20 and 22.)

[71] Sandeep Kalathimekkad, Jeroen Missinne, Juan Espinoza, Bram Van Hoe, Erwin Bosman, Edsger Smits, Rajesh Mandamparambil, Geert Van Steenberge, and Jan Vanfleteren. *Fluorescence-based optochemical sensor on flexible foils*, volume 8439. 04 2012. (Cited in pages 20, 22, 25, and 27.)

[72] Jack Barnes, Marian Dreher, Krista Plett, R. Stephen Brown, Cathleen M. Crudden, and Hans-Peter Loock. Chemical sensor based on a long-period fibre grating modified by a functionalized polydimethylsiloxane coating. *Analyst*, 133:1541–1549, 2008. (Cited in pages 20, 22, 28, and 29.)

[73] Civan Avci. *Zeolitic Imidazolate Framework-8: Control of Particle Size and Shape and its Self-Assembly.* PhD thesis, Universitat de Barcelona, 2019. (Cited in pages 20, 22, 28, and 29.)

[74] Ghenadii Korotcenkov. *Handbook of Gas Sensor Materials: Properties, Advantages and Shortcomings for Applications Volume 2: New Trends and Technologies, chapter 24.* 2013. (Cited in pages 21 and 118.)

[75] S. A. Stern and Joel R. Fried. *Permeability of Polymers to Gases and Vapors*, pages 1033–1047. Springer New York, New York, NY, 2007. (Cited in page 21.)

[76] Martin Ingvaldsen. Sensitivity to pressure and methane of a cryptophane-a doped polymer, 2015. (Cited in pages 21 and 27.)

[77] Brian P. Santora, Michel R. Gagné, Kenneth G. Moloy, and Nora S. Radu. Porogen and cross-linking effects on the surface area, pore volume distribution, and morphology of macroporous polymers obtained by bulk polymerization. *Macromolecules*, 34(3):658–661, Jan 2001. (Cited in pages 21 and 118.)

[78] Jeongsu Kim, Haneul Yoo, Viet Anh Pham Ba, Narae Shin, and Seunghun Hong. Dye-functionalized sol-gel matrix on carbon nanotubes for refreshable and flexible gas sensors. *Scientific Reports*, 8(1):11958, Aug 2018. (Cited in page 22.)

[79] A.K Hassan, A.V Nabok, A.K Ray, A Lucke, K Smith, C.J.M Stirling, and F Davis. Thin films of calix-4-resorcinarene deposited by spin coating and langmuir–blodgett techniques: determination of film parameters by surface plasmon resonance. *Materials Science and Engineering: C*, 8-9:251–255, 1999. (Cited in pages 22, 62, and 63.)

[80] Md. Rajibur Rahaman Khan, Byoung-Ho Kang, Se-Hyuk Yeom, Dae-Hyuk Kwon, and Shin-Won Kang. Fiber-optic pulse width modulation sensor for low concentration voc gas. *Sensors and Actuators B: Chemical*, 188:689–696, 2013. (Cited in page 22.)

[81] Daniel Pergande, Torsten M. Geppert, Andreas von Rhein, Stefan L. Schweizer, Ralf B. Wehrspohn, Susanne Moretton, and Armin Lambrecht. Miniature infrared gas sensors using photonic crystals. *Journal of Applied Physics*, 109(8):083117, 2011. (Cited in page 22.)

[82] Dongliang Fu, Jaehoon Chung, Qing Liu, Riazul Raziq, Jack Kee, Mi Park, Suresh Valiyaveettil, and Pyng Lee. Polymer coated silicon microring device for the detection of sub-ppm volatile organic compounds. *Sensors and Actuators B: Chemical*, 257, 10 2017. (Cited in page 22.)

[83] Todd H. Stievater, Marcel W. Pruessner, Doewon Park, William S. Rabinovich, R. Andrew McGill, Dmitry A. Kozak, Robert Furstenberg, Scott A. Holmstrom, and Jacob B. Khurgin. Trace gas absorption spectroscopy using functionalized microring resonators. *Opt. Lett.*, 39(4):969–972, Feb 2014. (Cited in pages 22, 24, and 25.)

[84] M. A. Butt, S. A. Degtyarev, S. N. Khonina, and N. L. Kazanskiy. An evanescent field absorption gas sensor at mid-ir 3.39 µm wavelength. *Journal of Modern Optics*, 64(18):1892–1897, 2017. (Cited in pages 23 and 25.)

[85] N. Pelin Ayerden, Julien Mandon, Frans J. M. Harren, and Reinoud F. Wolffenbuttel. Functionalizing a tapered microcavity as a gas cell for on-chip mid-infrared absorption spectroscopy. *Sensors*, 17(9), 2017. (Cited in pages 24 and 25.)

[86] Yuhua Chang, Dihan Hasan, Bowei Dong, Jingxuan Wei, Yiming Ma, Guangya Zhou, Kah Wee Ang, and Chengkuo Lee. Surface-enhanced infrared absorption-based co2 sensor using photonic crystal slab. In *2019 IEEE 32nd International Conference on Micro Electro Mechanical Systems (MEMS)*, pages 141–144, 2019. (Cited in pages 24 and 25.)

[87] A. Glière, P. Barritault, A. Berthelot, C. Constancias, J.-G. Coutard, B. Desloges, L. Duraffourg, J.-M. Fedeli, M. Garcia, O. Lartigue, H. Lhermet, A. Marchant, J. Rouxel, J. Skubich, A. Teulle, T. Verdot, and S. Nicoletti. Downsizing and silicon integration of photoacoustic gas cells. *International Journal of Thermophysics*, 41(2):16, Jan 2020. (Cited in page 24.)

[88] M. A. Butt, S. N. Khonina, and N. L. Kazanskiy. Silicon on silicon dioxide slot waveguide evanescent field gas absorption sensor. *Journal of Modern Optics*, 65(2):174–178, 2018. (Cited in page 25.)

[89] Babita Kumari, Ajanta Barh, R.K. Varshney, and B.P. Pal. Silicon-on-nitride slot waveguide: A promising platform as mid-ir trace gas sensor. *Sensors and Actuators B: Chemical*, 236:759–764, 2016. (Cited in page 25.)

[90] Mohamed Y. Elsayed, Yehea Ismail, and Mohamed A. Swillam. Semiconductor plasmonic gas sensor using on-chip infrared spectroscopy. *Applied Physics A*, 123(1):113, Jan 2017. (Cited in page 25.)

[91] Christian Ranacher, Cristina Consani, Andreas Tortschanoff, Reyhaneh Jannesari, Markus Bergmeister, Thomas Grille, and Bernhard Jakoby. Mid-infrared absorption gas sensing using a silicon strip waveguide. *Sensors and Actuators A: Physical*, 277:117–123, 2018. (Cited in page 25.)

[92] C. Consani, C. Ranacher, A. Tortschanoff, T. Grille, P. Irsigler, and B. Jakoby. Mid-infrared photonic gas sensing using a silicon waveguide and an integrated emitter. *Sensors and Actuators B: Chemical*, 274:60–65, 2018. (Cited in page 25.)

[93] Aldo Gutierrez-Arroyo, Emeline Baudet, Bodiou, Jonathan Lemaitre, Isabelle Hardy, François Faijan, Bruno Bureau, Virginie Nazabal, and Jol Charrier. Optical characterization at 7.7 um of an integrated platform based on chalcogenide waveguides for sensing applications in the mid-infrared. *Opt. Express*, 24(20):23109–23117, Oct 2016. (Cited in page 25.)

[94] L. Tombez, E. J. Zhang, J. S. Orcutt, S. Kamlapurkar, and W. M. J. Green. Methane absorption spectroscopy on a silicon photonic chip. *Optica*, 4(11):1322–1325, Nov 2017. (Cited in page 25.)

[95] P. Su, Z. Han, D. Kita, P. Becla, H. Lin, S. Deckoff-Jones, K. Richardson, L. C. Kimerling, J. Hu, and A. Agarwal. Monolithic on-chip mid-ir methane gas sensor with waveguide-integrated detector. *Applied Physics Letters*, 114(5):051103, 2019. (Cited in page 25.)

[96] Natnicha Koompai, Pichet Limsuwan, Xavier Le Roux, Laurent Vivien, Delphine Marris-Morini, and Papichaya Chaisakul. Analysis of si3n4 waveguides for on-chip gas sensing by optical absorption within the mid-infrared region between 2.7 and 3.4 μm. *Results in Physics*, 16:102957, 2020. (Cited in page 25.)

[97] Kevin S. Lee, Harry L. T. Lee, and Rajeev J. Ram. Polymer waveguide backplanes for optical sensor interfaces in microfluidics. *Lab Chip*, 7:1539–1545, 2007. (Cited in pages 25, 26, and 27.)

[98] Conor S. Burke, Orla McGaughey, Jean-Marc Sabattié, Henry Barry, Aisling K. McEvoy, Colette McDonagh, and Brian D. MacCraith. Development of an integrated optic oxygen sensor using a novel, generic platform. *Analyst*, 130:41–45, 2005. (Cited in pages 25, 26, and 27.)

[99] Bernhard Lamprecht, Elke Kraker, Martin Sagmeister, Stefan Köstler, Nicole Galler, Harald Ditlbacher, Birgit Ungerböck, Tobias Abel, and Torsten Mayr. Integrated waveguide sensor utilizing organic photodiodes. *physica status solidi (RRL) - Rapid Research Letters*, 5:344–346, 09 2011. (Cited in pages 25, 26, and 27.)

[100] V. Savvate'ev, Z. Chen-Esterlit, J. Aylott, B. Choudhury, C. Kim, L. Zou, J. Friedl, Ruth Shinar, Joseph Shinar, and Raoul Kopelman. Integrated organic light-emitting device/fluorescence-based chemical sensors. *Appl. Phys. Lett.*, 81, 12 2002. (Cited in pages 25, 26, and 27.)

[101] Aitor Urrutia, Ignacio Del Villar, Pablo Zubiate, and Carlos Zamarreño. A comprehensive review of optical fiber refractometers: Toward a standard comparative criterion. *Laser & Photonics Reviews*, 13, 10 2019. (Cited in pages 27 and 52.)

[102] Helge Kragh. The lorenz-lorentz formula: Origin and early history. *Substantia*, 2(2):7–18, 2018. (Cited in page 27.)

[103] Enxiao Luan, Hossam Shoman, Daniel M. Ratner, Karen C. Cheung, and Lukas Chrostowski. Silicon photonic biosensors using label-free detection. *Sensors*, 18(10), 2018. (Cited in pages 27 and 28.)

[104] Kurt E Oughstun and Natalie A Cartwright. On the lorentz-lorenz formula and the lorentz model of dielectric dispersion: addendum. *Optics express*, 11(21):2791–2792, 2003. (Cited in page 27.)

[105] Guangcan Mi, Cameron Horvath, Mirwais Aktary, and Vien Van. Silicon microring refractometric sensor for atmospheric co2 gas monitoring. *Opt. Express*, 24(2):1773–1780, Jan 2016. (Cited in pages 28, 29, 96, 119, and 124.)

[106] Dominic J. Wales, Richard M. Parker, Priscilla Quainoo, Peter A. Cooper, James C. Gates, Martin C. Grossel, and Peter G.R. Smith. An integrated optical bragg grating refractometer for volatile organic compound detection. *Sensors and Actuators B: Chemical*, 232:595–604, 2016. (Cited in pages 28 and 29.)

[107] Shon Schmidt. *Enhancing the performance of silicon photonic biosensors for clinical applications*. PhD thesis, University of Washington, 2016. (Cited in pages 31 and 47.)

[108] Fiber optical communication band. https://www.fiberlabs.com/glossary/about-optical-communication-band/. (Cited in page 32.)

[109] Roel Baets, Ananth Z. Subramanian, Stéphane Clemmen, Bart Kuyken, Peter Bienstman, Nicolas Le Thomas, Günther Roelkens, Dries Van Thourhout, Philippe Helin, and Simone Severi. Silicon photonics: Silicon nitride versus silicon-on-insulator. In *2016 Optical Fiber Communications Conference and Exhibition (OFC)*, pages 1–3, 2016. (Cited in page 32.)

[110] R Takei, M Suzuki, E Omoda, S Manako, T Kamei, M Mori, and Y Sakakibara. Silicon knife-edge taper waveguide for ultralow-loss spot-size converter fabricated by photolithography. *Applied Physics Letters*, 102(10):101108, 2013. (Cited in page 33.)

[111] Jaime Cardenas, Carl B. Poitras, Kevin Luke, Lian-Wee Luo, Paul Adrian Morton, and Michal Lipson. High coupling efficiency etched facet tapers in silicon waveguides. *IEEE Photonics Technology Letters*, 26(23):2380–2382, 2014. (Cited in page 33.)

[112] Angelo Bozzola, Lee Carroll, Dario Gerace, Ilaria Cristiani, and Lucio Claudio Andreani. Optimising apodized grating couplers in a pure soi platform to-0.5 db coupling efficiency. *Optics express*, 23(12):16289–16304, 2015. (Cited in pages 33 and 36.)

[113] Yun Wang. *Grating coupler design based on silicon-on-insulator*. PhD thesis, University of British Columbia, 2013. (Cited in pages 33, 36, and 66.)

[114] P. Bienstman, E. Six, A. Roelens, M. Vanwolleghem, and R. Baets. Calculation of bending losses in dielectric waveguides using eigenmode expansion and perfectly matched layers. *IEEE Photonics Technology Letters*, 14(2):164–166, 2002. (Cited in page 34.)

[115] M. Heiblum and J. Harris. Analysis of curved optical waveguides by conformal transformation. *IEEE Journal of Quantum Electronics*, 11(2):75–83, 1975. (Cited in page 34.)

[116] Thomas YL Ang, Jun Rong Ong, Soon Thor Lim, Ching Eng Png, X Guo, and Hong Wang. Versatile bezier bends for silicon photonics. In *Conference on Lasers and Electro-Optics/Pacific Rim*, page s1869. Optical Society of America, 2017. (Cited in page 35.)

[117] C.M. Bruinink, Matteo Burresi, M. Burresi, Meint J. de Boer, Franciscus B. Segerink, Henricus V. Jansen, Johan W. Berenschot, David Reinhoudt, Jurriaan Huskens, and L. Kuipers. Nanoimprint lithography for nanophotonics in silicon. *Nano letters*, 8(9):2872–2877, August 2008. http://dx.doi.org/10.1021/nl801615c. (Cited in page 40.)

[118] Linghua Wang, Weiqiang Xie, Dries Van Thourhout, Yazhen Zhang, Hui Yu, and Shaohao Wang. Nonlinear silicon nitride waveguides based on a pecvd deposition platform. *Opt. Express*, 26(8):9645–9654, Apr 2018. (Cited in pages 41 and 51.)

[119] Khawaja Nizammuddin Subhani, Nayana Remesh, Niranjan S, Srinivasan Raghavan, Muralidharan R, Digbijoy N. Nath, and K.N. Bhat. Nitrogen rich pecvd silicon nitride for passivation of si and algan/gan hemt devices. *Solid-State Electronics*, 186:108188, 2021. (Cited in page 41.)

[120] H. Rose and W. Wan. Aberration correction in electron microscopy. In *Proceedings of the 2005 Particle Accelerator Conference*, pages 44–48, 2005. (Cited in page 42.)

[121] Ziyang Zhang. *Silicon-based photonic devices: Design, fabrication and characterization*. PhD thesis, KTH, 2008. (Cited in page 43.)

[122] Yuewang Huang, Qiancheng Zhao, Lobna Kamyab, Ali Rostami, Filippo Capolino, and Ozdal Boyraz. Sub-micron silicon nitride waveguide fabrication using conventional optical lithography. *Opt. Express*, 23(5):6780–6786, Mar 2015. (Cited in page 51.)

[123] Martin H. P. Pfeiffer, Junqiu Liu, Arslan S. Raja, Tiago Morais, Bahareh Ghadiani, and Tobias J. Kippenberg. Ultra-smooth silicon nitride waveguides based on the damascene reflow process: fabrication and loss origins. *Optica*, 5(7):884–892, Jul 2018. (Cited in page 51.)

[124] Cheng Li, Gang Bai, Yunxiao Zhang, Min Zhang, and Aoqun Jian. Optofluidics refractometers. *Micromachines*, 9(3):136, Mar 2018. 30424070[pmid]. (Cited in page 52.)

[125] K. Tiefenthaler and W. Lukosz. Sensitivity of grating couplers as integrated-optical chemical sensors. *J. Opt. Soc. Am. B*, 6(2):209–220, Feb 1989. (Cited in page 53.)

[126] G.J. Veldhuis, O. Parriaux, H.J.W.M. Hoekstra, and P.V. Lambeck. Sensitivity enhancement in evanescent optical waveguide sensors. *Journal of Lightwave Technology*, 18(5):677–682, 2000. (Cited in pages 53 and 144.)

[127] David Large and James Farmer. Chapter 4 - linear fiber-optic signal transportation. In David Large and James Farmer, editors, *Broadband Cable Access Networks*, The Morgan Kaufmann Series in Networking, pages 81–126. Morgan Kaufmann, Boston, 2009. (Cited in page 54.)

[128] Rajiv Ramaswami, Kumar N. Sivarajan, and Galen H. Sasaki. chapter 2 - propagation of signals in optical fiber. In Rajiv Ramaswami, Kumar N. Sivarajan, and Galen H. Sasaki, editors, *Optical Networks (Third Edition)*, pages 47–112. Morgan Kaufmann, Boston, third edition edition, 2010. (Cited in page 54.)

[129] E. A. J. Marcatili. Modal dispersion in optical fibers with arbitrary numerical aperture and profile dispersion. *The Bell System Technical Journal*, 56(1):49–63, 1977. (Cited in page 54.)

[130] Zuoqin Ding and Yaocheng Shi. Demonstration of an ultra-sensitive temperature sensor using an asymmetric mach-zehnder interferometer. *IEEE Photonics Journal*, 13(4):1–5, 2021. (Cited in page 56.)

[131] Zahra Khajemiri, Dukhyung Lee, Seyedeh Mehri Hamidi, and Dai-Sik Kim. Rectangular plasmonic interferometer for high sensitive glycerol sensor. *Scientific Reports*, 9(1):1378, Feb 2019. (Cited in page 58.)

[132] Athanasios Manolis, Evangelia Chatzianagnostou, George Dabos, Dimitra Ketzaki, Dimitris Tsiokos, Bartos Chmielak, Stephan Suckow, Anna L. Giesecke, Caroline Porschatis, Piotr J. Cegielski, Laurent Markey, Jean-C. Weeber, Alain Dereux, and Nikos Pleros. Bringing plasmonics into cmos photonic foundries: Aluminum plasmonics on si for biosensing applications. *J. Lightwave Technol.*, 37(21):5516–5524, Nov 2019. (Cited in pages 58 and 63.)

[133] Yuxin Liang, Mingshan Zhao, Zhenlin Wu, and Geert Morthier. Bimodal waveguide interferometer ri sensor fabricated on low-cost polymer platform. *IEEE Photonics Journal*, 11(2):1–8, 2019. (Cited in page 58.)

[134] Kun Qin, Shuren Hu, Scott T. Retterer, Ivan I. Kravchenko, and Sharon M. Weiss. Slow light mach–zehnder interferometer as label-free biosensor with scalable sensitivity. *Opt. Lett.*, 41(4):753–756, Feb 2016. (Cited in page 58.)

[135] G. Zhang, H. Cai, Y. D. Gu, J. F. Song, B. Dong, Z. C. Yang, Y. F. Jin, Y. L. Hao, S. P. Sivalingam, P. H. Yap, D. L. Kwong, and A. Q. Liu. High sensitivity and large measurement range refractometric sensing based on mach-zehnder interferometer. In *2016 IEEE 29th International Conference on Micro Electro Mechanical Systems (MEMS)*, pages 298–301, 2016. (Cited in page 58.)

[136] Xiaowei Guan and Lars H. Frandsen. All-silicon interferometer with multimode waveguides for temperature-insensitive filters and compact biosensors. *Opt. Express*, 27(2):753–760, Jan 2019. (Cited in page 58.)

[137] Utku G. Yasa, Ibrahim H. Giden, and Hamza Kurt. Optical modulators and biochemical sensors based on low-symmetric nanophotonic structures with interferometric configurations. In Ali Adibi, Shawn-Yu Lin, and Axel Scherer, editors, *Photonic and Phononic Properties of Engineered Nanostructures VIII*, volume 10541, pages 100 – 107. International Society for Optics and Photonics, SPIE, 2018. (Cited in page 58.)

[138] Owen A. Marsh, Yule Xiong, and Winnie N. Ye. Slot waveguide ring-assisted mach–zehnder interferometer for sensing applications. *IEEE Journal of Selected Topics in Quantum Electronics*, 23(2):440–443, 2017. (Cited in page 58.)

[139] A. Manolis, E. Chatzianagnostou, G. Dabos, N. Pleros, B. Chmielak, A. L. Giesecke, C. Porschatis, P. J. Cegielski, L. Markey, J.-C. Weeber, A. Dereux, and D. Tsiokos. Plasmonics co-integrated with silicon nitride photonics for

high-sensitivity interferometric biosensing. *Opt. Express*, 27(12):17102–17111, Jun 2019. (Cited in page 58.)

[140] L. Torrijos-Morán, A. Griol, and J. García-Rupérez. Experimental study of subwavelength grating bimodal waveguides as ultrasensitive interferometric sensors. *Opt. Lett.*, 44(19):4702–4705, Oct 2019. (Cited in page 58.)

[141] Owen Marsh, Yule Xiong, and Winnie N. Ye. Soi sensor based on mmi-coupled ring-assisted mach zehnder interferometer (ramzi). In *2016 IEEE SENSORS*, pages 1–3, 2016. (Cited in page 58.)

[142] Daiying Zhang, Liqiu Men, and Qiying Chen. Femtosecond laser microfabricated optofluidic mach–zehnder interferometer for refractive index sensing. *IEEE Journal of Quantum Electronics*, 54(6):1–7, 2018. (Cited in page 58.)

[143] Mohamed M. El-Rayany, Raghi S. El Shamy, and Mohamed A. Swillam. A compact silicon-on-insulator gas sensor. In Graham T. Reed and Andrew P. Knights, editors, *Silicon Photonics XIV*, volume 10923, pages 189 – 196. International Society for Optics and Photonics, SPIE, 2019. (Cited in page 58.)

[144] E. Chatzianagnostou, G. Dabos, A. Manolis, L. Markey, J.-C. Weeber, A. Dereux, D. Tsiokos, and N. Pleros. Ultra-compact single-arm interferometric plasmonic sensor co-integrated on a TiO2 photonic waveguide platform. In Sonia M. García-Blanco and Pavel Cheben, editors, *Integrated Optics: Devices, Materials, and Technologies XXIII*, volume 10921, pages 189 – 194. International Society for Optics and Photonics, SPIE, 2019. (Cited in page 58.)

[145] Mohamed Y. Elsayed, Aya O. Zaki, Yehea Ismail, and Mohamed A. Swillam. Integrated lab-on-a-chip sensor using shallow silicon waveguide multimode interference (MMI) device. In Sonia M. García-Blanco and Gualtiero Nunzi Conti, editors, *Integrated Optics: Devices, Materials, and Technologies XXI*, volume 10106, pages 185 – 190. International Society for Optics and Photonics, SPIE, 2017. (Cited in page 58.)

[146] Fangcao Peng, Zhuoran Wang, Guohui Yuan, Lei Guan, and Zhenming Peng. High-sensitivity refractive index sensing based on fano resonances in a photonic crystal cavity-coupled microring resonator. *IEEE Photonics Journal*, 10(2):1–8, 2018. (Cited in pages 59 and 61.)

[147] Michele Calvo, Guillaume Beaudin, Laurence Mercier-Coderre, Pauline Girault, Pedro Rojo-Romeo, Regis Orobtchouk, Romain Stricher, Stephane Monfray, Serge Ecoffey, Dominique Drouin, Frederic Boeuf, Michael Canva, and Paul G. Charette. Improving silicon nitride ring resonator performances on 300 mm industrial environment for point of care applications (Conference Presentation). In Michael T. Canva, Ambra Giannetti, Hatice Altug, and

Julien Moreau, editors, *Biophotonics in Point-of-Care*, volume 11361. International Society for Optics and Photonics, SPIE, 2020. (Cited in pages 59 and 61.)

[148] M. A. Butt, S. N. Khonina, and N. L. Kazanskiy. Hybrid plasmonic waveguide-assisted metal–insulator–metal ring resonator for refractive index sensing. *Journal of Modern Optics*, 65(9):1135–1140, 2018. (Cited in pages 59, 61, and 63.)

[149] M. A. Butt, S. N. Khonina, and N. L. Kazanskiy. Metal-insulator-metal nano square ring resonator for gas sensing applications. *Waves in Random and Complex Media*, 31(1):146–156, 2021. (Cited in pages 59 and 61.)

[150] Yongheng Yue, Huihui Zhu, Ziwei Cao, Jianjun He, and Mingyu Li. Wide-range optical sensors based on a single ring resonator with polarization multiplexing. *Chin. Opt. Lett.*, 17(3):031301, Mar 2019. (Cited in pages 59 and 61.)

[151] Long Tu, Liang Huang, and Wenhui Wang. A novel micromachined fabry-perot interferometer integrating nano-holes and dielectrophoresis for enhanced biochemical sensing. *Biosensors and Bioelectronics*, 127:19–24, 2019. (Cited in pages 59 and 61.)

[152] João M. Maia, Vítor A. Amorim, Duarte Viveiros, and P. V. S. Marques. Femtosecond laser micromachining of Fabry-Pérot interferometers in fused silica for refractive index sensing. In Manuel Filipe P. C. M. Martins Costa, editor, *Fourth International Conference on Applications of Optics and Photonics*, volume 11207, pages 229 – 234. International Society for Optics and Photonics, SPIE, 2019. (Cited in pages 59 and 61.)

[153] Wenqin Mo, Huiyun Liu, Fang Jin, Junlei Song, and Kaifeng Dong. Theoretical analysis of a microring resonator array with high sensitivity and large dynamic range based on a multi-scale technique. *Sensors (Basel, Switzerland)*, 18(7):1987, Jun 2018. 29933604[pmid]. (Cited in page 59.)

[154] Xuefeng Jiang, Abraham Qavi, Steven Huang, and Lan Yang. Whispering gallery microsensors: a review. 04 2018. (Cited in page 59.)

[155] Xi Wu, Tianren Fan, Ali A. Eftekhar, Amir H. Hosseinnia, and Ali Adibi. High-q spiral-based coupled-resonator device on a si3n4 platform for ultra-sensitive sensing applications. *OSA Continuum*, 3(12):3390–3398, Dec 2020. (Cited in page 59.)

[156] A. Tavousi, M.R. Rakhshani, and M.A. Mansouri-Birjandi. High sensitivity label-free refractometer based biosensor applicable to glycated hemoglobin detection in human blood using all-circular photonic crystal ring resonators. *Optics Communications*, 429:166–174, 2018. (Cited in page 61.)

[157] M.A. Butt, S.N. Khonina, and N.L. Kazanskiy. An array of nano-dots loaded mim square ring resonator with enhanced sensitivity at nir wavelength range. *Optik*, 202:163655, 2020. (Cited in page 61.)

[158] Sujith Chandran, Ramesh K. Gupta, and Bijoy Krishna Das. Dispersion enhanced critically coupled ring resonator for wide range refractive index sensing. *IEEE Journal of Selected Topics in Quantum Electronics*, 23(2):424–432, 2017. (Cited in page 61.)

[159] N. Ashok, Yeung Lak Lee, and WooJin Shin. Geasse chalcogenide slot optical waveguide ring resonator for refractive index sensing. In *2017 25th Optical Fiber Sensors Conference (OFS)*, pages 1–4, 2017. (Cited in page 61.)

[160] Liaquat Ali, Mahmood Uddin Mohammed, Mahrukh Khan, Abdul Hamid Bin Yousuf, and Masud H. Chowdhury. High-quality optical ring resonator-based biosensor for cancer detection. *IEEE Sensors Journal*, 20(4):1867–1875, 2020. (Cited in page 61.)

[161] Jonas Flueckiger, Shon Schmidt, Valentina Donzella, Ahmed Sherwali, Daniel M. Ratner, Lukas Chrostowski, and Karen C. Cheung. Sub-wavelength grating for enhanced ring resonator biosensor. *Opt. Express*, 24(14):15672–15686, Jul 2016. (Cited in page 61.)

[162] Anup M Upadhyaya, Maneesh Srivastava, Preeta Sharan, and T Srinivas. Performance analysis of optical mems based pressure sensor using ring resonators structure on circular diaphragm. In *TENCON 2019 - 2019 IEEE Region 10 Conference (TENCON)*, pages 668–672, 2019. (Cited in page 61.)

[163] Viphretuo Mere, Hemalatha Muthuganesan, Yusuf Kar, Cor Van Kruijsdijk, and Shankar Kumar Selvaraja. On-chip chemical sensing using slot-waveguide-based ring resonator. *IEEE Sensors Journal*, 20(11):5970–5975, 2020. (Cited in page 61.)

[164] Shwetha Malthesh and Narayan Krishnaswamy. Improvement in quality factor of double microring resonator for sensing applications. *Journal of Nanophotonics*, 13(2):1 – 9, 2019. (Cited in page 61.)

[165] Zhengrui Tu, Dingshan Gao, Meiling Zhang, and Daming Zhang. High-sensitivity complex refractive index sensing based on fano resonance in the subwavelength grating waveguide micro-ring resonator. *Opt. Express*, 25(17):20911–20922, Aug 2017. (Cited in page 61.)

[166] Heming Wei and Sridhar Krishnaswamy. Direct laser writing polymer micro-resonators for refractive index sensors. *IEEE Photonics Technology Letters*, 28(24):2819–2822, 2016. (Cited in page 61.)

[167] Lijun Huang, Hai Yan, Xiaochuan Xu, Swapnajit Chakravarty, Naimei Tang, Huiping Tian, and Ray T. Chen. Low detection limit sensor based on subwavelength grating racetrack resonator. In Alexander N. Cartwright, Dan V. Nicolau, and Dror Fixler, editors, *Nanoscale Imaging, Sensing, and Actuation for Biomedical Applications XIV*, volume 10077, pages 82 – 88. International Society for Optics and Photonics, SPIE, 2017. (Cited in page 61.)

[168] M. de Goede, M. Dijkstra, R. Obregón Núñez, E. Martínez, and S. M. García-Blanco. High quality factor Al2O3 microring resonators for on-chip sensing applications. In Sonia M. García-Blanco and Pavel Cheben, editors, *Integrated Optics: Devices, Materials, and Technologies XXII*, volume 10535, pages 1 – 7. International Society for Optics and Photonics, SPIE, 2018. (Cited in page 61.)

[169] Patrick Steglich, Claus Villringer, Silvio Pulwer, Friedhelm Heinrich, Joachim Bauer, Birgit Dietzel, Christian Mai, Andreas Mai, Mauro Casalboni, and Sigurd Schrader. Hybrid-waveguide ring resonator for biochemical sensing. *IEEE Sensors Journal*, 17(15):4781–4790, 2017. (Cited in page 61.)

[170] Y. Tomono, H. Hoshi, and H. Shimizu. Co2 detection with si slot waveguide ring resonators toward on-chip specific gas sensing. In *Conference on Lasers and Electro-Optics*, page JTh2A.96. Optical Society of America, 2019. (Cited in page 61.)

[171] Md Jubayer Al Mahmod, Rakib Hyder, and Md Zahurul Islam. A highly sensitive metal–insulator–metal ring resonator-based nanophotonic structure for biosensing applications. *IEEE Sensors Journal*, 18(16):6563–6568, 2018. (Cited in page 61.)

[172] Ali Butt, N. Kazanskiy, and Svetlana Khonina. Carbon dioxide gas sensor based on polyhexamethylene biguanide polymer deposited on silicon nanocylinders metasurface. 2020. (Cited in pages 62 and 119.)

[173] Mahmoud H. Elshorbagy, Alexander Cuadrado, and Javier Alda. High-sensitivity integrated devices based on surface plasmon resonance for sensing applications. *Photon. Res.*, 5(6):654–661, Dec 2017. (Cited in pages 62 and 64.)

[174] Da-Shin Wang and Shih-Kang Fan. Microfluidic surface plasmon resonance sensors: From principles to point-of-care applications. *Sensors*, 16(8), 2016. (Cited in pages 62 and 63.)

[175] Liuwen Zeng, Miao Chen, Wei Yan, Zhaofeng Li, and Fuhua Yang. Si-grating-assisted spr sensor with high figure of merit based on fabry–pérot cavity. *Optics Communications*, 457:124641, 2020. (Cited in pages 62 and 64.)

[176] Yijun Tang, Xiangqun Zeng, and Jennifer Liang. Surface plasmon resonance: An introduction to a surface spectroscopy technique. *Journal of chemical education*, 87(7):742–746, Jul 2010. 21359107[pmid]. (Cited in page 62.)

[177] Jun Zhu, Ge Wang, Frank Jiang, Yunbai Qin, and Hu Cong. Temperature sensor of mos2 based on hybrid plasmonic waveguides. *Plasmonics*, 14(6):1863–1870, Dec 2019. (Cited in pages 62 and 64.)

[178] Aya O Zaki, Khaled Kirah, and Mohamed A Swillam. Integrated optical sensor using hybrid plasmonics for lab on chip applications. *Journal of Optics*, 18(8):085803, jul 2016. (Cited in pages 62 and 64.)

[179] S M Sherif, D C Zografopoulos, L A Shahada, R Beccherelli, and M Swillam. Integrated plasmonic refractometric sensor using fano resonance. *Journal of Physics D: Applied Physics*, 50(5):055104, jan 2017. (Cited in page 64.)

[180] Anuj K. Sharma and Ankit Kumar Pandey. Design and analysis of plasmonic sensor in communication band with gold grating on nitride substrate. *Superlattices and Microstructures*, 130:369–376, 2019. (Cited in page 64.)

[181] Pankaj Arora and Sambhavi Shukla. Self-referenced integrated plasmonic device based on engineered periodic nanostructures for sensing applications. page 54, 02 2020. (Cited in page 64.)

[182] Jiong Xu, Yunqing Lu, Min Xu, Ji Xu, Jin Wang, and Jiajin Zheng. Highly riu-sensitive plasmonic metal-dielectric-metal device with two side-coupled fano cavities. In *2018 Asia Communications and Photonics Conference (ACP)*, pages 1–3, 2018. (Cited in page 64.)

[183] L. Augel, S. Bechler, R. Körner, M. Oehme, J. Schulze, and I. A. Fischer. An integrated plasmonic refractive index sensor: Al nanohole arrays on ge pin photodiodes. In *2017 IEEE International Electron Devices Meeting (IEDM)*, pages 40.5.1–40.5.4, 2017. (Cited in page 64.)

[184] Xu Han, Guanghui Ren, Thach G. Nguyen, Huifu Xiao, Yonghui Tian, and Arnan Mitchell. On-chip biochemical sensor using wide gaussian beams in silicon waveguide-integrated plasmonic crystal. *Opt. Lett.*, 45(8):2283–2286, Apr 2020. (Cited in page 64.)

[185] Mohammad Reza Rakhshani and Mohammad Ali Mansouri-Birjandi. High sensitivity plasmonic refractive index sensing and its application for human blood group identification. *Sensors and Actuators B: Chemical*, 249:168–176, 2017. (Cited in page 64.)

[186] Rui Cheng and Lukas Chrostowski. Spectral design of silicon integrated bragg gratings: A tutorial. *Journal of Lightwave Technology*, PP:1–1, 11 2020. (Cited in page 66.)

[187] A. Brandenburg and A. Gombert. Grating couplers as chemical sensors: a new optical configuration. *Sensors and Actuators B: Chemical*, 17(1):35–40, 1993. (Cited in page 66.)

[188] Xingwang Zhang, Guangya Zhou, Peng Shi, Han Du, Tong Lin, Jinghua Teng, and Fook Siong Chau. On-chip integrated optofluidic complex refractive index sensing using silicon photonic crystal nanobeam cavities. *Opt. Lett.*, 41(6):1197–1200, Mar 2016. (Cited in pages 66 and 68.)

[189] L. Augel, S. Bechler, R. Körner, M. Oehme, J. Schulze, and I. A. Fischer. An integrated plasmonic refractive index sensor: Al nanohole arrays on ge pin photodiodes. In *2017 IEEE International Electron Devices Meeting (IEDM)*, pages 40.5.1–40.5.4, 2017. (Cited in pages 66 and 68.)

[190] Fujun Sun, Zhongyuan Fu, Chunhong Wang, Zhaoxiang Ding, Chao Wang, and Huiping Tian. Ultra-compact air-mode photonic crystal nanobeam cavity integrated with bandstop filter for refractive index sensing. *Appl. Opt.*, 56(15):4363–4368, May 2017. (Cited in pages 66 and 68.)

[191] Guohui Yuan, Fangcao Peng, Lei Guan, Zhenming Peng, and Zhuoran Wang. Autler;townes splitting biosensing based on a nonuniform photonic crystal waveguide with feedback loop. *Appl. Opt.*, 57(24):6976–6981, Aug 2018. (Cited in pages 66 and 68.)

[192] Yonghao Liu, Shuling Wang, Deyin Zhao, Weidong Zhou, and Yuze Sun. High quality factor photonic crystal filter and its application for refractive index sensing. *Opt. Express*, 25(9):10536–10545, May 2017. (Cited in pages 66 and 68.)

[193] Peipeng Xu, Jiajiu Zheng, Jun Zhou, Yueyang Chen, Chen Zou, and Arka Majumdar. Multi-slot photonic crystal cavities for high-sensitivity refractive index sensing. *Opt. Express*, 27(3):3609–3616, Feb 2019. (Cited in pages 66 and 68.)

[194] Dorota Pawlak. Metamaterials and photonic crystals - potential applications for self-organized eutectic micro- and nanostructures. *Scientia Plena*, 4, 01 2008. (Cited in page 67.)

[195] Hibiki Kagami, Tomohiro Amemiya, Makoto Tanaka, Yuning Wang, Nobuhiko Nishiyama, and Shigehisa Arai. Metamaterial infrared refractometer for determining broadband complex refractive index. *Opt. Express*, 27(20):28879–28890, Sep 2019. (Cited in page 67.)

[196] Jian Zhou, Lijun Huang, Zhongyuan Fu, Fujun Sun, and Huiping Tian. Higher q factor and higher extinction ratio with lower detection limit photonic crystal–parallel-integrated sensor array for on-chip optical multiplexing sensing. *Appl. Opt.*, 55(35):10078–10083, Dec 2016. (Cited in page 68.)

[197] Penghao Liu and Yaocheng Shi. Simultaneous measurement of refractive index and temperature using cascaded side-coupled photonic crystal nanobeam cavities. *Opt. Express*, 25(23):28398–28406, Nov 2017. (Cited in page 68.)

[198] Penghao Liu and Yaocheng Shi. Simultaneous measurement of refractive index and temperature using cascaded side-coupled photonic crystal nanobeam cavities. *Opt. Express*, 25(23):28398–28406, Nov 2017. (Cited in page 68.)

[199] Mohammad Danaie and Behnam Kiani. Design of a label-free photonic crystal refractive index sensor for biomedical applications. *Photonics and Nanostructures - Fundamentals and Applications*, 31:89–98, 2018. (Cited in page 68.)

[200] Penghui Dong, Daoxin Dai, and Yaocheng Shi. Low-index-mode photonic crystal nanobeam cavity for refractive index sensing m wavelength band. *Appl. Opt.*, 58(12):3059–3063, Apr 2019. (Cited in page 68.)

[201] Nihal F. F. Areed, Mohamed Farhat O. Hameed, and S. S. A. Obayya. Highly sensitive face-shaped label-free photonic crystal refractometer for glucose concentration monitoring. *Optical and Quantum Electronics*, 49(1):5, Dec 2016. (Cited in page 68.)

[202] Daquan Yang, Chuan Wang, and Yuefeng Ji. Silicon on-chip one-dimensional photonic crystal nanobeam bandgap filter integrated with nanobeam cavity for accurate refractive index sensing. *IEEE Photonics Journal*, 8(2):1–8, 2016. (Cited in page 68.)

[203] Lijun Huang, Jian Zhou, Fujun Sun, Zhongyuan Fu, and Huiping Tian. Optimization of one dimensional photonic crystal elliptical-hole low-index mode nanobeam cavities for on-chip sensing. *Journal of Lightwave Technology*, 34(15):3496–3502, 2016. (Cited in page 68.)

[204] Abdul Shakoor, Boon Chong Cheah, Mohammed A. Al-Rawhani, Marco Grande, James Grant, Luiz Carlos Paiva Gouveia, and David R. S. Cumming. Cmos nanophotonic sensor with integrated readout system. *IEEE Sensors Journal*, 18(22):9188–9194, 2018. (Cited in page 68.)

[205] Sourabh Sahu, Jalil Ali, Preecha P. Yupapin, and Ghanshyam Singh. Optical biosensor based on a cladding modulated grating waveguide. *Optik*, 166:103–109, 2018. (Cited in page 68.)

[206] Chao Ying Zhao, Lei Zhang, and Cheng Mei Zhang. Compact soi optimized slot microring coupled phase-shifted bragg grating resonator for sensing. *Optics Communications*, 414:212–216, 2018. (Cited in page 68.)

[207] Christoph Prokop, Nico Irmler, Bert Laegel, Sandra Wolff, Arnan Mitchell, and Christian Karnutsch. Optofluidic refractive index sensor based on air-suspended su[U+2010]8 grating couplers. *Sensors and Actuators A: Physical*, 263:439–444, 2017. (Cited in page 68.)

[208] U.S. Tripathi and Vipul Rastogi. Temperature insensitive long period waveguide gratings in rib waveguide. *Optik*, 186:15–21, 2019. (Cited in page 68.)

[209] Enxiao Luan, Han Yun, Minglei Ma, Daniel M. Ratner, Karen C. Cheung, and Lukas Chrostowski. Label-free biosensing with a multi-box sub-wavelength phase-shifted bragg grating waveguide. *Biomed. Opt. Express*, 10(9):4825–4838, Sep 2019. (Cited in page 68.)

[210] Sourabh Jain, Sulabh Srivastava, Swati Rajput, Lalit Singh, Pragya Tiwari, Arvind K. Srivastava, and Mukesh Kumar. Thermally stable optical filtering using silicon-based comb-like asymmetric grating for sensing applications. *IEEE Sensors Journal*, 20(7):3529–3535, 2020. (Cited in page 68.)

[211] Mandeep Singh, Sanjeev Kumar Raghuwanshi, and Om Prakash. Modeling of grating assisted hybrid plasmonic filter and its on-chip gas sensing application. *IEEE Sensors Journal*, 19(11):4039–4044, 2019. (Cited in page 68.)

[212] H.F. Taylor and A. Yariv. Guided wave optics. *Proceedings of the IEEE*, 62(8):1044–1060, 1974. (Cited in page 71.)

[213] K. O. Hill, Y. Fujii, D. C. Johnson, and B. S. Kawasaki. Photosensitivity in optical fiber waveguides: Application to reflection filter fabrication. *Applied Physics Letters*, 32(10):647–649, 1978. (Cited in page 71.)

[214] K.O. Hill. Efficient mode conversion in telecommunication fibre using externally written gratings. *Electronics Letters*, 26:1270–1272(2), August 1990. (Cited in page 71.)

[215] Ashish M. Vengsarkar, Paul J. Lemaire, J. B. Judkins, V. Bhatia, T. Erdogan, and J. E. Sipe. Long-period fiber gratings as band-rejection filters. In *Optical Fiber Communications Conference*, page PD4. Optical Society of America, 1995. (Cited in page 71.)

[216] Turan Erdogan. Cladding-mode resonances in short- and long-period fiber grating filters. *J. Opt. Soc. Am. A*, 14(8):1760–1773, Aug 1997. (Cited in page 71.)

[217] Kin Seng Chiang and Qing Liu. Long-period grating devices for application in optical communication. In *Proc. 5th International Conference on Optical Communications and Networks (ICOCN 2006*, 2006. (Cited in page 71.)

[218] Hiroshi Tsuda and Kei Urabe. Characterization of long-period grating refractive index sensors and their applications. *Sensors*, 9(6):4559–4571, 2009. (Cited in page 71.)

[219] S. Pal, A. Chauhan, M. Singh, P. Kumar, M. Sharma, N. Pradhan, K. Singh, and C. Dhanavantri. Realization of long-period corrugated grating in silica-on-silicon-based channel waveguide. *IEEE Photonics Technology Letters*, 21(20):1490 – 1492, 2009. (Cited in page 71.)

[220] Wen Bin Ji, Swee Chuan Tjin, Bo Lin, and Choong Leng Ng. Highly sensitive refractive index sensor based on adiabatically tapered microfiber long period gratings. *Sensors*, 13(10):14055–14063, 2013. (Cited in page 71.)

[221] Yin Liu, Hongchang Deng, and Libo Yuan. Arc-discharge-induced off-axis spiral long period fiber gratings and their sensing characteristics. *Optical Fiber Technology*, 52:101950, 2019. (Cited in page 71.)

[222] H. A. LORENTZ. The theorem of poynting concerning the energy in the electromagnetic field and two general propositions concerning the propagation of light. *Amsterdammer Akademie der Wetenschappen*, 4:176, 1896. (Cited in pages 71 and 72.)

[223] James Clerk Maxwell. A dynamical theory of the electromagnetic field. *Philosophical Transactions of the Royal Society of London*, 155:459–513, 1865. (Cited in page 72.)

[224] Allan W Snyder and John Love. *Optical waveguide theory*. Springer Science & Business Media, 2012. (Cited in pages 74 and 104.)

[225] Haiming Wang. Measurement of optical waveguide scattering loss: an improved method by the use of a coblentz mirror. *Appl. Opt.*, 33(9):1707–1714, Mar 1994. (Cited in page 82.)

[226] Xin-Wu Zhao and Qi Wang. Mini review: Recent advances in long period fiber grating biological and chemical sensors. *Instrumentation Science & Technology*, 47(2):140–169, 2019. (Cited in page 85.)

[227] Yu Qian, Yong Zhao, Qi lu Wu, and Yang Yang. Review of salinity measurement technology based on optical fiber sensor. *Sensors and Actuators B: Chemical*, 260:86–105, 2018. (Cited in page 85.)

[228] Ming jie Yin, Bobo Huang, Shaorui Gao, A. Ping Zhang, and Xuesong Ye. Optical fiber lpg biosensor integrated microfluidic chip for ultrasensitive glucose detection. *Biomed. Opt. Express*, 7(5):2067–2077, May 2016. (Cited in page 85.)

[229] Rosane Falate, Ricardo Kamikawachi, J.L. Fabris, M. Muller, H.J. Kalinowski, F.A.S. Ferri, and L.K. Czelusniak. Petroleum hydrocarbon detection with long period gratings. pages 907 – 910 vol.2, 10 2003. (Cited in page 85.)

[230] Matthew Partridge, Rebecca Wong, Stephen W. James, Frank Davis, Séamus P.J. Higson, and Ralph P. Tatam. Long period grating based toluene sensor for use with water contamination. *Sensors and Actuators B: Chemical*, 203:621–625, 2014. (Cited in pages 85 and 90.)

[231] L. Marques, F.U. Hernandez, S.W. James, S.P. Morgan, M. Clark, R.P. Tatam, and S. Korposh. Highly sensitive optical fibre long period grating

biosensor anchored with silica core gold shell nanoparticles. *Biosensors and Bioelectronics*, 75:222–231, 2016. (Cited in page 85.)

[232] Sergiy Korposh, Iva Chianella, Antonio Guerreiro, Sarah Caygill, Sergey Piletsky, Stephen W. James, and Ralph P. Tatam. Selective vancomycin detection using optical fibre long period gratings functionalised with molecularly imprinted polymer nanoparticles. *Analyst*, 139:2229–2236, 2014. (Cited in page 85.)

[233] Helena M.R. Gonçalves, Luis Moreira, Leonor Pereira, Pedro Jorge, Carlos Gouveia, Paula Martins-Lopes, and José R.A. Fernandes. Biosensor for label-free dna quantification based on functionalized lpgs. *Biosensors and Bioelectronics*, 84:30–36, 2016. (Cited in page 85.)

[234] Aloka B. Bandara, Ziwei Zuo, Siddharth Ramachandran, Alfred Ritter, James R. Heflin, and Thomas J. Inzana. Detection of methicillin-resistant staphylococci by biosensor assay consisting of nanoscale films on optical fiber long-period gratings. *Biosensors and Bioelectronics*, 70:433–440, 2015. (Cited in page 85.)

[235] Marta Janczuk-Richter, Beata Gromadzka, Łukasz Richter, Mirosława Panasiuk, Karolina Zimmer, Predrag Mikulic, Wojtek Bock, Sebastian Maćkowski, Mateusz Smietana, and Joanna Jönsson. Immunosensor based on long-period fiber gratings for detection of viruses causing gastroenteritis. *Sensors*, 20:813, 02 2020. (Cited in page 85.)

[236] Bashir Tahir, M. Saeed, Rashid Ahmed, Maqsood Ahmed, and Muhammad Gul. Long-period grating as strain sensor. *Journal of Ovonic Research*, 8:113–120, 09 2012. (Cited in page 85.)

[237] H. Patrick, C. C. Chang, and S. Vohra. Long period fibre gratings for structural bend sensing. *Electronics Letters*, 34:1773–1775, 1998. (Cited in page 85.)

[238] S.W. James, S. Khaliq, and R.P. Tatam. A long period grating liquid level sensor. In *2002 15th Optical Fiber Sensors Conference Technical Digest. OFS 2002(Cat. No.02EX533)*, pages 127–130 vol.1, 2002. (Cited in page 86.)

[239] T.W. MacDougall, S. Pilevar, C.W. Haggans, and M.A. Jackson. Generalized expression for the growth of long period gratings. *IEEE Photonics Technology Letters*, 10(10):1449–1451, 1998. (Cited in page 87.)

[240] Xuewen Shu, Lin Zhang, and Ian Bennion. Sensitivity characteristics of long-period fiber gratings. *J. Lightwave Technol.*, 20(2):255, Feb 2002. (Cited in pages 87 and 92.)

[241] E. Simões, I. Abe, J. Oliveira, O. Frazão, P. Caldas, and J.L. Pinto. Characterization of optical fiber long period grating refractometer with nanocoating. *Sensors and Actuators B: Chemical*, 153(2):335 – 339, 2011. (Cited in page 88.)

[242] Haifeng Hu, Chao Du, Qi Wang, Xiaoli Wang, and Yong Zhao. High sensitivity internal refractive index sensor based on a photonic crystal fiber long period grating. *Instrumentation Science & Technology*, 45(2):181–189, 2017. (Cited in page 88.)

[243] Qing Liu, Zhonghua Gu, Mi Kyoung Park, and Jaehoon Chung. Experimental demonstration of highly sensitive optical sensor based on grating-assisted light coupling between strip and slot waveguides. *Opt. Express*, 24(12):12549–12556, Jun 2016. (Cited in pages 89 and 92.)

[244] Eric Dulkeith, Fengnian Xia, Laurent Schares, William M. J. Green, and Yurii A. Vlasov. Group index and group velocity dispersion in silicon-on-insulator photonic wires. *Opt. Express*, 14(9):3853–3863, May 2006. (Cited in page 89.)

[245] Xuewen Shu, Liren Zhang, and Ian Bennion. Sensitivity characteristics near the dispersion turning points of long-period fiber gratings in b/ge codoped fiber. *Optics letters*, 26:1755–7, 12 2001. (Cited in page 90.)

[246] Jens Høvik, Mukesh Yadav, Jong Wook Noh, and Astrid Aksnes. Waveguide asymmetric long-period grating couplers as refractive index sensors. *Opt. Express*, 28(16):23936–23949, Aug 2020. (Cited in pages 90, 92, and 113.)

[247] A.P. Zhang, Li-Yang Shao, Jin-Fei Ding, and Sailing He. Sandwiched long-period gratings for simultaneous measurement of refractive index and temperature. *IEEE Photonics Technology Letters*, 17(11):2397–2399, 2005. (Cited in page 92.)

[248] Yan en Fan, Tao Zhu, Leilei Shi, and Yun-Jiang Rao. Highly sensitive refractive index sensor based on two cascaded special long-period fiber gratings with rotary refractive index modulation. *Appl. Opt.*, 50(23):4604–4610, Aug 2011. (Cited in page 92.)

[249] Jinhua Yan, A. Ping Zhang, Li-Yang Shao, Jin-Fei Ding, and Sailing He. Simultaneous measurement of refractive index and temperature by using dual long-period gratings with an etching process. *IEEE Sensors Journal*, 7(9):1360–1361, 2007. (Cited in page 92.)

[250] Edward Davies, Pouneh Saffari, Chengbo Mou, Kaiming Zou, and Lin Zhang. Refractive index sensitivity enhancement of 81° tilted Bragg gratings by cladding etching. In Julian D. C. Jones, editor, *20th International Conference on Optical Fibre Sensors*, volume 7503, pages 995 – 998. International Society for Optics and Photonics, SPIE, 2009. (Cited in page 92.)

[251] Chien-Hsing Chen, Shan-Chien Chen, Yi-Chun Chen, Hao-Teng Hu, Tai Huei Wei, Wei-Te Wu, Jian-Neng Wang, and Jaw-Luen Tang. Laser-induced long-period fiber grating sensor modified with gold nano-rods. In *2009 Conference on Lasers Electro Optics The Pacific Rim Conference on Lasers and Electro-Optics*, pages 1–2, 2009. (Cited in page 92.)

[252] Fei Tian, Xiangzhi Li, Jiri Kanka, and Henry Du. Fiber optic index sensor enhanced by gold nanoparticle assembly on long period grating. *Optik*, 132:445–449, 2017. (Cited in page 92.)

[253] Edward Davies, Reeta Viitala, Mikko Salomäki, Sami Areva, Lin Zhang, and Ian Bennion. Sol–gel derived coating applied to long-period gratings for enhanced refractive index sensing properties. *Journal of Optics A Pure and Applied Optics*, 01 2009. (Cited in page 92.)

[254] Jianchun Yang, Chuanyi Tao, Xueming Li, Guangqin Zhu, and Weimin Chen. Long-period fiber grating sensor with a styrene-acrylonitrile nano-film incorporating cryptophane a for methane detection. *Opt. Express*, 19(15):14696–14706, Jul 2011. (Cited in pages 92 and 119.)

[255] Sergiy Korposh, Seung-Woo Lee, Stephen James, and Ralph Tatam. Refractive index sensitivity of fibre-optic long period gratings coated with sio2 nanoparticle mesoporous thin films. *Measurement Science and Technology*, 22:075208, 06 2011. (Cited in page 92.)

[256] X. Yu, P. Shum, and G. B. Ren. Highly sensitive photonic crystal fiber-based refractive index sensing using mechanical long-period grating. *IEEE Photonics Technology Letters*, 20(20):1688–1690, 2008. (Cited in page 92.)

[257] Marta Nespereira, João M. P. Coelho, Manuel Abreu, and José Manuel Rebordão. Ultrashort long-period fiber grating sensors inscribed on a single mode fiber laser radiation. *Journal of Sensors*, 2017:4196431, Aug 2017. (Cited in page 92.)

[258] Jian Yang, Li Yang, Chang-Qing Xu, Chenglin Xu, Weiping Huang, and Yingfu Li. Long-period grating refractive index sensor with a modified cladding structure for large operational range and high sensitivity. *Appl. Opt.*, 45(24):6142–6147, Aug 2006. (Cited in page 92.)

[259] Jian Tang, Cailing Fu, Zhiyong Bai, Changrui Liao, and Yiping Wang. Sensing characteristics of tilted long period fiber gratings inscribed by infrared femtosecond laser. *Sensors*, 18(9), 2018. (Cited in page 92.)

[260] Jianjun Cao, Yuan Sun, Yan Kong, and Weiying Qian. The sensitivity of grating-based spr sensors with wavelength interrogation. *Sensors*, 19(2), 2019. (Cited in page 92.)

[261] Rebecca Wong, Dora Hu, Morten Ibsen, and Ping Shum. *Optical Fibre Long-Period Grating Sensors Operating at and around the Phase Matching Turning Point*. 01 2019. (Cited in pages 92 and 113.)

[262] Flavio Esposito, Anubhav Srivastava, Stefania Campopiano, and Agostino Iadicicco. Sensing features of arc-induced long period gratings. *Proceedings*, 15(1), 2019. (Cited in page 92.)

[263] U.S. Tripathi and Vipul Rastogi. Temperature insensitive long period waveguide gratings in rib waveguide. *Optik*, 186:15 – 21, 2019. (Cited in pages 92, 95, and 105.)

[264] Pradip Dey and Pranabendu Ganguly. A technical report on fabrication of su-8 optical waveguides. *Journal of Optics (India)*, 43,:79–83, 04 2014. (Cited in page 96.)

[265] John E. Saunders, Connor Sanders, Hao Chen, and Hans-Peter Loock. Refractive indices of common solvents and solutions at 1550 nm. *Appl. Opt.*, 55(4):947–953, Feb 2016. (Cited in page 101.)

[266] Amir Arbabi and Lynford Goddard. Measurements of the refractive indices and thermo-optic coefficients of si3n4 and siox using microring resonances. *Optics Letters*, 38, 10 2013. (Cited in page 101.)

[267] Marc Ibrahim, Jens Schmid, Alireza Aleali, Pavel Cheben, Jean Lapointe, S. Janz, Przemek Bock, Adam Densmore, Boris Lamontagne, Rubin Ma, DanXia Xu, and Winnie Ye. Athermal silicon waveguides with bridged subwavelength gratings for te and tm polarizations. *Optics express*, 20:18356–61, 07 2012. (Cited in page 101.)

[268] Qing Liu, Kin Seng Chiang, and Kar Pong Lor. Condition for the realization of a temperature-insensitive long-period waveguide grating. *Optics letters*, 31(18):2716–2718, 2006. (Cited in page 105.)

[269] Timo Aalto, Kimmo Solehmainen, Mikko Harjanne, Markku Kapulainen, and Päivi Heimala. Low-loss converters between optical silicon waveguides of different sizes and types. *Photonics Technology Letters, IEEE*, 18:709 – 711, 02 2006. (Cited in page 106.)

[270] Sarvagya Dwivedi, Alfonso Ruocco, Michael Vanslembrouck, Thijs Spuesens, Peter Bienstman, Pieter Dumon, Thomas Van Vaerenbergh, and Wim Bogaerts. Experimental extraction of effective refractive index and thermo-optic coefficients of silicon-on-insulator waveguides using interferometers. *Journal of Lightwave Technology*, 09 2015. (Cited in pages 115 and 140.)

[271] Global Market Insights, editor. *Gas sensor market size by product,technology,connectivity,application, industry analysis report*. 2020. (Cited in page 117.)

[272] G.J Qureshi, N Padha, V.K Gupta, M.N Kamalasanan, A.P Singh, A Kapoor, and K.N Tripathi. Styrene acrylonitrile (san) based polymeric waveguides. *Optics Laser Technology*, 35(5):401–407, 2003. (Cited in page 119.)

[273] Gilvan Barroso, Quan Li, Rajendra K. Bordia, and Günter Motz. Polymeric and ceramic silicon-based coatings – a review. *J. Mater. Chem. A*, 7:1936–1963, 2019. (Cited in page 119.)

[274] Zahra Abbasian Chaleshtari and Mohammad Reza Moghbeli. Preparation of highly open porous styrene/acrylonitrile and styrene/acrylonitrile/organoclay polymerized high internal phase emulsion (polyhipe) foams via emulsion templating. *Journal of Applied Polymer Science*, 119:3728 – 3738, 03 2011. (Cited in page 119.)

[275] Haris Apriyanto. *Study, analysis and experimental validation of fiber refractometers based on single-mode, multimode and photonic crystal fibers for refractive index measurements with application for the detection of methane.* Theses, Institut National Polytechnique de Toulouse (INP Toulouse), February 2019. (Cited in page 119.)

[276] Susan M. Lindecrantz. *Waveguide Mach-Zehnder interferometer for measurement of methane dissolved in water.* PhD thesis, The arctic university of norway, 2016. (Cited in page 119.)

[277] Wenwen Ma, Jiaxian Xing, Ruohui Wang, Qiangzhou Rong, Wenlu Zhang, Yaocun Li, Junying Zhang, and Xueguang Qiao. Optical fiber fabry–perot interferometric co2 gas sensor using guanidine derivative polymer functionalized layer. *IEEE Sensors Journal*, 18(5):1924–1929, 2018. (Cited in page 119.)

[278] Opinion on phmb, from the european commission-scientific committee. https://ec.europa.eu/health/sites/default/files/scientificcommittees/consumersafety/docs/sccso204.pdf. substance info. (Cited in page 120.)

[279] H. Kogelnik and T. Tamir. *Topics in Applied Physics: integrated optics*, pages vol. 7,ch. 2. Springer, Berlin, Heidelberg, 1975. (Cited in page 144.)